frontiers | Research Topics

Role of mathematical modeling in advanced power generation systems

Edited by
Arijit Ganguli, Sagar Deshpande, Mandar Tabib and Mahesh Dhotre

Published in
Frontiers in Energy Research
Frontiers in Thermal Engineering

ISSN 1664-8714
ISBN 978-2-8325-3880-7
DOI 10.3389/978-2-8325-3880-7

About Frontiers

Frontiers is more than just an open access publisher of scholarly articles: it is a pioneering approach to the world of academia, radically improving the way scholarly research is managed. The grand vision of Frontiers is a world where all people have an equal opportunity to seek, share and generate knowledge. Frontiers provides immediate and permanent online open access to all its publications, but this alone is not enough to realize our grand goals.

Frontiers journal series

The Frontiers journal series is a multi-tier and interdisciplinary set of open-access, online journals, promising a paradigm shift from the current review, selection and dissemination processes in academic publishing. All Frontiers journals are driven by researchers for researchers; therefore, they constitute a service to the scholarly community. At the same time, the *Frontiers journal series* operates on a revolutionary invention, the tiered publishing system, initially addressing specific communities of scholars, and gradually climbing up to broader public understanding, thus serving the interests of the lay society, too.

Dedication to quality

Each Frontiers article is a landmark of the highest quality, thanks to genuinely collaborative interactions between authors and review editors, who include some of the world's best academicians. Research must be certified by peers before entering a stream of knowledge that may eventually reach the public - and shape society; therefore, Frontiers only applies the most rigorous and unbiased reviews. Frontiers revolutionizes research publishing by freely delivering the most outstanding research, evaluated with no bias from both the academic and social point of view. By applying the most advanced information technologies, Frontiers is catapulting scholarly publishing into a new generation.

What are Frontiers Research Topics?

Frontiers Research Topics are very popular trademarks of the *Frontiers journals series*: they are collections of at least ten articles, all centered on a particular subject. With their unique mix of varied contributions from Original Research to Review Articles, Frontiers Research Topics unify the most influential researchers, the latest key findings and historical advances in a hot research area.

Find out more on how to host your own Frontiers Research Topic or contribute to one as an author by contacting the Frontiers editorial office: frontiersin.org/about/contact

Role of mathematical modeling in advanced power generation systems

Topic editors

Arijit Ganguli — Ahmedabad University, India

Sagar Deshpande — Grasim Industries Limited, India

Mandar Tabib — SINTEF, Norway

Mahesh Dhotre — Hitachi Energy Switzerland, Switzerland

Citation

Ganguli, A., Deshpande, S., Tabib, M., Dhotre, M., eds. (2023). *Role of mathematical modeling in advanced power generation systems*. Lausanne: Frontiers Media SA.

doi: 10.3389/978-2-8325-3880-7

Table of contents

frontiers | Frontiers in Energy Research

TYPE Editorial
PUBLISHED 23 October 2023
DOI 10.3389/fenrg.2023.1301851

OPEN ACCESS

EDITED AND REVIEWED BY
Ellen B. Stechel,
Arizona State University, United States

*CORRESPONDENCE
Arijit Ganguli,
ganguliarijit@gmail.com

†PRESENT ADDRESS
Mahesh Dhotre,
Hitachi Energy Ltd., Switzerland

RECEIVED 25 September 2023
ACCEPTED 11 October 2023
PUBLISHED 23 October 2023

CITATION
Ganguli A, Tabib M, Deshpande S and Dhotre M (2023), Editorial: Role of mathematical modeling in advanced power generation systems.
Front. Energy Res. 11:1301851.
doi: 10.3389/fenrg.2023.1301851

Editorial: Role of mathematical modeling in advanced power generation systems

Arijit Ganguli[1,2]*, Mandar Tabib[3], Sagar Deshpande[2] and Mahesh Dhotre[2†]

[1]School of Engineering and Applied Sciences, Ahmedabad University, Ahmedabad, India, [2]Department of Chemical Engineering, Institute of Chemical Technology, Mumbai, India, [3]Stiftelsen for Industriell og Teknisk Forskning, Trondheim, Norway

KEYWORDS

sustainable development goals - SDGs, solar PV (photovoltaic), machine learning, biomass gasification and power generation, nuclear power, distributed heating systems (DHS), hydrogen production

Editorial on the Research Topic
Role of mathematical modeling in advanced power generation systems

Sustainable development needs the use of alternate sources of energy across the globe. The reduction of carbon emissions (in other words, having a low carbon footprint) depends on the effective utilization of resources and lesser use of fossil fuels. The Sustainable Development Goals (SDGs) decided, during the Paris Agreement, to bring prosperity to all countries across the globe and save the planet. The most prominent goals out of the 17 SDGs related to the current Research Topic are goals 7, 9, 12, and 13. Some of the key targets of Goal 7 include ensuring universal access to affordable, reliable, and modern energy services, substantially increasing the share of renewable energy in the global energy mix, and doubling the global rate of improvement in energy efficiency by 2030. Similarly, Goal 9 talks about building resilient infrastructure, promoting inclusive and sustainable industrialization, and fostering innovation. Goal 12 targets improving energy efficiency and promoting the adoption of sustainable practices in industries. Goal 13 targets limiting global warming to 1.5°C above preindustrial levels by decreasing emissions to half using different technological advancements and behavioral actions. The above four goals can be better achieved by harnessing the advances in mathematical modeling. The present Research Topic was published on 10th February 2022 to call for contributions on how mathematical modeling can play a big role in optimizing energy utilization and reduction of greenhouse gas (GHG) emissions for sustainable industrialization. Around 230 researchers around the globe were contacted for this purpose.

Frontiers in Energy Research in combination with Frontiers in Thermal Engineering published nine articles involving 23 authors from six countries, involving diverse areas of research in mathematical modeling being used in synergy with our objective. Despite the diversity, the six key areas were 1) the optimization of district heating systems (SDG 9), 2) the optimization of safety systems involving condensation in tubes in nuclear power plants (SDG 7, 9, and 12), 3) the optimization of solar photo voltaic modules for power generation (SDG 7, 12, and 13), 4) the characterization of equipment related to thermochemical processing of biomass (SDG 7, 9, 13) 5) the process optimization for CO_2 sequestration during hydrogen production from steam methane reforming (SDG 7, 9, 12, and 13), and 6) mathematical

models to predict the identification of personnel who did not wear protective equipment during the construction of power plants (SDG 9 and 12). Mathematical modeling included computational fluid dynamics (CFD) [areas (2), (3), and (4)] and process modeling [area (5)] using commercial software such as Ansys Fluent and Aspen Plus, respectively, while linear programming models were used in studies in area (1) and deep learning models in area (6).

Power plants are classified as coal based, nuclear based, or made of renewables such as solar, wind, or hydro. With the world grappling with climate change Research Topic, power from renewable sources would reduce carbon dioxide (CO_2) emissions, which, in turn, would help in achieving certain SDG targets mentioned earlier. In this context, some important sources of power production include hydrogen and solar photovoltaics. Furthermore, an innovative way of heating rooms can be obtained by optimized district heating.

Hydrogen has emerged as a source of energy and an alternative to fossil fuels. Though green hydrogen (for example, hydrogen production from electrolysis where the electricity is obtained from renewable sources such as solar and wind, *etc.*) is preferred, hydrogen from chemical processes such as steam methane reforming can also be used for energy needs. Thermochemical processes such as gasification of biomass can be used to generate electricity. The particle size distribution in such gasifiers is non-uniform, and the heat and mass transfer effects are different from the ones for uniformly sized particles. The hydrodynamics in such beds depend on geometric and operating parameters and have a huge effect on equipment performance. Experiments are very difficult in such cases, and mathematical modeling is very important. Ganguli and Bhatt have approached the CFD of such gasifiers both in qualitative and quantitative terms. The CFD model developed showed the characteristics of fluidized beds for Geldart B-type particles with seven different binary mixtures. The segregation and mixing of different operating parameters, such as the superficial velocity of fluid, and geometric parameters, such as bed height, were analyzed, and correlations were developed for the minimum fluidization velocity and pressure drop (Ganguli and Bhatt).

District Heating Systems (DHS) involve the combustion of renewable materials (such as biomass) to produce steam and heating buildings through pipe networks. The advanced versions of DHS offer parallel heating and cooling. Sporleder et al. provided a thorough literature review of the DHS systems until March 2022 and found the research gaps that existed in the area of DHS systems. The role of several technologies such as photovoltaics and heat pumps, with their significant contributions (10% and 25%, respectively) to DHS in buildings, was highlighted. The major contribution from the authors was highlighting the fact that the design of large-scale high-temperature DHS into a sustainable system has not yet been looked at. Mathematical modeling has been restricted to using linear programming models for present systems, while for large-scale systems, heuristic models need to be used. The authors recommended that work needs to be majorly undertaken in the direction of 1) the performance improvement of computational efforts using spatial and temporal aggregation and 2) designing a structure for a sustainable supply system that may have an integration of energy converters and heat sources (such as geothermal energy and large-scale heat pumps). These would need multi-objective optimization based on heuristic solvers.

Nuclear power plants also face the challenge of accidents with the risk of radiation coming out into the atmosphere and causing huge damage to life and property. Passive containment cooling systems (PCCS) in nuclear power plants have innovative condensers in which film condensation takes place in the presence of non-condensable gases such as air or helium. The non-condensable gases cause a decrease in condensation, while the wavy effects of the film cause an enhancement in condensation. However, for many decades, research work has been carried out largely through experimental measurements and analytical modeling. Li et al. performed two-phase CFD simulations using the volume of fluid (VOF) approach to visualize the effect of non-condensable gases on the condensation process. The authors found that for small concentrations of non-condensable gases (5%–10%), the boundary layer of the non-condensable gas layer decreased with the time period of condensation. For lower concentrations of the non-condensable layer, the thermal resistance of the film could be 20%–26%. Another study on such condensers focused on the distribution of steam in specially designed heat exchangers for safety systems in nuclear power plants. These exchangers absorb the heat during shutdown operations or during accidental conditions of nuclear power plants. Ganguli and Pandit carried out single-phase CFD simulations to understand the distribution of steam in such exchangers for higher pressures ranging from 10 to 70 bar since nuclear power plants operate at these pressures. The authors developed a new correlation to find the heat transfer coefficient from the Chilton Colburn analogy. The friction factor was obtained from the pressure drops for the different operating conditions of the condenser.

Safety Research Topic are of prime importance, and during the construction of large power plant sites, it becomes difficult to keep track of them. A case study related to the safety of personnel during the construction of a power plant, in which a deep learning model instead of a manual method was employed to ensure whether each and every personnel was abiding by rules, was developed by Chen et al. The authors developed a deep learning model (modified convolution neural network) to identify the safety of power workers. This included the detection and identification of safety helmets, work clothes, and safety gloves for each worker automatically without manual intervention. The application of this algorithm to real-life scenarios ensured that the algorithm was able to identify the staff who did not wear safety equipment as per the rules and regulations provided to them.

The steam methane reforming (SMRs) process produces hydrogen and a lot of carbon dioxide (CO_2), which must be prevented from emitting into the atmosphere. One of the methods is capturing CO_2 using carbon capture storage and utilization (CCSU). Pellegrini et al. carried out process simulations using ASPEN Plus (with necessary modifications to incorporate mass transfer with reaction and changes in the thermodynamics of the system) to design units for treatment of PSA tail gas by washing with methyldiethanolamine (MDEA). They used a combination of absorber and regenerator for removing the CO_2. The authors chose seven different designs of the absorber and carried out sensitivity analyses of the operating parameters to understand the maximum removal of CO_2 with the conservation of energy and minimum energy change. The developed model gave promising predictions for the implementation of the suggested

modifications. While steam methane reforming is one of the oldest and most effective processes for hydrogen production, there has been considerable work on process intensification, especially in advanced reactor configurations. The current status of advanced reactors for hydrogen production in SMR was reviewed by Ganguli and Bhatt. A comparison of the reactors based on residence time, surface area, scale-up, coke formation, conversion, space velocity, and yield of hydrogen was presented. Furthermore, all the recent kinetic models and coke formation mechanisms were listed. The authors concluded that all the reactors considered had their own strengths. However, implementation on a large scale had a few challenges. Microreactors were shown to be of higher potential in terms of higher yields and lower residence times.

Nassar et al. developed an innovative three-dimensional numerical analysis to understand the view factors of solar PV for arrangement in solar photovoltaics (PV) to increase energy yields. The authors conducted a sensitivity analysis on the tilt angles of solar PV modules placed in different rows for receiving a range of solar irradiations. The primary reason for taking up such a study was the insufficient amount of received radiations on these panels due to the hindrance of PV panels ahead of them. The objective was to improve the performance of PV panels for different incident radiations. The model developed by the authors could accurately estimate the reduction in the incident solar rays and reduction in energy yields in the second and third rows of the PV channels. The model was tested for energy yields with data from different regions of the world. The authors claimed that the model was a viable alternative to other available models [such as the crossed-strings method (CSM)] that failed for the conditions considered for the undertaken study.

In conclusion, it has been observed that mathematical models can play a key role in design optimization and the optimization of safety systems in cities and power plants, such as solar or nuclear. For example, optimization using linear programing in DHS was able to reduce the carbon footprint of cities and contribute to not only low carbon emissions but also building resilient infrastructure. CFD models have shown good promise to predict modifications in both geometric and operating variables, which aided in the optimization of 1) biomass gasifier designs, 2) the distribution of steam under high pressure ensuring a robust design of safety systems in nuclear power plants, and 3) solar PV panel arrangements for better power generation using renewable energy. Deep learning models were proven to be of exceptional use for identification to ensure the safety of personnel. Process modeling using Aspen Plus was able to optimize the process of CO_2 sequestration by optimizing the design of key equipment in the process, such as absorbers, while deep learning models were able to accurately identify personnel who did not wear protective equipment during the construction of a power plant, which was not possible by manual intervention. This provides us with more confidence about the role of mathematical models in achieving the targets of the specific SDGs mentioned at the start of the editorial.

Author contributions

AG: Conceptualization, Formal Analysis, Methodology, Writing–original draft, Writing–review and editing. MT: Writing–review and editing. SD: Writing–review and editing. MD: Writing–review and editing.

Acknowledgments

We would like to express our gratitude to all the authors who proposed their work, all the researchers who proposed their work, and all the researchers who reviewed the submissions to this Research Topic. We would also like to thank the institutions for providing the resources for the research presented in the articles.

Conflict of interest

The authors declare that the research was conducted in the absence of any commercial or financial relationships that could be construed as a potential conflict of interest.

Publisher's note

frontiers in Energy Research

ORIGINAL RESEARCH
published: 27 May 2020
doi: 10.3389/fenrg.2020.00077

Design of the CO_2 Removal Section for PSA Tail Gas Treatment in a Hydrogen Production Plant

*Laura A. Pellegrini, Giorgia De Guido and Stefania Moioli**

GASP, Group of Advanced Separation Processes and GAS Processing, Dipartimento di Chimica, Materiali e Ingegneria Chimica "Giulio Natta", Politecnico di Milano, Milan, Italy

CO_2 capture, storage, and, recently, utilization (CCSU) is considered effective in achieving the target of 2°C established to reduce the gradual increase in global warming. In the literature, most of research has focused on the removal of carbon dioxide from power plants, particularly those fed with coal, which account for higher amounts of CO_2 emissions if compared with those fed with natural gas. CCSU in other non-power sectors is still not fully considered, while its importance in mitigating the environmental impact of industrial activities is equivalent to that of power plants. In the field of hydrogen production, treatment of gaseous streams to remove carbon dioxide is performed for producing a stream of almost pure H_2 starting from syngas and for reducing carbon dioxide emissions, so that CO_2 removal units can be part of different sections of the plant. In this work, a state-of-the-art steam-methane-reforming (SMR) plant for the production of 100,000 Nm^3/h of hydrogen has been considered. Hydrogen is produced from syngas by employing the pressure swing adsorption (PSA) technology, and the exiting tail gas is fed to the burners of the SMR unit, after removal of carbon dioxide. This work focuses on the design of the units for the treatment of the PSA tail gas by employing an aqueous solution of methyldiethanolamine (MDEA). Simulations have been performed with the commercial process simulator ASPEN Plus®, customized by the GASP group of Politecnico di Milano for best representing both the thermodynamics of the system and the mass transfer with reaction. For the scheme composed of the absorber and the regenerator, several column configurations have been considered, and the optimal solution, which minimizes the energy requirements of the plant, has been selected.

Keywords: CO_2, CCS, SMR, hydrogen plant, PSA tail gas, MDEA

OPEN ACCESS

Edited by:
Nannan Sun, Shanghai Advanced Research Institute (CAS), China

Reviewed by:
Hasmukh A. Patel, Aramco Services Company, United States
Kun Yu, Globalfoundries, United States

****Correspondence:***
Stefania Moioli
stefania.moioli@polimi.it

Specialty section:
This article was submitted to Carbon Capture, Storage, and Utilization, a section of the journal Frontiers in Energy Research

Received: *10 December 2019*
Accepted: *14 April 2020*
Published: *27 May 2020*

Citation:
Pellegrini LA, De Guido G and Moioli S (2020) Design of the CO_2 Removal Section for PSA Tail Gas Treatment in a Hydrogen Production Plant. Front. Energy Res. 8:77. doi: 10.3389/fenrg.2020.00077

INTRODUCTION

The carbon capture and storage (CCS) technology has recently received great attention as a mitigation action for decreasing the environmental impact of energy conversion processes based on the use of fossil fuels. Another example of mitigation action includes the switch from a fossil fuel-based economy to an economy that relies on the use of renewable energy sources such as biomass, solar, and wind energies (Jäger-Waldau, 2007; Blanco, 2009; Nema et al., 2012; Schaber et al., 2012; Timilsina et al., 2012; Corsatea, 2014). However, given the current state of development of the latter ones, fossil fuels will continue to play an important role in the future, and as a result, actions such as CCS are worthy being investigated. In recent years, attention has also been paid to CO_2 utilization, promoting the use of the expression "Carbon Capture, Storage, and Utilization" (CCSU) (Hasan et al., 2015).

In order to capture CO_2, a number of processes are currently available, which can be categorized as follows: pre-combustion, post-combustion, and oxy-fuel combustion. A pre-combustion system consists of CO_2 capture before the combustion step. In contrast, a post-combustion system consists of removing CO_2 from flue gases after the combustion of fossil fuels in air has taken place (Alie et al., 2005; Rochelle, 2009; Moioli et al., 2019a,b). In oxy-fuel combustion, nearly pure oxygen is used for combustion instead of air, resulting in a flue gas that mainly consists of CO_2 and H_2O, which would allow using simpler post-combustion separation techniques (e.g., condensation) with significantly lower energy and capital costs. To cope with the demerits of other CCS technologies, the chemical looping combustion (CLC) process has also been recently considered as a solution for CO_2 separation (De Guido et al., 2018).

Another possible integration of CCS is in a steam-methane-reforming (SMR)-based hydrogen plant. On a large industrial scale, SMR is the leading technology for H_2 production from natural gas or light hydrocarbons, which involves a concurrent production of CO_2 as a by-product (Rostrup-Nielsen and Rostrup-Nielsen, 2002; Riis et al., 2005). In particular, in this plant, CO_2 can be captured from three possible locations: the shifted syngas, the PSA tail gas, and the SMR flue gas. Using aqueous solutions of methyldiethanolamine (MDEA) can be a possible method for removing carbon dioxide from these streams (Del Ben, 2018).

MDEA washing is certainly a well-established technology (Aroonwilas and Veawab, 2004), but it is well-known that the main drawback related to CO_2 capture by amine absorption is due to the energy consumption for solvent regeneration (Pellegrini et al., 2019). This also applies when CO_2 separation from natural gas is considered for producing either a pipeline-quality natural gas (De Guido et al., 2015) or liquefied natural gas (LNG) (Pellegrini et al., 2015b). Indeed, when the CO_2 content exceeds 8–9 mol% (Langè et al., 2015), separation by means of chemical absorption into aqueous amine solutions becomes energy intensive and other types of technologies (e.g., low-temperature/cryogenic ones) can be considered valuable alternatives. This also applies when CO_2 separation from biogas is considered for producing liquefied biomethane (Pellegrini et al., 2017), since biogas can be seen as a particular natural gas stream, characterized by a fixed composition (i.e., about 40 mol% CO_2). Indeed, also for biogas upgrading, even if MDEA washing is more profitable than water scrubbing considering the same feedstock (Pellegrini et al., 2015a), it involves higher energy consumption (due to the heat needed for solvent regeneration and for CO_2 pressurization, if considered) with respect to low-temperature technologies (Pellegrini et al., 2017).

Considering the integration of CCS in an SMR-based hydrogen plant and the energy-consumption-related issues associated with MDEA washing for CO_2 capture, this work investigates the CO_2 removal section for the treatment of the PSA tail gas, which can achieve a CO_2 avoidance of 52% (IEAGHG, 2017) with additional energy consumption. The reference plant is the one presented in the IEAGHG technical report, which produces 100,000 Nm^3/h of H_2 using natural gas as feedstock and fuel. It includes the hydrogen plant, the cogeneration plant, the demi-water plant, and utilities and balance of plant (BOP) consisting of other systems (cooling water system, etc.).

The capture step, based on chemical absorption of CO_2 into an MDEA aqueous solution, consists of an absorber, a flash unit, and a distillation column for solvent regeneration. Several column configurations have been taken into account. For each of them, a sensitivity analysis has been performed varying the CO_2 lean loading, in order to determine the optimal configuration from an energy point of view, namely, the one that minimizes the energy required for solvent regeneration.

METHODS

In the following, the model used in the simulations and the analysis procedure are outlined.

Model Used for Simulation

The analysis of the system has been carried out by using the commercial process simulator ASPEN Plus® V9.0 (AspenTech, 2016), which was previously user customized.

In particular, vapor-liquid equilibrium with chemical reactions generating ions in the liquid phase occurs and the system is strongly non-ideal. Its description can be well-accomplished by a γ/ϕ method, based on Electrolyte-NRTL (Chen et al., 1979, 1982; Chen and Evans, 1986; Mock et al., 1986) for the calculation of the activity coefficient in the liquid phase and on the Redlich-Kwong equation of state (Redlich and Kwong, 1949) for the calculation of the fugacity coefficient in the vapor phase.

The kinetics and mass transfer of reactions have also been considered in the simulation, and the performance of the columns has been determined on the basis of a rate-based approach. To this purpose, ASPEN Plus® V9.0 has been integrated with a homemade routine developed by the GASP group of Politecnico di Milano (Moioli et al., 2013).

Procedure Employed in This Study

The analysis, the results of which are presented in this work, involved the simulation of the CO_2 capture section from the PSA tail gas for the reference plant previously reported. The following seven alternatives have been taken into account, which differ because of the internal configuration of the absorption column:

- *case A*: tray column with 51 four-pass valve trays;
- *case B*: tray column with 51 two-pass valve trays;
- *case C*: tray column with 21 four-pass valve trays;
- *case D*: tray column with 21 two-pass valve trays;
- *case E*: packed column with structured packing (*Sulzer Mellapak Standard 250X*);
- *case F*: tray column with 24 four-pass valve trays;
- *case G*: tray column with 24 two-pass valve trays.

Case E is the only one involving a packed column: for it, the structured *Sulzer Mellapak Standard 250X* packing has been chosen because of its excellence performance in columns with

a diameter of up to 15 m as reported industrially (Mellapak, 2015) and because of its choice also in previous literature studies (Zhang and Rochelle, 2014; Moioli and Pellegrini, 2019). Indeed, it offers a low pressure drop and it can be used for a quite wide range of liquid loads. For the simulation of this case, 51 stages have been considered for the discretization of the column height.

As far as the other cases, which involve a tray column, are concerned, the choice of the tray type has been made on the basis of a previous work (Cassiano, 2015). The standard tray spacings of 0.60 m and 0.76 m have been considered, and the column dimensions have been selected taking into account the sizes provided in the report (IEAGHG, 2017). According to the available data, the internal diameter and the total height of the absorption column are, respectively, 3.399 and 20 m. The value of the column diameter has been checked in the simulations by means of the tool *Tray Sizing* available in ASPEN Plus® V9.0 (AspenTech, 2016): the result has been found to be in accordance with the one provided in the IEAGHG report.

Case A and *case B* refer to an absorber with a different height, selected on the basis of a previous work concerning CO_2 removal by MDEA scrubbing applied to pre-combustion syngas purification (Cassiano, 2015).

A sensitivity analysis of the CO_2 lean loading has been performed, varying it in a suitable range depending on the case study under investigation, with the aim of determining the value that minimizes the reboiler duty. For each value of the CO_2 lean loading, the solvent flow rate has been varied in order to meet the design specification on the CO_2 capture rate (i.e., 96.49%), which can be calculated on the basis of the data available in the report (IEAGHG, 2017), as explained in the next section.

In the following, the reference case and the data available for it and relevant to the analysis are described for the sake of clarity (section Reference Case). Then, more details are given about the simulations (section Simulations).

Reference Case

The flow sheet of the simulated CO_2 capture section on the basis of the reference case study is shown in **Figure 1**, and the data on the main streams are reported in **Table 1**.

The *TAIL GAS* stream, with a CO_2 content of about 51 mol% on a wet molar basis, is initially compressed to 1.1 MPa, before being fed into the bottom of the absorption column (*ABSORBER*). Here, the CO_2 in the gas stream is absorbed by contacting it counter-currently with the lean solvent fed at the top. The purified tail gas (*GASOUT*) that exits from the top of the absorber is characterized by a CO_2 content of nearly 3.5 mol% on a wet molar basis. At the bottom of the absorption tower, the rich solvent is recovered and sent to the *FLASH*: the vapor outlet stream is sent to the burners to be employed as additional fuel in the steam reformer. In contrast, the liquid outlet stream, which is the rich solvent, is sent to the lean/rich heat exchanger, where it is heated up by the hot lean solvent coming from the reboiler of the solvent regeneration column (*REGOCO21)*.

After being heated in the lean/rich heat exchanger, the hot rich solvent is fed into the top of the *REGOCO21* for regeneration. This is accomplished by a counter-current contact with the vapor stream traveling upward, which is generated at the bottom reboiler, where low-pressure steam from the back-pressure steam turbine of the cogeneration plant is used as heating medium.

The gas stream leaving the top of the distillation column is sent to the condenser, where the steam present in the overhead gas is condensed, collected, and returned as reflux to the column. As for the CO_2-rich gas exiting from the top condenser, it is delivered to the CO_2 compression and dehydration unit.

From the data reported in **Table 1**, it is possible to calculate the CO_2 capture rate according to Equation (1), where $F_{CO_2,GASIN}$ and $F_{CO_2,GASOUT}$ denote, respectively, the molar flow rate of CO_2 in the gas streams entering and leaving the absorption column. Thus, the CO_2 capture rate is 96.49%. It represents the target to be met in all the simulations described in the following section.

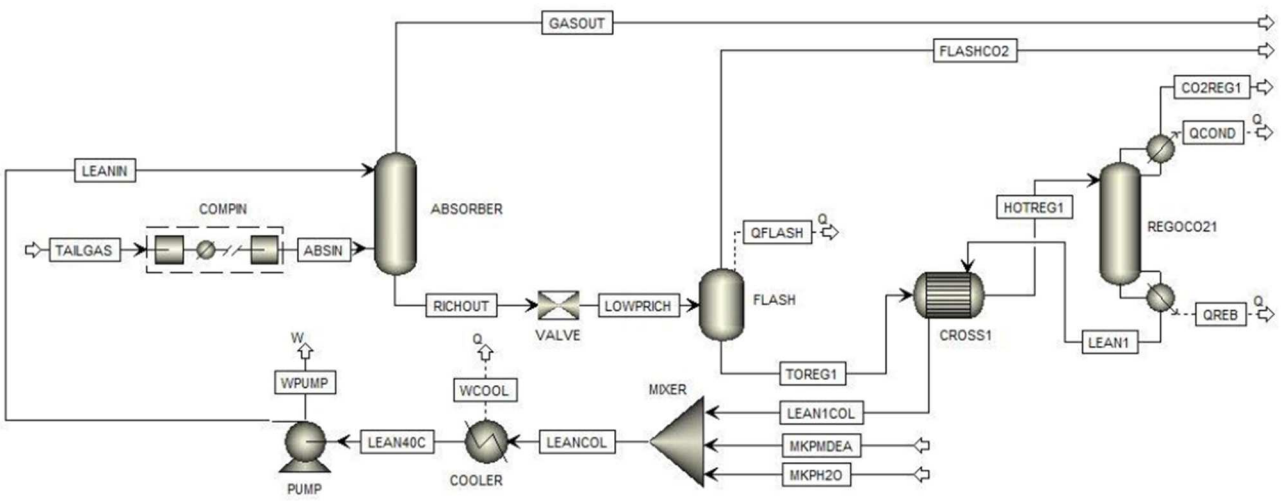

FIGURE 1 | Flow sheet of the simulated CO_2 capture system.

TABLE 1 | Data on the main streams involved in the CO_2 capture section studied in this work (IEAGHG, 2017).

Variable	Unit	Streams		
		Tail gas from PSA	Sweet tail gas to burners	CO_2 to compressor
T	[°C]	28	44	49
P	[MPa]	0.13	0.98	0.29
Molar flow	[kmol/h]	2106.3	1062.9	1080.0
Mass flow	[kg/h]	60658	14939	46362
Composition				
CO_2	[mol/mol]	0.5095	0.0354	0.9585
CO	[mol/mol]	0.1454	0.2878	0.0001
Hydrogen	[mol/mol]	0.2369	0.4694	0.0001
Nitrogen	[mol/mol]	0.0062	0.0122	0.0002
Oxygen	[mol/mol]	0.0000	0.0000	0.0000
Methane	[mol/mol]	0.0945	0.1870	0.0000
Ethane	[mol/mol]	0.0000	0.0000	0.0002
H_2O	[mol/mol]	0.0076	0.0080	0.0409

TABLE 2 | Data on the PSA tail gas stream entering the absorber after compression (*ABSIN* in **Figure 1**) and on the lean amine solvent stream (*LEANIN* in **Figure 1**) (the composition of the lean solvent corresponds to an MDEA weight fraction of 0.5 and to a CO_2 lean loading of 0.0203 mol CO_2/mol MDEA).

Variable	Unit	Stream	
		ABSIN	LEANIN
T	[°C]	28	40
P	[MPa]	1.1	1.0
Molar flow	[kmol/h]	2106.3	(*)
Mass flow	[kg/h]	60658	(*)
Composition			
CO_2	[mol/mol]	0.5095	0.0026914
CO	[mol/mol]	0.1454	0.0000
Hydrogen	[mol/mol]	0.2369	0.0000
Nitrogen	[mol/mol]	0.0062	0.0000
Methane	[mol/mol]	0.0945	0.0000
H_2O	[mol/mol]	0.0076	0.86499
MDEA	[mol/mol]	0.0000	0.1323

**Varied in the sensitivity analysis of the CO_2 lean loading, in order to meet the target CO_2 capture rate of 96.49%.*

$$CO_2\ capture\ rate = 100 \cdot \frac{F_{CO_2,GASIN} - F_{CO_2,GASOUT}}{F_{CO_2,GASIN}} \quad (1)$$

Simulations

Figure 1 illustrates the flow sheet of the CO_2 capture section that has been simulated in ASPEN Plus® V9.0 (AspenTech, 2016).

The PSA tail gas ("*TAIL GAS*") is compressed from 0.13 to 1.1 MPa before being fed into the bottom of the absorption column (*ABSORBER*). This value is different from the one reported in the IEAGHG report (i.e., 1 MPa), and this is due to the definition of the pressure profile in the absorber in the simulations: the pressure at the first stage from the top has been set equal to the pressure of the gas stream exiting the top of the absorber (i.e., 0.98 MPa, as reported in **Table 1**). When varying the solvent flow rate in the simulations in order to obtain the target CO_2 absorption rate of 96.49% for each value of CO_2 lean loading, for high values of the solvent flow rate, a high pressure was reached at the bottom of the absorber, higher than 1 MPa (i.e., the pressure of the PSA tail gas entering the bottom of the absorption column, according to the IEAGHG report). By setting the outlet pressure from the compression train at 1.1 MPa (rather than at 1 MPa), this has been avoided.

The data on the two streams entering the absorber are reported in **Table 2**. The conditions of the lean amine solvent stream ("*LEANIN*") in terms of the temperature, pressure, and composition of the free MDEA solvent (composed only of MDEA and water) have been kept constant in this study in order to ensure comparison consistency. Obviously, its molar composition and flow rate vary in the sensitivity analysis of the CO_2 lean loading, so that the target CO_2 capture rate is always met. The composition of the lean solvent reported in **Table 2** corresponds to an MDEA weight fraction of 0.5 and to a CO_2 lean loading of 0.0203 mol CO_2/mol MDEA.

TABLE 3 | Design parameters and specifications of the stripping column.

Variable	Value
Internal diameter [m]	5.155
Number of trays	8
Tray type	Valve
Condenser temperature [°C]	49
CO_2 loading [mol CO_2/mol MDEA]	CO_2 lean loading "*LEANIN*"

The absorption tower has been simulated defining its internals depending on which of the seven case studies previously reported (see section Procedure Employed in This Study) is considered.

The rich solvent from the bottom of the absorption tower is sent to the separator (*FLASH*), which is operated at 74°C and 0.45 MPa. The liquid outlet stream (*TOREG1*) is sent to the lean/rich heat exchanger (*CROSS1*), in which the temperature approach between the hot outlet stream and the cold inlet stream has been set equal to 10°C, with the minimum temperature approach set equal to 5°C.

The pre-heated rich solvent (*HOTREG1*) is then fed at the top of the regeneration column (*REGOCO21*). It has been designed on the basis of the internal diameter and total height available in the IEAGHG report (IEAGHG, 2017) and making reference to a previous work (Cassiano, 2015) for what concerns the number of stages and internal type. The specifications and design parameters for the stripping column are reported in **Table 3**.

Taking into account the availability of cooling water at 25°C, it is assumed that the condenser works at 49°C (temperature of the stream "*CO_2 to compressor*" in **Table 1**, named stream *CO2REG1* in **Figure 1**). This specification ensures a CO_2 concentration in the gas stream exiting the distillation column of 96 mol%.

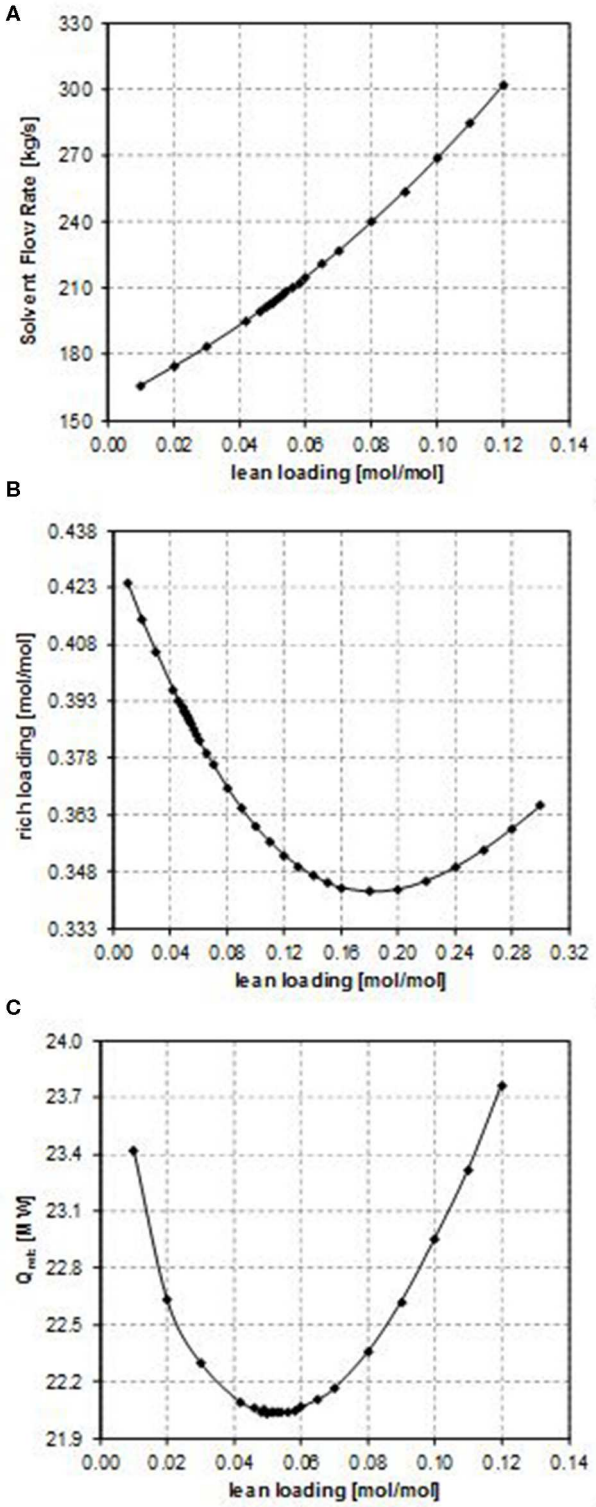

FIGURE 2 | Effect of the CO_2 lean loading on **(A)** the solvent flow rate, **(B)** the rich loading, and **(C)** the reboiler duty (*case B*).

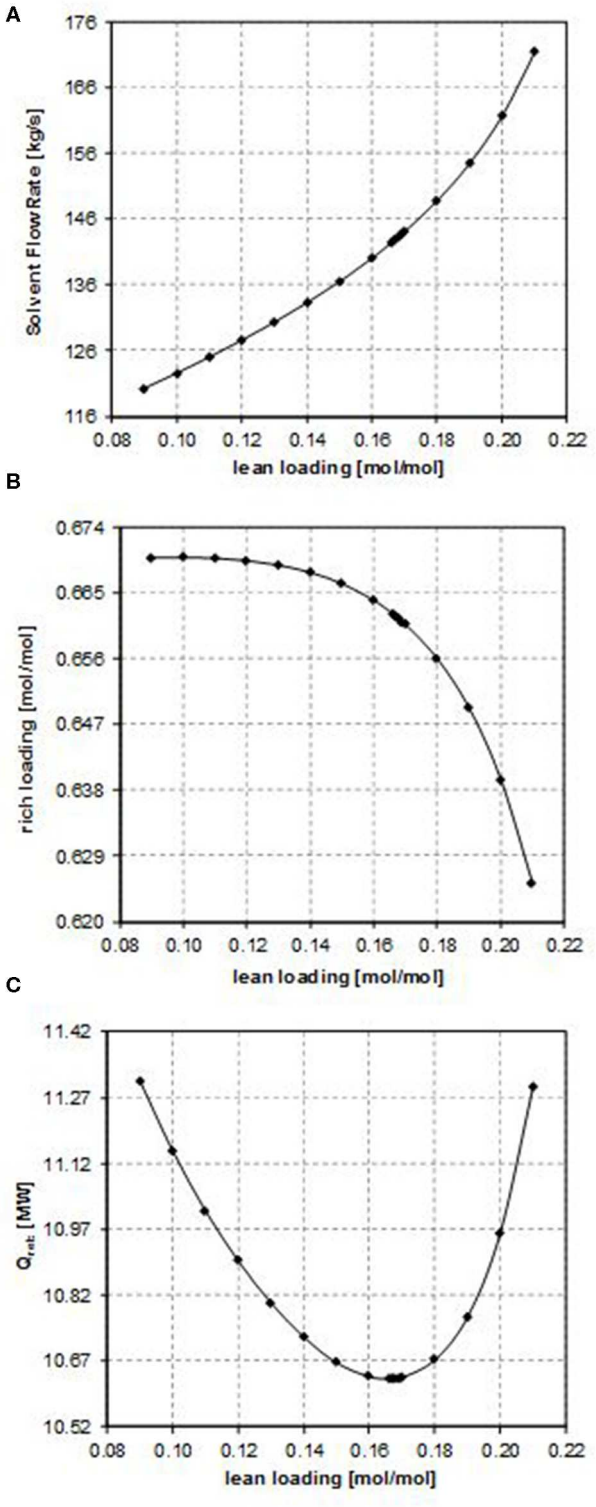

FIGURE 3 | Effect of the CO_2 lean loading on **(A)** the solvent flow rate, **(B)** the rich loading, and **(C)** the reboiler duty (*case E*).

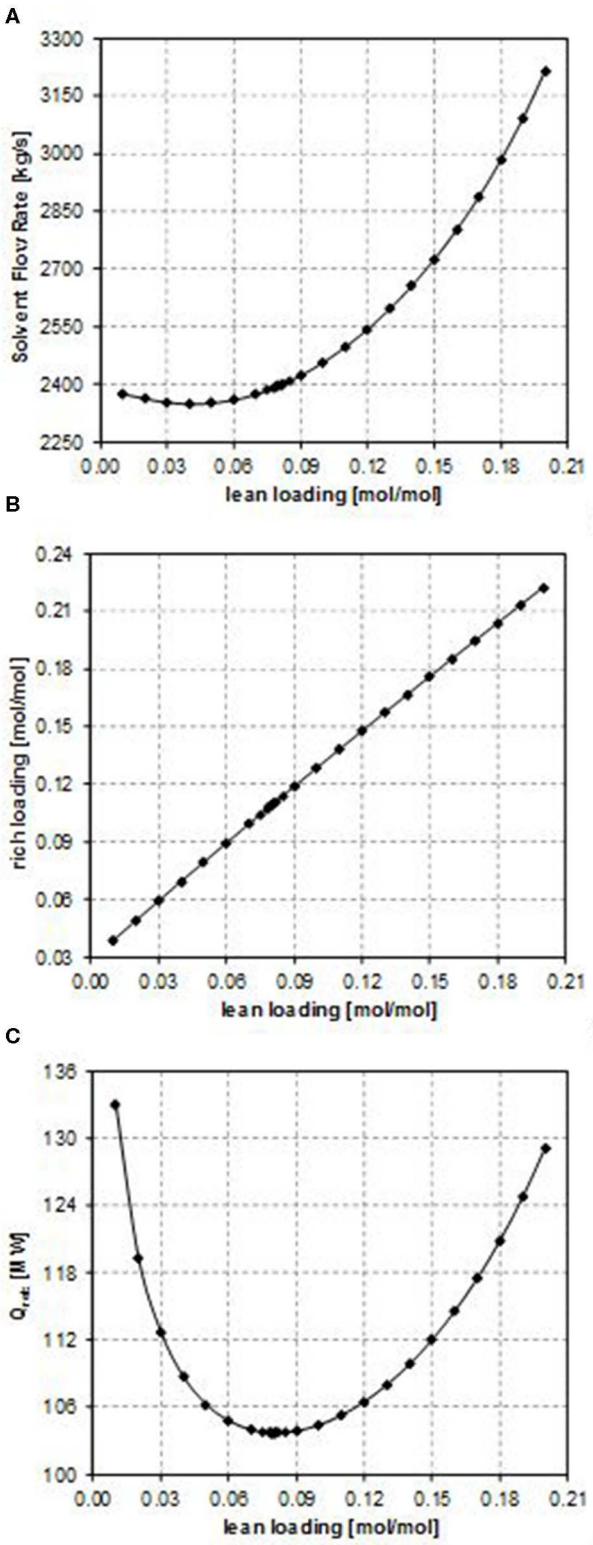

FIGURE 4 | Effect of the CO_2 lean loading on **(A)** the solvent flow rate, **(B)** the rich loading, and **(C)** the reboiler duty (*case G*).

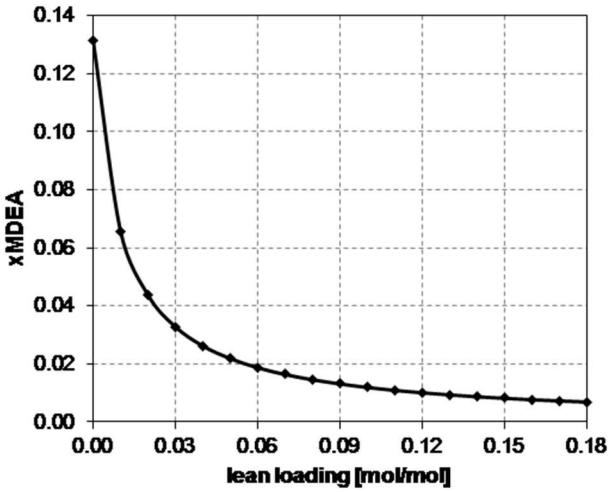

FIGURE 5 | Effect of the CO_2 lean loading on the mole fraction of MDEA in the solvent.

The other specification required to simulate the stripping column refers to the CO_2 apparent molar fraction in the regenerated solvent stream, which is equal to the CO_2 apparent molar fraction in the lean solvent stream fed to the CO_2 capture plant (namely, stream "*LEANIN*" in **Figure 1**).

The operating pressure has been set equal to 0.29 MPa, considering the available datum for the CO_2 stream exiting from the top of the column (as reported in **Table 1**). A sensitivity analysis was actually performed also on this operating condition, by varying it in the range 0.1–0.3 MPa. However, the reboiler and condenser duties of the stripping column were found to vary only slightly with the regeneration pressure.

With reference to **Figure 1**, it is possible to define the CO_2 lean loading (*LL*) and the CO_2 rich loading (*RL*) according to Equations (2) and (3), respectively.

$$LL = \frac{\text{moles of } CO_2 \text{ in the lean solvent}}{\text{moles of MDEA in the lean solvent}} = \frac{F_{CO_2,\text{LEANIN}}}{F_{\text{MDEA,LEANIN}}} \quad (2)$$

$$RL = \frac{\text{moles of } CO_2 \text{ in the rich solvent}}{\text{moles of MDEA in the rich solvent}} = \frac{F_{CO_2,\text{RICHOUT}}}{F_{\text{MDEA,RICHOUT}}} \quad (3)$$

RESULTS AND DISCUSSION

The results of the sensitivity analysis performed on the CO_2 lean loading are illustrated in **Figures 2–4** for *case B*, *case E*, and *case G*, respectively (they are representatives of the trends observed in the considered case studies), showing the effect on the most important process parameters, namely, the solvent flow rate, the CO_2 rich loading, and the energy requirements. It is important to point out that while performing such analysis, the

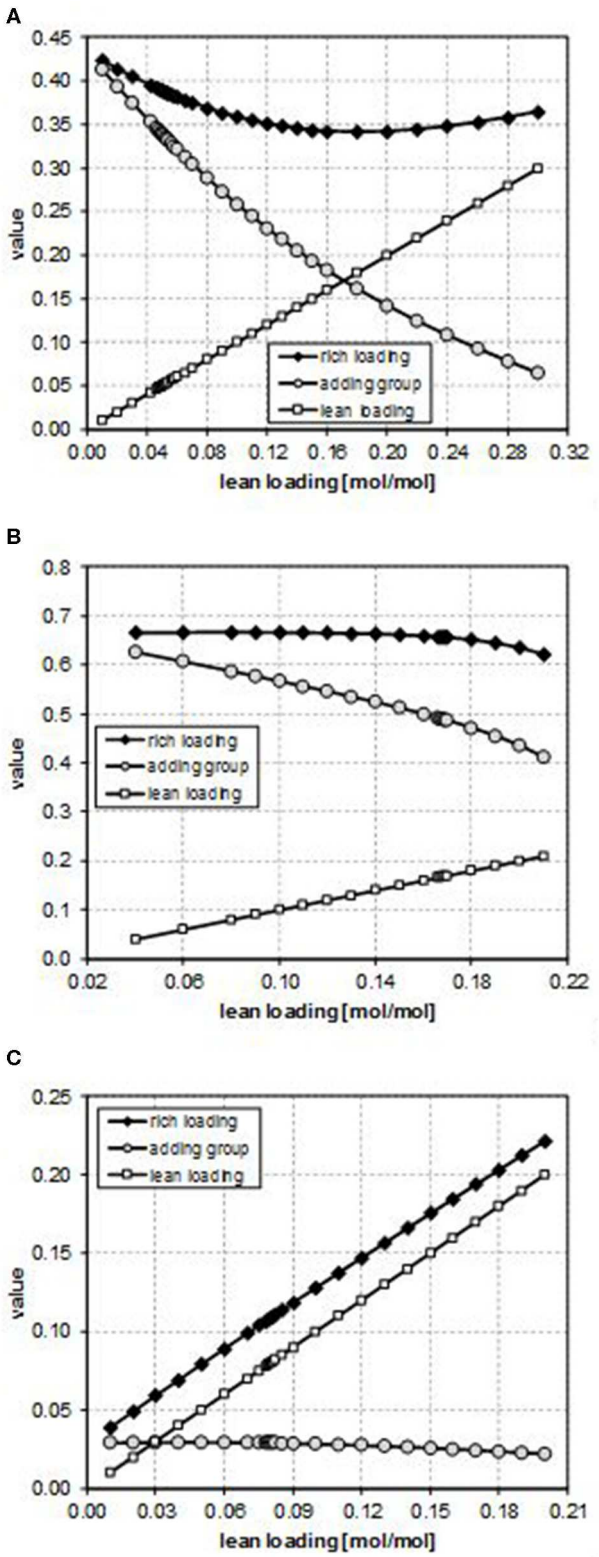

FIGURE 6 | Effect of the CO_2 lean loading on the second term ("adding group") of Equation (4) for **(A)** *case B*, **(B)** *case E*, and **(C)** *case G*.

operating constraint on the CO_2 rich loading should also be taken into account, considering that the maximum allowable value is in the range 0.7–0.8 [mol/mol] in the case of MDEA to avoid corrosion problems. Nevertheless, for all the examined cases, the investigated values of the CO_2 lean loading have led to values of CO_2 rich loading that are significantly lower than the upper operational limit (as shown in **Figure 2B**, in **Figure 3B**, and in **Figure 4B**). Therefore, for each of the examined configurations, the optimum CO_2 lean loading can be identified on the basis of the minimization of the energy requirements only.

Considering the influence of the CO_2 lean loading on the solvent flow rate (as shown in **Figure 2A**, in **Figure 3A**, and in **Figure 4A**), obviously when increasing the CO_2 lean loading, larger solvent flow rates are required to guarantee the same CO_2 removal efficiency. Indeed, an increase in the *LL* results in a lower purity of the solvent, thus penalizing its absorption capacity. As a result, more solvent is required in order to capture the same amount of CO_2.

If accounting for the influence of the CO_2 lean loading on the CO_2 rich loading, different trends result from the sensitivity analysis. The functional dependence of the *RL* on the *LL* is expressed by Equation (4).

$$RL = LL + CO_2\ capture\ rate \cdot \frac{F_{CO_2,ABSIN}}{F_{MDEA,LEANIN}} \tag{4}$$

Since the CO_2 capture rate and the molar flow rate of CO_2 in the inlet gas do not change in the sensitivity analysis and in all the considered case studies, the specific trend observed in **Figure 2B**, in **Figure 3B**, and in **Figure 4B** depends on the relative increase in the MDEA flow rate in the lean solvent with respect to the increase in the *LL* as the *LL* increases. This increase can be more or less relevant, thus providing different trends in **Figure 2B**, in **Figure 3B**, and in **Figure 4B**, on the type of the characteristics of the column considered, also because of the kinetics occurring in the system.

In particular, for *case B*, the rich loading presents a minimum (**Figure 2B**); for *case E*, it decreases though remaining within a small range (**Figure 3B**); and for *case G*, it monotonically increases as the lean loading increases (**Figure 4B**). These trends can be fully understood by considering **Figures 5**, **6**. Indeed, as previously reported, the total flow rate generally increases as the lean loading increases. However, as can be outsourced from **Figure 5**, the mole fraction of MDEA in the solvent decreases (due to the higher amount of carbon dioxide), so at different values of *LL*, the trend of the flow rate of MDEA may be different from the one of the total amine flow rate. Considering that all the analyses are carried out with the same gaseous stream to be treated (so with a fixed amount of carbon dioxide entering the absorber) and with a constant % removal of carbon dioxide, it follows that only $F_{MDEA,LEANIN}$ varies in the second term of Equation (4) (named "adding group" in **Figure 6**). Therefore, since at different values of the lean loading different values of $F_{MDEA,LEANIN}$ occur, different values of the "adding group" also result. The rich loading, obtained as the sum of this term and

TABLE 4 | Optimal operating conditions resulting from the lean loading sensitivity analysis.

Case	CO_2 lean loading [mol CO_2/mol MDEA]	CO_2 rich loading [mol CO_2/mol MDEA]	Solvent flow rate [kg/s]	Reboiler duty [MW]	Condenser duty [MW]
A	0.070	0.254	377.7	29.13	3.98
B	0.050	0.390	203.4	22.03	3.89
C	0.076	0.089	5484.2	216.18	5.76
D	0.074	0.096	3155.6	131.91	5.73
E	0.168	0.661	143.2	10.63	0.67
F	0.082	0.101	3705.7	151.04	5.10
G	0.080	0.109	2395.9	103.70	5.12

the related lean loading, is then characterized by a specific trend depending on the considered case (**Figure 6**).

Finally, the dependence of the reboiler duty on the CO_2 lean loading is discussed. Two factors affect this, namely, the sensible heat that has to be supplied to bring the solvent temperature to the reboiler temperature and the latent heat that must be supplied in order to vaporize the needed amount of the stripping agent in the regeneration column, provided that the heat needed to reverse the chemical reaction that occurred in the absorber is the same. At low values of the lean loading, a lower solvent flow rate is sufficient to reach the target CO_2 capture rate, but a higher amount of the stripping agent is necessary in the regeneration column to strip more CO_2 off. Therefore, the latent heat of vaporization plays a more important role. In contrast, at high values of the lean loading, as it increases, the solvent flow rate needed to reach the target CO_2 capture rate also increases and more energy is required to heat it up to the desired temperature in the regeneration column, even if less stripping agent can be produced because less CO_2 has to be stripped off. Therefore, the sensible heat plays a more important role in this case. For these reasons, a minimum in the reboiler duty as a function of the CO_2 lean loading is observed (as shown in **Figures 2C**, **3C**, **4C**).

For each of the examined configurations, the optimum CO_2 lean loading, which guarantees the minimum energy requirement, is reported in **Table 4**. It is possible to observe that the optimum CO_2 lean loading obtained for *case E* is much higher than the one involved in all the other cases. This is a direct consequence of the fact that in this case, the absorber is a packed column, with different fluid dynamics (also influenced by the type of considered packing) and mass transfer occurring inside the unit. In addition, the number of theoretical stages is different from the one of the other cases with tray columns, thus exerting an influence on the total solvent flow rate needed to perform the CO_2 removal and, thus, on the optimal lean loading.

Another important observation concerns the extremely high solvent flow rates required to reach the desired CO_2 capture rate for *case C*, *case D*, *case F*, and *case G*. This is due to the fact that in these cases, the absorption column has been modeled as a tray column with a number of stages (respectively, 21 and 24) that is considerably lower than the one involved in *case A* and in *case B* (i.e., 51). For this reason, it has been necessary to significantly increase the solvent flow rate in order to push the CO_2 removal from the gaseous stream to the target value.

When comparing all the investigates case studies, *case E* turns out to be the most convenient one from an energy point of view: indeed, the use of a packed absorption column rather than a tray column allows reaching the target CO_2 capture rate using less solvent and requiring lower energy consumptions at the reboiler of the solvent regeneration column.

CONCLUSIONS

This work has focused on the study of a purification process for the CO_2 removal from PSA tail gas within an SMR-based hydrogen plant, for which data are available in the literature. For this purpose, an aqueous solution of MDEA has been employed. Despite the advantages associated with this technology, it is fundamental to account for the fact that amine-based CO_2 capture processes are generally quite energy intensive. Therefore, the application of this technology at a large scale is mainly subject to the optimization of the process energy performance, with the aim of specifically reducing the energy requirement at the reboiler of the regeneration column for the solvent purification.

To this aim, different configurations have been taken into account for the absorber, performing the simulations in ASPEN Plus® V9.0, integrated with a homemade routine developed by the GASP group of Politecnico di Milano. The different configurations differ for the type of column internals. A sensitivity analysis has been performed to investigate the effect of the lean loading on the reboiler duty, as well as on the rich loading and on the solvent flow rate required to meet the target CO_2 capture rate of 96.49%. The lean loading, which provides the minimum reboiler duty, varies from 0.05 to 0.17 depending on the considered case. Kinetics and mass transfer influence the needed solvent flow rate, which, in turn, has an effect on the value of the rich loading, for which different trends result as the lean loading varies, each one specific for each configuration.

When comparing all the investigated case studies, the one that has turned out to be the most convenient one from an energy point of view is the case in which the absorber has been modeled as a packed column. Indeed, in such a case, because of the characteristics of the considered column, a lower solvent flow rate can be used to reach the target CO_2 capture rate, requiring lower energy consumption at the reboiler of the solvent regeneration column.

DATA AVAILABILITY STATEMENT

The raw data supporting the conclusions of this article will be made available by the authors, without undue reservation, to any qualified researcher.

AUTHOR CONTRIBUTIONS

All authors listed have made a substantial, direct and intellectual contribution to the work, and approved it for publication.

REFERENCES

Alie, C., Backham, L., Croiset, E., and Douglas, P. L. (2005). Simulation of CO_2 capture using MEA scrubbing: a flowsheet decomposition method. *Energy Convers. Manag.* 46, 475–487. doi: 10.1016/j.enconman.2004.03.003

Aroonwilas, A., and Veawab, A. (2004). Characterization and comparison of the CO_2 absorption performance into single and blended alkanolamines in a packed column. *Ind. Eng. Chem. Res.* 43, 2228–2237. doi: 10.1021/ie0306067

AspenTech (2016). *Aspen Plus*®. Burlington, MA: AspenTech.

Blanco, M. I. (2009). The economics of wind energy. *Renew. Sust. Energy Rev.* 13, 1372–1382. doi: 10.1016/j.rser.2008.09.004

Cassiano, C. (2015). *Energy* saving per la purificazione pre-combustione del syngas (M.Sc.thesis). Politecnico di Milano, Milan, Italy.

Chen, C. C., Britt, H. I., Boston, J. F., and Evans, L. B. (1979). Extension and application of the pitzer equation for vapor-liquid equilibrium of aqueous electrolyte systems with molecular solutes. *AIChE J.* 25, 820–831. doi: 10.1002/aic.690250510

Chen, C. C., Britt, H. I., Boston, J. F., and Evans, L. B. (1982). Local composition model for excess gibbs energy of electrolyte systems. Part I: single solvent, single completely dissociated electrolyte systems. *AIChE J.* 28, 588–596. doi: 10.1002/aic.690280410

Chen, C. C., and Evans, L. B. (1986). A local composition model for the excess gibbs energy of aqueous electrolyte systems. *AIChE J.* 32, 444–454. doi: 10.1002/aic.690320311

Corsatea, T. D. (2014). Technological capabilities for innovation activities across Europe: evidence from wind, solar and bioenergy technologies. *Renew. Sust. Energy Rev.* 37, 469–479. doi: 10.1016/j.rser.2014.04.067

De Guido, G., Compagnoni, M., Pellegrini, L. A., and Rossetti, I. (2018). Mature versus emerging technologies for CO_2 capture in power plants: key open issues in post-combustion amine scrubbing and in chemical looping combustion. *Front. Chem. Sci. Eng.* 12, 315–325. doi: 10.1007/s11705-017-1698-z

De Guido, G., Langè, S., and Pellegrini, L. A. (2015). Refrigeration cycles in low-temperature distillation processes for the purification of natural gas. *J. Nat. Gas Sci. Eng.* 27, 887–900. doi: 10.1016/j.jngse.2015.09.041

Del Ben, L. (2018). *Study of Energy Saving Configurations in the CO2 Removal Section of a SMR-based H2 Plant. MsC Thesis, Politecnico di Milano, Milano, Italy.*

Hasan, M. F., First, E. L., Boukouvala, F., and Floudas, C. A. (2015). A multi-scale framework for CO_2 capture, utilization, and sequestration: CCUS and CCU. *Comput. Chem. Eng.* 81, 2–21. doi: 10.1016/j.compchemeng.2015.04.034

IEAGHG (2017). *Techno-Economic Evaluation of SMR Based Standalone (Merchant) Hydrogen Plant With CCS*. IEAGHG Report No. 2017-02: IEA Greenhouse Gas R&D Programme.

Jäger-Waldau, A. (2007). Photovoltaics and renewable energies in Europe. *Renew. Sust. Energy Rev.* 11, 1414–1437. doi: 10.1016/j.rser.2005.11.001

Langè, S., Pellegrini, L. A., Vergani, P., and Lo Savio, M. (2015). Energy and economic analysis of a new low-temperature distillation process for the upgrading of high-CO_2 content natural gas streams. *Ind. Eng. Chem. Res.* 54, 9770–9782. doi: 10.1021/acs.iecr.5b02211

Mellapak (2015). *Mellapak Brochure, Structured Packings - Energy-Efficient, Innovative and Profitable*. Available online at: https://www.sulzer.com/-/media/files/products/separation-technology/liquid_liquid_extraction/brochures/structured_packings.ashx

Mock, B., Evans, L. B., and Chen, C. C. (1986). Thermodynamic representation of phase equilibria of mixed-solvent electrolyte systems. *AIChE J.* 32, 1655–1664. doi: 10.1002/aic.690321009

Moioli, S., Ho, M. T., Wiley, D. E., and Pellegrini, L. A. (2019a). Assessment of carbon dioxide capture by precipitating potassium taurate solvent. *Int. J. Greenhouse Gas Control* 87, 159–169. doi: 10.1016/j.ijggc.2019.05.013

Moioli, S., and Pellegrini, L. (2019). Design of a CO_2 removal section treating very high flue gas flowrates. *Chem. Eng. Trans.* 74, 859–864. doi: 10.3303/CET1974144

Moioli, S., Pellegrini, L. A., Ho, M. T., and Wiley, D. E. (2019b). A comparison between amino acid based solvent and traditional amine solvent processes for CO_2 removal. *Chem. Eng. Res. Des.* 146, 509–517. doi: 10.1016/j.cherd.2019.04.035

Moioli, S., Pellegrini, L. A., Picutti, B., and Vergani, P. (2013). Improved rate-based modeling of H_2S and CO_2 removal by methyldiethanolamine scrubbing. *Ind. Eng. Chem. Res.* 52, 2056–2065. doi: 10.1021/ie301967

Nema, P., Nema, S., and Roy, P. (2012). An overview of global climate changing in current scenario and mitigation action. *Renew. Sust. Energy Rev.* 16, 2329–2336. doi: 10.1016/j.rser.2012.01.044

Pellegrini, L. A., De Guido, G., Consonni, S., Bortoluzzi, G., and Gatti, M. (2015a). From biogas to biomethane: how the biogas source influences the purification costs. *Chem. Eng. Trans.* 43, 409–414. doi: 10.3303/CET1543069

Pellegrini, L. A., De Guido, G., and Langé, S. (2017). Biogas to liquefied biomethane via cryogenic upgrading technologies. *Renew. Energy* 124, 75–83. doi: 10.1016/j.renene.2017.08.007

Pellegrini, L. A., De Guido, G., and Valentina, V. (2019). Energy and exergy analysis of acid gas removal processes in the LNG production chain. *J. Nat. Gas Sci. Eng.* 61, 303–319. doi: 10.1016/j.jngse.2018.11.016

Pellegrini, L. A., Langè, S., Baccanelli, M., and De Guido, G. (2015b). "Techno-economic analysis of LNG production using cryogenic vs conventional techniques for natural gas purification," in *Offshore Mediterranean Conference and Exhibition.* Offshore Mediterranean Conference (Ravenna).

Redlich, O., and Kwong, J. N. S. (1949). On the thermodynamics of solutions. V: an equation of state. fugacities of gaseous solutions. *Chem. Rev.* 44, 233–244. doi: 10.1021/cr60137a013

Riis, T., Hagen, E. F., Vie, P. J., and Ulleberg, Ø. (2005). *Hydrogen Production and Storage- R&D Priorities and Gaps.* International Energy Agency (IEA).

Rochelle, G. T. (2009). Amine scrubbing for CO_2 capture. *Science* 325, 1652–1654. doi: 10.1126/science.1176731

Rostrup-Nielsen, J. R., and Rostrup-Nielsen, T. (2002). Large-scale hydrogen production. *CATTECH* 6, 150–159. doi: 10.1023/A:1020163012266

Schaber, K., Steinke, F., Mühlich, P., and Hamacher, T. (2012). Parametric study of variable renewable energy integration in Europe: advantages and costs of transmission grid extensions. *Energy Policy* 42, 498–508. doi: 10.1016/j.enpol.2011.12.016

Timilsina, G. R., Kurdgelashvili, L., and Narbel, P. A. (2012). Solar energy: markets, economics and policies. *Renew. Sust. Energy Rev.* 16, 449–465. doi: 10.1016/j.rser.2011.08.009

Zhang, Y., and Rochelle, G. T. (2014). Absorber performance with high CO_2. *Energy Proc.* 63, 1329–1338. doi: 10.1016/j.egypro.2014.11.142

Conflict of Interest: The authors declare that the research was conducted in the absence of any commercial or financial relationships that could be construed as a potential conflict of interest.

NOMENCLATURE

Acronyms	
BOP	Balance of plant
CCS	CO_2 capture and storage
CCSU	CO_2 capture, storage, and utilization
CLC	Chemical looping combustion
IEAGHG	International Energy Agency Greenhouse Gas R&D Programme
LL	CO_2 lean loading
LNG	Liquefied natural gas
MDEA	Methyldiethanolamine
PSA	Pressure swing adsorption
RL	CO_2 rich loading
SMR	Steam methane reforming
Symbols	
F	Molar flow rate [kmol/h]
P	Pressure [MPa]
Q_{reb}	Reboiler duty [MW]
T	Temperature [°C]
x_{MDEA}	Molar fraction of MDEA in the solvent [-]

frontiers | Frontiers in Energy Research

ORIGINAL RESEARCH
published: 11 May 2022
doi: 10.3389/fenrg.2022.859075

View Factors in Horizontal Plane Fixed-Mode Solar PV Fields

Yasser F. Nassar[1], Hala J. El-Khozondar[2], Said O. Belhaj[3], Samer Y. Alsadi[4] and Nassir M. Abuhamoud[5]*

[1]Department of Mechanical and Renewable Energy Engineering, Faculty of Engineering, Wadi Alshatti University, Brack, Libya, [2]Department of Electrical Engineering, Islamic University of Gaza, Gaza, Palestine, [3]Center for Solar Energy Research and Studies, Tripoli, Libya, [4]Department of Electrical Engineering, Palestine Technical University-Kadoorie, Tulkarm, Palestine, [5]Department of Electrical and Electronic Engineering, Faculty of Engineering, Wadi Alshatti University, Brack, Libya

In solar PV fields, solar photovoltaic panels are typically arranged in parallel rows one after the other. This arrangement introduces variations in the distribution of solar irradiance over the entire field, compared to measurements recorded at meteorological weather stations and data obtained from climatic database platforms. This is due to the difference in the view factors between the rows of the solar PV field and a single surface, as well as the presence of shade on rear sides and in the space separating the rows. These phenomena combined will reduce the intensity of solar irradiance incident on the PV solar field; consequently will reduce the energy yields. Accurate estimation of solar radiation on solar fields requires knowledge of the sky, ground, and rear side of the preceding row view factors, and an estimation of the time and space occupied by the row's shadow. Prior literature has addressed this issue using two-dimensional (2-D) techniques such as the crossed-strings method (CSM). This study developed a novel three-dimensional (3-D) analysis in addition to numerical analysis to determine the view factors associated with solar fields. The study uses both isotropic and anisotropic transposition analyses to determine solar irradiance incident on the solar field with varying tilt angles of solar panels and distance separating the rows (distance aspect ratio) for several latitudes. The present research also tested the validity of the CSM for wide ranges of distance separating rows and length aspect ratios, the obtained results show that the CSM shows good agreements in both sky and ground view factor in the range of length aspect ratio greater than one. But the CSM fails in rear-side view factor in the design ranges of PV solar fields, where the error rate was found about 11%, this result is important in the case of bifacial PV solar systems. Also, the present work compared the solar irradiance calculated for a single surface with that incident on a PV solar field for wide range of sky conditions and latitudes. The obtained results ensure the accuracy of using the solar irradiance incident on a single surface data for low latitudes and for most sky conditions for PV rooftop solar systems as well as PV solar fields. While it has remarked a large error in the case of cloudy skies, where the error rate exceeded 17% in the case of aspect ratio equals to 1.5 and about 15.5% in the aspect ratio of 2.0.

Keywords: solar PV field, view factor, rooftop solar PV installations, solar irradiance in solar PV fields, sky view factor, ground view factor

OPEN ACCESS

Edited by:
K Sudhakar,
Universiti Malaysia Pahang, Malaysia

Reviewed by:
Daniel Tudor Cotfas,
Transilvania University of Braşov, Romania
Boon Han Lim,
University of Technology Malaysia, Malaysia

****Correspondence:***
Yasser F. Nassar
y.nassar@wau.edu.ly

Specialty section:
This article was submitted to Solar Energy, a section of the journal Frontiers in Energy Research

Received: *20 January 2022*
Accepted: *31 March 2022*
Published: *11 May 2022*

Citation:
Nassar YF, El-Khozondar HJ, Belhaj SO, Alsadi SY and Abuhamoud NM (2022) View Factors in Horizontal Plane Fixed-Mode Solar PV Fields. Front. Energy Res. 10:859075. doi: 10.3389/fenrg.2022.859075

1 INTRODUCTION

The performance prediction of any engineering system is an important step in the designing process, especially in solar fields (thermal or photovoltaic). As it is important to estimate the sizing of solar panels, number of rows, distance separating rows, and tilt and azimuth angles of the panels (Nassar, 2006; Alsadi and Nassar, 2017a; Seme et al., 2019). The solar irradiation incident on a tilted single surface consists from three components; direct beam, sky diffuse, and ground-reflected solar irradiation. While the situation in the solar fields is different, excluding the first row of solar panels in the solar filed, the solar radiation on the rest of panels consists of direct beam, sky diffuse, ground reflected, and rear surface reflected irradiation. The amounts of the sky diffuse, ground reflected, and rear surface-reflected irradiation captured by the PV panels depend on the view factor of panels to sky, ground, and rear surface (Nassar, 2006; Appelbaum, 2018). The view factors are used commonly in analyzing radiative heat transfer of many energy engineering applications. An online compilation of view factors for over 300 common geometries is provided by Howell (2016), and the list is regularly updated with new geometries. View factor plays a crucial role in transferring irradiances from horizontal planes to tilted planes (Arias-Rosales and LeDuc, 2020; Nassar et al., 2020). A recently developed numerical–analytical model by Nassar (2020) is used to facilitate the simulation of all types of solar fields. The sky diffuse transposition models are considered as examples of view factor models (Arias-Rosales and LeDuc, 2020), several models are presented in literature to measure the sky diffuse view factor, that is, Liu-Jordan, Klucher, Perez, Hay, and Reindl models (Mubarak et al., 2017). The Liu-Jordan model is considered the most prominent and oldest definitions (Liu and Jordan, 1961).

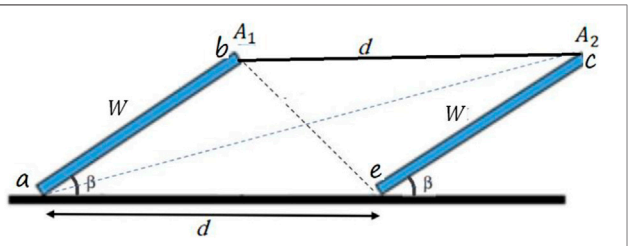

FIGURE 1 | Definition of the crossed-strings method for two surfaces of infinite length.

In the literature, several studies have performed, in which the view factor is used to estimate the diffuse radiation. Alam et al (2019) performed a numerical comparison study applied to several building depending on the view factor where radiative exchange takes place between surfaces such as ground and vertical walls or ground and sloping thermal or photovoltaic collectors. Alsadi and Nassar (2017a) performed a theoretical study using the view factor to analyze the solar field with a fixed reflector placed on the back-side top of the preceding row. Appelbaum (2018) presented an analytical expressions and numerical values of view factors between collectors to sky, between opposite collectors, and between collectors to shaded and not shaded grounds, for the front and rear sides of the collectors deployed on the horizontal and inclined planes. The complexity in handling the ground albedo for the entire solar field compared to a single-row

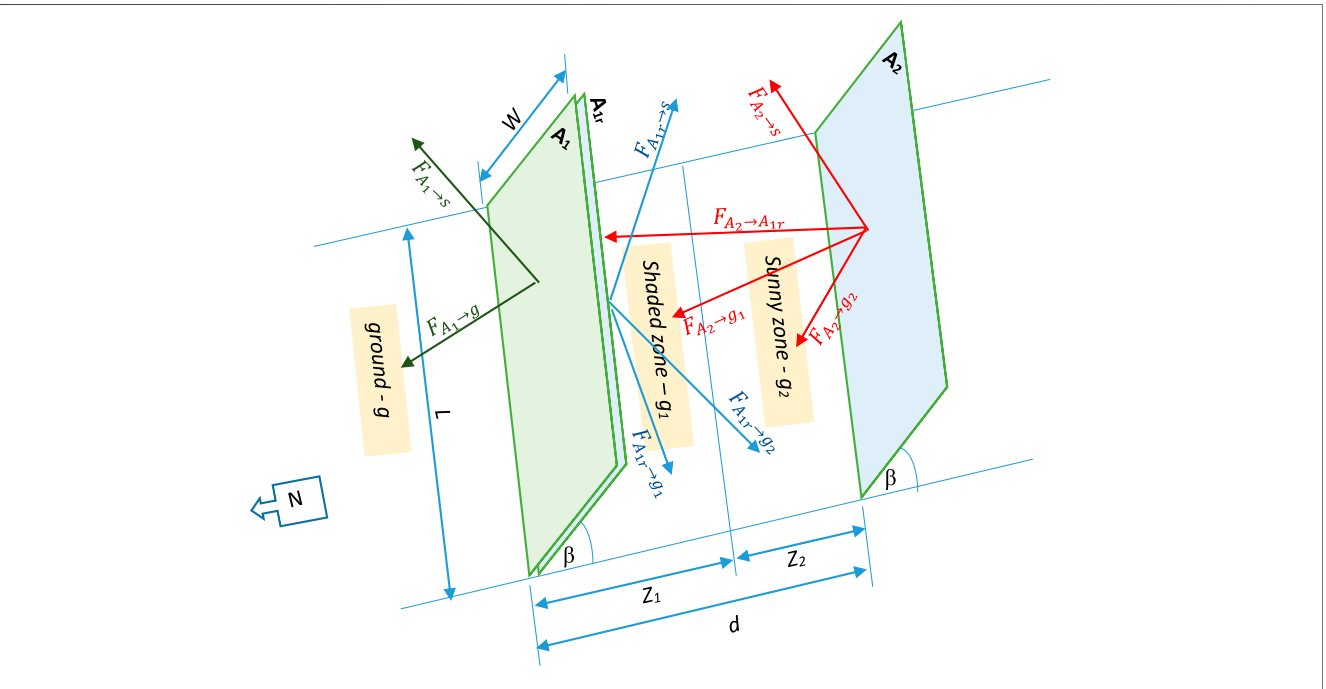

FIGURE 2 | View factors of a horizontal plane solar PV field at an instant of time.

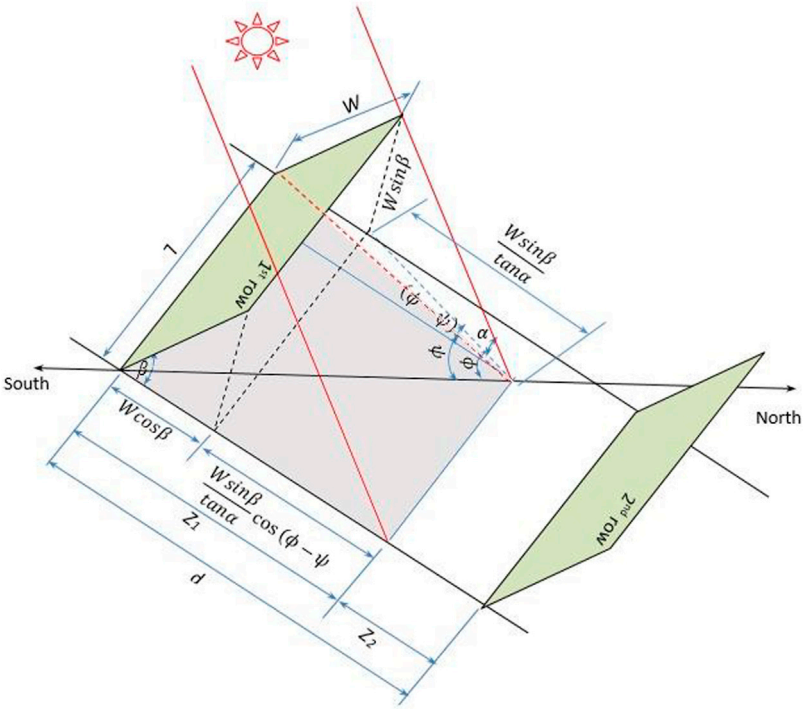

FIGURE 3 | Graphical representation of the shaded and unshaded zones in a solar field.

array or the first row of a solar field arose from the inherent differences in the sky and ground view factors among the solar field rows and the presence of shadows in the space separating the rows was discussed in Alsadi and Nassar (2017b); Alsadi and Nassar (2019).

To numerically solve the assigned model, various authors derived different methods to calculate the view factor. But the most commonly used methods are as follows: 1) direct integration method; 2) unit sphere method; 3) ray casting method; 4) cross string method; 5) Monte Carlo method; and 6) algebraic rule and matrix formulation (Gupta et al., 2017). Among all the aforementioned techniques, the crossed-string method (CSM) is the most widely used to determine the view factors of the sky and the ground as seen by the rows of the solar PV field (Alsadi and Nassar, 2016; Alsadi and Nassar, 2017b; Appelbaum, 2018).

Most studies relating to view factors were reviewed in Appelbaum (2018). View factors of PV panels on rooftops of buildings were reported in Appelbaum and Aronescu (2016), and view factors of solar collectors deployed on horizontal, inclined, and step-like planes were discussed in Nassar and Alsadi (2016). All previously mentioned studies addressed the solar PV field as a two-dimensional problem. In general, two-dimensional analysis is based on the hypothesis that the length of a row is infinitely longer than its height (Appelbaum and Aronescu, 2016). Although this assumption might be considered reasonable for large solar PV fields, the same cannot be said for rooftop solar PV installations. The installation of solar PV on rooftops of buildings is becoming more widespread and can be a solution to the energy problem in many countries (Nassar and Alsadi, 2019).

The present study distinguishes from its predecessors is the use of three-dimensional analysis to address the problem comprehensively, making it applicable to any type of solar field. A key finding of this work is the outline of two approaches to estimate solar irradiance incident on solar field rows for isotropic and anisotropic skies, something that has not thus far been studied, to the best of our knowledge. This represents the significance of the present research.

The rest of the article is further organized as follows: the theoretical framework of the study is outlined in **section 2**. The obtained results have been demonstrated graphically by several means and discussed in **section 3**. While **section 4** deals with the calculation of the solar irradiation incident on a solar field located in Tripoli city, Libya and Ankara city, Turkey as case studies for low and high latitudes sites. The conclusions drawn from the research are outlined in **Section 5**. Finally, the study is finished with a list of cited works.

2 MATHEMATICAL MODELING

In this section, the mathematical modeling of the problem is presented. It starts with defining the view factors, and then followed by introducing the analysis of the two-dimensional (2-D) and three-dimensional (3-D) view factors.

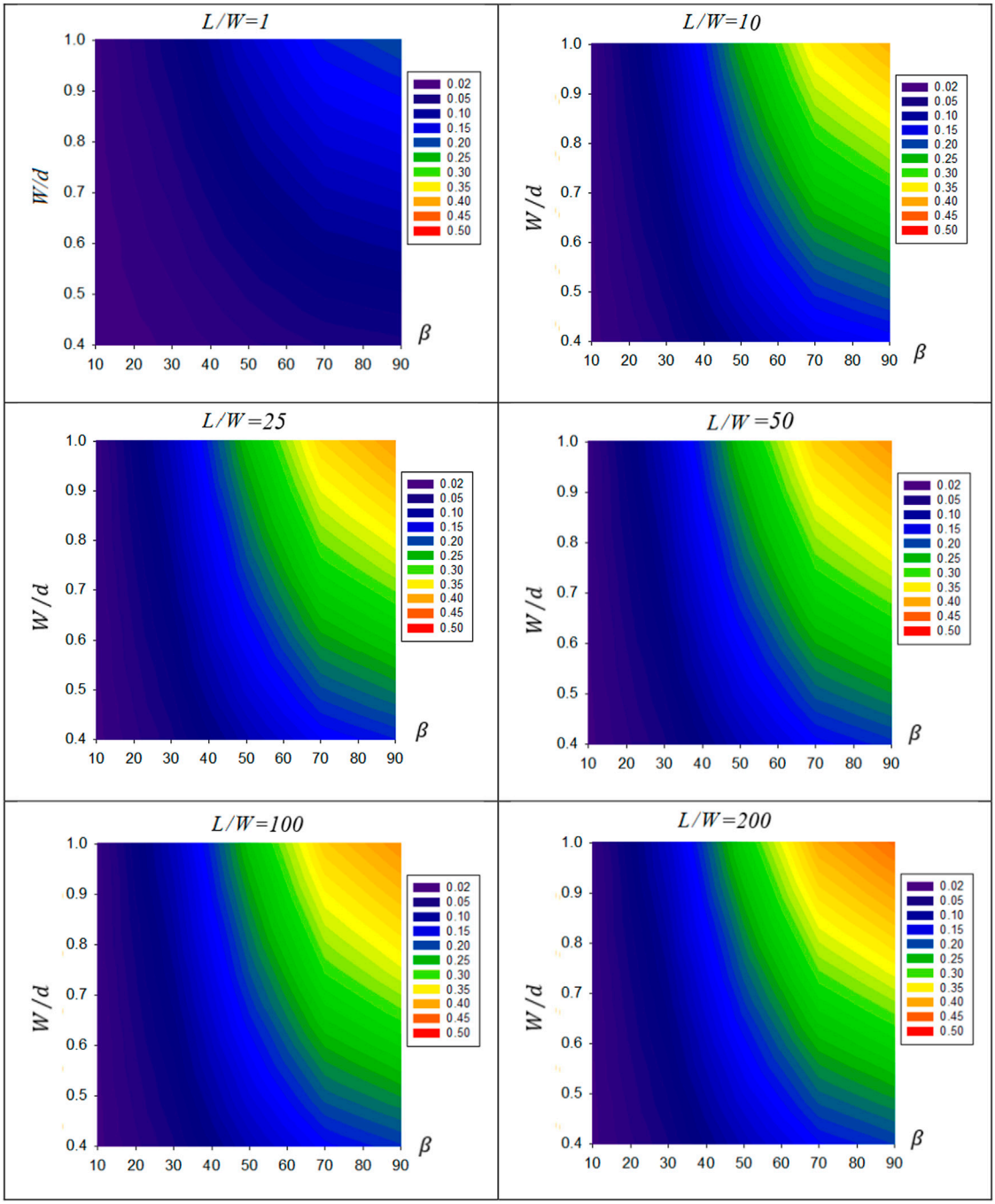

FIGURE 4 | Contour representation of $F_{A_2 \to A_{1r}}$ as a function of the aspect ratio $\frac{W}{d}$ and row tilt angle β, for various values of the aspect ratio $\frac{L}{W}$.

2.1 Definition and Algebra of the View Factors

In the literature, the view factor $F_{A_i-A_j}$ is defined as the fraction of radiation leaving surface A_i that is directly striking surface A_j (Vujičić et al., 2016). The view factor has properties that are important in analyzing and solving view factor problems, which are expressed as follows (Baehr and Karl, 2011):

$$A_i F_{A_i-A_j} = A_j F_{A_j-A_i} \quad \text{(The reciprocity rule)}, \tag{1}$$

$$\sum_{j=1}^{N} F_{A_i-A_j} = 1 \quad \text{(The summation rule)}, \tag{2}$$

$$F_{A_i-(A_{j1}+A_{j2})} = F_{A_i-A_{j1}} + F_{A_i-A_{j2}} \quad \text{(The superposition rule)}. \tag{3}$$

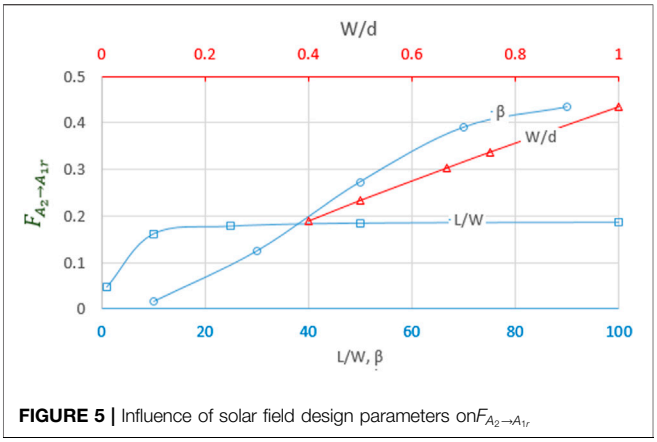

FIGURE 5 | Influence of solar field design parameters on $F_{A_2 \to A_{1r}}$

2.2 Two-Dimensional (2-D) Approach for Calculation of the View Factors

In this work, the crossed-strings method (CSM) approach is considered for two-dimensional (2-D) analysis of view factors. CSM is considered as a widely used approach for 2-D analysis. In particular, CSM is applied to geometries that are very long in one direction relative to the other directions. By attaching strings between corners, as illustrated in **Figure 1**, the view factor between two surfaces can be expressed as follows (Nassar and Alsadi, 2016):

$$F_{i \to j} = \frac{\sum crossed\ strings - \sum uncrossed\ strings}{2 \times string\ on\ surface\ i}, \text{so}$$
$$F_{A_2 \to A_1} = \frac{\left[\overline{be} + \overline{ac}\right] - \left[\overline{bc} + \overline{ae}\right]}{2\overline{ec}}. \tag{4}$$

According to this definition, the view factors may be derived and expressed as follows (Nassar and Alsadi, 2016):

$$F_{A_1 \to s} = \frac{1 + cos\beta}{2}, \tag{5}$$

$$F_{A_1 \to g} = \frac{1 - cos\beta}{2}, \tag{6}$$

$$F_{A_2 \to s} = \frac{1}{2}\left[1 + \frac{d}{W} - \sqrt{\left(\frac{d}{W} - cos\beta\right)^2 + (sin\beta)^2}\right], \tag{7}$$

$$F_{A_2 \to g} = \frac{1}{2}\left[1 + \frac{d}{W} - \sqrt{\left(\frac{d}{W} + cos\beta\right)^2 + (sin\beta)^2}\right], \tag{8}$$

$$F_{A_1 \to A_{1r}} = \frac{1}{2}\left[\sqrt{\left(\frac{d}{W} - cos\beta\right)^2 + (sin\beta)^2} + \sqrt{\left(\frac{d}{W} + cos\beta\right)^2 + (sin\beta)^2} - 2\frac{d}{W}\right]. \tag{9}$$

In the earlier mentioned relations, $F_{A_1 \to s}$ is the first row to the sky view factor, $F_{A_1 \to g}$ is the first row to the ground view factor, $F_{A_2 \to s}$ is second and the succeeding rows to the sky view factor, $F_{A_2 \to g}$ is second and the succeeding rows to the ground view factor, and $F_{A_1 \to A_{1r}}$ is the second row to rear surface of the first row view factor. Considering the length of the solar panels (L), the view factor can be calculated for different designs.

2.3 Three-Dimensional (3-D) Approach for Calculation of View Factors

For further improvement of predicated energy yields, costs, and optimum design, a 3-D analysis is adopted to accurately

TABLE 1 | Expressions for view factors depicted in **Figure 2**.

Definition	Expression	Source	Eq. No
Top surface of the first row to the ground	$F_{A_1 \to g} = \frac{1-cos\beta}{2}$	Refschneider (1967) †	(10)
Top surface of the first row to the sky	$F_{A_1 \to s} = \frac{1+cos\beta}{2}$	derived from **Eq. 2**	(11)
Top surface of the second row to the rear surface of first row	$F_{A_2 \to A_{1r}} = \frac{1}{WL}\int_{x1=0}^{W}\int_{y1=0}^{L}\int_{x2=0}^{W}\int_{y2=0}^{L}\frac{dsin^2\beta}{\pi[d^2+(y_1-y_2)^2+(x_1-x_2)^2 sin^2\beta]^2}dy_2dx_2dy_1dx_1$	modified from Rehman and Uzair (2017)	(12)
Top surface of the second row to space separating the rows	$F_{A_2 \to (g1+g_2)} = \frac{1}{WL}\int_{x1=0}^{W}\int_{y1=0}^{L}\int_{x2=0}^{d}\int_{y2=0}^{L}\frac{x_1x_2sin^2\beta}{\pi[x_1^2+x_2^2-2x_1x_2cos\beta+(y_1-y_2)^2]^2}dy_2dx_2dy_1dx_1$	modified from Refschneider (1967)	(13)
Top surface of the second row to unshaded space-separating rows	$F_{A_2 \to g_2} = \frac{1}{WL}\int_{x1=0}^{W}\int_{y1=0}^{L}\int_{x2=0}^{Z_2}\int_{y2=0}^{L}\frac{x_1x_2sin^2\beta}{\pi[x_1^2+x_2^2-2x_1x_2cos\beta+(y_1-y_2)^2]^2}dy_2dx_2dy_1dx_1$	modified from Refschneider (1967)	(14)
Top surface of the second row to the shaded space-separating rows	$F_{A_2 \to g_1} = F_{A_2 \to (g_1+g_2)} - F_{A_2 \to g_2}$	derived from **Eq. 3**	(15)
Top surface of the second row to sky	$F_{A_2 \to s} = F_{A_1 \to s} - F_{A_2 \to A_{1r}}$	derived from **Eq. 3**	(16)
Ground surrounding surface A_2, seen but not included in space-separating rows	$F_{A_2 \to g} = F_{A_1 \to s} - F_{A_2 \to A_{1r}} - F_{A_2 \to (g_1+g_2)}$	derived from **Eq. 3**	(17)
Rear surface of the first row to sky	$F_{A_{1r} \to s} = \frac{1-cos\beta}{2} - F_{A_{1r} \to A_2}$	modified from **Eq. 3**	(18)
Rear surface of the first row to the second row	$F_{A_{1r} \to A_2} = F_{A_2 \to A_{1r}}$	derived from **Eq. 1**	(19)
Rear surface of the first row to space-separating rows	$F_{A_{1r} \to (g1+g_2)} = \frac{1}{WL}\int_{x1=0}^{W}\int_{y1=0}^{L}\int_{x2=0}^{d}\int_{y2=0}^{L}\frac{x_1x_2sin^2\beta}{\pi[x_1^2+x_2^2+2x_1x_2cos\beta+(y_1-y_2)^2]^2}dy_2dx_2dy_1dx_1$	Refschneider (1967)	(20)
Rear surface of the first row to unshaded ground	$F_{A_{1r} \to g_1} = \frac{1}{WL}\int_{x1=0}^{W}\int_{y1=0}^{L}\int_{x2=0}^{Z_1}\int_{y2=0}^{L}\frac{x_1x_2sin^2\beta}{\pi[x_1^2+x_2^2+2x_1x_2cos\beta+(y_1-y_2)^2]^2}dy_2dx_2dy_1dx_1$	Refschneider (1967)	(21)

[a]*https://web.engr.uky.edu/rtl/Catalog/sectionc/C-9.html*

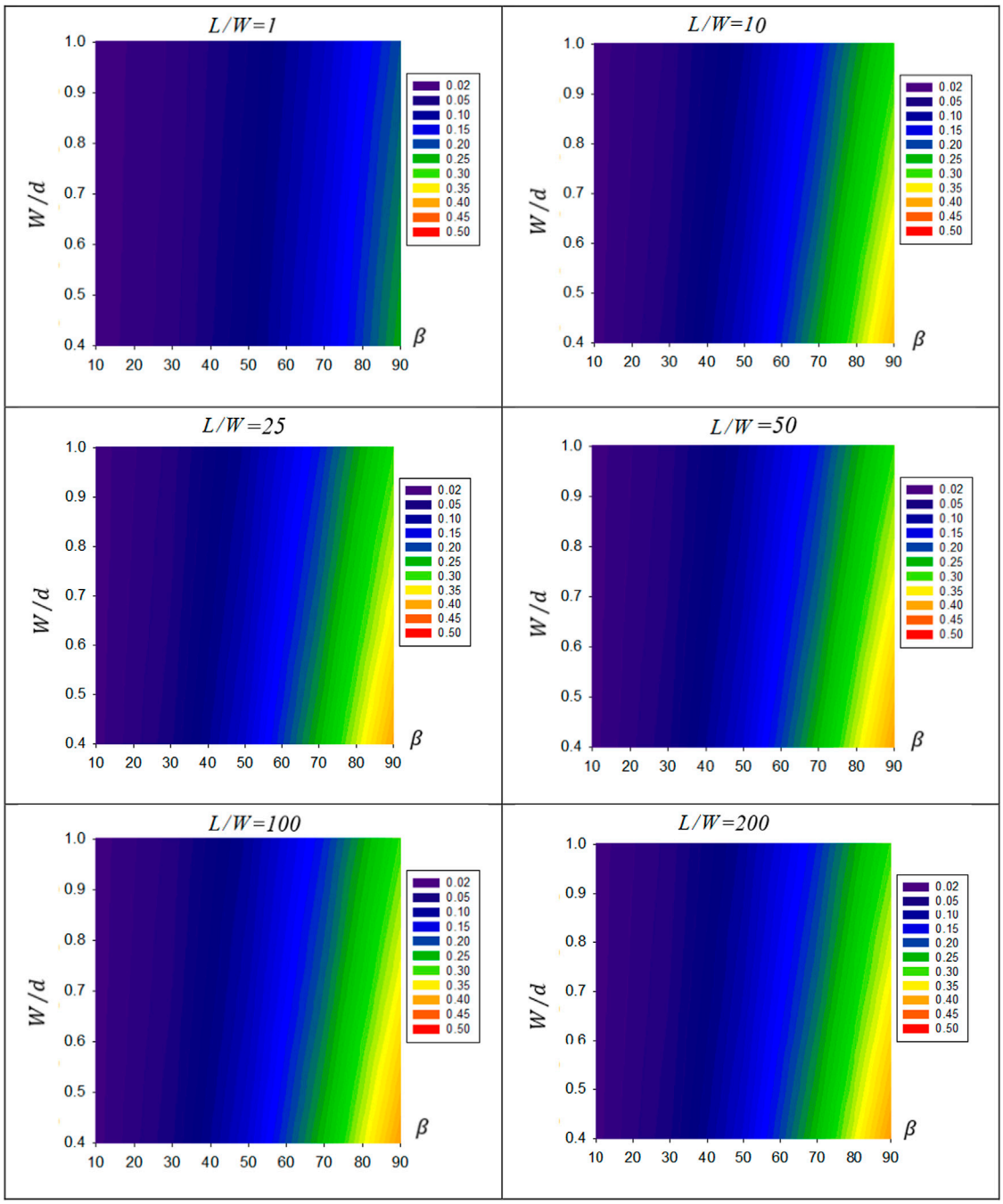

FIGURE 6 | Contour representation of $F_{A_2 \to (g_1+g_2)}$ as a function of the aspect ratio $\frac{W}{d}$ and row tilt angle β, for various values of aspect ratio $\frac{L}{W}$.

calculate view factors of solar PV fields. A schematic diagram for a successive solar collector in a solar field is shown in **Figure 2**. **Figure 2** displays all view factors that are associated with a horizontal plane PV field at an instant of time, which will be the reference to the rest of the discussion. All the nomenclature of view factors that is related to a horizontal plane fixed-mode solar PV field at any moment of time is also displayed in **Figure 2**.

For further analysis, the view factor expressions in Nassar (2020) have been reformed to match the geometry of the solar PV field depicted in **Figure 2**, as displayed in **Table 1**. It is worth mentioning that the multi-integration expressions in **Table 1** have no mathematical solution yet and can be evaluated *via* numerical techniques only.

The integrals in **Eq. 12–14**, **20**, **21** are partially solved with one term remaining unsolved. The unsolved term is solved in this

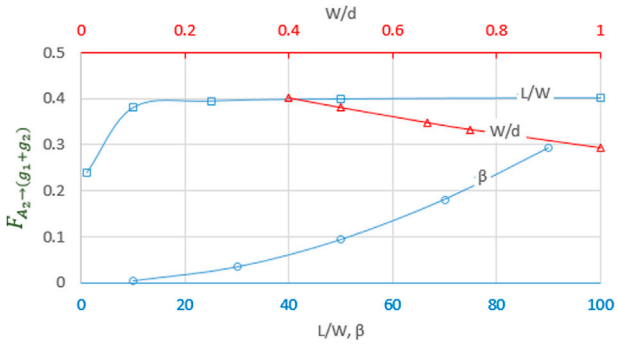

FIGURE 7 | Influence of solar field design parameters on $F_{A_2\to(g_1+g_2)}$

work numerically by means of the Gaussian quadrature five-point rule as shown in **Appendix A1**.

2.4 Calculation of Shadow in Space-Separating Rows

In solar PV fields, shadow has a great effect on the ground view factor for the second and subsequent rows. **Figure 3** presents a schematic for two plates in subsequent rows where the distance separates the rows (d) has the shaded zone (Z_1) and the unshaded zone (Z_2). For the solar field, the estimation of the effect of shadow is extensively studied (Groumpos and Khouzam, 1987; Nassar et al., 2008; Alsadi and Nassar, 2019). A general expression for shadow geometry in all types of solar fields is given in Alsadi and Nassar (2019). In **Figure 3**, it can be seen that the length of the shadow in the space separating the rows is much longer than its width. Thus, it can be assumed that the shadow is of rectangle shape, resulting in simplifying the problem without significant effect on the results.

Eq. 22 and **23** present the shaded g_1 and unshaded g_2 zone lengths in terms of dimensionless ratio of lengths Z_1 and Z_2 of the shaded and unshaded zones with respect to the distance separating the rows (d).

$$\frac{Z_1}{d}=\frac{W}{d}cos\beta+\frac{W}{d}\frac{sin\beta}{tan\alpha}cos(\varnothing-\psi)\quad if\begin{cases}\frac{Z_1}{d}<0;\ \frac{Z_1}{d}=0\\ \frac{Z_1}{d}>1;\ \frac{Z_1}{d}=1\end{cases} \tag{22}$$

$$\frac{Z_2}{d}=1-\frac{Z_1}{d}\quad if\begin{cases}\frac{Z_2}{d}<0;\ \frac{Z_2}{d}=0\\ \frac{Z_2}{d}>1;\ \frac{Z_2}{d}=1\end{cases}. \tag{23}$$

3 RESULTS AND DISCUSSION

3.1 First Row View Factors

To determine the incident solar radiation on the first row of a solar field and its view factor, it is treated as a single-tilted surface.

3.1.1 $F_{A_1\to g}$

The $F_{A_1\to g}$ presents the first row to the ground view factor in which g refers to the ground surface seen by the first-row surface A_1. Assuming the ground surface in front and on either sides of the first row is unshaded, the value of $F_{A_1\to g}$ is constant and depends only on the row tilt angle β, which can be calculated by **Eq. 10**. **Eq. 10** shows that $F_{A_1\to g}$ is directly proportional to the tilt angle β.

3.1.2 $F_{A_1\to s}$

The $F_{A_1\to s}$is the first row to sky view factor. It has a constant value and can only be affected by the row tilt angle β. It is clear from **Eq. 11** that $F_{A_1\to s}$ is inversely proportional to the tilt angle β.

3.2 Second Row View Factors

Numerous values of the second row view factors' contour representation are plotted in **Figures 4–7**.

3.2.1 $F_{A_2\to A_{1r}}$

The view factor $F_{A_2\to A_{1r}}$ represents the second row to the rear surface of the first row view factor. The view factor $F_{A_2\to A_{1r}}$ is displayed with respect to the design parameters of a solar PV field in a contour plot in **Figure 4**. **Figure 5** demonstrates the relationship between $F_{A_2\to A_{1r}}$ and the field design parameters.

Figures 4, **5** show that increasing the tilt angle β leads to a significant increase in the view factor $F_{A_2\to A_{1r}}$ by a cubic order polynomial. Similarly, an increase in the value of $F_{A_2\to A_{1r}}$ is almost proportional to that of the aspect ratio $\frac{W}{d}$. On the other hand, the influence of the aspect ratio $\frac{L}{W}$ is limited to values < 10 as in the case of rooftop solar installation.

3.2.2 $F_{A_2\to(g_1+g_2)}$

In this section, the value of the view factor $F_{A_2\to(g_1+g_2)}$ is partially evaluated by numerically solving the multi-integral **Eq. 13**, with solving the remaining part using the Gaussian quadrature five-point rule (**Appendix A1**). Where the subscripts g_1 and g_2 refer to the shaded and unshaded zones, respectively. The contour plot (**Figure 6**) exhibits the effect of solar field design parameters on the value of $F_{A_2\to A_{1r}}$. The result shows that the value of $F_{A_2\to(g_1+g_2)}$ is a constant, depending on solar field design parameters β and d.

Figures 7, **8** show that as the row tilt angle β increases the value of the view factor $F_{A_2\to(g_1+g_2)}$ increases in a quadratic power polynomial scale. It also shows that the value of $F_{A_2\to(g_1+g_2)}$ decreases linearly as the value of the aspect ratio $\frac{W}{d}$ increases. On the other hand, as the length of the row for the aspect ratio $\frac{L}{W}$ increases from 0 to 10 leads to a large logarithmical scale increase in the value $F_{A_2\to(g_1+g_2)}$ and flattened beyond $\frac{L}{W}>10$ into a straight line having zero slope as depicted in **Figure 7**.

3.2.3 $F_{A_2\to s}$

The sky view factor $F_{A_2\to s}$ is one of the important factors for its relatively large effect on the contribution of sky diffuse irradiance to the total global tilted solar irradiation. Where under an overcast sky all irradiance is diffuse, while under a standard clear-sky, about 70% of global tilted irradiance is direct, 23% diffuse, and the rest is ground reflected (Nassar, 2005). The value

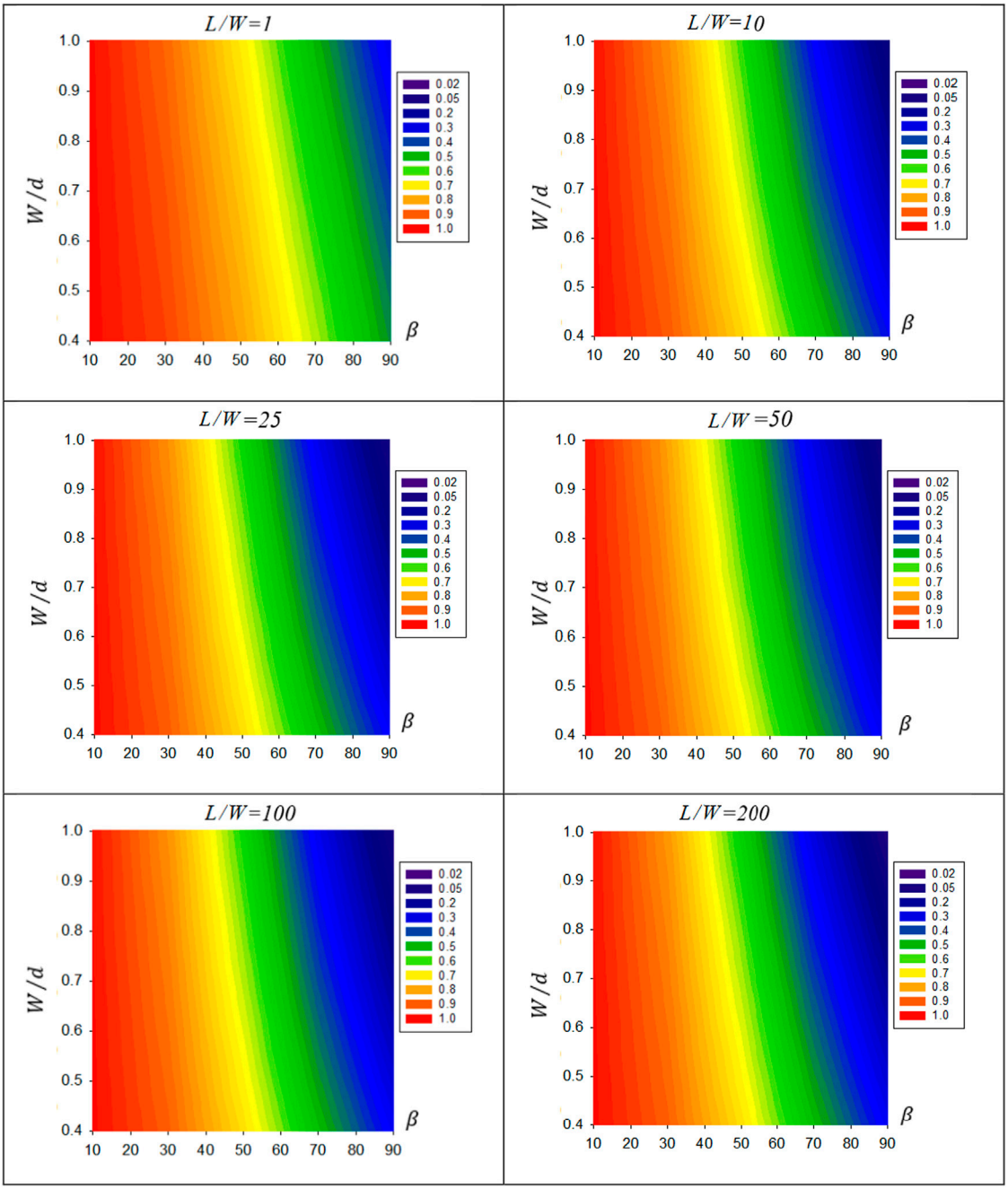

FIGURE 8 | Contour representation of $F_{A_2 \to s}$ as a function of $\frac{W}{d}$, β, and $\frac{L}{W}$.

of $\boldsymbol{F_{A_2 \to s}}$ can be obtained by applying the superposition rule. The second row sees the sky as the first row sees it ($\boldsymbol{F_{A_1 \to s}}$) less the blocking that takes place due to the presence of the first row in front of it ($F_{A_2 \to A_{1r}}$). **Figure 8** is a contour plot showing the behavior of $\boldsymbol{F_{A_2 \to s}}$ when changing the design parameters of the solar PV field β, $\frac{W}{d}$ and $\frac{L}{W}$.

The row tilt angle β is a critical parameter in the sky view factor. It is found that as β increases the value of sky view factor reduces by a cubic order polynomial. Also, the value of the sky view factor is inversely proportional to the aspect ratio $\frac{W}{d}$. Furthermore, the length of row has an inverse power effect on the sky view factor for the low aspect ratio $\frac{L}{W} < 10$, diminishing to have no effect for larger aspect ratios. **Figure 9** demonstrates that for typical solar field applications, the sky view factor is affected only by row tilt angle.

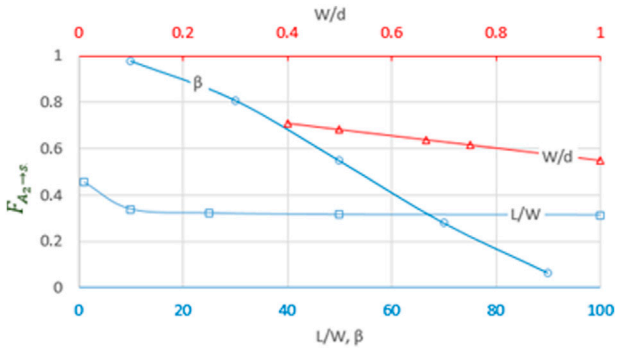

FIGURE 9 | Influence of solar field design parameters on $F_{A_2\to s}$

3.2.4 $F_{A_2\to g}$

The subscript *g* refers to ground seen by the row, in front and on either side of it. The view factor $F_{A_2\to g}$ value is obtained using the summation rule that is subtracting the total second row view factors from that of the first row view factor. In this case, the total ground area is assumed to be unshaded. **Figure 10** is a contour plot representing the relationship between $F_{A_2\to g}$ and the solar PV field's design parameters β, $\frac{W}{d}$ and $\frac{L}{W}$.

Figure 10 shows that $F_{A_2\to g}$ is affected significantly by tilt angle β, and they have almost direct linear relationship. With respect to the aspect ratio $\frac{L}{W}$, the view factor $F_{A_2\to g}$ has a power function relationship for $\frac{L}{W}$ <10, leading to a sharp decrease in $F_{A_2\to g}$. For higher ratios, the relation diminishes to no effect. On the other hand, the aspect ratio W/d has a lesser effect being almost directly proportional to $F_{A_2\to g}$, as depicted in **Figure 11**.

3.3 Dynamic View Factors

The four view factors defined in this work are dynamic due to the fact that they depend on the shadow in the space between separating rows, and shadow is function of time and location, hence the name "dynamic." As illustrated in **Figure 2**, the four view factors are as follows: view factor between the second row and the shaded zone g_1 ($F_{A_2\to g_1}$), view factor between the second row and the unshaded zone g_2 ($F_{A_2\to g_2}$), view factor between rear surface of the first row and the shaded zone g_1 ($F_{A_{1r}\to g_1}$), and view factor between the rear surface of the first row and the unshaded zone g_2 ($F_{A_{1r}\to g_2}$).

3.4 Calculation of Shadow

Shadow of an object depends on the design parameters, the location (∅), and time assigned by solar altitude and azimuth angles α and γ, respectively. It is a well-known fact that shadow is longer at high latitudes, early in the morning, and late in the evening. The longest show occurs in winter solstice. It gets shorter at solar noon, reaching its shortest at summer solstice. In relation to PV fields, in addition to location and time, shadow depends on field dimensions and row tilt angle β. Among these parameters, the most flexible and controllable parameter is the row tilt angle β in order to influence the effect of shadow. The tilt angle β was recommended not to exceed 30° for European installations (Vokony et al., 2018) while a tilt angle β of about 20° was recommended for North Africa (Agha and Sbita, 2000; Alsadi et al., 2016). **Figure 12** is a radar plot representing a comparison between two categories of locations: MENA with ∅ = 30°, β = 20° and Europe with ∅ = 40°, β = 30° for both longest and shortest shadows occurring on June 21st and December 21st, respectively, for several aspect ratios $\frac{W}{d}$ = 0.5, 0.667 , and 1.0.

3.5 Comparison of View Factors of the Surface F_{A_2} Obtained by CSM and 3-D Analysis

A comparison between second row surface view factors at different design parameters for CSM and 3-D analysis are presented in **Figure 13**. To produce **Figure 2**, *B* is considered 30° and the view factor is calculated at different aspect ratios $\frac{d}{W}$ for various aspect ratios $\frac{L}{W}$. Where the error between the two methods is calculated using **Eq. 24**.

$$Error = \frac{F_{A_2}\ (CSM) - F_{A_2}\ (3D)}{F_{A_2}\ (CSM)} \times 100. \tag{24}$$

It is found that for solar PV field with aspect ratios $\frac{d}{W} \approx 1.5$ and $\frac{L}{W} \approx 25$, the view factors estimate has errors of 3%, -1, and 44% for $F_{A_1\to s}$, $F_{A_2\to g}$, and $F_{A_2\to A_{1r}}$, respectively. For rooftop solar PV installations with aspect ratios $\frac{d}{W} \approx 1.5$ and $\frac{L}{W} \approx 5$, the errors were found consecutively to be 30%, -6, and 38% for $F_{A_1\to s}$, $F_{A_2\to g}$, and $F_{A_2\to A_{1r}}$. It should be noted that CSM produced a large $F_{A_2\to A_{1r}}$ error even for vertical planes compared with 3-D analysis. Applying **Eq. 24** for the same solar field ($\frac{d}{W} \approx 1.5$ and $\frac{L}{W} \approx 25$), the errors produced due to the use of CSM are as high as 11% in the case of $F_{A_2\to A_{1r}}$.

The inherent restriction of CSM where the length of a solar field is assumed to be much longer than its width (i.e. $\frac{L}{W} \cong \infty$) is applicable only in large solar PV fields >100 MW. In comparison, smaller solar PV fields such as rooftop installation where the aspect ratio $\frac{L}{W}$ is relatively small (<5), the view factors estimate exhibit significantly larger errors.

3.6 Case Study

In this part, author presented a case study in Libyan. The results presented here are for a horizontal plane fixed-mode solar PV field project planned by the Libyan government in an effort to transition to electricity generation using abundant renewable energy resources available in the country. The project is located on the outskirts of the capital city Tripoli (32.815°N, 13.439°E). The solar PV field is orientated due south (ψ = 0), having a tilt angle β = 20° from the horizontal, the rows dimensions $L \times W$ are 200 × 6 m, with the rows placed 9 m apart.

Applying **Eq. 22**, **23** for the aforementioned solar field yielded the results depicted as in **Figure 14**, which is represented as a radar chart for the 21st of every month for both shaded and unshaded zones.

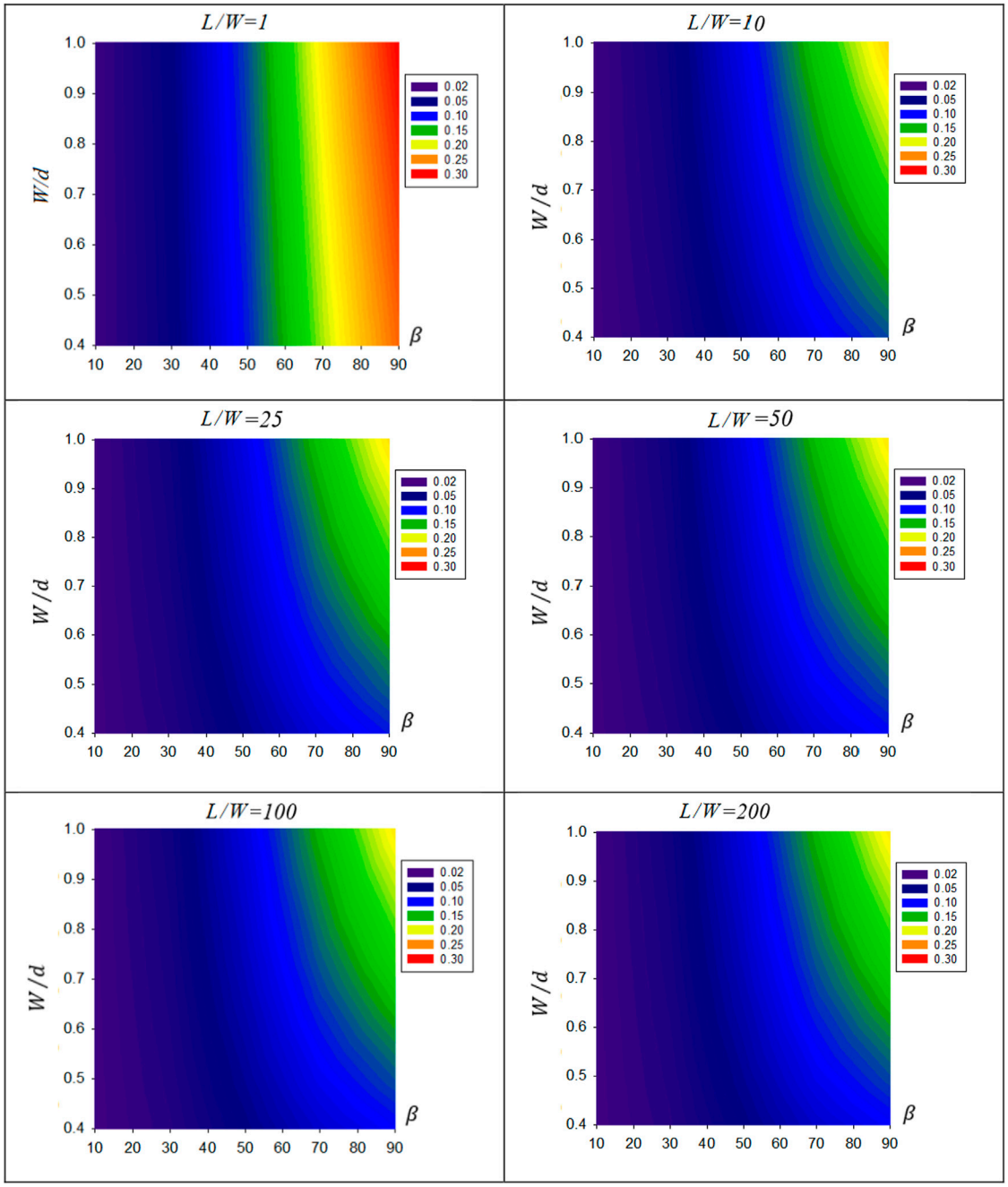

FIGURE 10 | Contour presentation of $F_{A_2 \to g}$ as a function of β, $\frac{W}{d}$, and $\frac{L}{W}$.

3.6.1 View Factor of the Second Row F_{A_2}

The view factor between surface of the second row and rear surface of the first row; $\boldsymbol{F_{A_2 \to A_{1r}}}$

The value of the view factor $F_{A_2 \to A_{1r}}$ was obtained by solving the multi-integral presented in **Eq. 11**. A modified version of FORTRAN code developed by Nassar (2020) was used to numerically evaluate the view factor $F_{A_2 \to A_{1r}}$. Result is given in **Eq. 25**.

$$F_{A_2 \to A_{1r}} = 0.0244. \tag{25}$$

The view factor between the surface of the second row and sky; $\boldsymbol{F_{A_2 \to s}}$

The view factor $F_{A_2 \to s}$ is a constant value that depends only on design parameters; its value is obtained by applying the superposition rule. The second and subsequent rows see the sky in the same manner as the first row ($F_{A_1 \to s}$), less blocking

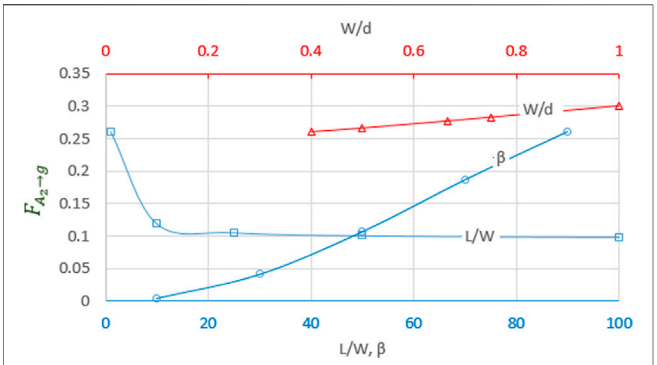

FIGURE 11 | Influence of solar field design parameters on $F_{A_2\to g}$

takes place due to the presence of the first row ($F_{A_2\to A_{1r}}$) and is given by the following equation:

$$F_{A_2\to s} = F_{A_1\to s} - F_{A_2\to A_{1r}} = \frac{1+cos\beta}{2} - F_{A_2\to A_{1r}} \tag{26}$$

$$F_{A_2\to s} = 0.9699 - 0.0244 = 0.9454.$$

The view factor between the surface of the second row and space-separating rows; $\boldsymbol{F_{A_2\to(g_1+g_2)}}$

The value view factor $\boldsymbol{F_{A_2\to(g_1+g_2)}}$ is a constant value that depends only on design parameters. This view factor represents the view factor between the surface of the second row and space-separating rows ($Z_1 + Z_2$). It is obtained by solving the multi-integral equation presented in **Eq. 11**. The value of $F_{A_2\to(g_1+g_2)}$ for given solar PV field characteristics was found as follows:

$$F_{A_2\to(g_1+g_2)} = 0.0179. \tag{27}$$

The view factor between the surface of the second row and the sunny zone; $\boldsymbol{F_{A_2\to g_2}}$

The value of the view factor $F_{A_2\to g_2}$ is obtained either by applying **Eq. 9** or in the same manner as calculating $F_{A_2\to(g1+g2)}$ substituting the length of the unshaded zone Z_2 for d such that the aspect ratio becomes $\frac{W}{Z_2}$ and $\frac{L}{Z_2}$.

The view factor between the surface of the second row and the shaded zone; $\boldsymbol{F_{A_2\to g_1}}$

The value of the view factor $F_{A_2\to g_1}$ is calculated directly from the superposition rule by subtracting $F_{A_2\to g_2}$ from $F_{A_2\to(g_1+g_2)}$, giving the following equation:

$$F_{A_2\to g_1} = F_{A_2\to(g_1+g_2)} - F_{A_2\to g_2}. \tag{28}$$

The dynamic values of $F_{A_2\to g_1}$ and $F_{A_2\to g_2}$ are depicted in the form of a radar chart in **Figure 15** for the 21st of every month.

Since the values of $F_{A_2\to g_1}$ and $F_{A_2\to g_2}$ are complementary and dependent on shaded and unshaded profiles, increasing the shadow length leads to an increase in $F_{A_2\to g_1}$ and a decrease in $F_{A_2\to g_2}$, and vice versa. The symmetry of the two profiles can be observed in **Figure 15**.

The view factor between the surface of the second row and surrounding ground; $\boldsymbol{F_{A_2\to g}}$

The subscription g refers to the ground surrounding the second, not including the space separating the rows ($g_1 + g_2$) and assumed to be unshaded. The value of $F_{A_2\to g}$ is obtained by applying the summation rule as follows:

$$F_{A_2\to g} = 1 - \left(F_{A_2\to(g_1+g_2)} + F_{A_2\to sky} + F_{A_2\to A_{1r}}\right) \tag{29}$$

$$F_{A_2\to g} = 1 - (0.0179 + 0.9454 + 0.0244) = 0.0123.$$

3.6.2 View Factor of the Rear Surface of the First Row $F_{A_{1r}}$

In actuality, the rear surface of the first row is a reverse image of the second row and deal in the same manner as the second row.

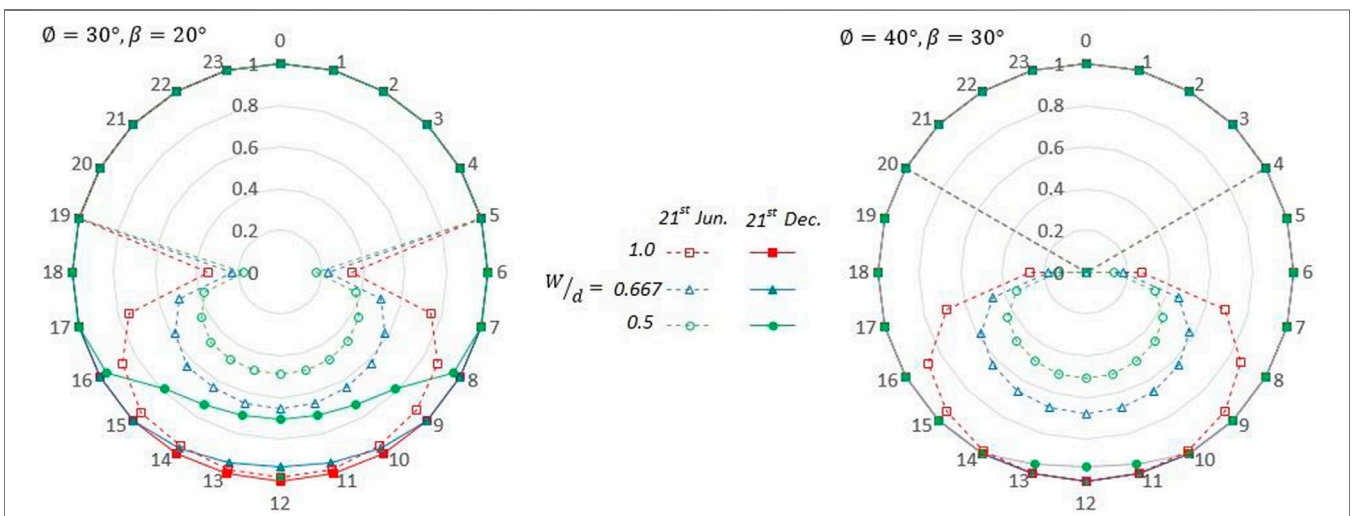

FIGURE 12 | Comparison of the shadow zone length ratio $\frac{Z_1}{d}$ between two locations with different tilt angles on the 21st of summer and winter solstices. The aspect ratio $\frac{W}{d}$ is a parameter.

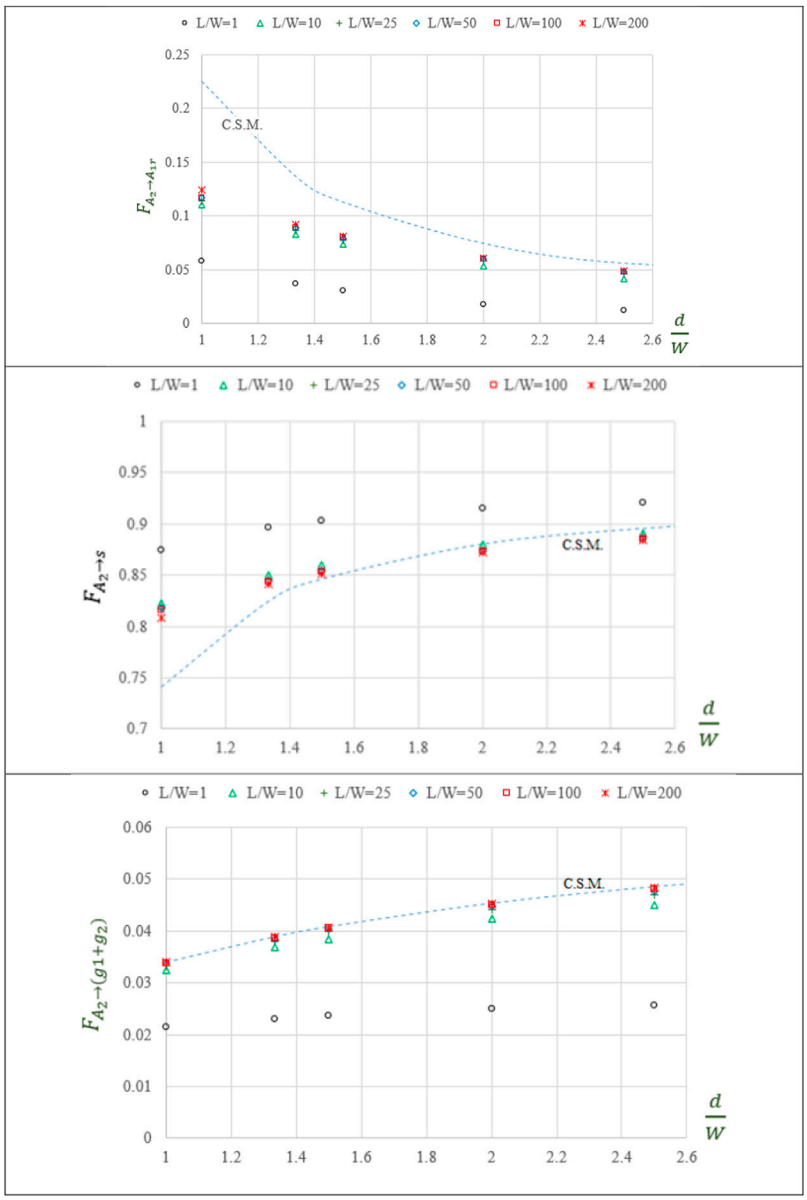

FIGURE 13 | Comparison of view factors of surface F_{A_2} obtained by CSM and 3-D analysis as a function of the aspect ratio $\frac{d}{W}$ for various aspect ratios $\frac{L}{W}$ andβ = 30°

The view factor between the rear surface of the first row and space-separating rows; $\boldsymbol{F_{A_{1r}\to(g1+g_2)}}$

The view factor $F_{A_{1r}\to(g1+g_2)}$ is a constant value dependent only on design parameters. It is determined from **Eq. 18**.

$$F_{A_{1r}\to(g1+g_2)} = 0.9176. \tag{30}$$

The view factor between the rear surface of the first row and the shaded zone; $\boldsymbol{F_{A_{1r}\to g_1}}$

The view factor between the rear surface of the first row and the shaded zone g_1 is calculated by applying **Eq. 15**.

The view factor between the surface of the second row and the sunny zone; $\boldsymbol{F_{A_{1r}\to g_2}}$

The view factor between the rear surface of the first row and the unshaded zone g_2 is obtained by using the view factor algebra summation rule **Eq. 2** by subtracting the value of $F_{A_{1r}\to g_1}$ from the view factor of the total space separating the rows $F_{A_{1r}\to(g1+g_2)}$.

$$F_{A_{1r}\to g_2} = F_{A_{1r}\to(g_1+g_2)} - F_{A_{1r}\to g_1}. \tag{31}$$

The dynamic values of $F_{A_{1r}\to g_1}$ and $F_{A_{1r}\to g_2}$ are depicted in the form of radar charts in **Figure 16** for the 21st of every month.

The value of $F_{A_{1r}\to g_1}$ is high at low tilt angles, influenced largely by the width of the shaded zone Z_1. The relationship is clearly demonstrated by the similarities in **Figure 16** in that the value of $F_{A_{1r}\to g_1}$ goes up with an increase in width of the shaded zone Z_1 and vice versa.

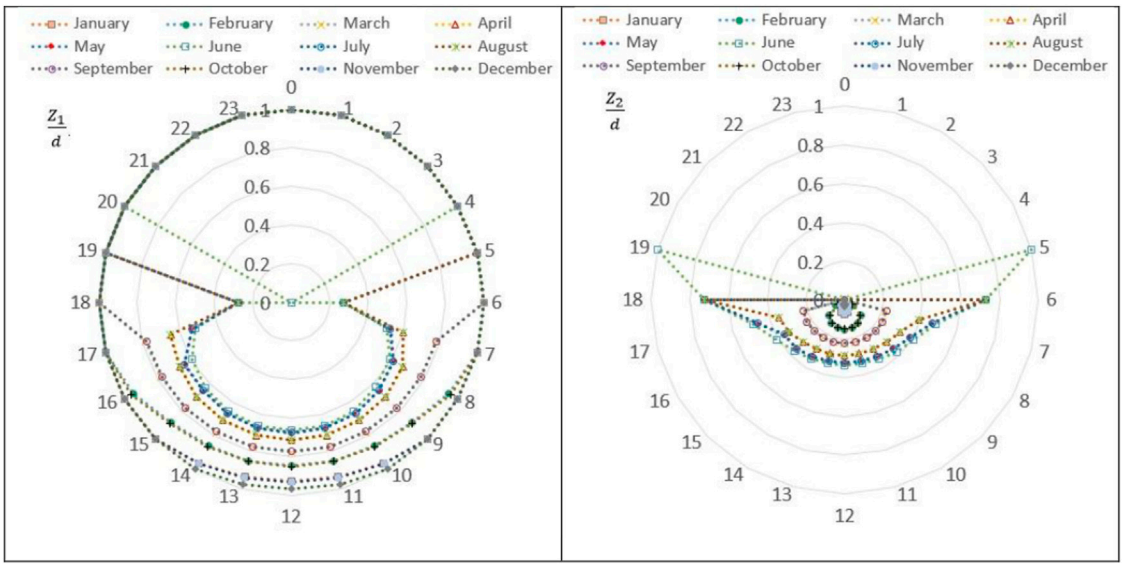

FIGURE 14 | Aspect ratio of the shaded and unshaded zones $\frac{Z_1}{d}$ and $\frac{Z_2}{d}$ for the 21st of every month for given design parameters ∅ = 32.815°N, $\psi = 0$, $\beta = 20°$, $L \times W = 200 \times 6\,m$, and $d = 9.0\,m$

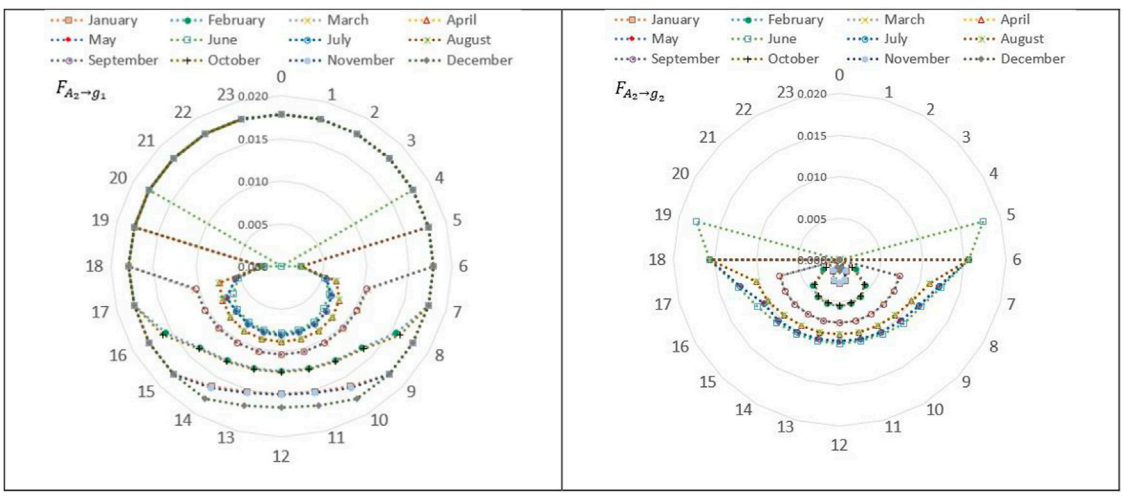

FIGURE 15 | Radar chart representing $F_{A_2 \to g_1}$ and $F_{A_2 \to g_2}$ for the 21st of every month.

The view factor between the rear surface of the first row and surrounding ground; $\boldsymbol{F_{A_{1r} \to g}}$

The view factor $F_{A_{1r} \to g}$ is treated in the same way as with sky view factor of the second row $F_{A_2 \to sky}$ using the superposition rule. The rear surface of the first row sees the surrounding ground in the same manner as the first row sees the sky ($F_{A_1 \to s}$), less blocking takes place due to the presence of the second row ($F_{A_2 \to A_{1r}}$) and the space separating the rows, giving the following equation:

$$F_{A_{1r} \to g} = \frac{1 + cos\beta}{2} - \left(F_{A_{1r} \to (g_1 + g_2)} + F_{A_2 \to A_{1r}} \right)$$
$$F_{A_{1r} \to g} = 0.9698 - (0.9176 + 0.0244) = 0.0278. \quad (32)$$

This value represents what the row sees from the ground surrounding the row, assumed to be unshaded.

The view factor between the rear surface of the first row and sky; $\boldsymbol{F_{A_{1r} \to s}}$

The view factor $F_{A_{1r} \to s}$ is a constant value and it is dependent only on the design parameters and treated in the same manner as $F_{A_2 \to g}$ using the summation rule, giving the following equation:

$$F_{A_{1r} \to s} = 1 - \left(F_{A_1 \to g} + F_{A_1 \to (g_1 + g_2)} + F_{A_2 \to A_{1r}} \right)$$
$$F_{A_{1r} \to s} = 1 - (0.0278 + 0.9176 + 0.0244 = 0.0302. \quad (33)$$

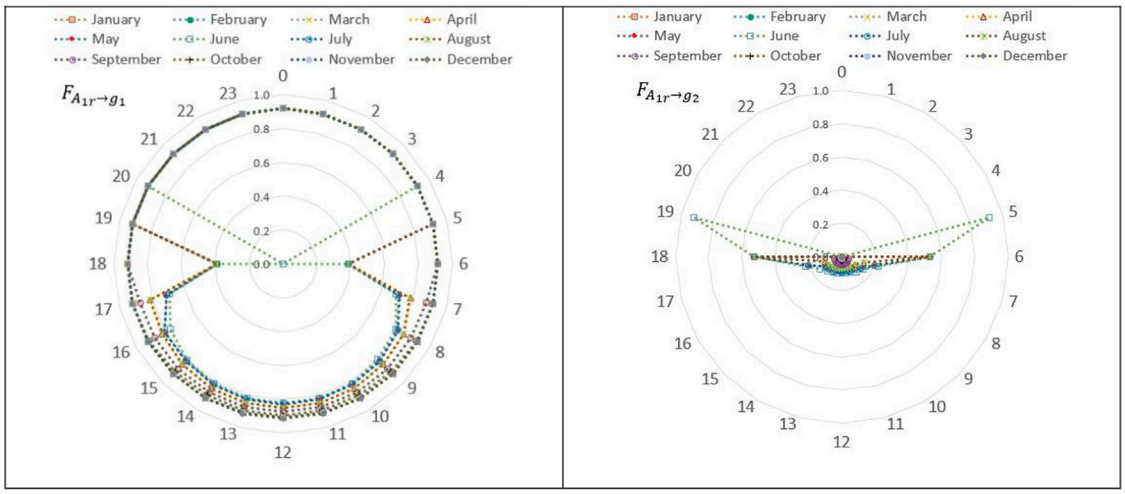

FIGURE 16 | Hourly values of $F_{A_{1r}\to g_1}$ and $F_{A_{1r}\to g_2}$ for the 21st of every month.

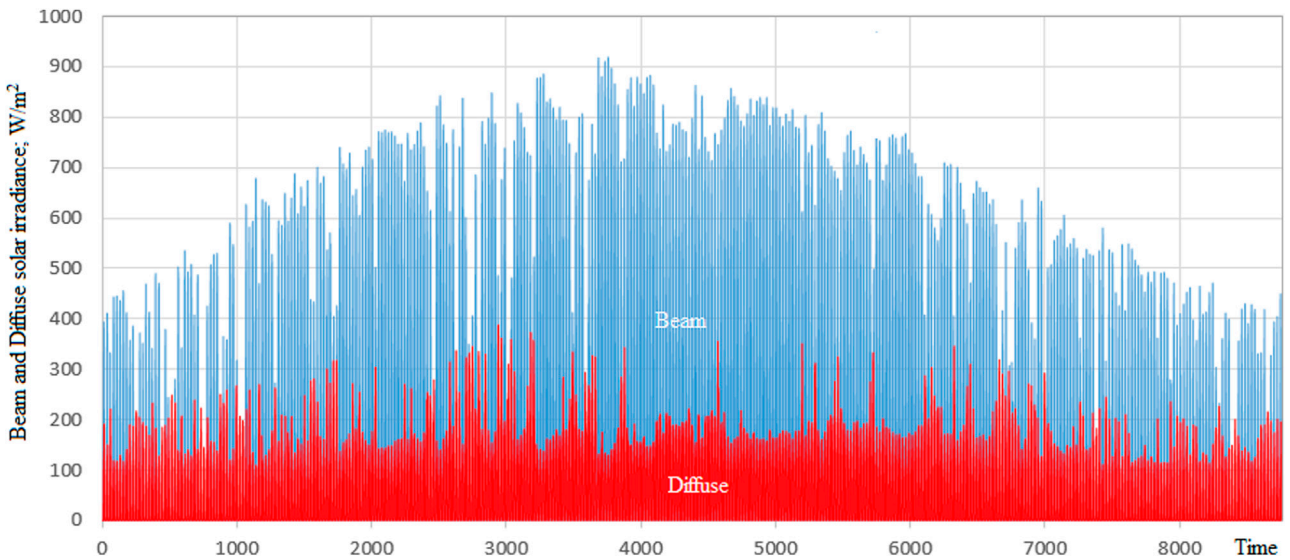

FIGURE 17 | Hourly horizontal beam and diffuse solar irradiance for Tripoli (32.815°N, 13.439°E).

4 SOLAR IRRADIANCE CALCULATION

The main objective of this research is the estimation of solar irradiance incident on the second and subsequent rows of a horizontal plane fixed-mode solar PV fields. The classical approach for calculating solar irradiance incidents on a single-tilted surface is well documented in solar energy engineering textbooks (Nassar, 2006; Duffie and Beckman, 2013). Calculating global solar irradiance (I_t) incident on an inclined surface requires global horizontal (I_h) data. I_h has two components direct beam (I_{bh}) and sky diffuse (I_{dh}) irradiance. The global horizontal solar irradiance (I_h) is given by the following equation:

$$I_h = I_{bh} + I_{dh}. \tag{34}$$

I_h and I_{dh} can be measured and are obtainable from databases on solar energy websites. The horizontal solar radiation data used in this research is 13-years hourly time series obtained from Solargis (https://solargis.com/). **Figures 17**, **18** present the diffuse and beam solar irradiance as function of time for Tripoli and Ankara.

Transposition models are used to transpose global horizontal solar irradiance to tilted irradiance, giving global irradiance for tilted surface (I_t) at a tilt angle (β) from the horizontal as follows:

$$I_t = I_{bh}R_b + I_{dh}F_{A_1\to s} + I_h\,\rho_g\,F_{A_1\to g}, \tag{35}$$

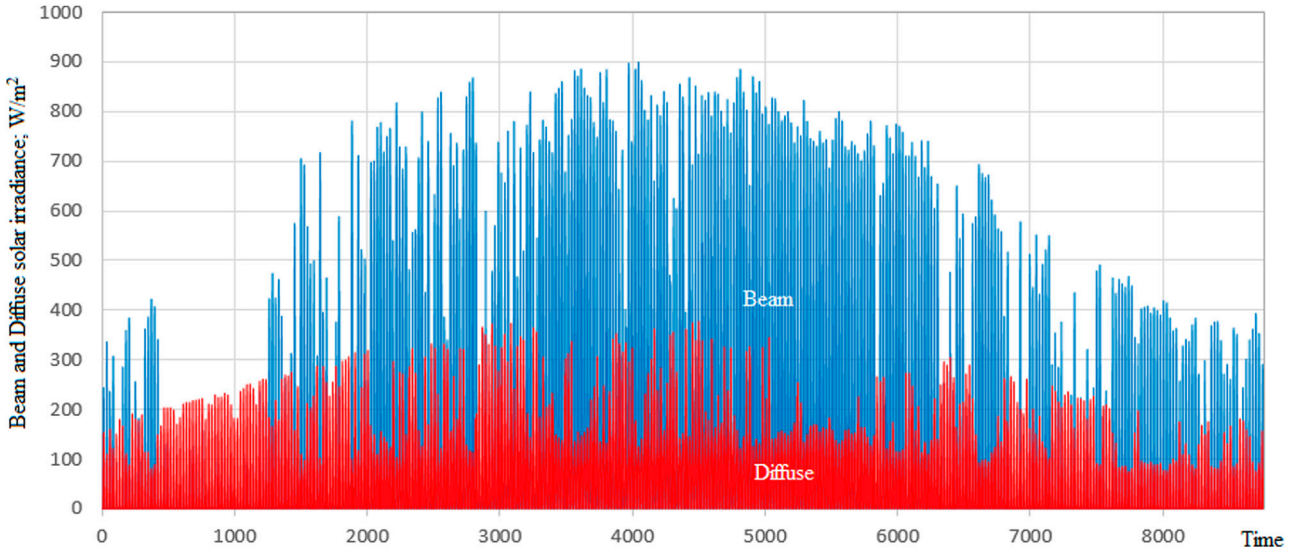

FIGURE 18 | Hourly horizontal beam and diffuse solar irradiance for Ankara (40.05°N, 32.867°E).

TABLE 2 | Daily solar radiation [W/m^2/day] incident on the solar PV field and the single surface, no shading conditions. ($\forall_{A_2} = 1$)

Transposition model	Solar PV field				Single surface		Reduction in solar energy %			
	ø = 32.8°N, β = 20°		ø = 40°N, β = 30°		β = 20	β = 30	ø = 32.8°N, β = 20°		ø = 40°N, β = 30°	
	d/W = 1.5	d/W = 2	d/W = 1.5	d/W = 2			d/W = 1.5	d/W = 2	d/W = 1.5	d/W = 2
Isotropic model	5,718	5,737	5,114	5,152	5,777	5,229	1.0%	0.7%	2.3%	1.5%
Anisotropic model	5,791	5,806	5,211	5,242	5,837	5,303	0.8%	0.6%	1.8%	1.2%

TABLE 3 | Daily solar radiation [W/m^2/day] incident on the solar PV field and the single surface, shading conditions ($\forall_{A_2} = 0$).

Transposition model	Solar PV field				Single surface		Reduction in solar energy %			
	ø = 32.8°N, β = 20°		ø = 40°N, β = 30°		ø = 32.8°N, β = 20	ø = 40°N, β = 30	ø = 32.8°N, β = 20°		ø = 40°N, β = 30°	
	d/W = 1.5	d/W = 2	d/W = 1.5	d/W = 2			d/W = 1.5	d/W = 2	d/W = 1.5	d/W = 2
Isotropic model	1,485	1,495	1,305	1,326	5,777	5,229	290%	286%	300%	294%
Anisotropic model	1,485	1,495	1,305	1,326	5,837	5,303	293%	290%	306%	300%

TABLE 4 | Daily solar radiation [W/m^2/day] incident on the solar PV field and the single surface, under overcast sky conditions.

Transposition model	Solar PV field				Single surface		Reduction in solar energy %			
	ø = 32.8°N, β = 20°		ø = 40°N, β = 30°		ø = 32.8°N, β = 20	ø = 40°N, β = 30	ø = 32.8°N, β = 20°		ø = 40°N, β = 30°	
	d/W = 1.5	d/W = 2	d/W = 1.5	d/W = 2			d/W = 1.5	d/W = 2	d/W = 1.5	d/W = 2
—	1,485	1,495	1,305	1,326	1,550	1,532	4.4%	3.7%	17.3%	15.5

where ρ_g is the albedo radiation factor, generally assumed to be 0.2. The transposition factor (R_b) is given as a function of geometrical parameters of inclined surface and position of the Sun:

$$R_b = max\left(0, \frac{cos\,\theta_i}{cos\,\theta_z}\right), \tag{36}$$

where θ_i and θ_z are solar incidence and zenith angles, respectively.

TABLE 5 | Daily solar radiation [W/m2/day] incident on rooftop solar PV installation ($\frac{L}{W}$ = 5).

Transposition model	Rooftop solar PV		Single surface		Reduction in solar energy %	
	ø = 32.8°N, β = 20°, d/W = 1.5	ø = 40°N, β = 30°, d/W = 2	ø = 32.8°N, β = 20	ø = 40°N, β = 30	ø = 32.8°N, β = 20°, d/W = 1.5	ø = 40°N, β = 30°, d/W = 2
Isotropic model	5,715	5,119	5,777	5,229	1.1%	2.2%
Anisotropic model	5,734	5,174	5,837	5,303	1.8%	2.5%

Similarly, $F_{A_1 \to g}$ is the view factor between a single surface and ground-reflected solar irradiance. It is given by the following equation:

$$F_{A_1 \to g} = \frac{1 - \cos\beta}{2}. \tag{37}$$

The diffuse irradiance is due to the scattering of solar radiation by different elements of the atmosphere. Therefore, it has a naturally non-uniform distribution throughout the sky. However, some models consider diffuse irradiance uniform or isotropic, known as isotropic models. Other models are based on the assumption that all the diffuse irradiance can be represented by two parts the isotropic and the circumsolar. Other models try to depict the scattering process by adding the diffuse irradiance coming from the circumsolar region and the horizon band to the isotropic background. The last two approaches are known as anisotropic models. Therefore, the models used to estimate (I_{dt}) or the transposition models could be divided into two groups as follows: isotropic and anisotropic (Nassar et al., 2020).

The most popular model used in the isotropic family is the Liu-Jordan Model (Liu and Jordan, 1961), where the sky view factor ($F_{A_1 \to S}$) is given by the following equation:

$$F_{A_1 \to S} = \frac{(1 + \cos\beta)}{2}. \tag{38}$$

An example of the anisotropic approach is the Hay–Davies Model (Hay and Davies, 1978) expressed as follows:

$$F_{A_1 \to S} = F_{Hay} R_b + \left(1 - F_{Hay}\right)\left(\frac{1 + cos\beta}{2}\right), \tag{39}$$

where $F_{Hay} = I_{bh}/I_{sc}$ is the modified Hay's factor.

The irradiance components associated with a solar PV field are more complex than those of a single surface. The classical approach accounts for beam (I_{bh}) irradiance, diffuse (I_{dh}) irradiance, and reflected irradiance from the ground (I_r) and from the rear of the front row. In reality, there are additional components that ought to be considered in a solar PV field, namely the view factors between the second and proceeding rows with the sky dome and with the ground surface.

Alsadi and Nassar (2017b) presented a mathematical form for an isotropic sky model as follows:

$$I_{f,iso=}\begin{cases} I_{bh}\forall_{A_2} R_{bA_2} + \\ I_{dh} F_{A_2 \to S} + \\ \left[(I_{bh} + I_{dh})\left(\frac{Z_2}{W} F_{A_2 \to g_2} + F_{A_2 \to g}\right) + I_{dh}\frac{Z_1}{W} F_{A_2 \to g_1} \right]\rho_g + \\ + \left[\rho_g \left[(I_{bh} + I_{dh})\left(\frac{Z_2}{W} F_{A_{1r} \to g_2} + F_{A_{1r} \to g}\right) + I_{dh}\frac{Z_1}{W} F_{A_{1r} \to g_1} \right] + \right. \\ \left. + \left[I_{bh}\forall_{A_{1r}} R_{bA_{1r}} + I_{dh} F_{A_{1r} \to S} \right] \right] \rho_{A_{1r}} F_{A_2 \to A_{1r}} \end{cases} \tag{40}$$

where $\forall_{A_2}$ is the ratio of the unshaded area to the total surface area.

The Hay–Davies model may be rearrangement according to the definition of the problem stated graphically in **Figure 1** as follows:

$$I_{f,aniso=}\begin{cases} I_{bh}\forall_{A_2} R_{bA_2} \\ + I_{dh}\left[\left(F_{Hay} R_{bA_2}\right) + \left(1 - F_{Hay}\right) F_{A_2 \to s} \right] \\ \left[(I_{bh} + I_{dh})\left(\frac{Z_2}{W} F_{A_2 \to g_2} + F_{A_2 \to g}\right) + I_{dh}\frac{Z_1}{W} F_{A_2 \to g_1} \right]\rho_g + \\ + \left[\rho_g \left[(I_{bh} + I_{dh})\left(\frac{Z_2}{W} F_{A_2 \to g_2} + F_{A_2 \to g}\right) + I_{dh}\frac{Z_1}{W} F_{A_2 \to g_1} \right] + \right. \\ \left. + I_{dh}\left[\left(F_{Hay} R_{bA_{1r}}\right) + \left(1 - F_{Hay}\right) F_{A_{1r} \to s} \right] \right] \rho_{A_{1r}} F_{A_2 \to A_{1r}} \end{cases} \tag{41}$$

To illustrate the impact of view factors on the estimation of solar irradiance incident on a solar harvester, we will investigate the performance of three different solar PV systems; a solar PV field, a rooftop solar PV system, and a single PV surface. For the purpose of this comparison, the aspect ratio $\frac{L}{W}$ for the solar PV field and rooftop solar PV installation is assumed 33.33 and 5, respectively. The analysis was carried for two locations, Tripoli ($\varnothing = 32.8^{\circ}N$) and Ankara ($\varnothing = 40°N$).

First, we will consider the case where the solar PV field rows are shadow-free ($\forall_{A_2} = 1$). The obtained results are tabulated in **Table 2**.

The analysis results (**Table 2**) clearly show reduced solar energy yield for the solar PV field compared to the single surface. The results also show the impact of location on solar energy yield, where energy reduction at high latitudes is more than twice than that at middle latitudes. The impact of location is directly related to the row's tilt angle, optimized to receive maximum solar energy, and the distance separating the rows, which is governed by economic considerations.

Next, we will consider the effect of shadow falling on the solar PV field rows ($\forall_{A_2} = 0$). The hourly solar radiation incident on the surface of the second and subsequent rows can be calculated

using **Eq. 38** for the isotropic model and **Eq. 39** for the anisotropic model. The obtained results are tabulated in **Table 3**.

A side note of the results in **Table 3** is the similarity of isotropic and anisotropic model results. This is a direct consequence of eliminating the beam component of solar radiation. The influence of the view factors, especially the sky view factor, become more pronounced and the reduction in solar radiation becomes dramatic (exceeding 300% at high latitudes).

An investigation for overcast sky leads to more specific results as tabulated in **Table 4**.

Again, the performance of isotropic and anisotropic models is the same in the absence of beam radiation.

Table 4 shows that reduction in solar energy in the solar PV field is significantly higher compared to single surface under overcast sky conditions (exceeding 4 and 17% at mid and high latitudes, respectively). This is explained by the increase in the diffuse component of solar radiation, which in turn is a function of the sky view factor.

The other aspect of this investigation looks into the second type of solar PV installations, namely rooftop solar PV. The obtained results are tabulated in **Table 5**.

Table 5 shows that the solar energy incident on a rooftop solar PV installation is approximately 2% lower than that of a single surface.

5 CONCLUSION

This research used 3-D numerical analysis to calculate the view factors of a horizontal plane fixed-mode solar PV field. However, it can equally be applied to all types of solar fields, including rooftops and building façades. It only requires defining the view factors between the PV panels and the environment. The influence of the design parameters, location, and time are analyzed. The present study shows that the tilt angle has a higher weighting compared to other design parameters.

The key finding of this research is improved accuracy of estimation of solar PV field potential by introducing a model for estimating reduction in solar irradiance incident on the second and subsequent rows relative to the first row of a solar field. The obtained results showed that reduction in solar irradiance is higher at high latitudes, reaching 2.3%. In addition, the reduction in solar irradiance is high under overcast sky conditions, reaching 17% at high latitudes and up to 5% in the North African region, and 300% reduction in solar radiation for shaded zones. It is highly advisable that shading in solar fields can be avoided where possible measures might be affected, such as reducing the tilt angle and/or increasing the distance separating the rows. The latter measure has some economic implications which need to be considered.

The present research is also tested the validity of the CSM for wide ranges of distance separating rows and length aspect ratios, the obtained results show that, the CSM shows good agreements in both sky and the ground view factor in the range of the length aspect ratio greater than one, but it fails in the rear side view factor in the design ranges of PV solar fields, where the error rate was found about 11%, this result is important in the case of bifacial PV solar systems.

DATA AVAILABILITY STATEMENT

The original contributions presented in the study are included in the article/Supplementary Material, further inquiries can be directed to the corresponding author.

AUTHOR CONTRIBUTIONS

YN: conceptualization; methodology; programming; and writing—original draft. HE-K: formal analysis and writing—reviewing and editing. SB: programming and writing and editing. SA: data collection and formal analysis. NA: revising the manuscript; formal analysis.

REFERENCES

Agha, K. R., and Sbita, M. N. (2000). On the Sizing Parameters for Stand-Alone Solar-Energy Systems. *Appl. Energ.* 65, 73–84. doi:10.1016/s0306-2619(99)00093-8

Alam, M., Gul, M. S., and Muneer, T. (2019). Radiation View Factor for Building Applications: Comparison of Computation Environments. *Energies* 12, 3826. doi:10.3390/en12203826

Alsadi, S. Y., and Nassar, Y. F. (2017). A Numerical Simulation of a Stationary Solar Field Augmented by Plane Reflectors: Optimum Design Parameters. *Sgre* 08, 221–239. doi:10.4236/sgre.2017.87015

Alsadi, S. Y., and Nassar, Y. F. (2017). Estimation of Solar Irradiance on Solar Fields: An Analytical Approach and Experimental Results. *IEEE Trans. Sustain. Energ.* 8 (4), 1601–1608. doi:10.1109/TSTE.2017.2697913

Alsadi, S. Y., and Nassar, Y. F. (2019). A General Expression for the Shadow Geometry for Fixed Mode Horizontal, Step-like Structure and Inclined Solar fields. *Solar Energy* 181, 53–69. doi:10.1016/j.solener.2019.01.090

Alsadi, S., Nassar, Y., and Ali, K. (2016). General Polynomial for Optimizing the Tilt Angle of Flat Solar Energy Harvesters Based on ASHRAE clear Sky Model in Mid and High Latitudes. *Energy and Power* 6 (2), 29–38. doi:10.5923/j.ep.20160602.0

Appelbaum, J., and Aronescu, A. (2016). View Factors of Photovoltaic Collectors on Roof Tops. *J. Renew. Sust. Energ.* 8, 025302. doi:10.1063/1.4943122

Appelbaum, J. (2018). The Role of View Factors in Solar Photovoltaic fields. *Renew. Sust. Energ. Rev.* 81, 161–171. doi:10.1016/j.rser.2017.07.026

Arias-Rosales, A., and LeDuc, P. R. (2020). Comparing View Factor Modeling Frameworks for the Estimation of Incident Solar Energy. *Appl. Energ.* 277, 115510. doi:10.1016/j.apenergy.2020.115510

Baehr, H. D., and Karl, S. (2011). *Heat and Mass Transfer*. 3rd ed. Berlin, Heidelberg: Springer, 588.

Duffie, J., and Beckman, W. (2013). *Solar Engineering of Thermal Processes*. 4th ed. New York: Wiley.

Groumpos, P. P., and Khouzam, K. (1987). A Generic Approach to the Shadow Effect of Large Solar Power Systems. *Solar Cells* 22 (1), 29–46. doi:10.1016/0379-6787(87)90068-8

Gupta, M. K., Bumtariya, K. J., Shukla, H., Patel, P., and Khan, Z. (2017). Methods for Evaluation of Radiation View Factor: A Review. *Mater. Today Proc.* 4, 1236–1243. doi:10.1016/j.matpr.2017.01.143

Hay, J., and Davies, J. (1978). "Calculation of the Solar Radiation Incident on an Inclined Surface," in *Proceedings of the First Canadian Solar Radiation Data Workshop, April 17-19, 1978: Toronto, Ontario, Canada* (Ottawa: Minister of Supply and Services Canada), 59–72.

Howell, J. R. (2016). A Catalog of Radiation Heat Transfer Configuration Factors. Available at: http://www.thermalradiation.net/indexCat.html (Accessed date January 14, 2022).

Liu, B., and Jordan, R. (1961). Daily Insolation on Surfaces Tilted towards Equator. *ASHRAE Trans.* 67, 526–541. Available at: https://www.osti.gov/scitech/biblio/5047843.

Mubarak, R., Hofmann, M., Riechelmann, S., and Seckmeyer, G. (2017). Comparison of Modelled and Measured Tilted Solar Irradiance for Photovoltaic Applications. *Energies* 10, 1688. doi:10.3390/en10111688

Nassar, Y. F., and Alsadi, S. Y. (2016). View Factors of Flat Solar Collectors Array in Flat, Inclined, and Step-like Solar Fields. *ASME. J. Sol. Energ. Eng.* 138 (6), 061005. doi:10.1115/1.4034549

Nassar, Y. F., and Alsadi, S. Y. (2019). Assessment of Solar Energy Potential in Gaza Strip-Palestine. *Sustainable Energ. Tech. Assessments* 31, 318–328. doi:10.1016/j.seta.2018.12.010

Nassar, Y. F., Hadi, H. H., and Salem, A. A. (2008). Time Tracking of the Shadow in the Solar Fields. *J. Sebha Univ.* 7 (2), 59–73.

Nassar, Y. F., Hafez, A. A., and Alsadi, S. Y. (2020). Multi-Factorial Comparison for 24 Distinct Transposition Models for Inclined Surface Solar Irradiance Computation in the State of Palestine: A Case Study. *Front. Energ. Res.* 7, 163. doi:10.3389/fenrg.2019.00163

Nassar, Y. (2005). Simulation of Solar Tracking Systems. *Energ. Life J.* 21, 81–90.

Nassar, Y. F. (2006). *Solar Energy Engineering-Active Applications*. Libya: Sebha University.

Nassar, Y. F. (2020). Analytical-Numerical Computation of View Factor for Several Arrangements of Two Rectangular Surfaces with Non-common Edge. *Int. J. Heat mass transfer* 159, 120130. doi:10.1016/j.ijheatmasstransfer.2020.120130

Pomax, M. K. (2011). Gaussian Quadrature Weights and Abscissae. Available at: https://pomax.github.io/bezierinfo/legendre-gauss.html (Accessed date March 31, 2022).

Refschneider, W. E. (1967). Radition Geometry in Measurement and Interpretation of Radiation Balance. *Agric. Meteorol.* 4, 255–265.

Rehman, N. U., and Uzair, M. (2017). The Proper Interpretation of Analytical Sky View Factors for Isotropic Diffuse Solar Irradiance on Tilted Planes. *J. Renew. Sust. Energ.* 9, 053702. doi:10.1063/1.4993069

Seme, S., Sredenšek, K., Štumberger, B., and Hadžiselimović, M. (2019). Analysis of the Performance of Photovoltaic Systems in Slovenia. *Solar Energy* 180 (1), 550–558. doi:10.1016/j.solener.2019.01.062

Vokony, I., Hartmann, B., Talamon, A., and Viktor, R. (2018). On Selecting Optimum Tilt Angle for Solar Photovoltaic Farms. *Int. J. Renew. Energ. Res.* 8 (No.4), 1926–1935. doi:10.20508/ijrer.v8i4.8285.g7501

Vujičić, M., Lavery, N., and Brown, S. (2016). Numerical Sensitivity and View Factor Calculation Using the Monte Carlo Method. *Proc. Imeche Part. C: J. Mech. Eng. Sci.* 220, 697–702. doi:10.1243/09544062JMES139

Weisstein, E. W. (2013). Legendre-Gauss Quadrature, MathWorld--A Wolfram Web. Available at: https://mathworld.wolfram.com/Legendre-GaussQuadrature.html (Accessed date April 19, 2022).

Conflict of Interest: The authors declare that the research was conducted in the absence of any commercial or financial relationships that could be construed as a potential conflict of interest.

Publisher's Note: All claims expressed in this article are solely those of the authors and do not necessarily represent those of their affiliated organizations, or those of the publisher, the editors, and the reviewers. Any product that may be evaluated in this article, or claim that may be made by its manufacturer, is not guaranteed or endorsed by the publisher.

APPENDIX I

Two rectangles with one common edge and included angle Φ (Howell, 2016).

$$A = \frac{a}{c},\ B = \frac{b}{c},\ C = A^2 + B^2 - 2AB\cos\varnothing,\ \text{and } D = \left(1 + A^2 \sin^2\varnothing\right)^{1/2}$$

$$\begin{aligned} F_{1-2} = -\frac{\sin 2\Phi}{4\pi B}\Bigg[& AB\sin\Phi + \left(\frac{\pi}{2} - \Phi\right)\left(A^2 + B^2\right) \\ & + B^2 \tan^{-1}\left(\frac{A - B\cos\Phi}{B\sin\Phi}\right) + A^2 \tan^{-1}\left(\frac{B - A\cos\Phi}{A\sin\Phi}\right)\Bigg] \\ & + \frac{\sin^2\Phi}{4\pi B}\left\{\left(\frac{2}{\sin^2\Phi} - 1\right)\ln\left[\frac{\left(1 + A^2\right)\left(1 + B^2\right)}{1 + C}\right]\right. \\ & \left. + B^2 \ln\left[\frac{B^2\left(1 + C\right)}{\left(1 + B^2\right)C}\right] + A^2 \ln\left[\frac{A^2\left(1 + A^2\right)^{\cos 2\Phi}}{C\left(1 + C\right)^{\cos 2\Phi}}\right]\right\} \\ & + \frac{1}{\pi}\tan^{-1}\left(\frac{1}{B}\right) + \frac{A}{\pi B}\tan^{-1}\left(\frac{1}{A}\right) - \frac{\sqrt{C}}{\pi B}\tan^{-1}\left(\frac{1}{\sqrt{C}}\right) \\ & + \frac{\sin\Phi\sin 2\Phi}{2\pi B} AD\Bigg[\tan^{-1}\left(\frac{A\cos\Phi}{D}\right) \\ & + \tan^{-1}\left(\frac{B - A\cos\Phi}{D}\right)\Bigg] \\ & + \frac{\cos\Phi}{\pi B}\int_0^B \sqrt{1 + \xi^2\sin^2\Phi}\left[\tan^{-1}\left(\frac{\xi\cos\Phi}{\sqrt{1 + \xi^2\sin^2\Phi}}\right)\right. \\ & \left. + \tan^{-1}\left(\frac{A - \xi\cos\Phi}{\sqrt{1 + \xi^2\sin^2\Phi}}\right)\right] d\xi \end{aligned}$$

The last term remains unsolved. In this research, this term is solved numerically by means of Gaussian quadrature five-point rule. The weights (w_i) and abscissae (x_i) for use in performing Legendre–Gauss quadrature integral approximation, which tries to solve the following function (Weisstein, 2013):

$$\int_a^b f(x)dx \cong \sum_{i=1}^{n} w_i f(x_i)$$

$$\int_a^b f(x)dx \cong \frac{b-a}{2}\int_{-1}^{1} f\left(\frac{b-a}{2}x_i + \frac{b+a}{2}\right) \cong \frac{b-a}{2}\sum_{i=1}^{n} w_i\, f\left(\frac{b-a}{2}x_i + \frac{b+a}{2}\right)$$

Weights and Abscissae Table for n = 5 (Pomax, 2011).

i	Weight - w_i	Absciss - x_i
1	0.5688888889	0.0000000000
2	0.4786286705	–0.5384693101
3	0.4786286705	0.5384693101
4	0.2369268851	–0.9061798460
5	0.2369268851	0.9061798460

For more n up to 64, see (Pomax, 2011).

NOMENCLATURE

A Surface area; m^2

F_{i-j} View factor between surfaces i and j

d Distance separating rows of the solar field; m

W Width of row of the solar field; m

L Length of the row of the solar field; mLatitude angle

Z_1 Width of the shadow zone; m

Z_2 Width of the unshaded zone; m

I_h Global horizontal solar irradiance; W/m^2

I_{bh} Beam horizontal solar irradiance; W/m^2

I_{dh} Sky diffuse solar irradiance on the horizontal surface; W/m^2

I_t Global tilted surface solar irradiance; W/m^2

I_f Global solar irradiance in the solar field; W/m^2

β Surface tilt angle

ψ Surface azimuth angle

ϕ Solar azimuth angle

α Solar altitude angle

L Length of the row of the solar field; mLatitude angle

θ_i Solar incident angle

θ_z Solar zenith angle

ρ Reflectivity

$\forall$ Shaded to total surface area ratio

Subscriptions:

g: Ground

s: Sky

g_1: ground shaded zone

g_2: ground unshaded zone

A_1: First row surface

A_2: Second row surface

A_{1r}: rear surface of the first row

iso: Isotropic sky analysis

aniso: Anisotropic sky analysis

frontiers | Frontiers in Energy Research

TYPE Review
PUBLISHED 07 October 2022
DOI 10.3389/fenrg.2022.971912

OPEN ACCESS

EDITED BY
Arijit Ganguli,
Ahmedabad University, India

REVIEWED BY
Robert Sekret,
Częstochowa University of Technology, Poland
Channamallikarjun Mathpati,
Institute of Chemical Technology, India

*CORRESPONDENCE
Maximilian Sporleder,
maximilian.sporleder@ieg.fraunhofer.de

SPECIALTY SECTION
This article was submitted to Process and Energy Systems Engineering, a section of the journal Frontiers in Energy Research

RECEIVED 17 June 2022
ACCEPTED 20 September 2022
PUBLISHED 07 October 2022

CITATION
Sporleder M, Rath M and Ragwitz M (2022), Design optimization of district heating systems: A review. *Front. Energy Res.* 10:971912. doi: 10.3389/fenrg.2022.971912

Design optimization of district heating systems: A review

Maximilian Sporleder[1,2]*, Michael Rath[1,3] and Mario Ragwitz[1,2]

[1]Fraunhofer Research Institution for Energy Infrastructures and Geothermal Systems IEG, Cottbus, Germany, [2]Department of Electrical and Thermal Energy Systems, Brandenburg University of Technology Cottbus-Senftenberg BTU, Cottbus, Germany, [3]Department of Civil and Environmental Engineering, Bochum University of Applied Science, Bochum, Germany

District heating systems offer the possibility of lowering emissions and support the goal of reaching a carbon-neutral energy system by integrating renewable heat sources. Therefore, this work provided a systematic literature review to identify potential research gaps and show the literature distribution over the relevant topics. The focus is on the design optimization with (non-)linear programming of district heating systems in the context of decarbonization. Furthermore, crucial energy balance equations were extracted from the literature for a potential optimization problem. The systematic literature review limited its search to two databases, 10 years timespan, a quality measure, and uses keywords regarding topic and method. Categories were derived based on the subject and literature to cluster the found publications and identify potential research gaps. The results showed potential research gaps in the depiction of different stakeholder decisions, reduction of computational efforts, and their resulting uncertainties. Additionally, they identified gaps in the integration of low-grade heat sources, thermal storage facilities, and energy converters, especially geothermal energy, large-scale heat pumps, and seasonal storages.

KEYWORDS

district heating, design optimization, linear programming, nonlinear programming, decarbonization, review

Introduction

Since the millennium, global climate change has shown devastating outcomes due to natural disasters. The integration of renewables in the energy system is essential to limit the enhancement of global climate change. District heating systems (DHS) would offer the possibility to enhance the integration of renewables if the system's design was optimized. In addition to global climate change, the independency of fossil fuels is more crucial than ever to European countries due to rising gas prices caused by the Ukrainian conflict (Global Conflict Tracker, 2022). Natural gas is an essential heat carrier in Europe, with a share of 36% gross heat generationin 2019 (DG Energy, 2020; European Commission, 2021b). Figure 1 illustrates the high dependency on fossil fuels in DHS in relation to net heat

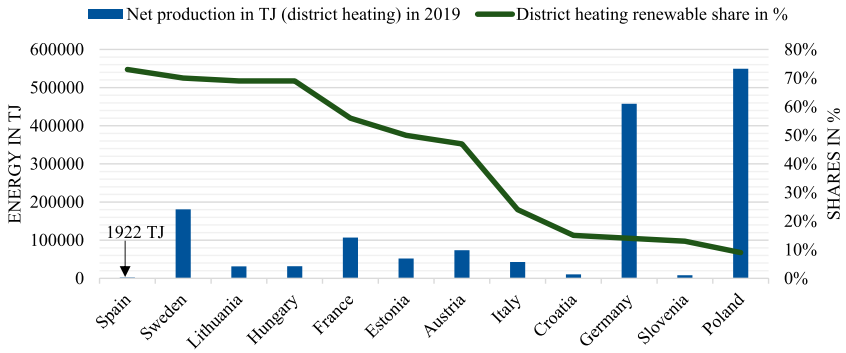

FIGURE 1
Renewable share and net heat production in DHS in dependency of some European countries in the year 2019 (European Commission, 2021a; Corscadden et al., 2021, p. 34, p. 34).

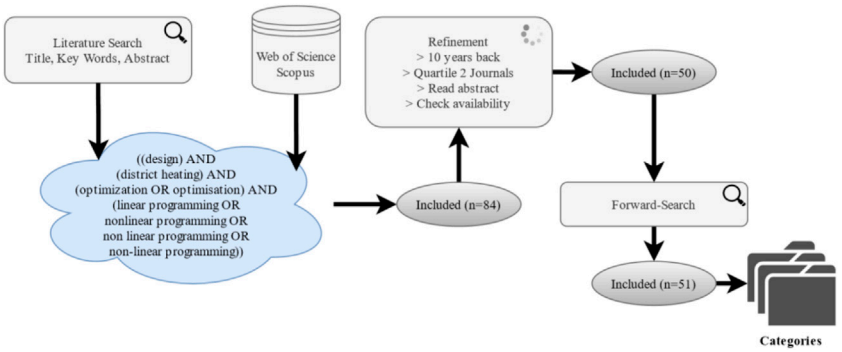

FIGURE 2
Summary of the methodology for the systematic literature review.

production. 66% of the net heat production was generated from less than 15% renewables[1]. Because of the increasing demand for the independency of natural gas and other fossil fuels, most countries will face a decarbonization process in the upcoming years. The heat supply in countries like Germany is at a temperature of 80–130°C. High temperatures further complicate the decarbonization process due to higher losses and decreasing efficiencies for renewable heat sources (Paardekooper et al., 2018; EnBW Company, 2021). Mathematical optimization is a commonly applied method to support planners and operators in transforming their DHS (Sameti and Haghighat, 2017). The optimization tries to find a mathematical minimum of a cost function designing energy converters, storages, pipes, or other components.

The field of optimization in DHS was reviewed by several researchers in the literature. The focus of those publications can be summarized as follows:

- Sameti and Haghighat (2017) discussed mathematical approaches on optimizing district heating and cooling systems in detail. The review described possible modeling techniques for energy conversion technologies or thermal storages and objective functions. The objectives minimized costs or CO_2 emissions. It gave a broad overview of optimization approaches in the literature, describing the method, the objective, and the type of installation (centralized, decentralized). The research was conducted in 2017. Therefore, our review focused on new topics with relevance, like the integration of renewable heat sources. In addition, we concluded the relevance or irrelevance of mathematical formulations for the grid.

1 Not all European countries are included due to the lack of data.

- Lake et al. (2017) reviewed case studies of district heating and cooling systems to identify the advantages and drawbacks of different energy sources. Furthermore, the publication reviewed energy policies to determine their influence on designing such systems. Additionally to Lake et al. (2017), we provided a literature distribution on the different technology solutions.
- Li et al. (2017) examined smart grids, energy storages, and the integration of renewable energy sources in optimizing district heating and cooling systems. The publication highlighted the conversion of energy, its distribution, heat transfer stations, terminal users, and approaches in the literature. In addition to Li et al. (2017), we contributed with a strong focus on DHS' design optimization.
- Mazhar et al. (2018) reviewed DHS's progress, focusing on technical configurations, regulations, and policies. The review identified an urgent need to expand DHS to accelerate the transformation process in the heating sector. Our work extended Mazhar et al.'s (2018) review by examining mathematical approaches with a strong focus on the grid.
- Olsthoorn et al. (2016) reviewed modeling and optimization approaches for integrating storage and renewable energy. Energy sources were classified depending on their sustainability and complexity of integration. The paper reviewed modeling approaches regarding computational time, detail level, and results certainty. In addition to Olsthoorn et al. (2016), we provided knowledge on equations for DHS.
- Paiho and Reda (2016) reviewed DHS in Finland and how they can possibly be transformed into a sustainable system. The review's focus was an overview of promising innovative and realistic technologies for integration into DHS. In addition, we identified research gaps in the literature for the design optimization of DHS.
- Sarbu et al. (2017) reviewed different optimization techniques for DHS and proposed a detailed optimization model focusing on the network's hydraulics. In addition, the authors presented the economics of DHS. We expanded Sarbu et al.'s (2017) work with different temperature models for the network based on the necessary level of detail.
- Sarbu et al. (2019) reviewed optimization and modeling techniques in DHS, discussing deterministic and heuristic optimization. Furthermore, they highlighted the numerical description of DHS and their components. The state-of-the-art was also categorized. We added a literature distribution over relevant technologies for the decarbonization process to Sarbu et al.'s (2019) work.
- Sarbu et al. (2020) provided an overview of DHS's optimization, focusing on heuristic methods. In addition, an optimization problem (single-objective and multi-objective) was formulated, and the criteria for optimizing DHS was described. Again, we complemented this work with a literature distribution over relevant technologies for the decarbonization process.

The literature reviews provided valuable knowledge in the field of optimizing DHS. In addition to the state-of-the-art, we conducted a systematic literature review (SLR) based on a generic and reproducible method. Our review was driven by the question *if the current optimization methods at hand can calculate a sustainable re-design of DHS facing a decarbonization process?* In conclusion, our contribution was a SLR on DHS's optimization focusing on their transformation process and identifying research gaps on the topic. Our scope is not only on the general design of DHS but on the method of linear programming. The SLR was explained in detail in the method section, and categories were derived for structuring the results. The result section followed, giving an overview of the found literature sorted into the categories. In the discussion section, major research gaps were identified. In the conclusion, the SLR's main findings were described to give an outlook for upcoming research.

Methods

The SLR was based on Webster and Watson (2002) and Jan vom Brocke et al. (2009). The scope of the literature review was a *sequential search* of *bibliographic databases* using a *comprehensive* set of techniques such as *keyword*, *backward search,* and *forward search* (vom Brocke et al., 2015). This method ensured transparency and reproducibility of the results. The methodology was divided into five steps: selecting the databases, creating the search string, searching (forward/backward), refining the results, and deriving categories. In Figure 2, the applied methodology was visualized.

The search was conducted on Scopus and Web of Science as they are one of the largest scientific databases, and they allowed the implementation of search strings in contrast to Google Scholar (Paperpile, 2012). The search string consisted of the field, the problem, and the method. The main research question focused on DHS; therefore, the field was identified as district heating. The problem was the DHS's design optimization to reach a carbon-neutral supply system. The literature usually formulated its problems as linear or nonlinear (Sameti and Haghighat, 2017). To conclude, the search string read (district heating) AND (optimization OR optimisation) AND (linear programming OR nonlinear programming OR non linear programming OR non-linear programming). The search resulted in 83 publications on the 22^{cd} of February 2022. This method does not exclude any regions or researchers. If a

publication was not selected, it would have been excluded by the chosen key words, the refinement, or it would not be available on the searched databases.

A quality measure refined the 83 publications quartile one and two in the year 2020—excluding 12 journals: mathematical problems in engineering, Computer aided chemical engineering, Journal of energy engineering, Journal of physics conference series, Chemical engineering transactions, WIT Transactions on ecology and environment, Chemical Product and Process, Environmental and Climate Technologies, Yingyong Kexue Xuebao/Journal of Applied Sciences, Nippon Kikai Gakkai Ronbunshu, C Hen/Transactions of the Japan Society of Mechanical Engineers, Part C, Nihon Enerugi Gakkaishi/Journal of the Japan Institute of Energy (SCImago, 2007).

Additionally, all publications published before 2012 were excluded to create comparability due to significant developments in computational time (Sameti and Haghighat, 2017). On top of that, ten publications[2] were excluded because the topic did not match the DHS's design optimization. Through the forward search, Krug et al. (2020) were included in the literature review due to their detailed model of the DHS in an optimization problem. In conclusion, 51 publications were selected to be reviewed in this article.

The categories clustered the 51 publications and enhanced a fast overview of the topic regarding the research question. In addition, it shows possible research gaps in the state-of-the-art. The categories were divided into nine supercategories: *system, objective, method, solver, computational time, the validity of results, consumer, grid,* and *supply structure*. Each of those supercategories consisted of subcategories to further describe the content of the literature. The arrangement and meaning of each category were explained in the results section, supported by figures illustrating the literature's distribution concerning the DHS's (re-)design optimization.

Results

The results section consisted of three subsections: District Heating System, Optimization, Modeling of District Heating Systems in Optimization, and Significant Findings of the Literature. In those subsections, the subcategories were derived, and the literature's distribution was displayed. In addition, standard approaches to the topic were explained. The considered literature was documented in Table 1. Figure 3 is an overview of the literature distribution based on the categories for method, unit type, technology, system, computational time, and objective. Due to the applied method, all publications provided knowledge on those supercategories except for measures of lowering computational time. The graphic showed that most publications dealt with small scale-systems using a mix of renewable and nonrenewable heat sources or energy converters that are centrally installed. Usually, the mathematical model was linear and optimized towards a single objective. In 40 publications, computational methods were applied to decrease the calculation time. The following sections provide a more profound knowledge of the categories and the publication's content.

District heating system

DHS transport heat through pipes to consumers. Usually, DHS have a forward-flow transporting heat from the production units to the consumers and a backward-flow transporting the fluid back to the production unit. Some DHS operate on temperatures over 90°C, while the 4th Generation of DHS operates below 60°C (Lund et al., 2021). If the forward-temperature is below 60°C, the warm water must be heated decentrally to prevent *legionella*. The 5th generation of DHS enables parallel cooling and heating. Consumers can extract or inject energy into the grid. In that case, consumers become prosumers (Wirtz et al., 2020). Therefore, the three subcategories of the *system* were *high temperature* > *90°C*, *medium temperature 60–90°C*, and *low temperature* < *60°C*.

The DHS's size influences the model complexity due to the need for spatial discretization (Sameti and Haghighat, 2017). Some DHS supply small districts, while others supply cities (Biedermann and Kolb, 2014). Therefore, *large-scale* and *small-scale system* were subcategories of the supercategory *system*. A system was considered small-scale if the problem was not spatially discretized or the optimization was performed over a few nodes. Furthermore, this work differentiated between real case studies and synthetic case studies.

About 70% of the literature used real case studies to support their model inputs. In Figure 3, most systems were small-scale: Bornand et al. (2020) derived an investment planning methodology and implemented it for a hospital site. This problem was categorized as small-scale due to the low number of nodes. The same category was set for Wirtz et al. (2021a) because the problem was not spatially discretized. In general, the temperature level was not always clearly identified; therefore, some methods can be applied to high- and medium-temperature systems. The vast majority of systems (~85%) covered by the literature are small-scale systems with temperatures over 60°C.

Optimization

Mathematical optimization is a tool to support decision-making processes, e. g. designing and operating energy systems

2 Excluded publications: Ryohei Yokoyama et al. (2016); Mojica et al. (2017); Wu et al. (2018); Sameti and Haghighat (2019); Alghool et al. (2020); Scolan et al. (2020); Campos et al. (2021); Halmschlager and Hofmann (2021); Liu et al. (2021); Neri et al. (2022).

TABLE 1 Publications from the SLR for the literature distribution.

Bartolini et al. (2018)	Best et al. (2020)	Blommaert et al. (2020)
Bordin et al. (2016)	Bornand et al. (2020)	Bracco et al. (2013)
Buoro et al. (2013)	Casisi et al. (2019)	Dancker et al. (2019)
Delubac et al. (2020)	Delubac et al. (2021)	Elsido et al. (2017)
Fazlollahi et al. (2015)	Fazlollahi et al. (2014)	Fitó et al. (2020)
Haikarainen et al. (2016)	Halmschlager et al. (2021)	Hirsch et al. (2016)
Khatibi et al. (2019)	Li and Svendsen, (2013)	Li et al. (2016)
Marguerite et al. (2013)	Marquant et al. (2017)	Mavromatidis and Petkov, (2021)
Mertz et al. (2017)	Mertz et al. (2016)	Morvaj et al. (2016)
Ommen et al. (2016)	Pantaleo et al. (2014b)	Pantaleo et al. (2014a)
Quaggiotto et al. (2021)	Renaldi et al. (2017)	Rieder et al. (2013)
Rieder et al. (2014)	Röder et al. (2021)	Schütz et al. (2018)
Stange et al. (2018)	Szypowski et al. (2019)	Unternährer et al. (2017)
van der Heijde et al. (2019)	Vian et al. (2020)	Walter et al. (2020)
Wang et al. (2021a)	Wang et al. (2021b)	Weinand et al. (2019)
Wirtz et al. (2019)	Wirtz et al. (2021a)	Wirtz et al. (2020)
Yılmaz Balaman and Selim, (2016)	Zhang et al. (2021)	—

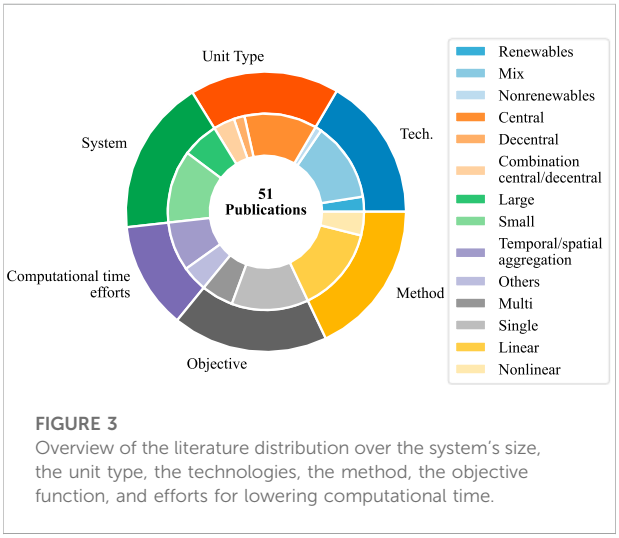

FIGURE 3
Overview of the literature distribution over the system's size, the unit type, the technologies, the method, the objective function, and efforts for lowering computational time.

(Sameti and Haghighat, 2017). Mathematically, "optimization" means the determination of the maximum or minimum of a function f. In the literature, the function inherited economic, technical (exergy), social, or ecologic factors and was defined on a (restricted) domain S or state space. Classic optimization theory deals with cases where S is coherent, and the function f is optimized and continuous. The function f was also called the objective function in the optimization environment. The pending decisions (e.g., investments or dimensions of energy converters) were linked to the degrees of freedom of the problem. In an optimization model, variables represented degrees of freedom (e.g., the storage volume). The optimization algorithm assigned values to the variables resulting in the objective function's optima reflecting the consequences of the decisions.

$$\mathrm{Min}\left\{ f(x,y) \middle| \begin{matrix} h(x,y)=0 & x\in\mathbb{R} \\ g(x,y)\geq 0\,, & y\in\mathbb{R} \end{matrix} \right\} \tag{1}$$

is a generic objective function with $h(x,y)$ representing the equality and $g(x,y)$ the inequality constraints. Various factors influenced the objective value in the literature, e. g. subsidies for CO_2 lowering measures. The design optimization was usually performed over a given time period τ, optimizing the variables at every timestep t (Delubac et al., 2020). The objective function usually consisted of capital expenditures (CAPEX) and operational expenditures (OPEX). For example, the CAPEX could depend on the installed capacity for production units or the installed length of a pipe. The OPEX was often divided into fixed and variable costs. The variable costs usually depend on the operation power multiplied by specific costs, e.g., gas price for a gas boiler. The fixed OPEX depended on the nominal heat and the device, usually including costs for controlling devices, maintenance, and repair. Further information concerning costs for components in a DHS can be found in VDI 2067 or Steinbach et al. (2020). (Kallrath, 2013, pp. 1–2; Khatibi et al., 2019; Steinbach et al., 2020)

The depiction of different objectives in mathematical optimization was achieved *via* three methods. The first one was the introduction of a boundary for a variable, e.g., for CO_2 emissions. Nevertheless, introducing a boundary constraint is not a multi-objective problem (Gurobi, 2018). Bornand et al. (2020) used the supplementary ε-constraint with a key performance indicator (here CO_2-emissions) to generate n different solutions for Eq. 1 with

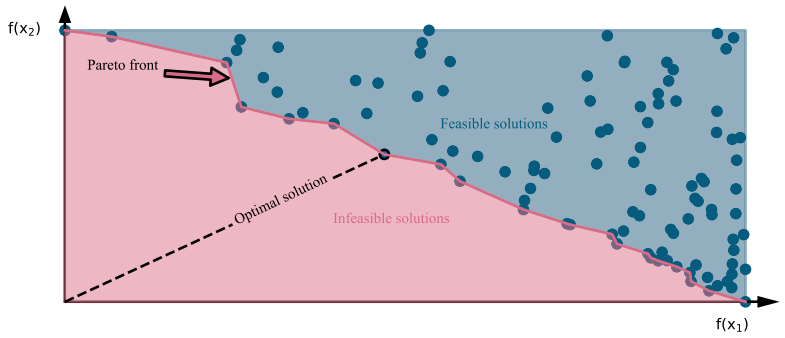

FIGURE 4
Qualitative graph of a Pareto front for a multi-objective optimization with two objective functions, f (x_1) and f (x_2).

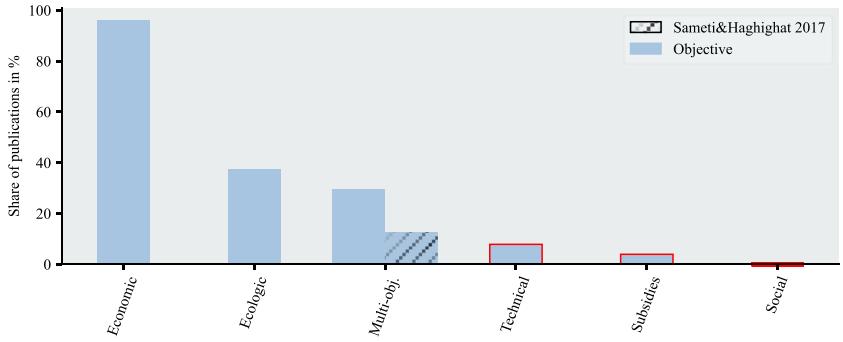

FIGURE 5
Literature distribution for the supercategory objective with a comparison of multi-objective with (Sameti and Haghighat, 2017); low numbers of publications are marked red as an indication of a potential research gap.

$$\left\{KPI \le \varepsilon_i \middle| \varepsilon_i = KPI_{\min} + i\frac{KPI_{\max} - KPI_{\min}}{n-1} \right. \\ \left. for\, i \in [0, n-1]\right\}, \tag{2}$$

where the parametric boundary ε_i is gradually increased.

The second method formulated two separate objective functions, e.g., for costs and CO_2 emissions (Fazlollahi et al., 2015). The solver then forms a Pareto front of the optimal solutions depending on the objective functions. The Pareto front is the border between feasible and infeasible solutions. All solutions on the Pareto front are optimal. Figure 4 illustrates the solution space of two objective functions. The point of intersection is the minimum for both functions. The optima considering both functions' objectives is the solution (dashed line in Figure 4) with the shortest distance to the point of intersection.

The third method used a weighted-sum function, e. g. including CO_2 costs in the objective function (Sameti and Haghighat, 2017). Based on the influential factors for the objective and the possibility of multi-objective optimization, the subcategories *ecologic, technical, economic, social, subsidies,* and *multi-objective* were derived for the *objective*.

Figure 5 shows the distribution over the subcategories for *objective*. Schütz et al. (2018) considered subsidies for combined heat and power plants (CHP) to exploit total nominal power for CHP plants until a nominal limit is reached. Only two publications in total considered subsidies. Technology subsidies are often regionally limited; therefore, their publication does not significantly impact the international community. The influence of social factors on the objective had not been viewed at all.

Most publications (>95%) used a cost function as their objective. Some publications (~40%) combined the cost function with ecologic factors, e.g., limitation of CO_2 emissions (Walter et al., 2020) or multi-objective optimization (Mavromatidis and Petkov, 2021). The application of multi-objective optimization doubled (12.5% vs. 29.4%) relative to the samples taken by Sameti and Haghighat (2017).

As explained and shown in Figure 4, the constraints define the solution space for the objective function. The constraints can

be formulated linearly and continuously (referred to as linear programming–LP), linearly and non-continuously (referred to as mixed-integer linear programming–MILP). Nonlinear problems can be formulated nonlinearly and continuously (referred to as nonlinear programming–NLP), or nonlinearly and non continuously (referred to as mixed-integer nonlinear programming–MINLP) (Kallrath, 2013). The decision to formulate the optimization depends on the task and the time at hand. In general, nonlinear problems can depict physical systems more in detail–e.g., modeling temperature gradients along a pipe segment (Krug et al., 2020)—but require higher computational time. Mixed-integer variables were often used for control strategies in energy systems (on/off) or designing components (Elsido et al., 2017). The introduction of those variables causes increased computational time as well. Mixed-integer variables were commonly used to design DHS (Sameti and Haghighat, 2017); therefore, the category *method* only consisted of the subcategories *linear* and *nonlinear*.

Besides the problem formulation, the solver can also influence the computational time. It can be distinguished between classic optimization (mathematical programming) and soft computing (heuristics and metaheuristics). However, this work focused on classic optimization because most energy system optimizations applied this method (Sameti and Haghighat, 2017). Therefore, most publications used global solvers such as cplex, gurobi, or ipopt (open-source) (Sameti and Haghighat, 2017). Nevertheless, some publications solved problems with heuristic solvers such as NSGA-II (van der Heijde et al., 2019).

The significant difference is that a heuristic solver can quickly find a solution; however, might be a local minimum and not a global one (Silveira et al., 2021). Silveira et al. (2021) suggested that heuristic solvers were better suited for large-scale systems. The category *solver* contained *global* and *heuristic* as subcategories.

Some problems required too much computational effort independent of the solving method. If that was the case, measures were considered to reduce the problem. The aggregation of space and time was one of those measures, e.g., one year is represented by a few days (van der Heijde et al., 2019), or two buildings were aggregated to one. Another measure decomposed the problem into several stages (Mavromatidis and Petkov, 2021). Based on the efforts to reduce computational time, the category *computational time* consisted of *time aggregation*, *spatial aggregation*, *staged process/decomposition*, and *others*.

Applying measures to reduce the computational time, simplifying the mathematical formulation of the physical system, or having uncertainties in the input data always caused errors. The technical validity of the results can be ensured by performing a detailed simulation after the optimization (Quaggiotto et al., 2021). Dealing with uncertainties in the input data can be done with a sensitivity analysis to examine the influence of inputs on the results. A more sophisticated approach would be a Monte Carlo method; however, that requires additional knowledge of the inputs and enormous computational power (Kausche, 2018, pp. 71–77). Therefore, the category *validity of results* consisted of *simulation*, *sensitivity analysis/scenarios*, and *uncertainties*.

Figure 6 shows the literature distribution for the mentioned supercategories. The figure compares Sameti and Haghighat's (2017) results for the method and the solver. The results indicate that the optimizations of nonlinear problems using heuristic solvers had declined; however, this SLR was applied from 2012 until 2022. In addition, the search string included linear and nonlinear programming that might have excluded publications using heuristic solvers.

Most publications (~80%) formulated a linear programming model and solved it with a global solver (~90%). Computational efforts were mostly (~30%) reduced by time series aggregation. Elsido et al. (2017) used a two-stage process to solve a MINLP problem. Other methods were the relaxation of constraints. This method was applied by Krug et al. (2020), resulting in decreased computational time. Most of the viewed literature (~80%) validated their results with different scenarios or a sensitivity analysis. The technical validation of results with a detailed simulation or an uncertainty analysis for the input data was rarely performed in the literature.

Modeling of district heating systems in optimization

Equations

A DHS consists of consumers, production units, and the grid transports the heat, as shown in Figure 7. The modeling of DHS was divided into several energy balances for consumers (marked lilac), production units (marked red), pipes, and nodes (marked grey and blue). For a better understanding, equations for these energy balances were explained (see Table 2 for symbols). All equations used in the literature assumed incompressibility with a constant density over space and time and constant velocity over space (Krug et al., 2020). Furthermore, the following equations assumed that the flow directions are known. Krug et al. (2020) derived an approach to solving the problem of unknown flow directions. The constraints were initialized through a node set with $V = [1, \ldots, 8]$ and a pipe set with $\gamma = [12, 23, 34, 41, 56, 67, 78, 85]$ (Krug et al., 2020). The following equations excluded boundary constraints.

The consumer balance can be modeled temperature-dependent (Krug et al., 2020) or independent with (Schütz et al., 2018)

$$\frac{\dot{Q}_{i,t}}{\mu} = \dot{Q}_{i,t}^{\text{in}} - \dot{Q}_{i,t}^{\text{out}} = \dot{m}_{i,t} c_{\text{p}} \left(T_{i,t}^{\text{in}} - T_{i,t}^{\text{out}} \right) \quad for\, t \in \tau,\ i \in [a, b, d], \tag{3}$$

where for the independent case $\dot{Q}_{i,t}^{\text{in}}$ flowed from the forward-flow node into the consumer i and $\dot{Q}_{i,t}^{\text{out}}$ flows from the consumer i into

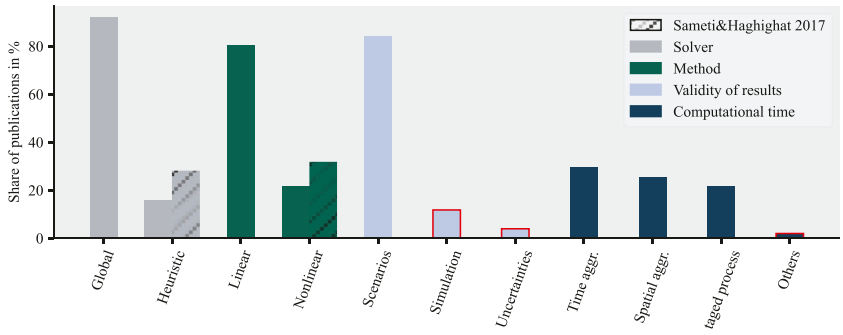

FIGURE 6
Literature distribution over the supercategories method, solver, computational time, and validity of results with comparison to (Sameti and Haghighat, 2017); low numbers of publications (<15%) are marked red as an indication of a potential research gap.

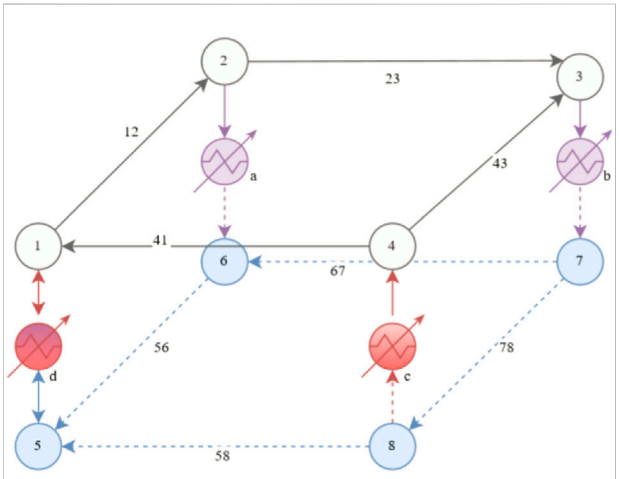

FIGURE 7
Exemplary DHS with two consumers–node 2 and 3—one production unit–node 4—one prosumer–node 1 (Krug et al., 2020).

the backward-flow node. The right part of the equal sign was temperature-dependent, and models $\dot{m}_{i,t}$, $T^{\text{in}}_{i,t}$ and $T^{\text{out}}_{i,t}$ as variables resulting in a nonlinear constraint. μ represents the efficiency of the transfer station. With the development of new DHS in the 5th generation, prosumers were modeled in the literature for an efficient design. In Figure 7, at node 1, a prosumer was depicted, which can consume or convert energy. The left-hand side of Eq. 3 would transform to $\frac{\dot{Q}^{\text{con}}_{i,t}}{\mu} - \dot{Q}^{\text{pro}}_{i,t}\,\mu$ with $\dot{Q}^{\text{pro}}_{i,t}$ representing the converted energy at the prosumer (Wirtz et al., 2020). The concept of prosumers was a subcategory for the supply system as decentral.

The mass balance in the nodes was given by (Baehr and Kabelac, 2006, p. 85, p. 85)

$$\sum_{i\in\delta^{\text{in}}(u)} \dot{m}_{i,t} = \sum_{i\in\delta^{\text{out}}(u)} \dot{m}_{i,t} \quad for\, t \in \tau,\, u \in V, \tag{4}$$

where $\delta^{\text{in}}(u)$ was a set describing pipes, consumers, or production units entering the node u.

The fluid left the node with a mixing temperature $T^{\text{mix}}_{u,t}$ (Krug et al., 2020) given by

$$T^{\text{in}}_{i\,\in\,\delta^{\text{out}}(u),t} = T^{\text{mix}}_{u,t} = \frac{\sum_{i\in\delta^{\text{in}}(u)} \dot{m}_{i,t} T^{\text{out}}_{i,t}}{\sum_{i\in\delta^{\text{in}}(u)} \dot{m}_{i,t}} \quad for\, t \in \tau, u \in V, \tag{5}$$

where $T^{\text{in}}_{i\,\in\,\delta^{\text{out}}(u),t}$ refers to the temperature entering pipe i and leaving node u. If temperatures were neglected, Eq. 5 would be irrelevant. The energy balance in the nodes was given by (Baehr and Kabelac, 2006, p. 85, p. 85)

$$\sum_{i\in\delta^{\text{in}}(u)} \dot{Q}^{\text{out}}_{i,t} = \sum_{i\in\delta^{\text{out}}(u)} \dot{Q}^{\text{in}}_{i,t} \quad for\, t \in \tau,\, u \in V, \tag{6}$$

where $\dot{Q}^{\text{out}}_{i,t}$ left the pipe i and entered node u.

The thermal energy balance at production units was modeled analogously to Eq. 3 (Krug et al., 2020), with

$$\dot{Q}_{i,t}\mu = \dot{Q}^{\text{out}}_{i,t} - \dot{Q}^{\text{in}}_{i,t} = \dot{m}_{i,t} c_{\text{p}} \left(T^{\text{out}}_{i,t} - T^{\text{in}}_{i,t}\right) \quad for\, t \in \tau,\, i \in [c], \tag{7}$$

where $\dot{Q}^{\text{in}}_{i,t}$ flowed from the backward-flow node 4 into the production unit and $\dot{Q}^{\text{out}}_{i,t}$ flowed from the production unit into the forward-flow. The equations for the optimization were formulated positively; therefore, the signs changed (Wirtz et al., 2019). $\dot{Q}_{i,t}$ can calculate the operation of the production unit at node 4. Further information on thermal storage equations can be found in van der Heijde et al. (2019).

In the design optimization of DHS, the capacity of production units was a crucial variable to be optimized due to high investments (Steinbach et al., 2020). The investment curve for technologies usually behaved nonlinearly. A solution to model nonlinear functions in a MILP or LP problem is

TABLE 2 Declarations of symbols with variables in the top and parameters in the bottom.

Symbol	Explanation	Unit
b_i	Buying decision as binary variable of technology i	—
C_i	Capex for technology i	€
$\dot{m}_{i,t}$	Mass flow in component i at timestep t	kg s^{-1}
$\Delta p_{i,t}$	Pressure difference in component i at timestep t	Pa
$\dot{Q}_{i,t}$	Heat flow in component i at timestep t	W
$\dot{Q}_i^{\mathrm{nom}}$	Heat flow of component i	W
$\dot{Q}_{i,t}^{\mathrm{in}}$	Heat flow into component i at timestep t	W
$\dot{Q}_{i,t}^{\mathrm{out}}$	Heat flow leaving component i at timestep t	W
$T_{i,t}^{\mathrm{in}}$	Temperature entering component i at timestep t	K
$T_{i,t}^{\mathrm{out}}$	Temperature leaving component i at timestep t	K
$T_{u,t}^{\mathrm{mix}}$	Mixing temperature in node u at timestep t	K
$v_{a,t}$	Velocity at timestep t	m s^{-1}
$\omega_{i,j} \in [0, 1]$	Auxiliary variable for component i and investment point j	—
A_i^{m}	lateral surface of pipe i	m^2
c_{p}	Specific heat capacity	J kg^{-1} K^{-1}
$C_{i,j}^{\mathrm{points}}$	Points of investment curve for technology i	€
D_i	Diameter of pipe i	m
g	Gravitational force	N
h_i	Height difference of two pipes i	m
KPI	Key performance indicator	—
KPI_{max}	Max. of the key performance indicator	—
KPI_{min}	Min. of the key performance indicator	—
L_i	Length of pipe i	m
m_i	Mass of pipe i	kg
$\dot{Q}_{i,t}^{\mathrm{loss}}$	Static heat flow loss of component i	W
$\dot{Q}_i^{\mathrm{nom,\,max}}$	Max. nominal heat flow of technology i	W
$\dot{Q}_i^{\mathrm{nom,\,min}}$	Min. nominal heat flow of technology i	W
Δt	Length of one timestep in optimization	s
T_t^{soil}	Temperature of the soil at timestep t	K
U_i	Heat transfer coefficient of pipe i	W m^{-2} K^{-1}
λ_i	Friction factor of pipe i	—
ρ	Density of the system's fluid	kg·m^{-3}
ε_i	supplementary ε-constraint	—

Special Ordered Set 2 (SOS2) (Williams, 2013). For the investment curve of a technology i, a table with N points for nominal power $\dot{Q}_{i,j}^{\mathrm{nom}}$ and investment $C_{i,j}^{\mathrm{points}}$ needed to be given. Assuming (Wirtz et al., 2019)

$$\dot{Q}_i^{\mathrm{nom}} \geq \dot{Q}_{i,t} \quad for\, t \in \tau, i \in [c], \tag{8}$$

where $\dot{Q}_i^{\mathrm{nom}}$ was the variable for the nominal heat flow. Auxiliary variables were introduced to calculate the correct investments for the technology with (Wirtz et al., 2019)

$$b_i \dot{Q}_i^{\mathrm{nom,\,min}} \leq \dot{Q}_i^{\mathrm{nom}} - (1 - b_i)\dot{Q}_i^{\mathrm{nom,\,max}} \leq \sum_{j \in N} \dot{Q}_{i,j}^{\mathrm{nom}} \omega_{i,j}, i \in [c], \tag{9}$$

where $\dot{Q}_i^{\mathrm{nom,\,min\,/\,max}}$ represented the upper and lower boundary for the production unit and b_i its buying decision. Eq. 9 calculated the auxiliary variables with the condition $b_{i \in [c]} = \sum_{j \in N} \omega_{i \in [c],j}$ passed into

$$C_{i \in [c]} = \sum_{j \in N} C_{i,j}^{\mathrm{points}} \omega_{i,j}. \tag{10}$$

$\sum_{i \in [c]} C_i$ was implemented in the objective function for the CAPEX of all production units. SOS2 was applied so that two neighboring auxiliary variables can be two at most (Williams, 2013). This methodology can be used to design other components of the DHS. (Wirtz et al., 2019)

The thermal energy balance of the pipes can be modeled with different degrees of freedom. The first degree was only to model the heat flow with (Weinand et al., 2019)

$$\dot{Q}_{i,t}^{\text{in}} - \dot{Q}_{i,t}^{\text{out}} - \dot{Q}_{i,t}^{\text{loss}} = 0 \quad for\, t \in \tau,\, i \in \gamma, \tag{11}$$

where $\dot{Q}_{i,t}^{\text{in}}$ was the heat flow entering pipes, $\dot{Q}_{i,t}^{\text{out}}$ leaving the pipes and $\dot{Q}_{i,t}^{\text{loss}}$ were the losses of the pipes. Another approach was to model losses in dependency on the temperature inside the pipe and the soil temperature with (Quaggiotto et al., 2021)

$$c_{\text{p}} m_i \frac{T_{i,t-1}^{\text{out}} - T_{i,t}^{\text{out}}}{\Delta t} + \dot{Q}_{i,t}^{\text{in}} - \dot{Q}_{i,t}^{\text{out}} - U_i A_i^{\text{m}} \left(T_{i,t}^{\text{out}} - T_t^{\text{soil}}\right) = 0 \quad for\, t \in \tau,\, i \in \gamma. \tag{12}$$

The first term of the equation described the storage capacity of the grid. The last term represented the thermal losses influenced by the pipe's surface A_i^{m}, the soil temperature T_t^{soil}, and the heat transfer coefficient U_i. The heat transfer coefficient was estimated based on the material and diameter of pipe and insulation (Nussbaumer et al., 2018). Some publications based their thermal losses on empirical calculations (Wirtz et al., 2021b). Eq. 12 can be rewritten by applying the first law of thermodynamics such as (Krug et al., 2020)

$$c_{\text{p}} m_i \frac{T_{i,t-1}^{\text{out}} - T_{i,t}^{\text{out}}}{\Delta t} + m_{i,t} c_{\text{p}} \left(T_{i,t-1}^{\text{in}} - T_{i,t}^{\text{out}}\right) - U_i A_i^{\text{m}} \left(T_{i,t}^{\text{out}} - T_t^{\text{soil}}\right) = 0 \quad for\, t \in \tau,\, i \in \gamma. \tag{13}$$

Eq. 13 increased the degree of freedom for the optimizer, and the optimization problem became nonlinear. This additional degree of freedom allowed the calculation of the mass flow $\dot{m}_{i,t}$ inside the pipe and the entering temperature $T_{i,t}^{\text{in}}$. To cluster the literature based on their temperature model, Eq. 11 represented the category *heat flow*, Eq. 12 the category *simple temperature model*, and Eq. 13 the category *detailed temperature model*.

The heat transport along a pipe was realized by generating pressure at the production units. In the literature, the modeling of hydraulics in a pipe differed from completely neglecting them (Szypowski et al., 2019) to pressure models based on the 1d momentum equation with the simplification of $\frac{d\rho}{dt} = \frac{d\rho}{dx} = \frac{dv}{dx} = 0$ (Krug et al., 2020)

$$\Delta p_{i,t} = L_i \rho \frac{v_{i,t} - v_{i,t-1}}{\Delta t} + g \rho h_i + L_i \lambda_i \frac{v_{i,t} v_{i,t} \rho}{2 D_i} \quad for\, t \in \tau,\, i \in \gamma, \tag{14}$$

where the first term on the right-hand side represented the pressure loss due to the velocity differences between timesteps t and $t-1$, and the second term represented the pressure delta due to height differences between the end and start of the pipe segment. The third term mathematically described the pressure losses due to friction. The pressure losses over a consumer can be attributed to the mass flow.

The hydraulic balance in the network can be described by Kirchhoff's circuit laws given by (Serway, 2004)

$$\sum_{i \in \gamma} \Delta p_{i,t} + \sum_{i \in [a,b,d]} \Delta p_{i,t} = \sum_{i \in [c]} \Delta p_{i,t} \quad for\, t \in \tau, \tag{15}$$

where $\Delta p_{i,t}$ had to be realized with (Krug et al., 2020)

$$P_{i,t}^{\text{pump}} \mu = \frac{\Delta p_{i,t} \dot{m}_{i,t}}{\rho} \quad for\, t \in \tau,\, i \in [c]. \tag{16}$$

Eq. 14, Eq. 15, and Eq. 16 represented the subcategory *pressure model*. The velocity along the pipe can be limited in dependency of a max. pressure loss along the pipe, avoiding nonlinearities (~200 Pa m^{-1} (Nussbaumer et al., 2018, p. 13). The subcategory–*hydraulic boundaries*–represented the fixed pressure loss.

Literature distribution

Modeling of DHS in optimization was divided into the supercategories *consumer, grid, and supply structure*. High demanding temperatures by consumers challenge the decarbonization process (Biedermann and Kolb, 2014). Therefore, *temperature* and *refurbishment* were subcategories of *consumer*. The *demand* was identified as the most crucial parameter in the design optimization of DHS; consequently, it was used in every publication of the SLR. The temperature is considered for half of the publications. Currently, refurbishment is an underrepresented topic, with only one publication.

Efficient transport of heat technically and economically[3] depends on the design of the grid. Therefore, the supercategory *grid* had *design, change of temperature level, combination of grids, and deconstruction* as subcategories for the output. Paardekooper et al. (2018) projected an increasing share of district heating in buildings from 12% in 2015 to 50% in 2050. Besides infrastructural changes, the temperature level is an influential factor in the decarbonization of DHS. This influence is caused by the high-temperature dependency of heat pumps and their limit of a potential temperature lift which is given by the Carnot efficiency (Arpagaus et al., 2018):

$$\mu^{\text{Carnot}} = \frac{T^{\text{supply}} - T^{\text{source}}}{T^{\text{supply}}} \rightarrow COP = \frac{1}{\mu^{\text{Carnot}}}. \tag{17}$$

Heat pumps were projected to integrate environmental heat sources (Paardekooper et al., 2018, p. 12). The complexity and mathematical formulation of the grid modeling varied in the literature depending on the research question, as shown in the equation section. The grid can be modeled as one node with a given efficiency (Wirtz et al., 2019) or with nodes and edges spatially discretized, as shown in Figure 7 (Krug et al., 2020).

3 The specific investments for a grid can typically be approximated with 700 €/m (year 2020 in Germany) Steinbach et al. (2020).

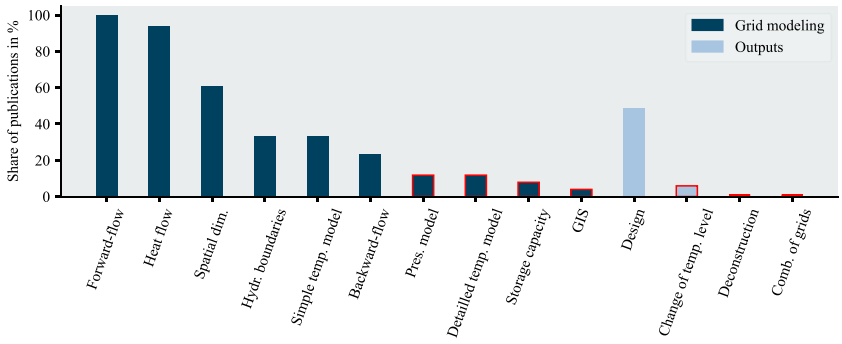

FIGURE 8
Literature distribution for the supercategory grid and the sublevels grid modeling and output; low numbers of publications (<15%) are marked red as an indication of a potential research gap.

For larger systems, geoinformation systems (GIS) can be a helpful tool to support planers in the design process of DHS (Bill, 2010; Weinand et al., 2019). In general, GIS are information systems that support the analysis, caption, editing, organization, and presentation of spatial data (Bill, 2010). Another important modeling element is the grid's water inertia (or storage capacity) (Wirtz et al., 2021b). Some publications modeled the forward-flow (grey lines in Figure 7) and the backward-flow (blue dashed lines in Figure 7) (Krug et al., 2020), while others neglected the backward-flow of the grid (Weinand et al., 2019).

Figure 8 shows that in the grid modeling, some subcategories were underrepresented (>12%) in the literature: *GIS, storage capacity, detailed temperature modeling,* and *pressure modeling*. A *spatial dimension* was used in 60% of the publications, and the *forward-flow* was modeled in every publication. Some publications focused on the hydraulics of the DHS causing the neglection of the *heat flow* in the grid (Li and Svendsen, 2013). The *design* of DHS was considered in half of the publications. The change of temperature level was viewed three times, and the combination of grids or infrastructural deconstruction was never content of the published work.

Besides the grid, the *supply structure* is crucial in the decarbonization process for DHS. Paardekooper et al. (2018) suggested a combination of DHS and individual *heat pumps* as decentral solutions for more minor dense. Therefore, this work differentiated between *central* and *decentral* units (Sameti and Haghighat, 2017). In general, the heat roadmap Europe projected a more versatile system for DHS in the future. A potential system would consist of *geo-* and *solar-thermal* heat, Power-to-Heat (*PtH*) technologies, *large-scale heat pumps*, *biomass boiler*, *CHP*, and *excess heat*. Furthermore, it was shown that CHP and large-scale heat pumps would cover 45–65% of the demand. Boilers were projected to cover peak demands up to 10% over the year. The storage capacities further increased the system's flexibility to react to the electricity market. It was differentiated between *short-term storages* and *long-term* or seasonal *storages* in the subcategories (Paardekooper et al., 2018, pp. 10–13).

Due to the high dependency on fossil fuels in Europe, with 40.1% in 2020 (Corscadden et al., 2021, p. 34), *fossil boiler* was another subcategory of the supercategory *supply structure*. Furthermore, the connection to the electricity market is given by sector-coupling technologies such as mainly CHP and heat pumps. The combination of photovoltaic cells (*PV*) and PtH technologies further increased the efficiency of the system. In addition, *fuel cells* were considered a subcategory for the SLR because they are sold for household solutions by companies like Viessmann (Rosenkranz, 2020). Regarding the modeling of storage and energy converters, *heat flow* and *temperature dependency* were subcategories of the *supply structure*. The output of the supply structure was represented by the *design*, *deconstruction*, *operation,* and *location*.

Figure 9 illustrates the literature distribution over technology types, installations, and output. The literature focused more on central units than on decentral units. Individual heat pumps (~40%), fossil boilers (~60%), CHP (~60%), and short-term storages (~65%) can be identified as one of the essential solutions in the literature. Solar thermal (~20%), PtH (~20%), biomass boilers (~20%), excess heat (~20%), and PV (~27%) were in the mid-range. In contrast, geothermal energy (~10%), large-scale heat pumps (~4%), fuel cells (0%), and long-term storages (~1%) were underrepresented. The operation of production units was in 92% part of the research, while the design decision was in 75% of the publications part of the undergone research. The location of the production units was optimized in about 20% of the literature, and deconstruction was never part of the optimization.

Significant findings of the literature

This section gathers crucial findings and results of the discussed literature. The findings divide into technical findings regarding technologies and methodologies. The citation

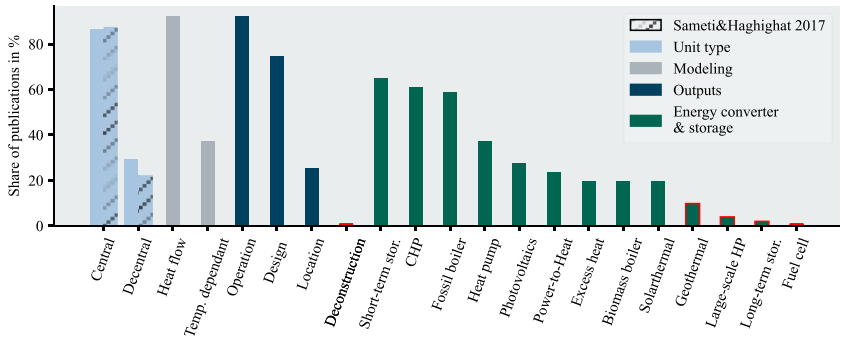

FIGURE 9
Literature distribution over the supercategory supply structure and the subcategories unit type, energy supply, modeling, outputs, and a comparison regarding the unit type with (Sameti and Haghighat, 2017); low numbers of publications (<15%) are marked red as an indication of a potential research gap.

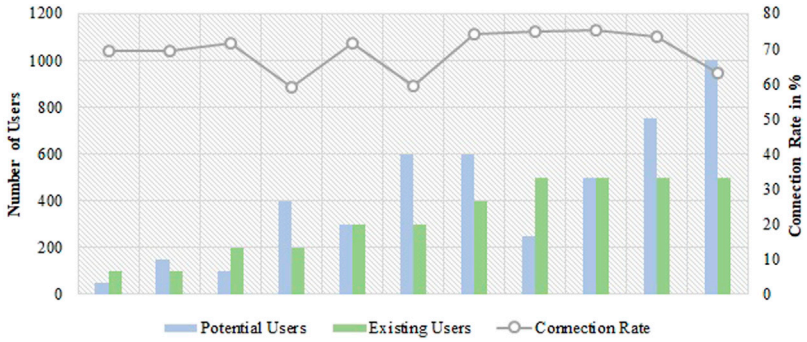

FIGURE 10
Sample of the distribution for connecting to the grid in dependency of the ratio potential vs. existing users; the capacity for the supplying plant was assumed as very high (Bordin et al., 2016).

frequency has been used to filter literature with the most significant impact on the scientific community.

The grid extension is crucial for grid operators and planners because infrastructural changes are connected to high costs. Bordin et al. (2016) developed a planning tool to address grid expansion changes. They assumed static conditions for the hydraulics, and the decision to connect a new consumer to the grid was dependent on the length and diameter of the pipe. The objective is to maximize the net profit consisting of investments for grid expansion and the cash flow. The computational time rised with the increase of potential users. For the biggest test case—1,000 potential users and 500 existing users–the model was solved in 29 s. While for 100 potential and 100 existing users, the solution was reached in less than a second.

Figure 10 illustrates the connection rate depending on the ratio of potential and existing users. The connection rate was generally high, between 60% and 80%. If the number of potential users were assumed to be twice as high as the existing users, the connection rate would decrease. Bordin et al. (2016)focused on grid expansion setting general rules for the physical description of the system. The focus was less on the technology selection and sizing but on infrastructural decisions providing a valuable expansion algorithm.

Compared to Bordin et al. (2016), Morvaj et al. (2016) also considered decisions for designing energy converters and storages besides the expansion of the grid. Consumers could either supply themselves or connect to the DHS. The viewed technologies were gas boilers, PV, CHP, and thermal storages. The examined system is relatively small, allowing for a more detailed approach. Binary decision variables were used for infrastructural decisions, design decisions, and controlling CHP plants. The optimization runs were divided into different scenarios with different carbon emissions limitations. The buildings were operated as prosumers, and the greenfield scenario's connection rate was exceptionally high. They were able to decrease carbon emissions by 33%, and the greenfield

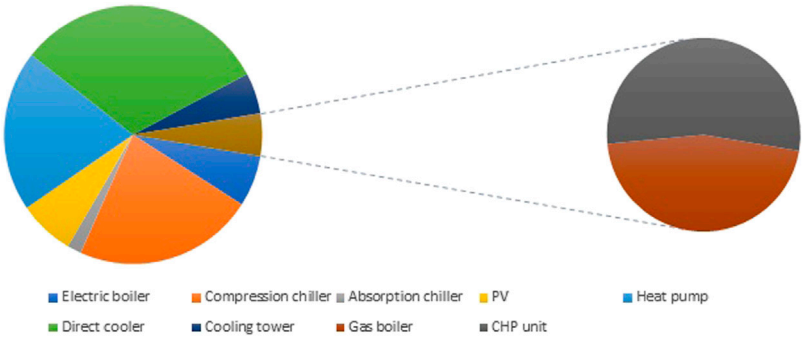

FIGURE 11
Distribution of the total capacity across the dimensioned technologies with separat focus on gas-based technologies from Wirtz et al. (2020).

scenario–all technologies were available–resulted in the best case for carbon emissions and costs.

Furthermore, it was highlighted that the electric grid modeling was neglected. This neglection might cause instability if consuming or producing technologies are connected to the electric grid without representation. With an increase in carbon emissions, the connection rate and the use of PV decreased. These results showed that for decarbonizing DHS.

- modeling the grid combined with the supply system affects the design of the grid,
- decentralized units gain more importance with a higher share of renewables,
- thermal grid-connected energy becomes crucial for decarbonized thermal systems,
- sector-coupled DHS requires a representation of the electric grid.

Bracco et al. (2013) optimized a four-node system consisting of a residential complex, a swimming pool, a school, and a city hall. The objective was the optimal connection between the nodes and the design and operation of gas engines, boilers, and turbines. The mathematical model is based on energy balances between the buildings and the grid. They reduced the primary energy consumption and emissions by 43% and the costs by 47%. The system was gas-based, and the gas turbine was used as a base load while the gas boilers were utilized during peak demands.

Compared to Bracco et al. (2013), Wirtz et al. (2020) vastly increased the technology variety and optimized a bidirectional low-temperature network. The network could supply heating and cooling energy to the connected consumers. The energy was provided in an energy hub, and the mathematical model describes the system with energy balances. The residential building also provided decentral units. The technologies in the energy hub were gas boiler, CHP unit, electric boiler, compression chiller, absorbtion chiller, cooling tower, and PV. The technologies in the buildiing were heat pump, electric boiler, compression chiller, direct cooler, and a cooling tower. Figure 11 illustrates the results for the technologies' capacities in Wirtz et al. (2020). Most publications before 2017 based their energy supply on gas being quite the contrary in Figure 11.

Discussion and identification of research gaps and potential developments

The results already showed potential research gaps in the literature, and the comparison with Sameti and Haghighat (2017) identified potential trends and developments in the design optimization of DHS. One major trend was using multi-objective optimization with economic and ecologic factors. Social factors did not influence the optimization outcome in the viewed literature and can be identified as a potential research gap. In addition, economic decisions by end-consumers were never part of the optimization, even though multi-objective optimization would give the possibility to depict several decisions. One scenario could be the decision for a consumer to connect its building to the grid for a given heat price vs. an individual solution as one objective and the cost-efficient design and operation of the DHS as the second objective for the grid operator. The depiction of this conflict of interest could be of high relevance for designing the grid.

With the increasing demand for multi-objective optimization, the demand for faster computing is increasing simultaneously. Methods like time series aggregation were gaining more importance, and difficulties were identified regarding seasonal storages (van der Heijde et al., 2019). Aggregating input data temporal or spatial might result in errors and predicting the input data itself. However, sophisticated uncertainty analyses of input data were only done twice in the SLR and can be identified as a research gap. In addition, the need for optimizing DHS supplying cities that require decarbonization strategies in the following years is

rising; therefore, the demand for decreased computational time is high. The computational time depends not only on the system's size but also on the model complexity. In general, the model complexity should always fit the research question. Suppose the research question focused on the thermal design of grid or production units. A detailed pressure model seems unnecessary because the CAPEX for energy converters and storages determine the design optimization (A. Rieder et al., 2013). However, boundaries for the flow in the pipes dependent on the diameter should be considered. Most publications can solve their design optimization with a MILP or LP model with reduced complexity regarding hydraulic equations (see Eq. 14, Eq. 15, and Eq. 16).

Besides model complexity, computational time, and multi-objectivity, the supply system is the key to transforming the DHS. Fuel cells had never been viewed in the literature; however, their significance seems relatively low regarding the results of the heat roadmap Europe. Nevertheless, excess heat from electrolyzes could be a coupling option for DHS. Considering the rising connection to the electric market due to sector-coupling technologies, the importance of storage capacities becomes significant. The total storage capacity in the grid can only be exploited by modeling the forward-flow and the backward-flow–a potential research gap. The design of the DHS's components was a well-known subject, but their deconstruction in the optimization model had not been done yet.

In addition to the deconstruction of components, the integration of low-grade heat sources is highly relevant for decarbonization favored by a low system temperature. Lowering the system's temperature can be identified as a research gap in the literature. Wirtz et al. (2019) examined different temperature levels for the DHS to find the optimal operation point for a large-scale heat pump. The heat pump's efficiency–also called the coefficient of performance (COP)—heavily depends on the sink and source temperature. Usually, the COP is calculated *a priori* with a model from the literature, e. g. in Jesper et al. (2021). Wirtz et al. (2019) performed a parameter study to calculate different resulting costs in dependency on the forward-flow temperature of the grid. However, the grid was not spatially discretized and worked as one consumer in the optimization. Methods to lower the demanding temperature were combining central and decentralized units, which had only been done for a few publications (see Figure 12), or refurbishment inside the optimization. Both methods are potential research gaps. Besides lowering the system's temperature, integrating solar thermal energy and PV supports the transformation process. PV and solar thermal energy were represented in the midrange of the literature, but both technologies require space and are competing technologies. This problem was not addressed in the literature for large-scale systems and is a potential research gap. Additionally, geothermal energy and long-term storages are potential research gaps of high significance because they were identified by the heat roadmap Europe as one of the technologies in a future supply system of a DHS.

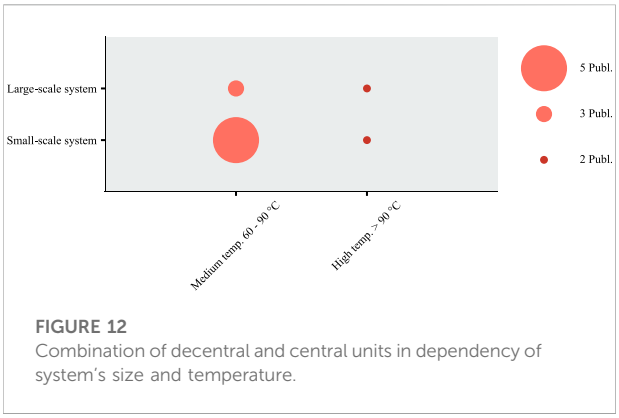

FIGURE 12
Combination of decentral and central units in dependency of system's size and temperature.

In Section 3.2, four significant publications were analyzed concerning the design decisions of the grid and its supply system. The increased computational power allows the calculation of complex systems, including infrastructural and supply system choices. Utilizing mathematical optimization to support decision-making processes decreases costs and emissions, as shown in the literature. Morvaj et al. (2016) showed that the grid's design is influenced not only by the consumers but also by the design of the supply system. Optimization algorithms depict these dependencies; however, the analyzed systems are often relatively small. To reduce the computational effort, the grid's and the supply system's design are often separated, e. g. in Wirtz et al. (2020). The decarbonization and electrification of the heating sector increase the complexity of the optimization. Optimizing larger systems with design decisions for the grid, a great variety of different technologies, and sector-coupling dependencies is a key challenge for the upcoming years.

Limitations

The major limitation of the SLR came with its advantage; publications with relevance to the topic might have been excluded due to the performed method. The exclusion can occur due to the limitation of databases, keywords, years, or quality measures. In addition, the derived categories might have excluded crucial topic information. The presented equations in Section 3.1.3 were representative, and the mathematical model can significantly vary from publication to publication. The mathematical description should always fit the problem at hand. Nevertheless, Section 3.1.3 showed the most critical energy balances for a problem dealing with designing a DHS thermally.

Conclusion

This work's main findings were identifying model complexity to answer the research question of design optimization for

decarbonized DHS and potential research gaps in the literature. The literature did not yet provide the results to design and transform a large-scale high-temperature DHS into a sustainable system.

Most publications used linear programming models solved with a global solver like Gurobi. If a large-scale system was optimized, a heuristic solver might result in a more efficient solution. Hydraulic equations were primarily neglected in the design optimization of a thermal supply system or grid. Some publications used hydraulic boundaries for the flow velocity, ensuring max. pressure loss in the pipe is not reached. The mathematical description of a DHS is divided into energy balances for pipes, nodes, consumers, and production units. Mostly, the objective was to find a cost-efficient design of the supply system and the grid. Sometimes ecologic factors were integrated, which led to multi-objective optimization. Multi-objective optimization can be performed with two different functions, a weighted sum function, or to run several optimizations with different boundaries for a KPI, e. g. CO_2 emissions. The optimization chose technologies like CHPs, boilers, individual heat pumps, and short-term storages. Most optimization problems concentrated on the central installation of the supply system. In conclusion, this work identified four major research fields:

- depiction of different stakeholder decisions in the DHS regarding the design;
- performance improvement of computational efforts through methods like spatial and temporal aggregation, especially regarding the problem of designing seasonal storages;
- uncertainty analysis for input data and the results;
- structure of a sustainable supply system, including measures for lowering the demanding temperature, integrating energy converters and heat sources like geothermal energy, large-scale heat pumps, seasonal storages, and other low-grade heat sources.

The depiction of different stakeholder decisions is often not the case. The optimizer usually finds a global minimum. However, this minimum might select the decisions of building owners they would never choose. Therefore, the depiction of those decisions, e. g. the connection to DHS, could be interesting for further investigation. Additionally, reducing computational time is always one of the key challenges in optimization. Some researchers apply spatial and temporal aggregation methods causing difficulties in designing seasonal storages due to the shift of time dependencies.

Furthermore, most optimization models base their results on one demand curve per consumer. This curve implies perfect foresight and might result in an energy system not being capable of supplying its consumers if the perfect foresight fails. One solution is the calculation of several scenarios. Then the output data can be analyzed to design a robust energy system. Other solutions often include methods like Monte Carlo simulations resulting in high computational times. Therefore, the analysis of uncertainties is also an important research field. Finally, all questions concerning the design of the grid and the supply system are key challenges in the optimization of DHS.

Besides the research gaps in the existing literature, several trends can be seen in the results. Generally, a carbon-free system benefits from grid-based energy resulting in high connection rates for potential consumers. The supply system's design shifted from a gas-based supply to an electric-based design. The decarbonization of DHS leads to increased complexity in handling central and decentral units, thermal and electric energy flows and more restrictive boundary conditions due to the limited availability of renewable energies. Mathematical optimization can handle this complexity and increase the efficiency of those systems with cost reduction between 30 and 40%. However, increased complexity often requires higher computational effort. Handling this increased complexity efficiently will be a significant challenge in the optimization community.

Author contributions

MS conducted the research and wrote the manuscript. MiR reviewed the manuscript and supported the graphical design. MaR acquired the financial resources to support the research and reviewed the manuscript.

Funding

The Fraunhofer IEG funded the study with the project ODH@Jülich.

Conflict of interest

The authors declare that the research was conducted in the absence of any commercial or financial relationships that could be construed as a potential conflict of interest.

Publisher's note

References

Alghool, D. M., Elmekkawy, T. Y., Haouari, M., and Elomri, A. (2020). Optimization of design and operation of solar assisted district cooling systems. *Energy Convers. Manag. X* 6, 100028. doi:10.1016/j.ecmx.2019.100028

Arpagaus, C., Bless, F., Uhlmann, M., Schiffmann, J., and Bertsch, S. S. (2018). High temperature heat pumps: Market overview, state of the art, research status, refrigerants, and application potentials. *Energy* 152, 985–1010. doi:10.1016/j.energy.2018.03.166

Baehr, H. D., and Kabelac, S. (2006). *Thermodynamik: Grundlagen und technische Anwendungen mit zahlreichen Tabellen*. Berlin, Germany: Springer-Verlag Berlin Heidelberg.

Bartolini, A., Carducci, F., Giovannelli, A., and Comodi, G. (2018). "Optimal planning of low carbon microgrids using primary energy savings as a constraining factor: The case of an industrial retrofit," in International Conference on Environment and Electrical Engineering and 2018 IEEE industrial and commercial Power Systems Europe New York, USA.

Best, R. E., Rezazadeh Kalehbasti, P., and Lepech, M. D. (2020). A novel approach to district heating and cooling network design based on life cycle cost optimization. *Energy* 194, 116837. doi:10.1016/j.energy.2019.116837

Biedermann, F., and Kolb, M. (2014). *Nah-/ fernwärme, fact sheet on behalf of the working association of chamber of commerce and industry (HIHK)*. Munich, Germany.

Bill, R. (2010). *Grundlagen der Geo-informationssysteme*. Berlin, Offenbach: Wichmann, 804.

Blommaert, M., Wack, Y., and Baelmans, M. (2020). An adjoint optimization approach for the topological design of large-scale district heating networks based on nonlinear models. *Appl. Energy* 280, 116025. doi:10.1016/j.apenergy.2020.116025

Bordin, C., Gordini, A., and Vigo, D. (2016). An optimization approach for district heating strategic network design. *Eur. J. Operational Res.* 252 (1), 296–307. doi:10.1016/j.ejor.2015.12.049

Bornand, B., Girardin, L., Belfiore, F., Robineau, J.-L., Bottallo, S., and Maréchal, F. (2020). Investment planning methodology for complex urban energy systems applied to a hospital site. *Front. Energy Res.* 8. doi:10.3389/fenrg.2020.537973

Bracco, S., Dentici, G., and Siri, S. (2013). Economic and environmental optimization model for the design and the operation of a combined heat and power distributed generation system in an urban area. *Energy* 55, 1014–1024. doi:10.1016/j.energy.2013.04.004

Buoro, D., Casisi, M., de Nardi, A., Pinamonti, P., and Reini, M. (2013). Multicriteria optimization of a distributed energy supply system for an industrial area. *Energy* 58, 128–137. doi:10.1016/j.energy.2012.12.003

Campos, G., Liu, Y., Schmidt, D., Yonkoski, J., Colvin, D., Trombly, D. M., et al. (2021). Optimal real-time dispatching of chillers and thermal storage tank in a University campus central plant. *Appl. Energy* 300, 117389. doi:10.1016/j.apenergy.2021.117389

Casisi, M., Buoro, D., Pinamonti, P., and Reini, M. (2019). A comparison of different district integration for a distributed generation system for heating and cooling in an urban area. *Appl. Sci.* 9 (17), 3521. doi:10.3390/app9173521

Corscadden, J., Möhring, P., and Krasatsenka, A. (2021). *Transformation of existing urban district heating and cooling systems from fossil to renewable energy sources*.

Dancker, J., Götze, J., Schulz, F., Könneke, N., Beyrau, F., and Wolter, M. (2019). Optimal design and operation of a CHP based district heating system including a heat storage and electrode boiler to increase self-consumption in 2019 IEEE PES Conference on Innovative Smart Grid Technologies, ISGT Latin America.

Delubac, R., Serra, S., Sochard, S., and Reneaume, J.-M. (2021). A dynamic optimization tool to size and operate solar thermal district heating networks production plants. *Energies* 14 (23), 8003. doi:10.3390/en14238003

Delubac, R., Serra, S., Sochard, S., and Reneaume, J.-M. (2020). "A multi-period tool to optimize solar thermal integration in district heating networks," in ECOS 2020 - Proceedings of the 33rd International Conference on Efficiency, Cost, Optimization, Simulation and Environmental Impact of Energy Systems.

DG Energy (2020). *Quarterly report energy on European gas markets: With focus on the impact of global LNG markets on EU gas imports*.

Elsido, C., Bischi, A., Silva, P., and Martelli, E. (2017). Two-stage MINLP algorithm for the optimal synthesis and design of networks of CHP units. *Energy* 121, 403–426. doi:10.1016/j.energy.2017.01.014

EnBW Company (2021). District heating: Energy with a future. Available at https://www.enbw.com/company/the-group/energy-production/district-heating/#:~:text=With%20an%20average%20annual%20district,district%20heating%20companies%20in%20Germany.&text=In%20such%20transport%20pipes%20with,80%20and%20130%C2%B0C (Accessed June 1, 2022).

European Commission (2021a). Fernwärmenetze - kapazitäten, Erzeugung und Verluste nach Netztyp und Anlagentyp. Available at https://appsso.eurostat.ec.europa.eu/nui/show.do?dataset=nrg_dhdc_cpl&lang=de (Accessed June 1, 2022).

European Commission (2021b). *Gross derived heat generation by fuel, EU, 2000-2019 (GWh)*. Available at https://ec.europa.eu/eurostat/statistics-explained/index.php?title=File:Gross_derived_heat_generation_by_fuel,_EU,_2000-2019_(GWh)_T4.png (Accessed June 1, 2022).

Fazlollahi, S., Becker, G., Ashouri, A., and Maréchal, F. (2015). Multi-objective, multi-period optimization of district energy systems: IV – a case study. *Energy* 84, 365–381. doi:10.1016/j.energy.2015.03.003

Fazlollahi, S., Becker, G., and Maréchal, F. (2014). Multi-objectives, multi-period optimization of district energy systems: II—daily thermal storage. *Comput. Chem. Eng.* 71, 648–662. doi:10.1016/j.compchemeng.2013.10.016

Fitó, J., Hodencq, S., Ramousse, J., Wurtz, F., Stutz, B., Debray, F., et al. (2020). Energy- and exergy-based optimal designs of a low-temperature industrial waste heat recovery system in district heating. *Energy Convers. Manag.* 211, 112753. doi:10.1016/j.enconman.2020.112753

Global Conflict Tracker (2022). Conflict in Ukraine. Available at https://www.cfr.org/global-conflict-tracker/conflict/conflict-ukraine (Accessed June 1, 2022).

Gurobi, J. (2018). Working with multiple objectives. Available at https://www.gurobi.com/documentation/9.5/refman/working_with_multiple_obje.html (Accessed April 7, 2022).

Haikarainen, C., Pettersson, F., and Saxén, H. (2016). A decomposition procedure for solving two-dimensional distributed energy system design problems. *Appl. Therm. Eng.* 100, 30–38. doi:10.1016/j.applthermaleng.2016.02.012

Halmschlager, V., Birkelbach, F., and Hofmann, R. (2021). Optimizing the utilization of excess heat for district heating in a chipboard production plant. *Case Stud. Therm. Eng.* 25, 100900. doi:10.1016/j.csite.2021.100900

Halmschlager, V., and Hofmann, R. (2021). Assessing the potential of combined production and energy management in Industrial Energy Hubs – analysis of a chipboard production plant. *Energy* 226, 120415. doi:10.1016/j.energy.2021.120415

Hirsch, P., Duzinkiewicz, K., Grochowski, M., and Piotrowski, R. (2016). Two-phase optimizing approach to design assessments of long distance heat transportation for CHP systems. *Appl. Energy* 182, 164–176. doi:10.1016/j.apenergy.2016.08.107

Jesper, M., Schlosser, F., Pag, F., Walmsley, T. G., Schmitt, B., and Vajen, K. (2021). Large-scale heat pumps: Uptake and performance modelling of market-available devices. *Renew. Sustain. Energy Rev.* 137, 110646. doi:10.1016/j.rser.2020.110646

Kallrath, J. (2013). *Gemischt-ganzzahlige Optimierung: Modellierung in der Praxis; mit Fallstudien aus Chemie, Energiewirtschaft, Papierindustrie, Metallgewerbe, Produktion und Logistik*. Wiesbaden, Germany: Springer Spektrum, 381p.

Kausche, M. (2018). *Wirtschaftlichkeit schwimmender offshore windenergieanlagen: Wiesbaden*. Springer Fachmedien Wiesbaden.

Khatibi, M., Bendtsen, J. D., Stoustrup, J., and Tougaard, J. (2019). Local heating concepts for upgrading district heating networks, a real world case study in ECOS 2019 - Proceedings of the 32nd International Conference on Efficiency, Cost, Optimization, Simulation and Environmental Impact of Energy Systems, 2019-June.

Krug, R., Mehrmann, V., and Schmidt, M. (2020). Nonlinear optimization of district heating networks. *Optim. Eng.* 19 (1), 783–819. doi:10.1007/s11081-020-09549-0

Lake, A., Rezaie, B., and Beyerlein, S. (2017). Review of district heating and cooling systems for a sustainable future. *Renew. Sustain. Energy Rev.* 67, 417–425. doi:10.1016/j.rser.2016.09.061

Li, H., and Svendsen, S. (2013). District heating network design and configuration optimization with genetic algorithm. *J. Sustain. Dev. energy water Environ. Syst.* 1 (4), 291–303. doi:10.13044/j.sdewes.2013.01.0022

Li, L., Mu, H., Li, N., and Li, M. (2016). Economic and environmental optimization for distributed energy resource systems coupled with district energy networks. *Energy* 109, 947–960. doi:10.1016/j.energy.2016.05.026

Li, Y., Rezgui, Y., and Zhu, H. (2017). District heating and cooling optimization and enhancement - towards integration of renewables, storage and smart grid. *Renew. Sustain. Energy Rev.* 72, 281–294. doi:10.1016/j.rser.2017.01.061

Liu, B., Bissuel, C., Courtot, F., Gicquel, C., and Quadri, D. (2021). "A hierarchical decomposition approach for the optimal design of a district cooling system," in

Proceedings of the 10th International Conference on Operations Research and Enterprise Systems, 317–328.

Lund, H., Østergaard, P. A., Nielsen, T. B., Werner, S., Thorsen, J. E., Gudmundsson, O., et al. (2021). Perspectives on fourth and fifth generation district heating. *Energy* 227, 120520. doi:10.1016/j.energy.2021.120520

Marguerite, C., Bourges, B., and Lacarriere, B. (2013). *Application of a district heating network (DHN) model for an ex-ante evaluation to support a multi-sources DH*. 80–87.

Marquant, J. F., Evins, R., Bollinger, L. A., and Carmeliet, J. (2017). A holarchic approach for multi-scale distributed energy system optimisation. *Appl. Energy* 208, 935–953. doi:10.1016/j.apenergy.2017.09.057

Mavromatidis, G., and Petkov, I. (2021). Mango: A novel optimization model for the long-term, multi-stage planning of decentralized multi-energy systems. *Appl. Energy* 288, 116585. doi:10.1016/j.apenergy.2021.116585

Mazhar, A. R., Liu, S., and Shukla, A. (2018). A state of art review on the district heating systems. *Renew. Sustain. Energy Rev.* 96, 420–439. doi:10.1016/j.rser.2018.08.005

Mertz, T., Serra, S., Henon, A., and Reneaume, J.-M. (2016). A MINLP optimization of the configuration and the design of a district heating network: Academic study cases. *Energy* 117, 450–464. doi:10.1016/j.energy.2016.07.106

Mertz, T., Serra, S., Henon, A., and Reneaume, J. M. (2017). A MINLP optimization of the configuration and the design of a district heating network: Study case on an existing site. *Energy Procedia* 116, 236–248. doi:10.1016/j.egypro.2017.05.071

Mojica, J. L., Petersen, D., Hansen, B., Powell, K. M., and Hedengren, J. D. (2017). Optimal combined long-term facility design and short-term operational strategy for CHP capacity investments. *Energy* 118, 97–115. doi:10.1016/j.energy.2016.12.009

Morvaj, B., Evins, R., and Carmeliet, J. (2016). Optimising urban energy systems: Simultaneous system sizing, operation and district heating network layout. *Energy* 116, 619–636. doi:10.1016/j.energy.2016.09.139

Neri, M., Guelpa, E., and Verda, V. (2022). Design and connection optimization of a district cooling network: Mixed integer programming and heuristic approach. *Appl. Energy* 306, 117994. doi:10.1016/j.apenergy.2021.117994

Nussbaumer, T., Thalmann, S., Ardens, A. J., and Ködel, J. (2018). *Planungshandbuch fernwärme, study on behalf of EnergieSchweiz*. Switzerland: Ittigen.

Olsthoorn, D., Haghighat, F., and Mirzaei, P. A. (2016). Integration of storage and renewable energy into district heating systems: A review of modelling and optimization. *Sol. Energy* 136, 49–64. doi:10.1016/j.solener.2016.06.054

Ommen, T., Markussen, W. B., and Elmegaard, B. (2016). Lowering district heating temperatures - impact to system performance in current and future Danish energy scenarios. *Energy* 94, 273–291. doi:10.1016/j.energy.2015.10.063

Paardekooper, S., Lund, R. S., Mathiesen, B. V., Chang, M., Petersen, U. R., Grundahl, L., et al. (2018). *Heat roadmap Europe 4: Quantifying the impact of low-carbon heating and cooling roadmaps*.

Paiho, S., and Reda, F. (2016). Towards next generation district heating in Finland. *Renew. Sustain. Energy Rev.* 65, 915–924. doi:10.1016/j.rser.2016.07.049

Pantaleo, A. M., Giarola, S., Bauen, A., and Shah, N. (2014a). Integration of biomass into urban energy systems for heat and power. Part I: An MILP based spatial optimization methodology. *Energy Convers. Manag.* 83, 347–361. doi:10.1016/j.enconman.2014.03.050

Pantaleo, A. M., Giarola, S., Bauen, A., and Shah, N. (2014b). Integration of biomass into urban energy systems for heat and power. Part II: Sensitivity assessment of main techno-economic factors. *Energy Convers. Manag.* 83, 362–376. doi:10.1016/j.enconman.2014.03.051

Paperpile, L. L. C. (2012). The top list of academic research databases. Available at https://paperpile.com/g/academic-research-databases/ (Accessed April 6, 2022).

Quaggiotto, D., Vivian, J., and Zarrella, A. (2021). Management of a district heating network using model predictive control with and without thermal storage. *Optim. Eng.* 22 (3), 1897–1919. doi:10.1007/s11081-021-09644-w

Renaldi, R., Kiprakis, A., and Friedrich, D. (2017). An optimisation framework for thermal energy storage integration in a residential heat pump heating system. *Appl. Energy* 186, 520–529. doi:10.1016/j.apenergy.2016.02.067

Rieder, A., Christidis, A., and Tsatsaronis, G. (2013). "Multi criteria dynamic design optimization of a distributed energy system," in Proceedings of the 26th International Conference on Efficiency, Cost, Optimization, Simulation and Environmental Impact of Energy Systems.

Rieder, A., Christidis, A., and Tsatsaronis, G. (2014). Multi criteria dynamic design optimization of a small scale distributed energy system. *Energy* 74, 230–239. doi:10.1016/j.energy.2014.06.007

Röder, J., Meyer, B., Krien, U., Zimmermann, J., Stührmann, T., and Zondervan, E. (2021). Optimal design of district heating networks with distributed thermal energy storages – method and case study. *Int. J. Sustain. Energy Plan. Manag.* 31, 5–22.

Rosenkranz, A. (2020). Brennstoffzellenheizung: Kosten, Funktion und Effizienz. Available at https://heizung.de/brennstoffzellenheizung/ (Accessed May 9, 2022).

Sameti, M., and Haghighat, F. (2019). Hybrid solar and heat-driven district cooling system: Optimal integration and control strategy. *Sol. Energy* 183, 260–275. doi:10.1016/j.solener.2019.03.034

Sameti, M., and Haghighat, F. (2017). Optimization approaches in district heating and cooling thermal network. *Energy Build.* 140, 121–130. doi:10.1016/j.enbuild.2017.01.062

Sarbu, I., Mirza, M., and Crasmareanu, E. (2019). A review of modelling and optimisation techniques for district heating systems. *Int. J. Energy Res.* 43 (13), 4600–6598. doi:10.1002/er.4600

Sarbu, I., Mirza, M., and Crasmareanu, E. (2017). Comprehensive review on modelling and optimisation of district heating systems. *Int. Multidiscip. Sci. GeoConference Surv. Geol. Min. Ecol. Manag. SGEM* 17–42.

Sarbu, I., Mirza, M., and Crasmareanu, E. (2020). Optimisation of district heating systems using heuristic methods: A review. *Proc. romanian Acad. Ser. a-mathematics Phys. Tech. Sci. Inf. Sci.* 21 (4), 319–328.

Schütz, T., Remy, S., Fuchs, M., and Müller, D. (2018). "Optimal design of local energy systems considering governmental subsidies: A German case study," in ECOS 2018 - Proceedings of the 31st International Conference on Efficiency, Cost, Optimization, Simulation and Environmental Impact of Energy Systems.

Scimago (2007). Scimago journal & country rank. Available at https://www.scimagojr.com/ (Accessed April 6, 2022).

Scolan, S., Serra, S., Sochard, S., Delmas, P., and Reneaume, J.-M. (2020). Dynamic optimization of the operation of a solar thermal plant. *Sol. Energy* 198, 643–657. doi:10.1016/j.solener.2020.01.076

Serway, R. A. (2004). *Physics for scientist and egineers: United States*. Thomson/Brooks/Cole.

Silveira, C. L. B., Tabares, A., Faria, L. T., and Franco, J. F. (2021). Mathematical optimization versus metaheuristic techniques: A performance comparison for reconfiguration of distribution systems. *Electr. Power Syst. Res.* 196, 107272. doi:10.1016/j.epsr.2021.107272

Stange, P., Matthees, A., and Sander, T. (2018). Operational optimization of energy systems, 25 years – established and promising use cases. *Energy Procedia* 149, 15–24. doi:10.1016/j.egypro.2018.08.165

Steinbach, J., Popovski, E., Henrich, J., Christ, C., Ortner, S., Pehnt, M., et al. (2020). *Umfassende Bewertung des Potenzials für eine effiziente Wärme- und Kältenutzung für Deutschland*.

Szypowski, M., Siewierski, T., and Wedzik, A. (2019). Optimization of energy-supply structure in residential premises using mixed-integer linear programming. *IEEE Trans. Ind. Electron.* 66 (2), 1368–1378. doi:10.1109/tie.2018.2793276

Unternährer, J., Moret, S., Joost, S., and Maréchal, F. (2017). Spatial clustering for district heating integration in urban energy systems: Application to geothermal energy. *Appl. Energy* 190, 749–763. doi:10.1016/j.apenergy.2016.12.136

van der Heijde, B., Vandermeulen, A., Salenbien, R., and Helsen, L. (2019). Representative days selection for district energy system optimisation: A solar district heating system with seasonal storage. *Appl. Energy* 248, 79–94. doi:10.1016/j.apenergy.2019.04.030

Vian, A., Bignucolo, F., and Cagnano, A. (2020). "Effects of environmental conditions on the optimal sizing and operation of an energy hub," in 2020 IEEE International Conference on Environment and Electrical Engineering and 2020 IEEE Industrial and Commercial Power Systems Europe (EEEIC / I CPS Europe), 1–6.

vom Brocke, J., Simons, A., Niehaves, B., Riemer, K., Plattfaut, R., and Cleven, A. (2009). in *Ecis. Reconstructing the giant: On the importance of rigour in documenting the literature search process*.

vom Brocke, J., Simons, A., Riemer, K., Niehaves, B., Plattfaut, R., and Cleven, A. (2015). Standing on the shoulders of giants: Challenges and recommendations of literature search in information systems research. *Commun. Assoc. Inf. Syst.* 37.

Walter, O., Tremel, A., Prenzel, M., Becker, S., and Schaefer, J. (2020). Techno-economic analysis of hybrid energy storage concepts via flowsheet simulations, cost modeling and energy system design. *Energy Convers. Manag.* 218, 112955. doi:10.1016/j.enconman.2020.112955

Wang, D., Li, X., Marquant, J., Carmeliet, J., and Orehounig, K. (2021a). Advancing the thermal network representation for the optimal design of distributed multi-energy systems. *Front. Energy Res.* 9. doi:10.3389/fenrg.2021.668124

Wang, X., Bie, Z., Liu, F., and Kou, Y. (2021b). Co-optimization planning of integrated electricity and district heating systems based on improved quadratic convex relaxation. *Appl. Energy* 285, 116439. doi:10.1016/j.apenergy.2021.116439

Webster, J., and Watson, R. (2002). Analyzing the past to prepare for the future: Writing a literature review. *MIS Q.* 26.

Weinand, J. M., Kleinebrahm, M., McKenna, R., Mainzer, K., and Fichtner, W. (2019). Developing a combinatorial optimisation approach to design district heating networks based on deep geothermal energy. *Appl. Energy*. 251.

Williams, H. P. (2013). *Model building in mathematical programming*. Chichester: WILEY, 411.

Wirtz, M., Hahn, M., Schreiber, T., and Müller, D. (2021a). Design optimization of multi-energy systems using mixed-integer linear programming: Which model complexity and level of detail is sufficient? *Energy Convers. Manag.* 240, 114249. doi:10.1016/j.enconman.2021.114249

Wirtz, M., Kivilip, L., Remmen, P., and Müller, D. (2020). 5th generation district heating: A novel design approach based on mathematical optimization. *Appl. Energy* 260, 114158. doi:10.1016/j.apenergy.2019.114158

Wirtz, M., Kivilip, L., Remmen, P., and Müller, D. (2019). "Optimal design and operation of large-scale heat pumps in district heating and cooling systems," in ECOS 2019 - Proceedings of the 32nd International Conference on Efficiency, Cost, Optimization, Simulation and Environmental Impact of Energy Systems.

Wirtz, M., Neumaier, L., Remmen, P., and Müller, D. (2021b). Temperature control in 5th generation district heating and cooling networks: An MILP-based operation optimization. *Appl. Energy* 288, 116608. doi:10.1016/j.apenergy.2021.116608

Wu, C., Gu, W., Xu, Y., Jiang, P., Lu, S., and Zhao, B. (2018). Bi-level optimization model for integrated energy system considering the thermal comfort of heat customers. *Appl. Energy* 232, 607–616. doi:10.1016/j.apenergy.2018.09.212,

Yılmaz Balaman, Ş., and Selim, H. (2016). Sustainable design of renewable energy supply chains integrated with district heating systems: A fuzzy optimization approach. *J. Clean. Prod.* 133, 863–885. doi:10.1016/j.jclepro.2016.06.001

Yokoyama, Ryohei, Nakamura, Ryo, Wakui, Tetsuya, and Shinano, Yuji (2016). "Evaluation of performance robustness of a gas turbine cogeneration plant based on a mixed-integer linear model," in ASME Turbo Expo 2016: Turbomachinery Technical Conference and Exposition, 1–9.

Zhang, L., Wang, Y., and Feng, X. (2021). A framework for design and operation optimization for utilizing low-grade industrial waste heat in district heating and cooling. *Energies (Basel).* 14 (8), 2190. doi:10.3390/en14082190

frontiers | Frontiers in Energy Research

TYPE Original Research
PUBLISHED 21 October 2022
DOI 10.3389/fenrg.2022.1013540

OPEN ACCESS

EDITED BY
Yilin Fan,
UMR6607 Laboratoire de Thermique et Énergie de Nantes (LTeN), France

REVIEWED BY
Seyed Soheil Mousavi Ajarostaghi,
Babol Noshirvani University of Technology, Iran
Min Wei,
Shandong University, China

*CORRESPONDENCE
Arijit A. Ganguli,
ganguliarijit@gmail.com

SPECIALTY SECTION
This article was submitted to Process and Energy Systems Engineering, a section of the journal Frontiers in Energy Research

RECEIVED 07 August 2022
ACCEPTED 27 September 2022
PUBLISHED 21 October 2022

CITATION
Ganguli AA and Pandit AB (2022), Computational fluid dynamics simulations to improve performance characteristics of a manifold having a central inlet and outlet.
Front. Energy Res. 10:1013540.
doi: 10.3389/fenrg.2022.1013540

Computational fluid dynamics simulations to improve performance characteristics of a manifold having a central inlet and outlet

Arijit A. Ganguli[1,2]* and Aniruddha B. Pandit[2]

[1]School of Engineering and Applied Science, Ahmedabad University, Ahmedabad, India, [2]Institute of Chemical Technology, Mumbai, India

In the present work, performance/flow characteristics (namely, the effect of operating parameters like pressure on flow patterns, pressure drop, and the extent of flow uniformity) and transport phenomena of a manifold (header tube assembly) having an inlet and outlet at the center are carried out on a macroscale geometry using CFD simulations. In this study, an existing design available in the published literature (with high flow non-uniformity) was considered and an optimized design (with minimum flow non-uniformity) was developed. The optimization is performed by incorporating a perforated plate (distributor) inside the top header of the manifold. First, CFD simulations for different configurations of the existing design with the perforated plate have been performed for a pressure of 10 bar with steam as a working fluid, and an optimized configuration having a minimum flow non-uniformity of less than 3% is obtained. CFD simulations for both the existing design and optimized design are then performed for a pressure range ($10 \leq p \leq 70$ bar) and the corresponding Reynolds number (Re) range (2.82E+05 ≤ Re ≤ 2.82E+06) with steam as the working fluid. The extent of non-uniformity (ENU) and pressure drop for the existing design (without a distributor) and optimized design (with a distributor) have been analyzed and compared. The optimized design gives the near uniform flow (~1–4%) for all pressures and Reynolds numbers considered. An empirical correlation relating the friction factor (as per the Chilton–Colburn analogy) and Re has been developed for both designs (with and without a distributor). The predicted friction factors are compared with the present CFD predictions, and experimental data of the shell and tube heat exchanger are available in the published literature. A good agreement within a 10–15% deviation has been observed. Based on the Chilton–Colburn analogy, a correlation for the Nusselt number is obtained from the friction factor correlations for both with and without distributor cases. The correlations for friction factors were found to be valid under any operating conditions for a pressure drop range within $0.05 < \Delta p < 1.8$ bar irrespective of the design of the distributor, assuming that the manifold is able to withstand the pressure drops in the given range.

KEYWORDS

optimized manifold, pressure drop, heat and mass transfer analogy, flow non-uniformity, microchannels, flow patterns

1 Introduction

In macroscale process equipment (like heat exchangers) or microscale equipment (like external manifold solid oxide fuel cell stack, microchips for electronic applications, water-cooled impingement microchannel, and proton exchange membrane fuel cells), the single-stream flow needs to be divided into several parallel streams (i.e., the flow gets distributed also termed as flow distribution) and then recombined into a single stream. The equipment involving such flows is in general termed as manifolds. The single stream entering the manifold can be a pipe or channel (generally termed as a main channel or top header) with entry from one side (left, right, or top) or center (top or bottom). The flow then gets divided into multiple pipes or channels (the size of which is less than one-fourth of the main channel). The flow then recombines into another main channel at the bottom (also called the bottom header) after which it goes downstream to another equipment or to the atmosphere. In these types of equipment, the dimensions range from micrometers to meters, depending on the applications for which they are used. An improper flow distribution affects the overall heat transfer coefficient in a heat exchanger or conversion and yields in a multichannel catalytic converter, thus affecting the performance of the equipment. The flow may be evenly distributed (termed as uniform flow distribution) in the manifold or may be non-evenly distributed (termed as maldistribution). One of the applications where such manifolds are used but less widely studied is as a condenser for safety applications in nuclear power plants for passive decay heat removal. In such applications, the fluids undergo turbulent natural convection (Ganguli et al., 2011) and two-phase flow, especially boiling and condensation (Ganguli et al., 2010; Dahikar et al., 2013; Ganguli et al., 2013). CFD modeling of these condensers for the single-phase uniform flow distribution has been studied by Gandhi et al. (2012). Another important aspect is the effect of maldistribution on transport phenomena. The analytical or empirical modeling of this aspect has not received greater attention for non-conventional heat exchangers like plate and frame heat exchangers and manifolds (side or central entry).

Studies on flow non-uniformity and pressure drops in macroscale manifolds were first studied more than 5 decades ago by Acrivos et al. (1959). In the past few years, however, the distribution of fluids at a microscale has received considerable attention. It was thought worthwhile to briefly review the literature of optimization of geometries of microscale and have a better understanding of strategies which might help in optimization of geometries at a macroscale. First, the geometrical and operating parameters of such research works are listed in Table 1 which have been complimented with the description in Section 2.

The basic shapes in a microchannel are 1) conservative types having rectangular, hemi-spherical, converging–diverging shapes with entry from the extreme bottom or top and exit from the extreme top or bottom (Figure 1A); 2) bifurcation shape where there is a central inlet, and the flow is split sequentially till it goes into two channels (Figure 1B); and 3) a manifold having a central inlet and outlet and a baffle divides the flow before it moves to a series of channels and divides the flow (Figure 1C). The flow distribution is a function of the flow area within the headers and the pressure loss in the tubes between the headers.

1.1 Literature review

In this section, the recent works carried out on flow distribution in microchannels with configurations are provided in Figure 1, and analytical works of flow distribution in manifolds have been discussed. Since a detailed literature study of CFD studies of flow distribution in manifolds is available in the published literature (Gandhi et al., 2012; Minocha and Joshi, 2020), a limited literature review on macroscopic manifolds is provided in Section 2.2.

1.2 Flow distribution studies on microscale manifolds with a central inlet and outlet

The distribution of fluids in microscopic manifolds has increased over the past decade. Wei et al. (2010) studied the effects of structural parameters on velocity distribution using numerical simulation of bifurcation structures as the manifolds of microchannel arrays in a plane (Figure 1B). The arrays considered by the authors were symmetric in nature. The authors highlighted that in bifurcation geometry, the complexity arose since channel parameters in each level downstream were independent and were represented as ratio parameters. The optimization of these ratios, namely, 1) the ratio of the length of the channel to the horizontal distance between two adjacent channels at a specific level and 2) the ratios of the right and left sides at a certain level in a bifurcation and channel width ratios helped achieve uniform distribution.

Devia et al. (2015) carried out a series of CFD simulations to infer the effects of a protrusion fitting (inside the header) on the single-phase distribution in parallel upward vertical channels fed by a common horizontal distributor. Numerical results were

TABLE 1 Experimental and CFD details of research works available in the published literature.

Author	Parameter detail								
	Geometry detail				Type of study				
	Mesh detail	Geometric dimension (depth and breadth, mm)	Flow rate range/temperature input	Input parameter and dimensionless number	Analytical/ experimental/CFD simulation	Fluid used	Boundary condition	Output parameter	Geometry and application
Alaqel et al. (2022)	Tetrahedral mesh	4 mm thickness, 2 m high, 0.2 m diameter at the lower end, and 0.4 m diameter at the upper end	N/A	Pressure, particle flow rates, air flow rates, and position of the air outlet	Experimental measurements and CFD simulation	Air–particle (red sand and bauxite) mixture	Velocity inlet and pressure outlet	Flow patterns, particle distribution, and loss	Particle fluid direct contact heat exchanger
Ghasabehi et al. (2021)	Hexahedral	Channel height: 1.2 mm; channel width: 1.52 mm; rib width: 0.83 mm; BP thickness: 2.4 mm; L inclined: 45.48 mm; W end: 1.52 mm; Cell active area: 25 cm^2; GDL thickness: 260 μm; CL thickness: 10 μm; and membrane thickness: 30 μm	298 K	Geometrical parameters, operating pressure, cell temperature, anode relative humidity, cathode relative humidity, anode stoichiometry, cathode stoichiometry, and tapering angle	Experimental measurements and CFD simulation	Water	Tapering angle and current density	Proton exchange membrane fuel cells	
Mohammadali et al. (2021)	Grid elements of 251,671 both convergence angles 0°, while grid elements of 552,946 for 6° convergence angle considered out of five different grids selected for mesh sensitivity	Circular manifold with converging inlet and diverging outlets and vice versa. Heights: 500–3,264 μm. Width: 1,204–3,875 μm. Inlet and outlet diameter is 4,000 μm. Channel length is 15,677 μm	N/A	Inlet–outlet arrangement, manifold geometry, location of the inlet and outlet off the manifold, and Reynolds number range - 10–1,000	3D CFD simulation with ANSYS Fluent	Water at 20°C	Velocity inlet with constant velocity, pressure outlet with pressure = 0, no slip boundary condition at the walls, and effect of gravity and volumetric forces are neglected	Flow patterns, velocity profiles, and flow maldistribution	
Buerkle et al. (2020)	Grid size: $4.75e10^{-6}$ hexahedral cells with correction for near wall for the low Reynolds number turbulence model	Channel width: 4 mm, depth: 1 mm, length - 65 cm, manifold width: 7.5 mm, depth: 12.5 mm, and hydraulic diameter: ≈9.5 mm	$4.496{\cdot}10^{-4}$ kgs^{-1} at 20°C	Velocity, pressure, and temperature; Reynolds number = 3,700	3D CFD simulation with AVL FIRE software and experimental measurements with the laser Doppler velocity profile sensor	Air	Constant mass flow at the inlet. Outlet pressure at 1 atm. No slip boundary conditions at the walls with a constant temperature of 20°C	Flow distribution, flow profiles, and flow patterns	
Hadad et al. (2020)	Unstructured grid with 70–122.5 million cells	Data for width, channel length, width of channels, and thicknesses of fins for entire microchannels are given	0.35L/min at 27°C	Electronic chip power, size, coolant flow rate, temperature, and effect of variation in channel geometry	Experimental measurements and CFD simulation	15% propylene glycol aqueous solution	Velocity inlet and constant temperature at the inlet, no slip at the walls, and pressure outlet. Constant heat flux boundary condition at the bottom	Pressure drop, thermal resistance, temperature profiles, and coefficient of performance	Water-cooled impingement microchannel with central entry and side exit with or without a distributor
Gilmore et al. (2021)	Unstructured mesh with 2D mesh elements of 264,142 and 3D mesh elements of 26,219,812 with COMSOL Multiphysics software	Total length of the domain is 65.1 mm, height is 1.2 mm, and grooves are 29.23 mm, and pin diameter maximum up to 0.615 mm	17.98 ml/min, 35.95 ml/min, and 53.93 ml/min at 20°C	Inlet velocity, Re = 200–600	Experimental measurements and CFD simulation	Water	Inlet as volumetric flow rate, symmetry boundary condition so that half of the geometry can be considered, and pressure outlet	Pressure drop, flow patterns (velocity vectors, contours, and pressure contours)	Microchips for electronic applications with central entry and exit
Zhao et al. (2020)	Structured mesh with 2.3 million mesh elements using ANSYS ICEM CFD 16	Inlet, outlet, and posterior diameter range from 20 mm to 60 mm with 5 mm interval; depth: 1 mm; distance between channels: 3.5 mm; area of the channel: 150 × 130 mm^2; manifold depth: 15 mm; length of the flared tube: 40 mm; and diameter of holes in sheet: 2, 5 mm	Inlet velocities as high as 34 m/s	Inlet and outlet tube size, inlet manifold structure, flow distribution, pressure drop, and Reynolds number	Experimental and CFD simulation	Air	Velocity inlet, pressure outlet with atmospheric pressure, and adiabatic walls with no-slip boundary condition	Mass flow rate, flow distribution, velocity and pressure contours, and pressure drop	External manifold solid oxide fuel cell stack and manifold with the central inlet and outlet
Zhuang et al. (2019)	1,991,070 mesh elements using ANSYS Fluent software for minichannels	Four-stage bifurcation inlet manifold: width 4.17 mm; 2.29 mm; 1.46 mm; 1 mm, length 5.40 mm; 4.28 mm; 3.38 mm; 0 mm. Parallel minichannels: depth 1 mm, width 1 mm, and length 100 mm. Rectangular outlet manifold: width 31 mm and length 10 mm	60–160 ml/min, Reynolds number	Steam to carbon molar ratio, weight hourly space velocity, operating temperature, and catalyst particle size	CFD simulation and experimental verification	Nitrogen gas and hydrogen–nitrogen mixture	Mass flow as inlet pressure, outlet at 1 atm pressure, and no-slip at the walls	Steam to carbon molar ratio, weight hourly space velocity, operating temperature, and catalyst particle size	Millireactor with the four-stage bifurcation structure manifold with the central entry and exit
Zoljalali and Omidbakhsh Amiri (2020)	Non-uniform hexahedral grid with 173,258 mesh elements	Depth: 100 μm, width: 500 μm, and length: 49.75 mm	Reynolds number in the range of 5–25	Manifold geometry, flow rate, Reynolds number 5 to 20, curvature wall, and corner angle	Experimental measurement and CFD simulation	De-ionized water	Velocity inlet, non-zero velocity at the walls, and atmospheric pressure as the outlet boundary condition	Pressure drop, flow patterns, and non-uniform flow distribution	Triangular manifold with five parallel microchips with

(Continued on following page)

10.3389/fenrg.2022.1013540

TABLE 1 (*Continued*) Experimental and CFD details of research works available in the published literature.

Author	Parameter detail								
	Geometry detail				Type of study				
	Mesh detail	Geometric dimension (depth and breadth, mm)	Flow rate range/temperature input	Input parameter and dimensionless number	Analytical/ experimental/CFD simulation	Fluid used	Boundary condition	Output parameter	Geometry and application
									a central entry (optimization using five variants of entry)
Ji et al. (2019)	N/A	50–75 μm	<0.3L/min^{-1} at 150°C–180°C	Flow rate of the H_2/N_2 mixture	Experimental measurements	H_2-N_2 mixture	N/A	Pressure drop, voltage, and current	HT-PEMFC stack
Zeng et al. (2018)	Tetrahedral mesh with the boundary layer mesh on the channel walls; 37,340, 46,154, and 61,205 mesh elements were generated	Diameter = 5 mm and channel width = 2 mm	0.1 m/s	Flow rate	CFD simulation	Solid–fluid mixture	Velocity inlet and pressure outlet and no-slip at the walls	Flow distribution error and pressure drop to measure non-uniformity	Electronic cooling hotspots and central solar receiver
Lim et al. (2018)	Two-dimensional grid of 739,456 elements using ANSYS Fluent 15	Cell distance: 3.6 mm; inlet and outlet width: 25.4 mm; and manifold width: 30 mm	Mass flow rate of the cathode mixture and thickness of the gas diffusion layer	Manifold configuration, mass flow rate, and number of cells in stack	Experimental and CFD simulation	Air	Inlet as velocity or mass flow rate, pressure outlet, and no slip wall	Pressure drop and flow patterns (pressure and velocity profiles and contours)	PEMFC stack with entry and exit from sides
Ju et al. (2018)	Three-dimensional unit cell has 71,266 nodes	Width of the square chip: 2 cm, basement thickness: 100 μm, cover thickness: 100 μm, width of the square micro-pin fin: 100 μm, height of the square micro-pin fin: 250 μm, length of the microchannel: 100 μm, width of the microchannel: 50 μm, height of the manifold (inlet and outlet): 200 μm, width of the manifold channel (inlet and outlet):100 μm, width of the square inlet and outlet nozzle: 50 μm, and height of the nozzle layer: 100 μm	0.151–0.754 m/s, 293.5 K	General parameters, micro-pin fin-related parameters, microchannel (formed between micro-pin fins)-related parameters, manifold channel-related parameters, nozzle-related parameters, and operating conditions	CFD and experimental simulations	Silicone as the solid material, and water as the coolant	Symmetry boundary conditions at the lateral surfaces at the interface, constant velocity condition at the inlet, and average static pressure at the outlet. All other surfaces are adiabatic	Heat transfer coefficient, pressure drop, total thermal resistance, average Nusselt number, and maximum temperature	Heat sink with manifold flow distributor, impinging nozzle, and micro-pin fin
Zhao et al. (2017)	Mix of tetrahedral and hexahedron grids with a total number of 7.6 million cells	Gas channel depth of 1 mm, distance between channels: 3.5 mm, manifold depth: 15 mm, inlet and outlet diameter: 20 and 10 mm, and area of distributor: 100 × 150 mm^2	4.2 m/s and 17.6 m/s to 20 mm and 10 mm inlet tube, respectively. Room temperature	Position of the inlet tube, depth of the manifold, and channel resistance	CFD simulation	Air	Velocity inlet as the boundary condition with standard liter per minute, pressure outlet at outlet, no slip at wall, and standard wall functions for flow near the wall	Pressure drop and flow patterns	Solid oxide fuel cell (SOFC) stack
Devia et al. (2015)	Hexahedral grid with 4,154,000 cells	Inner diameter: 26 mm, length: 500 mm, depth: 15 mm, width: 18 mm, protrusion diameter: 4 mm, header diameter: 0.026 m, and protrusion depth: 0.90	1.50–16.50 m/s and 0.20–1.20 m/s	Physical properties, temperature, and Reynolds number	Experimental and CFD simulation	Air and water	Velocity inlet as the boundary condition with the mass flow rate at inlet, pressure outlet at outlet with 0 bar gauge pressure, and no slip at walls	Pressure drop, localized pressure profiles, and flow distribution	
Wang and Wang (2015)	N/A	400 mm long and 3 mm internal diameter	0.5, 1, and 2 L/min at 25°C	Size of the tube, flow rate and Reynolds number	Analytical	Water	Boundary condition at the *i*th and i-1st iteration for position and velocity	Flow distribution	Radial flow reactors, electronic cooling, microreactors, heat exchangers, and solar collector
Tomor and Kristóf (2016)	Hexahedral mesh of 1,200,000 cells	Inner diameter D_1: 20 m and D_2: 10 m. Length of each branch tube: 12,5 mm. Distance of two neighboring laterals is 60 mm	10.20 m/s; 20.05 m/s; and 30.25 m/s at 24°C	Pressure, flow velocity, pressure recovery factor, and Reynolds number: 13,200–39,200	Experimental and CFD simulation	Air	Velocity and turbulence profiles from fully developed periodic BC of infinite length pipe flow, pressure outlet with zero pressure, and wall BC at the closed end of the header	Flow patterns and dimensionless flow distribution	
Wei et al. (2010)	N/A	Length: 20 mm, width: 500 μm, depth: 500 μm, and interval: 500 μm	N/A	Inlet velocity and bifurcation	Analytical	N/A	No slip at walls and velocity inlet with velocity as 1 mm/s	Degree of velocity distribution	Microchannels

10.3389/fenrg.2022.1013540

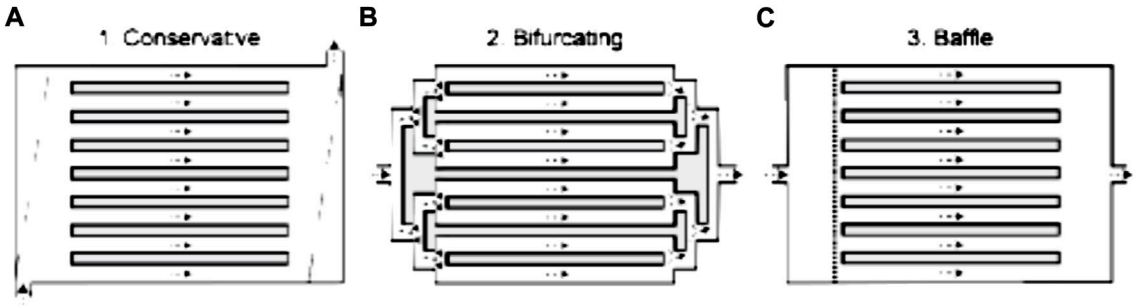

FIGURE 1
Different configurations in microchannels. **(A)** Conservative. **(B)** Bifurcating. **(C)** Baffle [reproduced from Gilmore et al. (2021)].

compared with both experimental single-phase and two-phase (liquid/gas) experimental data. An empirical correlation was developed between the pressure loss coefficients due to the protrusions in terms of the local Reynolds number based on the protrusion inner diameter. Both simulation and experimental results showed that the mass flow rate increased slightly in individual parallel channels while moving downstream inside the header, though the non-uniformity of flow rates was well within 5% in both numerical and experimental single-phase runs. The CFD simulations also revealed a peculiar pressure trend inside the header with a pressure recovery effect moving downstream along the header. The authors attributed this to the higher flow rates in the ending protrusion pipes. Furthermore, a two-phase flow investigation showed very different and much less uniform phase distribution profiles with respect to the corresponding single-phase ones. Single-phase standard deviations, from measured or numerical quantities, resulted well below 5%, while the two-phase counterparts can be 10 times as high as the single-phase deviations.

Tomor and Kristóf (2016) developed an analytical/discrete model with variable flow coefficients for the dividing-flow manifold design and compared their results with a 3D CFD model and experimental data. A good agreement between both experimental and CFD results was predicted.

Wang and Wang (2015) derived an analytical solution for the second-order nonlinear ordinary differential equation for flow distribution in a U-type manifold with a serpentine arrangement. The major complexity in U-type manifolds with a serpentine arrangement lied in losses from channels to headers in addition to frictional losses in channels that needed to be accounted for. The authors carried out momentum balance for different sections of a manifold and applied appropriate boundary conditions (two-point boundary conditions or initial and final boundary conditions for overall momentum balance). Appropriate corrections to the analytical solution were made using different coefficients for different sections. Furthermore, the

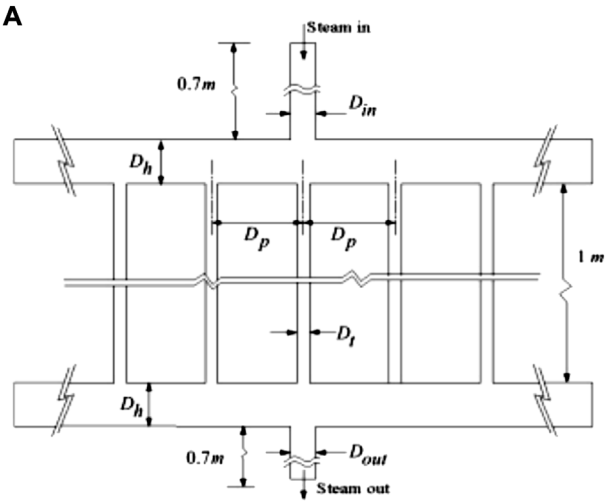

FIGURE 2
Schematic of configuration **(A)** as considered by Gandhi et al. (2012).

authors performed a comparison between the results of flow distribution between U-type and Z-type manifolds to understand the performance of the developed analytical/discrete model.

Zhao et al. (2017) analyzed gas flow distribution and pressure variation in a solid oxide fuel cell (SOFC) stack using CFD simulations. The authors considered three different designs, namely, 1) a manifold with both the inlet and outlet at the top, 2) a manifold with the inlet and outlet at the top and bottom headers, respectively, at their centers, and 3) a manifold with a rectangular distributor near the top header inlet. The authors named the aforementioned designs as T-manifold, C-manifold, and D-manifold, respectively. The authors carried out sensitivity analysis of different parameters like the position of the inlet, tube depth of the manifold, and resistance posed by channels. The authors concluded that a rectangular gas distributor improved

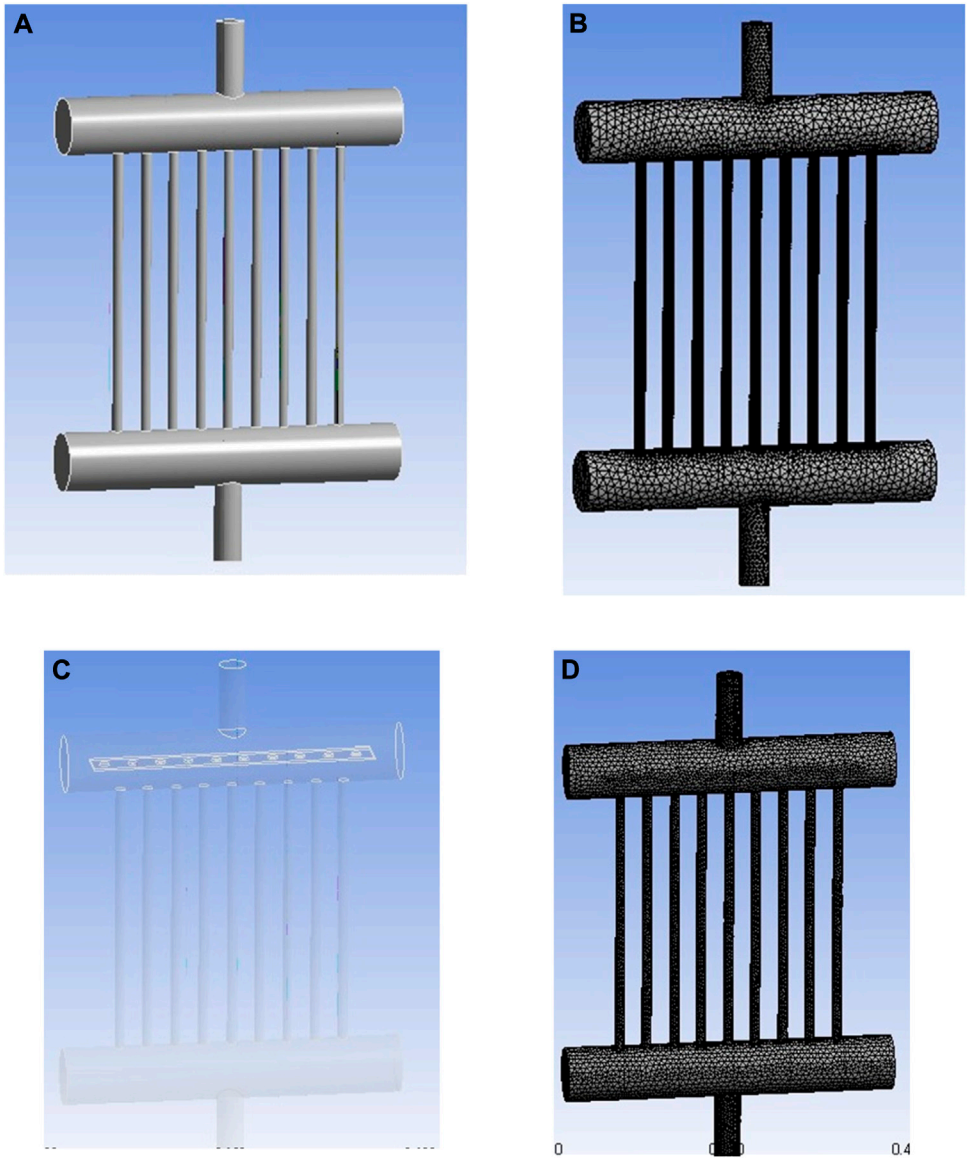

FIGURE 3
Geometry and mesh of header tube assemblies. **(A)** Geometry of the design without a distributor. **(B)** Mesh for the design without a distributor. **(C)** Geometry of the design with a distributor **(D)** Mesh for the design without a distributor.

the uniformity in flow and recommended this configuration since it also avoided damage of other accessories (like sealants) in addition to uniform flow distribution. Optimization of depth of the manifold caused an improvement of distribution in the T-manifold design while making not so significant change in the C-manifold design. Furthermore, the authors claimed that for pressure drops of 100 Pa, the non-uniformity decreased to 3%, while for 400 Pa, there was practically no non-uniformity.

Ju et al. (2018) carried out numerical studies to design a novel heat sink with a flow distributor. A three-dimensional numerical simulation was performed to investigate the thermal and hydrodynamic performances. Optimization of the design by selecting several configurations and investigating performances of each to the geometrical parameters were carried out, and the best configuration for the heat sink was chosen based on the optimum performance.

Lim et al. (2018) presented a numerical analysis of the flow distribution behavior within different manifold configurations. The authors developed a 2D CFD model for this purpose. Three different flow configurations were considered with different numbers of flow inlets and outlets. The flow characteristics, such as the pressure and velocity variations in the manifold,

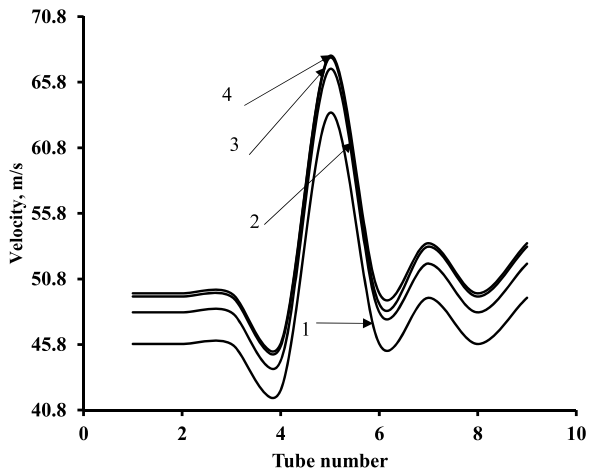

FIGURE 4
Grid independence sensitivity study. 1) 137,443 cells, 2) 187,731 cells, and 3) 229,154 cells.

were analyzed to determine the effects of the different flow configurations. The authors concluded that the configuration with two inlets and two outlets was the best for uniform flow distribution.

Zeng et al. (2018) developed a method for designing headers based on multi-stage topology optimization of fluid flow to minimize power dissipation. The authors also compared the method with a CFD-based evolutionary algorithm in the literature. The results proved that the proposed multi-stage topology optimization of fluid flow is an efficient method for addressing the general flow distribution device design problem.

Ji et al. (2019) developed an experimental method to measure flow distribution using the flow *versus* current relationship. Online measurement was carried out to optimize flow distribution, and the results for optimization of geometry on the performance of HT-PEMFC showed better flow uniformity.

Zhuang et al. (2019) used minichannel reactors with a bifurcation-structured inlet manifold and different types of outlet manifolds to study the flow distribution uniformity and pressure drop. The authors observed fully developed flow and uniform distribution when a longer channel length of bifurcation in the inlet manifold was provided. Furthermore, the authors investigated the effect of structures of bifurcation like triangle and rectangle, as well as the parallel minichannel length at the outlet of a manifold on the flow uniformity of minichannel reactors. The authors observed that the rectangular structure outlet manifold simplified the structure of minichannel reactors and reduced power losses. Furthermore, the flow uniformity of the minichannel reactor increased as the parallel minichannel length increased, and the impact was more significant at a high inlet flow rate than at a low inlet flow rate.

Gilmore et al. (2021) carried out experimental (flow visualization) and numerical studies (CFD simulations) for the design of microchannels. The authors considered three different configurations, two of which have an inlet and outlet from the middle of the manifold and one of which has an inlet from the bottom and an outlet at the top. In one of the geometries considered by the authors having a middle inlet and outlet, elliptical pins were used as baffles. The spacing between the baffles was optimized using numerical simulations to get a uniform distribution with a minor increase in pressure drop compared to a design without baffles. The introduction of elliptical pins reduced the normalized channel flow rate variation from 19% to 1% and the range from 0.59 to 0.02, while only increasing the pressure drop from 37.9 Pa to 41.3 Pa at a Reynolds number of 200. The authors suggested that future studies should seek to simplify optimization procedures, so that the performance enhancement of the solutions may be more practically implemented in real-world applications.

Hadad et al. (2020) numerically investigated the distributor and collector effects of modified impingement microchannel heat sinks having a reduced pressure drop compared to those of conventional microchannel heat sinks. Furthermore, the authors observed that the size of the inlet and outlet of the manifold has a significant effect on the thermal and hydraulic performance of the heat sink. The authors carried out a parametric study on the distributor and collector geometry effects on the hydraulic and thermal resistances and found satisfactory results for optimizing the geometry to enhance the performance.

Buerkle et al. (2020) performed CFD simulation and optical measurements to predict the flow distribution in a fuel cell stack. The authors found that by manipulating the ratio of the diameter of the inlet of the manifold to the diameter of individual fuel cells and using a non-uniform distribution of holes in the baffle-aided reduction in maldistribution, the average global deviation between the flow rates was reduced from 10.1% to 4.0%. Furthermore, the authors showed that the manufacturing

TABLE 2 Properties of steam at different pressures and header dimensions.

Pressure	Density (kg/m^3)	Viscosity (kg/ms)	Header diameter (m)
10	5.2	1.5E-05	0.058
40	20.37	1.75E-05	0.058
70	37.04	1.9E-05	0.058

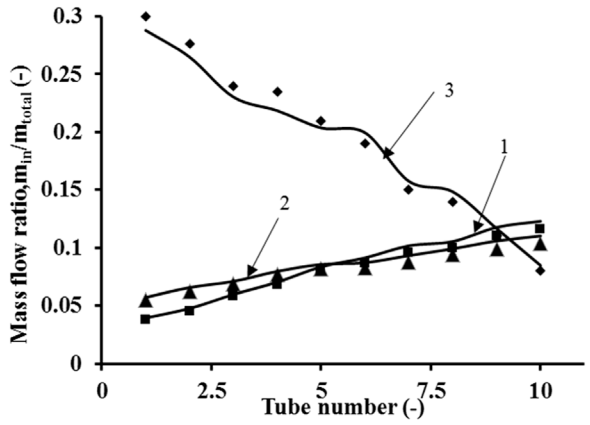

FIGURE 5
Model validation: 1) Kubo and Uuda (1969) case 1 experiment; 2) Kubo and Uuda (1969) case 2 experiment; Pigford et al. (1983).

tolerances have a strong influence on the flow maldistribution, and the modified design would help in rectifying the same.

Zoljalali and Omidbakhsh Amiri (2020) studied flow distribution and pressure drop in parallel microchannels, which are two effective parameters on the performance of different devices. For this work, the structure of a triangular inlet manifold with straight and curved walls was studied as the main subject. For this purpose, in a Reynolds number range of 5–25, four structures of inlet flow were investigated. Furthermore, the effect of the geometry parameters on the flow distribution was considered with a better structure of the manifold.

Zhuang et al. (2020) developed a novel multichannel micro-packed bed reactor with a bifurcation inlet manifold and a rectangular outlet manifold to improve the methanol steam-reforming performance. Catalyst particles were packed in the multichanneled reactor, and the flow distribution uniformity in the reactor was optimized numerically by carrying out sensitivity analysis of the geometrical parameters. The authors claimed that the developed optimized version multichannel micro-packed bed reactor can provide a solution to overcome the problems of the microchannel reactor coated with the catalyst. The authors have, however, not mentioned the studies on pressure drop for their optimized geometry.

Ghasabehi et al. (2021) carried out 3D CFD simulations for a manifold geometry (multichanneled reactor) for performance enhancement and lowering power losses. The authors considered the following two designs: the first of which was to taper the main channels without any baffles and the second was to manipulate the inlet and outlet diameters of the manifolds. The authors

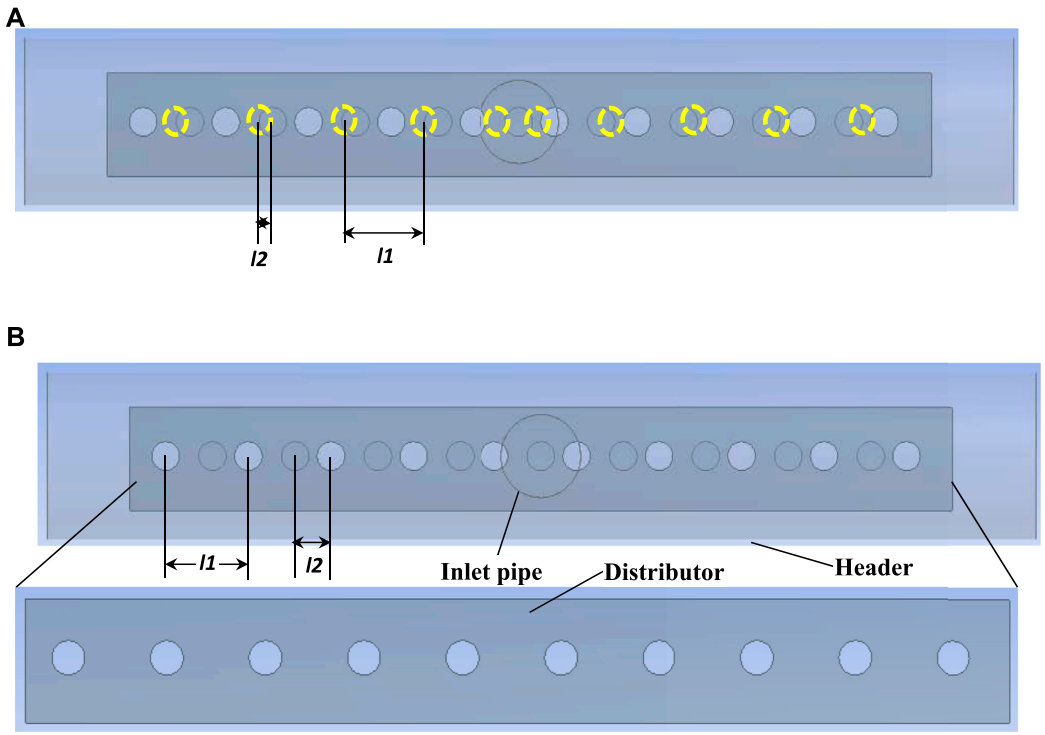

FIGURE 6
Geometrical details of the header and distributor along with parameters for configuration selection. **(A)** Configuration 1 and **(B)** configuration 5.

TABLE 3 %ENU variations for different configurations.

Re	C_1 ENU%	C_2 ENU%	C_3 ENU%	C_4 ENU%	C_5 ENU%
l_2/l_1	0.2	0.3	0.4	0.5	0.6
2.86E+05	6	3	3	2	1
9.86E+05	10	7.5	7	5	3
1.91E+06	12	9	8	5	4
2.86E+06	15	11.5	9	7	3

performed simulations on eight structures with different tapering angles that were compared with the simple parallel and serpentine flow fields. The authors found that the performance (in terms of yields) in the proposed tapered parallel flow geometry was much higher than that in the conventional one. The authors concluded that due to flow uniformity in the suggested modified design, there was an increase in performance and a reduction in power loss in both designs considered.

1.3 Flow distribution and transport phenomena in macroscale manifolds with a central inlet and outlet

Uniformity in flow distribution in any geometry (sparger, different manifolds: dividing, combining, parallel, and reverse) needs a proper balance between the pressure recovery and the frictional pressure drop. Based on this, analytical expressions for the extent of non-uniformity for dividing manifolds have been published in the open literature (Bassiouny and Martin, 1984; Turek et al., 2009; Wang, 2011; Midoux and Tondeur, 2015). Furthermore, experimental measurements for pressure drops have helped in developing empirical expressions for plate heat exchangers (PHEs) (Arsenyeva et al., 2012; Gusew and Stuke, 2019). Furthermore, numerical investigations in other applications causing enhancement in heat transfer characteristics include tubes with curved conical tubular inserts (Mousavi Ajarostaghi et al., 2021), rectangular channels in solar heaters with arc-shaped ribs (Kazemi Moghadam et al., 2021) or V-shaped ribs (Kadijani et al., 2022), or channels with partially inclined baffles (Salhi et al., 2022).

In the present work, the geometry considered is that of Gandhi et al. (2012) (as shown in Figure 2). The work on the present geometry was studied a decade ago by a few researchers (Gandhi et al., 2012; Minocha and Joshi, 2020). A comprehensive work has been carried out by Gandhi et al. (2012) on nine tube assemblies without the need for any distributor. Minocha and Joshi (2020) carried out investigations into a similar header tube assembly and used eight different design strategies to reduce maldistribution and pressure drop inside such header tube assemblies using a distributor. In their study, they concluded that the most effective design strategy for maximum flow uniformity and minimum energy dissipation would be the inclusion of the perforated baffle, which brings flow uniformity up to 95%.

1.4 Literature review summary

The literature on microscale devices (both experimental and CFD studies) has been discussed in detail in Section 2.1. Several significant strategies to address the issue of maldistribution through numerical/analytical techniques for different geometrical configurations include 1) analytical/discrete models preferred as compared to CFD by researchers (Devia et al., 2015; Wang and Wang, 2015; Tomor and Kristóf, 2016) for U- and Z-type manifolds, 2) incorporation of internals like distributors for manifolds with central inlets and outlets (Zhao et al., 2017; Gilmore et al., 2021), 3a) optimization of geometric parameters like (b) inlet diameter to individual tube ratios (Hadad et al., 2020); shape of the inlet (like triangular inlets) (Zoljalali and Omidbakhsh Amiri, 2020); and (c) other geometrical parameters (Zhuang et al., 2020; Ghasabehi et al., 2021), 4) header designs with multistage topologies (Ju et al., 2018; Zeng et al., 2018), and 5) number of flow inlets and outlets (Lim et al., 2018). Experimental works to study maldistribution include the following: 1) optimizing outlet diameters for bifurcation manifolds (Zhuang et al., 2019); 2) geometry optimization by measuring current as a function of flow (Ji et al., 2019). Gilmore et al. (2021) showed encouraging results (on microscale geometries) of reducing maldistribution to 1% with a nominal increase in pressure drop for the Reynolds number of 200, while Buerkle et al. (2020) showed optimization with the non-uniform hole distribution on the baffle showing a non-uniformity to decrease up to 4%.

The literature review also shows that in macroscale geometries, the transport phenomena in such manifolds would depend on empirical correlations relating transport coefficients with non-dimensional groups. Manifold designs are different than the benchmark geometries (for example, conventional heat exchangers such as shell and tube heat exchangers), and development of empirical correlations for friction factors and

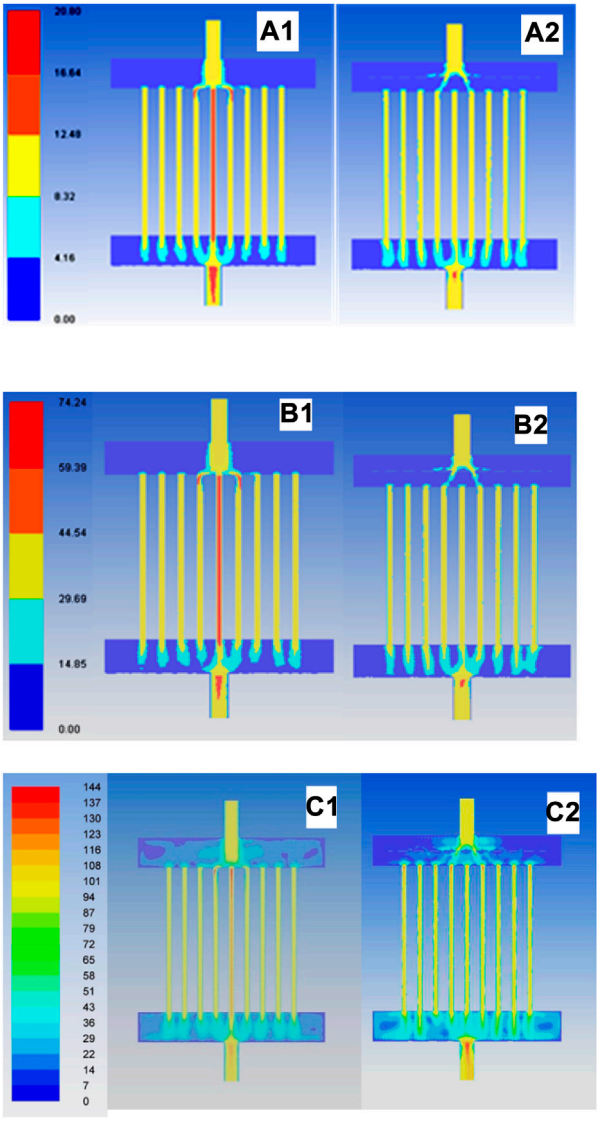

FIGURE 7
Velocity contours for p = 10 bar. Without distributor A1: Reynolds number (Re) = 2.82E+05; B1: Re = 9.86E+05; C1: Re = 1.91E+06. With distributor A2: Re = 2.82E+05; B2: Re = 9.86E+05; C2: Re = 1.91E+06 (all units of velocity are given in m/s for the color legend).

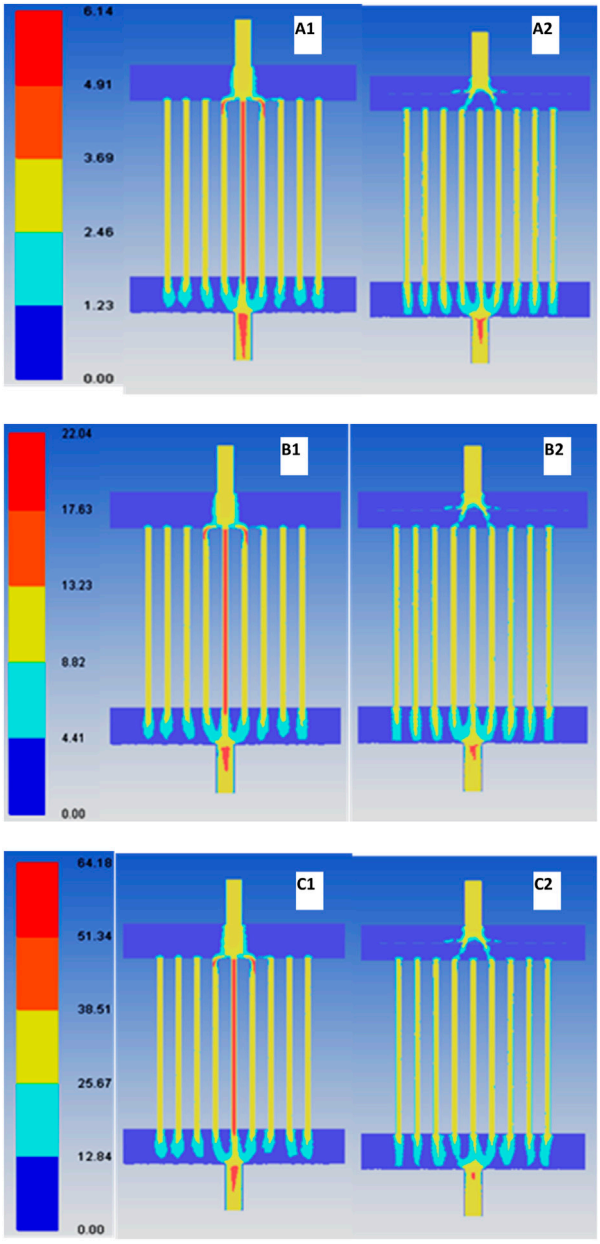

FIGURE 8
Velocity contours for p = 40 bar. Without distributor A1: Reynolds number (Re) = 2.82E+05; B1: Re = 9.86E+05; C1: Re = 2.82E+06. With distributor A2: Re = 2.82E+05; B2: Re = 9.86E+05; C2: Re = 2.82E+06 (all units of velocity are in given m/s for the color legend).

heat transfer coefficients is necessary. A brief discussion on research works on transport phenomena in unconventional heat exchangers has been provided in Section 2.2.

1.5 Objective of the present work

For the present geometry, no empirical correlation exists for transport coefficients like friction factor and heat transfer for this manifold geometry in terms of both the existing design and an optimized design. The Re number range of the present work is two orders of magnitude higher than that of the works available on the similar optimized manifold in the published literature. The lowest values of the extent of non-uniformity (ENU) reported in previous studies for the present manifold have been around 5% for lower Re number ranges ($<10^5$). The

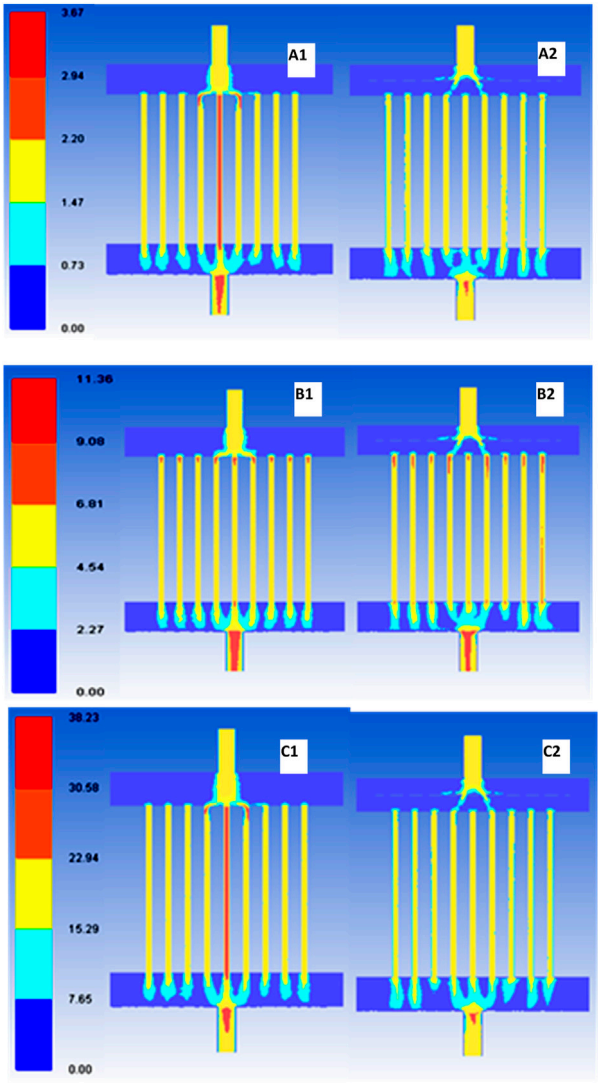

FIGURE 9
Velocity contours for p = 70 bar. Without distributor A1: Reynolds number (Re) = 2.82E+05; B1: Re = 9.86E+05; C1: Re = 2.82E+06. With distributor A2: Re = 2.82E+05; B2: Re = 9.86E+05; C2: Re = 2.82E+06 (all units of velocity are given in m/s for the color legend).

effect of operating pressure on the ENU and pressure drop in such a manifold has not been carried out till date.

In view of the aforementioned opportunities, the objectives of the present work have been defined and are as follows: 1) to analyze different configurations with a distributor in the existing design and select the best configuration which can reduce flow non-uniformity to less than 5%; 2) to carry out simulation studies to understand the performance characteristics of such geometry (the best configuration with a distributor) for different operating pressures; 3) to develop empirical correlations for transport properties (friction factor and heat transfer coefficient) for the chosen manifold (for both existing and optimized designs), and 4) to compare predictions of friction factors of the present manifold with the corresponding friction factors for benchmark geometries like shell and tube heat exchangers due to unavailability of empirical correlations from experimental data.

2 Mathematical modeling

2.1 Geometry and grid details

In this subsection, the details of the geometry and grid are presented. The geometry chosen for this system is a header tube assembly that consists of the top and the bottom headers, which are assumed to have diameters D_h, while the tubes have diameters D_t. The ratio D_t/D_h is assumed to be 0.2. The inlet and outlet diameters are one-quarter of the header diameters.

The pitch between the tube centers is D_p. The length is L = 1.125 H, where the height of the tubes is considered H, such that D_h = 0.1875 H. The fluid enters at high pressures ($10 < p < 70$ atm) from the inlet and departs at the outlet. Due to a high diameter ratio between the header tube and the tubes, the position of the inlet poses a problem. The number of holes in the distributor equals (n+1), where n is the number of tubes. The diameter of each hole of the distributor is the same as D_t. Figure 3 shows the geometry and mesh of the header tube assembly with and without a distributor.

2.2 Grid sensitivity

A three-dimensional grid has been considered in the study. A tetrahedral mesh has been created both for the header and tube assembly with and without a distributor. Grid sensitivity was performed with three grids: 1) 137,443 cells, 2) 187,731 cells, and 3) 229,154 cells. The results between 137,443 and 187,731 cells were approximately 6%, while those between 187,731 cells and 229,154 cells and 187,731 and 393,775 cells were approximately 3%. Hence, a mesh size of 183,771 cells was chosen for the study. Velocity variation with the tube number for three different grids is shown in Figure 4.

The mesh consisted of non-uniform hexahedral mesh with fine mesh near the walls and coarse at the center in case of the tubes of the manifold. Both headers however had a tetrahedral uniform mesh. For the design with distributor fine mesh near the distributor walls and uniform mesh in top header was used. For geometry with a distributor, the grid cells were 249,135 tetrahedral cells. Appropriate grid independence tests were carried out for both the cases. Table 2 shows the properties of saturated steam for three different pressures, namely, 10 bar, 40 bar, and 70 bar and the header dimensions.

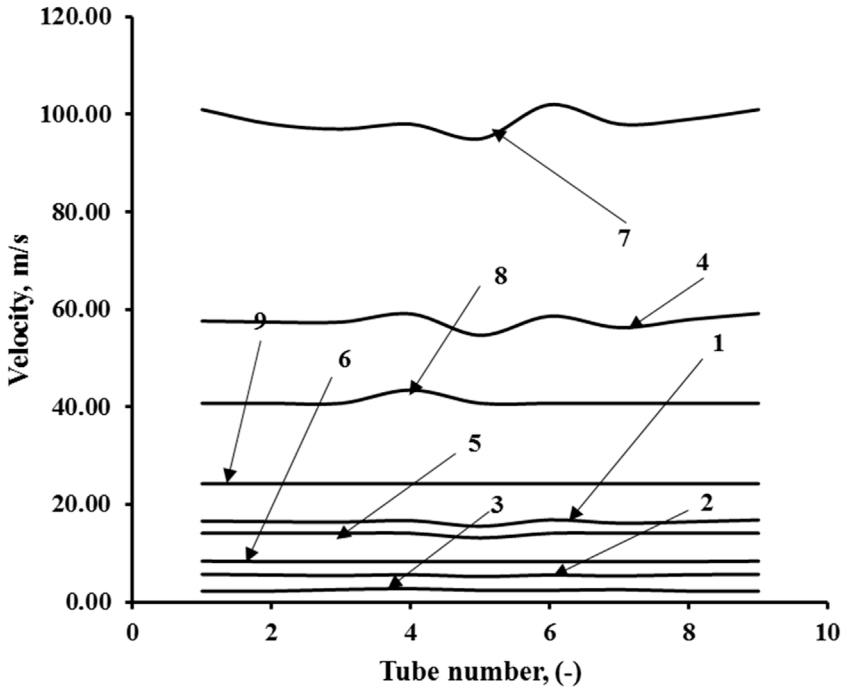

FIGURE 10
Velocity profiles after installation of distributors for different Reynolds numbers at different pressures. Re = 2.82E+05: 1) 10 bar, 2) 40 bar, and 3) 70 bar; Re = 9.86E+05: 4) 10 bar, 5) 40 bar, and 6) 70 bar; Re = 1.91E+06: 7) 10 bar; Re = 2.82E+06: 8) 40 bar and 9) 70 bar.

2.3 Governing equations

The steady-state governing equations of continuity and momentum have been used including the realizable k–ε turbulence model in cylindrical co-ordinates and have been solved using commercial software ANSYS Fluent 14. The comparison of different turbulence models (standard k–ε, realizable k–ε, and LES) on the extent of non-uniformity for a range of Re numbers has been performed by researchers (Zhang et al., 2018; Minocha and Joshi, 2020). Due to the intensive computational time and transient nature of LES simulations, it was decided to consider the best turbulence model of the standard k–ε and the realizable k–ε models. The authors have found that the realizable k–ε model is able to predict the non-uniformity well for both low and high Reynolds numbers. Hence, the realizable k–ε turbulence model has been considered for the present simulations.

2.4 Assumptions

The assumptions in modeling are 1) steady-state flow. 2) Incompressible fluid and compressible effects if any are neglected. 3) The mode of heat transfer is by sensible heat only, and no condensation occurs inside the geometry. 4) There is no spatial variation of steam properties for the pressure and Re range considered. 5) Steam properties are for saturated steam at the pressure chosen. 6) Single-phase flow throughout the geometry and no condensation occurs.

2.5 Boundary conditions

The boundary conditions are as follows: the inlet velocity boundary condition for the inlet tube connecting the top header and pressure outlet was used for the outlet tube connecting the bottom header. A wall boundary condition was used for the tube and header walls.

2.6 Method of solution

Details of the solution of discretized linear algebraic equations for different variables are as follows: a second-order upwind discretization scheme was used for the pressure, velocity, and k and ε equations, while all the discretized equations were solved in a segregated manner with the PISO (Pressure-Implicit with Splitting of Operators) algorithm. The under-relaxation was set to 0.3 for pressure, 1 for density and body forces, 0.7 for momentum, and 0.8 for

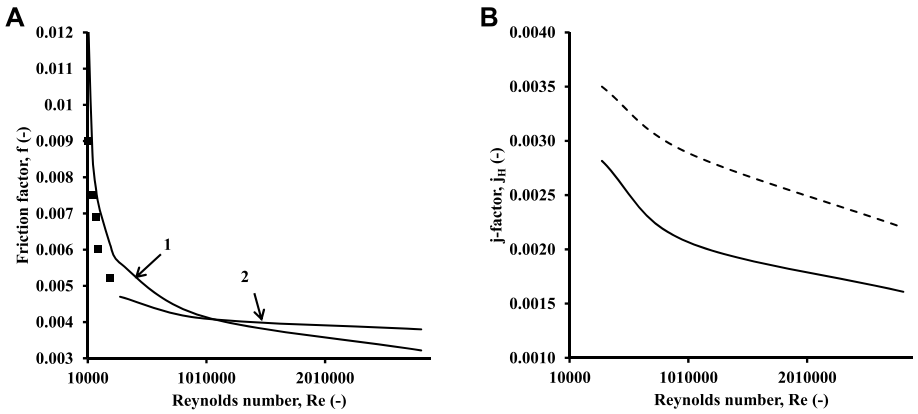

FIGURE 11
Friction factor and j-factor variation with Re for the without-distributor case. **(A)** Friction factor data prediction: 1) correlation and 2) CFD. Symbols denote experimental data of Gandhi et al. (2012). **(B)** j-factor vs. *Re*. Bold line: present work. Dotted line: j-factor for the tube-side of the shell and tube heat exchanger (Sinnott and Towler, 2019).

turbulence parameters. The solutions of the variables were considered to be fully converged when the sum of residuals was below 10^{-4}. All the computations were performed on an Intel machine with a quad-core processor with 4 GB RAM and 2.4 GHz processor speed.

2.7 Model validation

For model validation, the cases for Kubo and Uuda (1969) and Pigford et al. (1983) were simulated using ANSYS Fluent 14. The realizable k–ε model was able to capture the dynamics in all the three cases considered. The results of the mass flow ratio of experimental measurements from the published literature (Kubo and Ueda, 1969; Pigford et al., 1983) were compared with CFD predictions of simulations carried out on the same geometries for which experimental measurements were made. Good agreements between predicted and experimental results were obtained with a deviation in the range of 5–6% as shown in Figure 5. This is in agreement with the results of Gandhi et al. (2012) who used the same geometries to validate their model and found deviations of 8%. The higher deviations of Gandhi et al. (2012) are due to the fact that the authors used the standard k–ε model instead of the realizable k–ε model. The realizable k–ε model should be used for such simulations for high Reynolds number flows with high flow separation at the T-junctions (at the center in the present case) and stagnant zones at the end of the top and bottom headers (prominently in the present case) due to the limitations of the standard k–ε model. Furthermore, similar analysis carried out by Minocha and Joshi (2020) showed that the realizable k–ε model has been able to predict deviations within 5% for similar dividing manifolds.

3 Distributor configurations

In this subsection, optimization in terms of distance of the hole from the distributor to reduce flow non-uniformity has been carried out, and the best configuration has been chosen. The header and distributor plate used in the studies and the parameters associated with configurations are shown in Figure 6. Five different configurations were chosen for reducing the non-uniformity. The ratio of the distance between distributor plate perforations to the adjacent tube opening in the header (l_1) and the distance between the two consecutive perforations in the distributor (l_2) are vital in reducing the non-uniformity. Figure 6A shows the top view of the geometry created in ANSYS Workbench 14. The holes in the distributor represented by the yellow dotted circles are the configuration C_1 for which the magnitude of l_2 is very low. The dark circles represent the tube holes, while the bigger circle represents the inlet to the header. The white circles represent the configuration C_5 for which the magnitude of l_2 is the highest. This ratio was varied, and five configurations were defined (C_1–C_5). A detailed diagram of configuration 5 is provided in Figure 6B. Representative results of the reduction in %ENU with Re are shown in Table 3 for a pressure of 10 bar.

4 Results and discussion

In this section, the first flow patterns of the manifold with and without a distributor are presented to qualitatively understand the distribution in both cases for the three operating pressures considered. Furthermore, the quantitative understanding of improvement in distribution is represented in

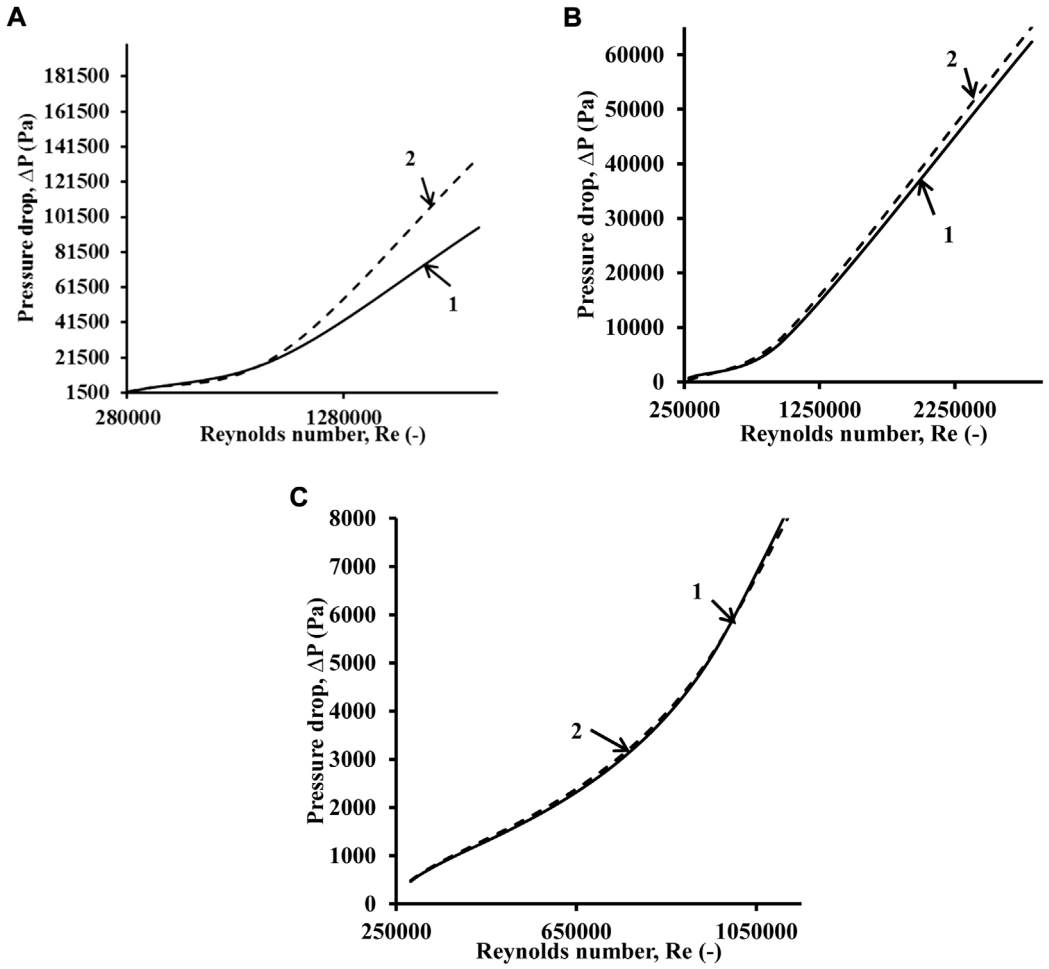

FIGURE 12
Pressure drop variation with the Reynolds number. **(A)** p = 10 bar, **(B)** p = 40 bar, and **(C)** p = 70 bar. 1) Bold line denotes the case without a distributor; 2) dotted line denotes the case with a distributor.

terms of velocity profiles. Quantification in terms of pressure drop variation and %ENU is also presented for both cases. All the data generated from the simulations have been used to develop an empirical correlation for the friction factor. The predictions of correlation are compared with the ones available for the conventional shell and tube heat exchangers for the same Re number range, and a correlation for heat transfer has been suggested using the Chilton–Colburn analogy.

4.1 Flow patterns

The flow distribution in manifolds depends on the type of flow being whether friction dominant, momentum dominant, or both. In the present geometry, the interplay of momentum and friction can be observed through the amount of flow passing through the central tube of the top header. The presence of a distributor brings in proper balance between the momentum and friction forces, resulting in a uniform distribution. This in turn improves the pressure recovery in the bottom header as well. In this section, we explain the velocity distribution for different Reynolds numbers for each pressure chosen. Furthermore, the pressure drop across the header tube assembly for the specified pressure range was also analyzed.

Figure 7 shows the velocity contours (2.82E+05 ≤ Re ≤ 1.91E+06) for a specified pressure of 10 bar. Figure 7 (A1) shows the velocity contour for flow distribution without a distributor for Re = 2.82E+05 and p = 10 bar, while Figure 7 (A2) shows the velocity contour for the same Re number and pressure for the geometry with a distributor. Figure 7 (A1) shows that the velocity in the central tube is 1.6 times the velocities of its neighboring tubes, while Figure 7 (A2) shows that the velocity in the central tube is nearly equal to that of its neighboring tubes. Similarly, Figure 7 (B1) shows the velocity of the central tube to be 1.69 times higher than its neighboring tubes, while Figure 7 (B2) shows an equal distribution in all tubes of the top

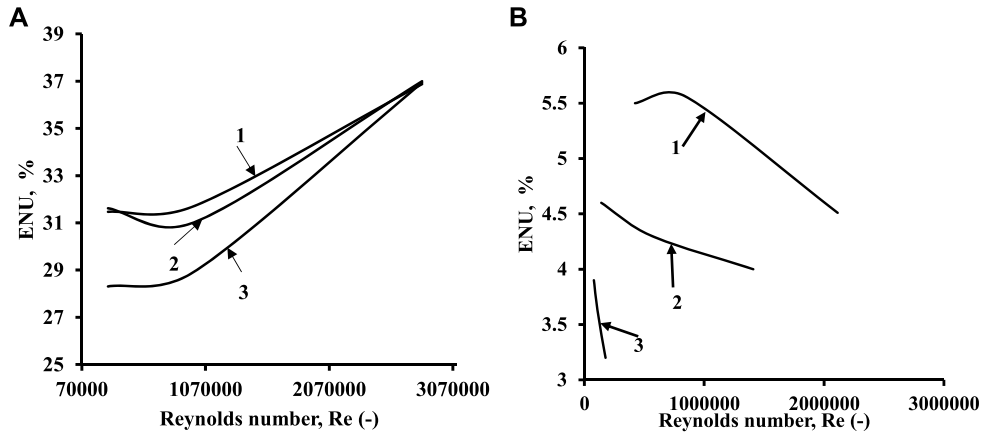

FIGURE 13
Variation of ENU with the Reynolds number for different pressures. **(A)** Without a distributor. **(B)** With distributor. Index: 1) p = 10 bar; 2) p = 40 bar; and 3) p = 70 bar.

header. For Figure 7 (C1), the central tube velocity is 1.72 times that of neighboring tubes, while near equal velocities are observed in Figure 7 (C2) with a distributor. With an increase in Re, it can be observed that the central tube velocity is 1.6–1.7 times the velocity in the adjacent tubes, while the cases with a distributor show the uniformity in distribution.

A similar observation to the ones found in Figure 7 can be observed in Figure 8. The velocities, as shown in Figures 8 (A1), (B1), and (C1), for central tubes are 1.75, 1.73, and 1.68 times the velocities of their neighboring tubes, respectively. With an increase in Re at this pressure, the velocity magnitudes of central tubes show a slight decreasing trend. Figures 8 (A2), (B2), and (C2), however, show equal velocities in all tubes.

Figure 9 shows velocity contours for a high pressure of 70 bar. The velocity magnitudes are lower due to the same Re maintained at an operating pressure of 70 bar. The velocities in the central tubes are 1.76, 1.72, and 1.8 times the velocities of the neighboring tubes for the geometry without a distributor as shown in Figures 9 (A1), 7 (B1), and 7 (C1), respectively.

4.2 Velocity profiles for the optimized design with a distributor

The flow patterns (velocity contours) in Section 5.1 show an improvement in flow distribution with the aim of comparing the flow patterns with and without a distributor. A further quantitative comparison of the flow distribution when a distributor is installed (with distributor case) has been provided in Figure 10. The comparison helps us understand the effect on flow distribution with an increase in inlet velocity. Curves 1, 2, and 3 are for the Reynolds number, which is constant (Re = 2.82E+05), and pressures are 10 bar, 40 bar, and 70 bar, respectively. The velocity profiles show an absolutely uniform distribution (0 %ENU) for these Reynolds numbers. Similarly, curves 4, 5, and 6 are for Re = 9.86E+05, and pressures are 10 bar, 40 bar, and 70 bar, respectively. For curve 4, the non-uniformity of approximately (%ENU) 2% is observed at the central tubes, while for curves 5 and 6, uniform distribution is observed. For higher velocity, (v = 95 m/s) Curve 7 is for Re = 1.91E+06 and a pressure of 10 bar. Here, the non-uniformity is approximately 4.5% (%ENU), which indicates that with the increase in Reynolds numbers, the non-uniformity from the configuration with a distributor increases. Previous studies have not investigated the extent of non-uniformity at this Re number and pressure. It should be noted that the configuration still gives better uniformity than previous studies, considering the fact that Re is higher than in previous studies. Curves 8 and 9 on the other hand show uniform distribution. Thus, the aforementioned analysis proves that the installation of a distributor facilitates good distribution within velocities of 5 < v < 96 m/s.

4.3 Development of correlations for the friction factor and Nusselt number

Pressure drop generally applied to manifolds (for example, plate heat exchangers) is given by as Eq. 1 as follows:

$$\Delta P = 4 f_{ch} \frac{\rho u^2}{2} \frac{L_e}{D_e}. \quad (1)$$

Pressure drop was obtained from the simulation data for different Reynolds numbers. Eq. 1 can be written for the friction factor as

$$f_{ch} = \frac{\Delta P}{\frac{2\rho u^2 L_e}{D_e}}. \quad (2)$$

The effect of the inlet pipe on the overall pressure drop has been neglected. Hence, the expression of equivalent diameter has been formulated as follows:

$$\mathbf{D_e} = \frac{\mathbf{2D_h^2 + 9D_t^2}}{\mathbf{2D_t + 9D_h}}. \quad (3)$$

The following correlations have been predicted for both cases:

1. Without a distributor:

$$f_{wod} = 0.119Re^{-0.243} \quad 10^4 \le \mathrm{Re} \le 3\mathrm{x}10^6; 0.8 \le \mathrm{Pr} \le 1.3; 10 \le \mathrm{P} \le 70\mathrm{bar}. \quad (4)$$

2. With a distributor:

$$f_{wd} = 0.119Re^{-0.25} \quad 10^4 \le \mathrm{Re} \le 3\mathrm{x}10^6; 0.8 \le \mathrm{Pr} \le 1.3; 10 \le \mathrm{P} \le 70\mathrm{bar}. \quad (5)$$

The validation for the correlation of the friction factor has been carried out by comparing the prediction of the correlation with experimental data of Gandhi et al. (2012) and then with the CFD predictions of the present work for the Re range. Figure 11A shows the friction factor for the case without a distributor. Both the magnitude and trends shown in Figure 11A are similar to the ones for turbulent flow through tubes as in the shell and tube heat exchangers with high values of friction factors for low Reynolds numbers. The decrease in the friction factor becomes less significant with an increase in Re. These results match well with experiments and CFD simulations with deviations ~6% with experimental data and ~10% with CFD data.

The Chilton–Colburn j-factor the relationship between momentum, heat, and mass transfer as follows:

$$j_h = \mathrm{St}Pr^{2/3} = f/2. \quad (6)$$

An analysis using the Chilton–Colburn j-factor (j_h) was also carried out. Figure 11B shows the comparison of j-factor variation for the present geometry without a distributor and the j-factors for the tube side in the shell and tube exchangers. The Re range (2.82 E+05 ≤ Re ≤ 2.82E+06) is used to make sure that the effect of baffles in the shell and tube heat exchangers (STHEs) is avoided. The slope of the decrease in the j-factor is nominal for the present geometry, while it is steeper for STHE. The deviations are attributed to two reasons: 1) vertical configuration in the present case and 2) large number of tubes in comparison to STHE.

Furthermore, an effort to predict an expression for heat transfer is taken though the scope is limited to friction and pressure drop. By applying the Chilton–Colburn analogy, the expression for the Nu number for both cases without a distributor and with a distributor is given as follows:

Without a distributor:

$$Nu = 0.0595Re^{0.757}Pr^{0.33} \quad 10^4 \le \mathrm{Re} \le 3\mathrm{x}10^6; 0.8 \le \mathrm{Pr} \le 1.3; 10 \le \mathrm{P} \le 70\mathrm{bar}. \quad (7)$$

With a distributor:

$$Nu = 0.0725Re^{0.75}Pr^{0.33} \quad 10^4 \le \mathrm{Re} \le 3\mathrm{x}10^6; 0.8 \le \mathrm{Pr} \le 1.3; 10 \le \mathrm{P} \le 70\mathrm{bar}. \quad (8)$$

The pressure drop variation for different Re and Pr ranges is performed using CFD simulations. Figures 12A–C show the pressure drop variation for all three pressures with and without a distributor. For high inlet velocities (~90 m/s), for p = 10 bar, the pressure drops for the configuration with the distributor range approximately 1.4 bar, while they are restricted to 0.08 bar for higher pressures (40 ≤ p ≤ 70 bars).

For all the pressures, 10 bar, 40 bar, and 70 bar, a seemingly linear trend is observed. Furthermore, most importantly, the geometry with a distributor is able to obtain a pressure recovery similar to the one without a distributor for the Reynolds number till 1.25E+06 and similar pressure losses. At higher Re, the increase in pressure losses is approximately 4–5%. An inference that can be drawn from this is that the fluid deceleration due to the presence of the distributor in the present design does not allow the friction forces to exorbitantly dominate over momentum forces. These results in controllable pressure increase even at high Re for the pressure range considered except in the case of 10 bar, where the pressure drops are higher and unless controlled would cause damage to upstream equipment due to back pressure. In other words, for inlet velocity magnitudes below 40 m/s, there is a reasonably good balance between the momentum and friction forces (if not equilibrium), and pressure drops are lower (<10,000 Pa) as far as pressure drop is concerned for both designs (with and without a distributor). However, as the velocities increase above 40 m/s, the friction forces overpower the momentum forces (friction dominant regime), causing a sudden increase in pressure drop.

Eqs. 4, 5, 7, 8 were found to be valid for a pressure drop range of 0.06 <Δp < 1.8 bar. Furthermore, the equations for cases with distributors would be valid for different distributor designs for the inlet velocities below 95 m/s and the Pr numbers and Re ranges mentioned. Simulations with a change in the diameter of the holes of the distributor and non-uniform pitch showed that the pressure drops might increase to a maximum by 0.05 bar for which Eqs. 5, 8 gave good predictions.

4.4 Extent of non-uniformity (ENU)

The average %ENU is defined similar to Gandhi et al. (2012) and is given by Eq. 9 as follows:

$$ENU = \sum_{i=1}^{N} \left| \frac{m_i - m_{avg}}{m_{avg}} \right| x100. \quad (9)$$

Figure 13A shows the ENU variation with Re over all the mentioned three pressures without a distributor, while

Figure 13B shows the ENU variation with a distributor. It is important to note that when there is no distributor, the %ENU variation varies from 30% to 40% for a pressure of 10, 40, and 70 bar. Figure 13B clearly shows that the non-uniformity is decreased to less than 2% for 70 bar pressures, while it is approximately 4% for 40 and 10 bar pressures.

5 Guidelines for the distributor design for the manifold

Following are the guidelines for designing a distributor for the manifold considered:

1 The perforations of the distributor should be misaligned from the tubes of the manifold.
2 The distributor can have perforations of single or multiple holes depending on the highest pressure drop for flows at high velocities.
3 The pitch between a single row of holes can be non-uniform, starting with the least pitch at the middle and increasing at a linear variation until the end of the distributor. This will again depend on the pressure drop limited to 1.8 bar.
4 The manifold tube diameter to distributor hole diameter ratio should not exceed more than 6 to avoid exceedingly high pressure drops.
5 The header to tube diameter ratios and pitch of the tubes should be as specified in the present work.
6 The distributor can have different sections of hole diameters and pitch for the central and ending sections provided the pressure drops are less than 1.8 bar.

6 Conclusion

Three-dimensional (3D) CFD simulations have been carried out for a header tube assembly for the central inlet and outlet of the top and bottom headers with and without a distributor. The following conclusions are drawn:

1 Incorporating a distributor in an existing design of a header tube assembly chosen for the present work promises good performance in terms of providing uniform flow distribution for a wide range of pressures and Reynolds numbers considered in the study. The non-uniformity is reduced to approximately 4% for the Re range (2.82E+05 ≤ Re ≤ 2.82E+06 and 10 ≤ P ≤ 70 bar). Thus, similar to microscale assemblies, the macroscale assemblies with the central inlet and outlet can also be classified into two variants, namely, (1) conservative without internals (all configurations considered by Gandhi et al. (2012)) and (2) baffle (with internals like perforated baffles as per the optimized design considered in the present work).
2 Pressure drop for such assemblies having the central inlet and outlet increases linearly for the Reynolds number range 7.5E+05 < Re < 1.91E+06 for P = 10 bar and 7.5E+05 < Re < 2.82E+06 for P = 40 bar, while for P = 70 bar and same Re range, there is a steady nonlinear increase following the power law profile.
3 The interplay of momentum and friction forces with respect to operating parameters like pressure and Re number shows different characteristics than anticipated. This is due to the interplay of the momentum and friction forces. For higher pressures (P = 40 and 70 bars) and Reynolds number range (70,000 < Re < 85,000)), there is a reasonable good force balance, while for lower pressures of 10 bar and Re number approximately 10^6 (velocities approximately 95 m/s, the momentum dominates over friction forces. For higher Reynolds numbers considered in the present study, momentum forces dominate friction forces, leading to flow non-uniformity. Installation of the distributor, however, ensures a reasonable balance between momentum and friction forces, causing a reduction in flow non-uniformity and a corresponding increase in pressure drop.
4 Correlations developed for the friction factor with and without distributors agree well within a 10% deviation with experimental data.
5 The j-factor becomes constant at high Re for the heat exchanger considered in the present work. The j-factor versus Re profiles for the present geometry differs from the conventional j-factors for STHE with flatter profiles after Re = 9×10^4.
6 The correlation for the Nusselt number has been presented based on the Chilton–Colburn analogy. A detailed heat transfer study is beyond the scope of the present work.
7 The correlations for both the friction factor and Nusselt number would be applicable for other distributor designs with pressure drops as high as 1.85 bar in Re and Pr ranges as in the present analysis.
8 Appropriate guidelines for a distributor design for such type of manifold have been provided.

7 Future work

Two-phase simulations (pure steam condensation inside tubes) in such exchangers need to be investigated for studies on pressure drop and heat transfer, and correlations need to be developed. This can then be extended to condensation in the presence of non-condensable gases like air and helium and compared with analytical models and experimental measurements.

Data availability statement

The simulation data supporting the conclusion of this article will be made available by the authors, without undue reservation.

Author contributions

Conceptualization, AG and AP; methodology, AG; software, AG; validation, AG; formal analysis, AG; investigation, AG; resources, AG; data curation, AG; writing—original draft preparation, AG; writing—review and editing, AG; visualization, AG; supervision, AP; project administration, AG; and funding acquisition, AG. All authors have read and agreed to the published version of the manuscript.

Conflict of interest

The authors declare that the research was conducted in the absence of any commercial or financial relationships that could be construed as a potential conflict of interest.

Publisher's note

All claims expressed in this article are solely those of the authors and do not necessarily represent those of their affiliated organizations, or those of the publisher, the editors, and the reviewers. Any product that may be evaluated in this article, or claim that may be made by its manufacturer, is not guaranteed or endorsed by the publisher.

References

Acrivos, A., Babcock, B., and Pigford, R. (1959). Flow distributions in manifolds. *Chem. Eng. Sci.* 10, 112–124. doi:10.1016/0009-2509(59)80030-0

Alaqel, S., Saleh, N. S., Saeed, R., Djajadiwinata, E., Sarfraz, M., Alswaiyd, A., et al. (2022). Particle-to-fluid direct-contact counter-flow heat exchanger: Simple-models validation and integration with a particle-based central tower system. *Case Stud. Therm. Eng.* 33, 101994. doi:10.1016/j.csite.2022.101994

Arsenyeva, O., Tovazhnyanskyy, L., Kapustenko, P., and Demirskiy, O. (2012). Heat transfer and friction factor in criss-cross flow channels of plate-and-frame heat exchangers. *Theor. Found. Chem. Eng.* 46, 634–641. doi:10.1134/s0040579512060024

Bassiouny, M. K., and Martin, H. (1984). Flow distribution and pressure drop in Plate heat exchangers—I U-type arrangement. *Chem. Eng. Sci.* 39, 693–700. doi:10.1016/0009-2509(84)80176-1

Buerkle, F., Moyon, F., Feierabend, L., Wartmann, J., Heinzel, A., Czarske, J., et al. (2020). Investigation and equalisation of the flow distribution in a fuel cell stack. *J. Power Sources* 448, 227546. doi:10.1016/j.jpowsour.2019.227546

Dahikar, S. K., Ganguli, A. A., Gandhi, M. S., Joshi, J. B., and Vijayan, P. K. (2013). Heat transfer and flow pattern in co-current downward steam condensation in vertical pipes-I: CFD simulation and experimental measurements. *Can. J. Chem. Eng.* 91, 959–973. doi:10.1002/cjce.21722

Devia, F., Marchitto, A., Fossa, M., and Guglielmini, G. (2015). CFD simulations devoted to the study of fitting effects on the phase distribution in parallel vertical channels. *Int. J. Chem. React. Eng.* 13, 551–559. doi:10.1515/ijcre-2014-0156

Gandhi, M. S., Ganguli, A. A., Joshi, J. B., and Vijayan, P. K. (2012). CFD simulation for steam distribution in header and tube assemblies. *Chem. Eng. Res. Des.* 90, 487–506. doi:10.1016/j.cherd.2011.08.019

Ganguli, A. A., Dahikar, S. K., Gandhi, M. S., Joshi, J. B., and Vijayan, P. K. (2013). Heat transfer and flow pattern in co-current downward steam condensation in vertical pipes-II: Comparison with published work. *Can. J. Chem. Eng.* 91, 974–991. doi:10.1002/cjce.21719

Ganguli, A. A., Pandit, A. B., Joshi, J. B., and Vijayan, P. K. (2011). Hydrodynamic and heat transfer characteristics of a centrally heated cylindrical enclosure: CFD simulations and experimental measurements. *Chem. Eng. Res. Des.* 89, 2024–2037. doi:10.1016/j.cherd.2011.02.003

Ganguli, A. A., Sathe, M. J., Pandit, A. B., Joshi, J. B., and Vijayan, P. K. (2010). Hydrodynamics and heat transfer characteristics of passive decay heat removal systems: CFD simulations and experimental measurements. *Chem. Eng. Sci.* 65, 3457–3473. doi:10.1016/j.ces.2010.02.031

Ghasabehi, M., Ashrafi, M., and Shams, M. (2021). Performance analysis of an innovative parallel flow field design of proton exchange membrane fuel cells using multiphysics simulation. *Fuel* 285, 119194. doi:10.1016/j.fuel.2020.119194

Gilmore, N., Hassanzadeh-Barforoushi, A., Timchenko, V., and Menictas, C. (2021). Manifold configurations for uniform flow via topology optimisation and flow visualisation. *Appl. Therm. Eng.* 183, 116227. doi:10.1016/j.applthermaleng.2020.116227

Gusew, S., and Stuke, R. (2019). Pressure drop in Plate heat exchangers for single-phase convection in turbulent flow regime: Experiment and theory. *Int. J. Chem. Eng.* 2019, 1–11. doi:10.1155/2019/3693657

Hadad, Y., Rangararajan, S., Nemati, K., Ramakrishnann, B., Pejman, R., Chiarot, P. R., et al. (2020). Performance analysis and shape optimization of a water-cooled impingement micro-channel heat sink including manifolds. *Int. J. Therm. Sci.* 148, 106145. doi:10.1016/j.ijthermalsci.2019.106145

Ji, F., Yang, L., Li, Y., Sun, H., and Sun, G. (2019). An experimental method to measure flow distribution in the cathode of high-temperature polymer electrolyte membrane fuel cells stack. *Energy Technol.* 7, 1900416. doi:10.1002/ente.201900416

Ju, X., Xu, C., Zhou, Y., Liao, Z., and Yang, Y. (2018). Numerical investigation of a novel manifold micro-pin-fin heat sink combining chessboard nozzle-jet concept for ultra-high heat flux removal. *Int. J. Heat Mass Transf.* 126, 1206–1218. doi:10.1016/j.ijheatmasstransfer.2018.06.059

Kadijani, O. N., Moghadam, H. K., Ajarostaghi, S. S. M., Asadi, A., and Pour, M. S. (2022). Hydrothermal performance of humid air flow in a rectangular solar air heater equipped with V-shaped ribs. *ENERGY Sci. Eng.* 10, 2276–2289. doi:10.1002/ese3.1136

Kazemi Moghadam, H., Mousavi Ajarostaghi, S. S., and Poncet, S. (2021). Numerical modeling of an innovative arc shape rib based solar air heater. *Proc. Institution Mech. Eng. Part C J. Mech. Eng. Sci.* 235, 7992–8012. doi:10.1177/09544062211039541

Kubo, T., and Ueda, T. (1969). On the characteristics of divided flow and confluent flow in headers. *Bull. JSME* 12, 802–809. doi:10.1299/jsme1958.12.802

Lim, B., Majlan, E., Daud, W., Rosli, M., and Husaini, T. (2018). Numerical analysis of flow distribution behavior in a proton exchange membrane fuel cell. *Heliyon* 4, e00845. doi:10.1016/j.heliyon.2018.e00845

Midoux, N., and Tondeur, D. (2015). The theory of parallel channels manifolds (ladder networks) revisited part 2: Design for uniform cross-flow distribution. *Can. J. Chem. Eng.* 93, 121–140. doi:10.1002/cjce.22099

Minocha, N., and Joshi, J. B. (2020). 3D CFD simulation of turbulent flow distribution and pressure drop in a dividing manifold system using openfoam. *Int. J. Heat Mass Transf.* 151, 119420. doi:10.1016/j.ijheatmasstransfer.2020.119420

Mohammadali, R., Bayareh, M., and Sheikhzadeh, G. A. (2021). Study of flow uniformity within convergent microchannels with a circular manifold. *J. Braz. Soc. Mech. Sci. Eng.* 43, 74–10. doi:10.1007/s40430-020-02784-7

Mousavi Ajarostaghi, S. S., Aghanezhad, M., Davudi, H., and Mohammadzadeh Amiri, M. (2021). Numerical evaluation of the heat transfer enhancement in a tube with a curved conical turbulator insert. *Int. J. Ambient Energy*, 1–14. doi:10.1080/01430750.2021.1945490

Pigford, R. L., Ashraf, M., and Miron, Y. D. (1983). Flow distribution in piping manifolds. *Ind. Eng. Chem. Fund.* 22, 463–471. doi:10.1021/i100012a019

Salhi, J. E., Mousavi Ajarostaghi, S. S., Zarrouk, T., Saffari Pour, M., Salhi, N., and Salhi, M. (2022). Turbulence and thermo-flow behavior of air in a rectangular channel with partially inclined baffles. *Energy Sci. Eng.* 10, 3540–3558. doi:10.1002/ese3.1239

Sinnott, R., and Towler, G. (2019). *Chemical engineering design*. SI Edition. Butterworth-Heinemann.

Tomor, A., and Kristóf, G. (2016). Validation of a discrete model for flow distribution in dividing-flow manifolds: Numerical and experimental studies. *Period. Polytech. Mech. Eng.* 60, 41–49. doi:10.3311/ppme.8518

Turek, V., Kohoutek, J., Jegla, Z., and Stehlík, P. (2009). Contribution to analytical calculation methods for prediction of uniform fluid flow dividing in tubular distributor. *Chem. Eng. Trans.* 18, 809–814. doi:10.3303/CET0918132

Wang, J. (2011). Theory of flow distribution in manifolds. *Chem. Eng. J.* 168, 1331–1345. doi:10.1016/j.cej.2011.02.050

Wang, J., and Wang, H. (2015). Discrete method for design of flow distribution in manifolds. *Appl. Therm. Eng.* 89, 927–945. doi:10.1016/j.applthermaleng.2015.06.069

Wei, X. L., Wang, Q. H., and Pan, M. Q. (2010). Numerical simulation of velocity distribution among microchannels with bifurcation structures as manifolds. *Adv. Mater. Res. Trans Tech Publ* 108-111, 1009–1012. doi:10.4028/www.scientific.net/AMR.108-111.1009

Zeng, S., and Lee, P. S. (2018). "A header design method for target flow distribution among parallel channels based on topology optimization," in Proceedings of the 2018 17th IEEE intersociety conference on thermal and thermomechanical phenomena in electronic systems (ITherm): IEEE, San Diego, CA, USA, 29 May 2018-01 June 2018, 156–163.

Zhang, W., Li, A., Gao, R., and Li, C. (2018). Effects of geometric structures on flow uniformity and pressure drop in dividing manifold systems with parallel pipe arrays. *Int. J. Heat Mass Transf.* 127, 870–881. doi:10.1016/j.ijheatmasstransfer.2018.07.111

Zhao, C., Wang, C., Zhang, T., and Pu, J. (2017). "Flow distribution analysis in the SOFC stack using CFD technique," in Proceedings of the International Conference on Fuel Cell Science, Engineering and Technology: American Society of Mechanical Engineers). V001T002A003, Charlotte, NC, June 26–30, 2017.

Zhao, C., Yang, J., Zhang, T., Yan, D., Pu, J., Chi, B., et al. (2020). Numerical modeling of manifold design and flow uniformity analysis of an external manifold solid oxide fuel cell stack. *Int. J. Hydrogen Energy* 45, 14440–14451. doi:10.1016/j.ijhydene.2020.02.143

Zhuang, X., Xia, X., Xu, X., and Li, L. (2020). Experimental investigation on hydrogen production by methanol steam reforming in a novel multichannel micro packed bed reformer. *Int. J. Hydrogen Energy* 45, 11024–11034. doi:10.1016/j.ijhydene.2020.02.034

Zhuang, X., Xu, X., Li, L., Xin, X., and Xu, W. (2019). "CFD and experimental analyses of flow distribution uniformity in minichannel reactors with a bifurcation structure manifold," in Proceedings of the IOP Conference Series: Earth and Environmental Science: IOP Publishing, Macao, China, 21–24 July 2019, 012045.

Zoljalali, M. A., and Omidbakhsh Amiri, E. (2020). Study of the flow distribution in parallel micro-channels with a triangular manifold. *J. Braz. Soc. Mech. Sci. Eng.* 42, 46–49. doi:10.1007/s40430-019-2140-x

Notations

C_n notations for different configurations (-); n varies from 1 to 5

D_e equivalent diameter of the channel (m)

D_h diameter of the header (m)

D_p pitch (m)

D_t tube diameter (m)

ENU extent of non-uniformity (-)

f Fanning friction factor (-)

f_{ch} Fanning friction factor in a channel (-)

f_{wod} Fanning friction factor for the without-distributor case (-)

f_{wd} Fanning friction factor for the with-distributor case (-)

H height of the tube connecting the headers (m)

h heat transfer coefficient (W m^{-2} K^{-1})

i iteration number

j_h j-factor as in the Chilton–Colburn analogy

k thermal conductivity of the fluid (W m^{-2} K^{-1})

l_1 ratio of the distance between distributor plate perforations to the adjacent tube opening in the header

l_2 the distance between the two consecutive perforations in the distributor

L header length (m)

L_e effective length of the manifold (m)

m_i mass flow rate of individual tubes (kg/s)

m_{avg} average mass flow rate (kg/s)

$Nu\ (hD/k)$ Nusselt number (-)

N number of tubes (-)

ΔP pressure drop in a channel

P pressure (bar)

Pr Prandtl number, $(C_p\mu/k)$(-)

Re Reynolds number $(Du\rho/\mu)$(-)

u, average velocity in a channel (m/s).

Greek symbols

ρ density of the fluid (kg m^{-3})

μ viscosity of the fluid (kg $m^{-1}s^{-1}$)

C_p specific heat of the fluid (J kg^{-1} K^{-1}).

frontiers | Frontiers in Energy Research

TYPE Original Research
PUBLISHED 12 January 2023
DOI 10.3389/fenrg.2022.1091322

OPEN ACCESS

EDITED BY
Cong Qi,
China University of Mining and Technology, China

REVIEWED BY
Zhekang Dong,
Hangzhou Dianzi University, China
Tiantian Chen,
China University of Mining and Technology, China

*CORRESPONDENCE
Zengyu Wang,
wangzengyugzps@gmail.com

SPECIALTY SECTION
This article was submitted to Process and Energy Systems Engineering, a section of the journal Frontiers in Energy Research

RECEIVED 06 November 2022
ACCEPTED 30 December 2022
PUBLISHED 12 January 2023

CITATION
Chen Z, Ma C, Ren J, Hao F and Wang Z (2023), Research on the identification method of safety wearing of electric power workers based on deep learning. *Front. Energy Res.* 10:1091322. doi: 10.3389/fenrg.2022.1091322

Research on the identification method of safety wearing of electric power workers based on deep learning

Zetao Chen, Cangui Ma, Jie Ren, Fangzhou Hao and Zengyu Wang*

Tianhe Power Supply Bureau of Guangzhou Power Supply Bureau, Guangdong Power Co., Ltd., Guangzhou, China

Aiming at the difficulties of manual monitoring and compliance with the current wear identification of electric power workers, the detection and identification of safety helmets, work clothes, and insulating gloves are used to carry out normative identification and warning, and a deep learning-based power worker safety wear identification method is proposed in this paper. The AlexNet and Inception are introduced to increase the width and depth of the artificial neural network. At the same time, the ReLU activation function with better performance is used to reduce the amount of network computation, and the Global Average Pooling layer is used to replace the fully connected layer with more parameters. The improved convolution neural network model has a total of 13 layers. In order to prevent the network from overfitting, the Early-stopping mechanism and the L2 regularization method are used to improve the performance of the network model. The experimental results show that the algorithm can achieve a good recognition effect on the staff who do not wear safety according to the regulations in the video, and the feasibility and effectiveness of the algorithm in practical application are verified.

KEYWORDS

deep learning, convolutional neural network, electric power work, safety wear recognition, safety

1 Introduction

As computer performance steadily improves, deep learning contributes to the development of society (Dourado et al., 2020; Liu et al., 2022). The environment of power construction sites is complex, and the types of tasks are diverse, so compliance with tooling is the basic requirement for safe production (Liu et al., 2020; Postalcıoğlu, 2020). Correctly wearing safety helmets and tooling can protect the personal safety of operators to a large extent (Jacob and Darney, 2021). However, due to the slack and negligence of the operators themselves and the relaxed vigilance of the management personnel, safety risks in the construction process have occurred from time to time (Yuan et al., 2022). To this end, a deep learning-based power worker safety-wearing recognition method is proposed to identify operators who do not wear tooling correctly and remind them in time, which can improve the effectiveness of supervision, enhance the safety awareness of operators, reduce potential safety risks, and ensure that construction safety is of great significance.

At present, the safety wear detection based on deep learning method is in its infancy, and few scholars have studied it. Literature (Gangolells et al., 2010) proposed a parallel two-way convolution neural network method to identify human body by improving LeNet 5, and then recognized helmet by color features, which basically met the demand. Literature (Mroszczyk, 2015) realized pedestrian detection by constructing a multi-layer convolutional neural network

(CNN), and then recognized helmets through both color and HOG features. In literature (Anastasiadou et al., 2021), OpenPose was used to locate the head and neck of the human body and automatically intercept the small enclosure sub images around it, and then Faster R-CNN was used to detect the safety helmet in the sub images. This kind of method still recognizes the human body first and then the safety wear. There are two parts of errors, so the defects of traditional detection methods still exist. Literature (Chen et al., 2022a) uses the improved YOLO V3 network to detect helmets with the whole human body as the detection target, but the detection accuracy is not very high because there are many features in the human body.

With the great contribution of deep learning to the field of target detection, relevant researchers are committed to combining deep learning with target detection of substation equipment. Literature (Yu et al., 2021) proposed a multi-target positioning method for infrared image of power equipment based on improved FAsT Match algorithm. This method overcomes the shortcomings of previous algorithms that are not suitable for infrared image target location and can only achieve single target location. However, the interference of complex background on target location is not considered, and changing different scenes may lead to poor recognition accuracy. The author of the literature (Qin et al., 2022) proposes a power equipment image recognition approach for the problem that the traditional methods are not clear in the classification of image features of power equipment, resulting in poor image recognition effect and difficulty in ensuring safe operation. The method can complete the effective identification of the collected images within 30s, which has a good practical application effect. According to (Yang et al., 2022), the Faster R-CNN was able to reduce the complexity of the RPN network by optimizing its convolution kernel. Reference (Yang et al., 2020), based on the recognition of the importance of safety helmet detection in construction site management, and considering practical issues such as cost control of hardware facilities in engineering projects, proposed a lightweight and improved version LT based on the deep learning network Tiny-YOLO v3 helmet detection technology method. Reference (Tang et al., 2020) designed a deep learning-based safety helmet and mask detection system in power construction scenarios by improving the CenterNet algorithm. Combined with system functions, it can effectively adapt to the detection of safety helmets and masks in power construction scenarios identification and violation management. Reference (Li et al., 2019) proposes an improved YOLO-v3 network for the problems of occlusion, variable illumination, and different target sizes in helmet detection under the complex background of the construction work surface. Due to the huge amount of computation and parameters, convolutional neural networks usually rely on hardware with strong computing power, such as GPU, to complete the training and inference process, but they often do not have high-performance computing hardware in construction sites. Additional purchases will bring unnecessary economic burdens to production enterprises.

Whether it is deep learning or traditional methods, the research on safety wear detection at home and abroad is still at the initial stage, and the accuracy of good and bad cannot evaluate the quality of each detection method. In addition, the following problems still exist in helmet wearing detection: 1) Single scene. Most of the detection environments studied are single and ideal, which are not close to the actual application scenarios, making their practicability greatly reduced. 2) The detection method of first detecting pedestrians and then locating the head. Most detection methods adopt this two-step detection method, which will lead to failure to give accurate warning

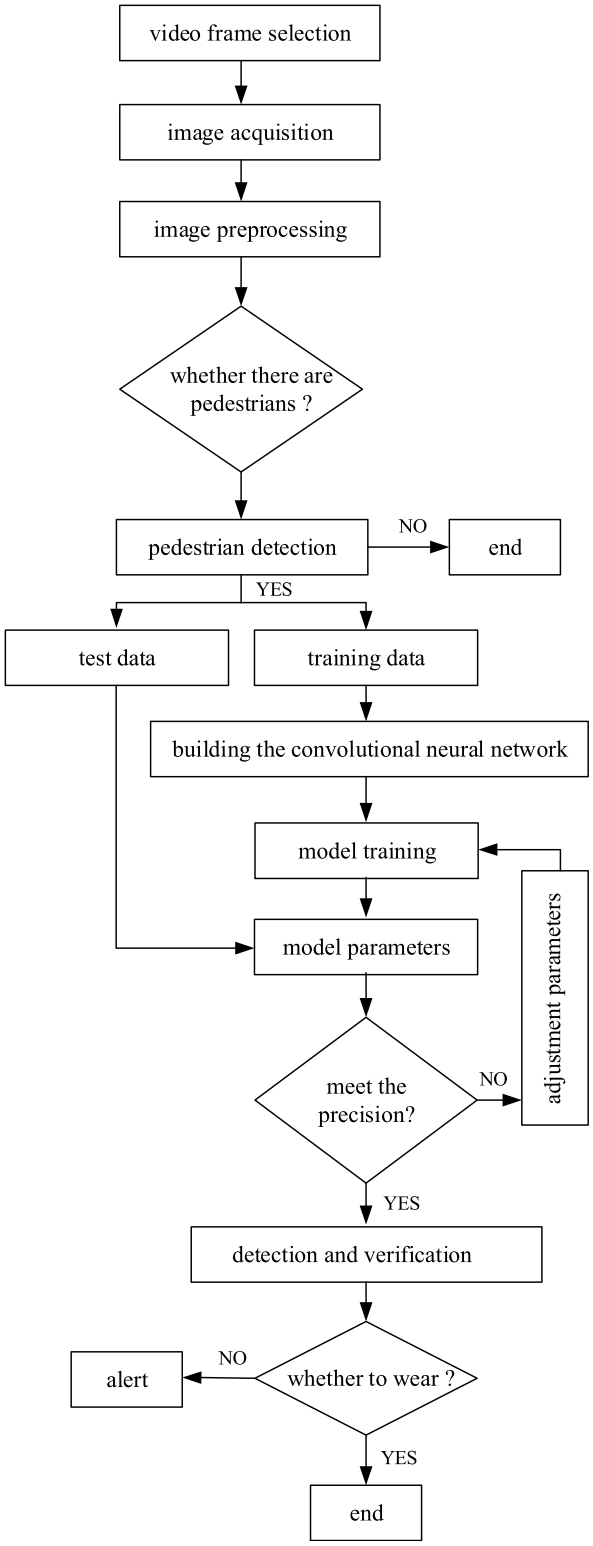

FIGURE 1
The identification process of safety wearing of electric power workers.

TABLE 1 Annotation of training samples.

Pilot electric room scene	Main category	Subcategory	Number of samples
Wear normative identification	Helmet	Red	280
		Blue	439
		White	184
	Work clothes (jacket)	Dark blue	509
		Light blue	288
		Blue	307
	Work pants	Dark blue	405
		Light blue	267
		Blue	229
	Insulated gloves	Black-brown	244
		Orange	306
		Light yellow	260
Work Behavior Status Recognition	Hand-held joystick	Handheld joystick without gloves	295
		Wear gloves while holding the joystick	287

information on whether to wear a helmet once the person is missed. Aiming at the difficulties of manual monitoring and compliance with the current wear identification of electric power workers, the detection and identification of safety helmets, work clothes, and insulating gloves are used to carry out normative identification and warning, and a deep learning-based power worker safety wear identification method is proposed. The main contributions of this paper are summarized as follows.

1) The AlexNet and Inception are introduced to increase the width and depth of the artificial neural network. At the same time, the ReLU activation function with better performance is used to reduce the amount of network computation.
2) The Global Average Pooling layer is used to replace the fully connected layer with more parameters. The improved convolution neural network model has a total of 13 layers.
3) In order to prevent the network from overfitting, the Early-stopping mechanism and the L2 regularization method are used to improve the performance of the network model.

This paper is organized as follows: The first section establishes the design framework for the identification of safety wearing of electric power workers; the second section establishes a deep learning-based safety wearing identification model and evaluation index for electric power workers; the third section is experiment verification and analysis; the last section is the conclusion.

2 Design framework for safety wearing identification of electric power workers

The safety wear identification process of electric power workers is divided into five steps. Firstly, select the frame of the video, convert the intercepted single-frame picture into a JPG format picture that the model can process, and input it into the pedestrian detection model to determine whether a pedestrian is detected. If a pedestrian is detected, proceed to the next stage of identification; The image after format conversion is preprocessed to make it meet the requirements of the model for image recognition; then, the model parameters are fine-tuned based on the training and test results, and finally realize image classification to meet the requirements of recognition accuracy, and return the wear recognition result. Figure 1 shows the safety wear identification process of electric power workers.

3 Safety wears recognition approach for electric power workers

3.1 Data preprocessing

In this paper, 4,300 site photos were collected at different construction sites and stages, and the samples were expanded to 8,600 by means of horizontal mirror image data enhancement. A data set containing 24,650 safety helmets of different scales, different light intensities and different shielding conditions was made. The ratio of training set and verification set during the training process was 8:2. Based on the samples in the pilot electric room scenario. The number of markings for pedestrians, work clothes, work caps, gloves, hand-held operations, and poles is shown in Table 1. The data preprocessing steps are as follows.

1) Resampling the training set data.
2) For the purpose of training and testing neural networks more easily, the size of the pictures is normalized, and the sizes of all pictures are normalized to 32*32.
3) Image enhancement using histogram equalization. Histogram equalization enhances contrast by transforming pixel intensities, turning the histogram distribution of an image into an approximately uniform distribution.

4) The image pixels are normalized to the [−1, 1] interval.
5) Set the random flip angle of the image to 10°, the random horizontal or vertical offset of the image to .08, and the random zoom parameter of the image to .2.

3.2 Model improvement strategies

At present, although the CNN algorithm has achieved a high recognition rate, the computational load is relatively large and does not meet the real-time requirements (Ramcharan et al., 2017). In practical application scenarios, it is not only necessary to take into account the accuracy of the identification of electric power workers' safety work, but also to consider the real-time nature of the identification, to inform the electric power workers in time and prevent the occurrence of safety accidents (Ker et al., 2017; Mezgec et al., 2019). Therefore, to improve the real-time performance of the CNN algorithm, we need to prune the original network model and propose a lightweight network model. Under the condition of ensuring the same accuracy, the recognition speed of the network model is accelerated, and the real-time performance of the network model is improved. This paper improves the CNN algorithm in the following aspects.

1) Replace the convolution kernels of all convolutional layers with 3*3 convolution kernels. Two 3*3 convolutional layers are equivalent to a 5*5 convolutional layer, and three 3*3 convolutional layers are equivalent to a 7*7 convolutional layer, in the case of the same field of view, the network level is deepened, the non-linear transformation is added, the feature learning ability of the network is stronger, and the network capacity is larger. Compared with the large convolution kernels of 5*5 and 7*7, the number of parameters of the small convolution kernel of 3*3 is significantly reduced.
2) The convolutional neural network is widened and deepened through the introduction of AlexNet and Inception. The Inception module combines convolutions of different scales on the same layer of convolution, and uses a 1*1 convolution kernel for feature dimensionality reduction. In the case of the same parameters, the network uses the Inception module to calculate more efficiently, extract more features, and train better.
3) Use the batch normalization method to process the input batch samples (Bashar, 2019). In order to unify the data distribution of each layer of the network, batch normalization is introduced after each convolutional layer, and the data of each layer is normalized to a mean of 0 and a variance of 1. The formula for batch normalization is:

$$\hat{x}^{(k)} = \frac{x^{(k)} - E[x^{(k)}]}{\sqrt{\mathrm{Var}[x^{(k)}]}} \tag{1}$$

where, $E[x^{(k)}]$ is the average value of each batch of training data neurons; $\sqrt{\mathrm{Var}[x^{(k)}]}$ is the standard deviation of the activation degrees of each batch of data neurons.

To protect the feature distribution learned by the network, the network changes are reconstructed and learnable parameters γ and β are introduced to inverse normalization, so $y^{(k)} = \gamma^{(k)}\hat{x}^{(k)} + \beta^{(k)}$. The batch normalization algorithm can prevent gradient disappearance or gradient explosion to some extent.

4) Use the ReLU activation function with better performance instead of the Sigmoid activation function, it can be expressed as:

$$\sigma(x) = \frac{1}{1 + e^{-x}} \tag{2}$$

When the Sigmoid activation function is used, there are the following three obvious disadvantages: 1) The network input is too large or small, the neuron gradient will tend to zero, and the neuron gradient will disappear during backpropagation, which will cause the neural network to fail to train; 2) The output means of sigmoid activation function is non-zero, and the non-zero mean signal output by the neurons in the previous layer will be used as the input signal of neurons in the next layer. When the input data is positive, the gradient will always be updated in the positive direction; 3) The calculation of the sigmoid activation function is more complicated, which will increase the network training time for large-scale deep networks (Aggarwal, 2019). The formula of the ReLU activation function is:

$$\sigma(x) = \max(0, x) \tag{3}$$

Compared with the Sigmoid activation function, the ReLU activation function performs better and helps in the propagation of gradients. The ReLU activation function has a relatively small amount of calculation, and only needs to do one arithmetic operation. The ReLU activation function is always 1 for the part greater than 0, and the gradient will not be saturated (the gradient will not be too small). During the backpropagation process, the gradient can be better propagated to the previous network, and the network will converge faster. The improved structure parameters of the CNN model are shown in Table 2.

About the improved CNN model, the input layer is a 32*32 work picture of electric power workers. There are four convolutional layers, the activation functions are all ReLU, the stride is 1, the padding equal to the same, and zeros are filled around the input picture. The size of the convolution kernels of the first and seventh layers of convolutional layers are both 3*3, and the number of convolutional kernels is 64 and 256 respectively. The third and fifth layers of convolutional layers are Inception modules, which consist of four parts.

3.3 Selection of the last convolutional layer

The number of neurons in the last convolutional layer is set to 128, 256 and 512 respectively, and the experimental results under different numbers of convolutional neurons are compared and analyzed, as shown in Table 3. According to the results, when the number of neurons in the last convolutional layer is 256, the recognition rate of the model is the highest, so the number of neurons in the last convolutional layer is selected as 256.

3.4 Optimizer selection

To select the better optimizer, the optimizers of the stochastic gradient descent algorithm (SGD) (Sharma, 2018), Momentum algorithm (Li et al., 2021), Adagrad algorithm (Traoré and Pauwels, 2021), RMS prop algorithm (Xu et al., 2021), and Adam algorithm (Jais et al., 2019) are compared with the gradient descent algorithm. Table 4 shows the performance of the network model in different optimization algorithms.

TABLE 2 Improved structure parameters of convolution neural network.

Network layer	Layer type	Kernel size	Stride	Feature map
0	Input layer	–	–	32*32*3
1	Convolutional layer	3*3	1	32*32*64
2	Pooling layer	2*2	2	16*16*64
3	Inception_v1	–	–	16*16*128
4	Pooling layer	2*2	2	8*8*128
5	Inception_v2	–	–	8*8*256
6	Pooling layer	2*2	2	4*4*256
7	Convolutional layer	3*3	1	4*4*256
8	GlobalAvg_pool	–	–	256
9	Softmax	–	–	43

TABLE 3 Comparison of the number of neurons in the last convolution layer.

Last convolutional layer	Training time/s	Recognition rate/%
128	1333	97.94
256	1609	98.59
512	1985	98.06

TABLE 4 Experimental results of different optimizers.

Optimizer	Parameters	Training time/s	Recognition rate/%
SGD	Momentum = 0.9	2389	94.74
Momentum	Rho = .95	2391	97.87
Adagrad	—	2450	97.07
RMSprop	Rho = 0.9	1,887	98.47
Adam	Beta1 = .9, Beta2 = .999	1606	98.59

In Table 4, when the network model adopts the Adam optimizer, the training time of the network model is the shortest and the recognition rate is the highest, so the Adam optimizer is used to identify the safety wear of electric power workers.

The loss function in the algorithm of safe wear recognition is designed as follows:

$$L(s, y) = \frac{1}{n}\sum_{t=1}^{n}(s_t - y_t)^2 \tag{4}$$

In 4), y is the label value; s is the predicted value of the network forward propagation.

The back-propagation process is as follows:

$$\frac{\partial L}{\partial s} = \frac{2}{n}\left((s_1 - y_1), \ldots, (s_n - y_n)\right) \tag{5}$$

3.5 Evaluation indicators

To evaluate the recognition effect, the average accuracy index is used to measure the matching accuracy of the detection frame to the target object, it can be expressed as follows (Chen et al., 2022b):

$$AP_i = \frac{\sum \frac{N(\text{TruePositives})_i}{N(\text{Totalobjects})_i}}{N(\text{TotalImages})_i} \tag{6}$$

where, $N(\text{TruePositives})_i$ is the actual quantity of pictures at ith category; $N(\text{Totalobjects})_i$ is the quantity of all objects at the data set category i; $N(\text{TotalImages})_i$ is the number of images containing objects in the category i.

The average precision metric is:

$$mAP = \sum_{i}^{N} AP_i \Big/ N \tag{7}$$

TABLE 5 Setting of network training parameters.

Parameter	Parameter value
Enter image size	32*32
Dynamic learning rate	The initial learning rate is .001, monitor = "val_loss", min_1r = 10^{-6}, factor = .1, patience = 10
Mini-batch	64
Epoch	40
Weight decay term for L2 regularization	10^{-5}
Early-stopping early stop mechanism	monitor = "val_loss", patience = 50, verbose = 2
Loss function	Cross-drop loss function

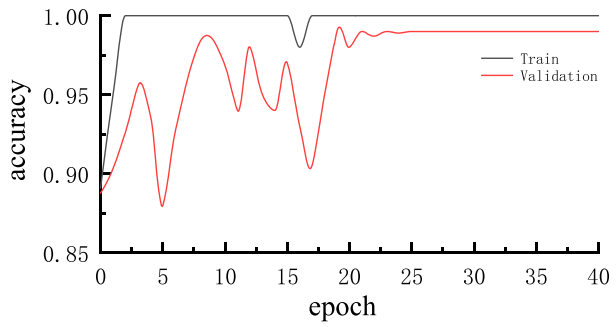

FIGURE 2
Accuracy curve of network training.

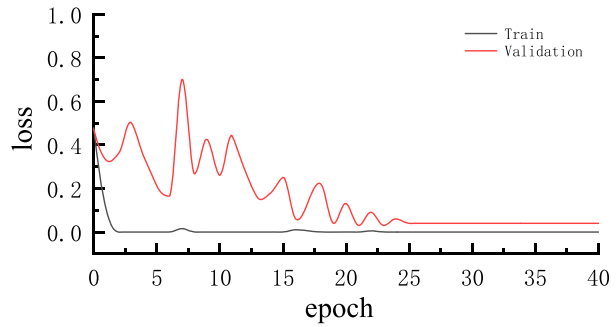

FIGURE 3
Loss change curve of network training.

4 Experimental verification and analysis

4.1 Parameter settings

During the network training process, the early-stopping mechanism is used to prevent the network from overfitting, and the parameter is set to 15. Training is stopped when the loss on the training set drops while the loss on the validation set remains the same for 15 consecutive epochs. To avoid the network from overfitting, the weight of the network model is only taken as a small value to limit the complexity of the network model and make the weight distribution more regular. This is weight regularization, adding the cost associated with larger weights to the network loss function to make the absolute value of the weight coefficients small enough. Based on the L2 regularization method (Chen and Zhao, 2021; Wang et al., 2021; Liu et al., 2023), the formula is as follows:

$$J = J_0 + \frac{\lambda}{2}\|w\|_2^2 \tag{8}$$

The training parameters are set as shown in Table 5.

4.2 Experimental results

The training time of the improved CNN network model is 1531s. The accuracy curve of the network training curve is shown in Figure 2 and the loss change curve of the network training curve is shown in Figure 3.

In Figures 2, 3, we can see that the accuracy in the early stage of training gradually increased, and the loss of the training set and the validation set also gradually decreased. There was a slight oscillation in the middle, and it gradually became stable with iterations. The network accuracy eventually tends to 100%, and the network loss eventually tends to 0. When the epoch is equal to 14, the loss of the training set is still decreasing, the loss of the validation set tends to remain unchanged, and when the loss of the validation set does not change for 10 consecutive times, the early-stopping mechanism will end the training of the network in advance, so the final training is taken. The network model was obtained 25 times. The safety wear recognition results of the electric staff working are shown in Table 6.

To verify the superiority of the improved CNN algorithm, the network model proposed in this paper is compared with the other network model under the same parameters. The performance comparison result is shown in Table 7.

In Table 7, the recognition method used in this paper has the highest recognition accuracy, reaching 96%. The highest recognition rate of other algorithms is 92.5%. Although these

TABLE 6 Safety wears identification results.

	Correct number	Incorrect number	Accuracy (%)
Pedestrian detection box	95	2	97.94
Helmet	72	3	96.00
Work clothes	96	1	98.97
Work pants	71	4	94.67
Insulated Gloves	75	6	92.00
Joystick	70	5	93.33

In Table 6, the safety wear recognition has high accuracy in each category.
The result shows that the improved CNN has the advantages of high accuracy and good real-time performance.

TABLE 7 Performance comparison under different models.

Model	mAP	Recognition rate/%	Running time/s
Proposed algorithm	.884	96.2	126
SSD	.863	92.5	334
Faster-RCNN	.886	89.6	258
YOLOv3	.858	90.8	361
EMD-SVM	.847	86.5	389
BPNN algorithm	.859	80.3	184
DBN	.852	82.8	159

recognition methods solve the problem of image recognition to some extent, when the image features are too mixed, these algorithms cannot well complete the mapping from feature extraction to state recognition, which is not conducive to model recognition. Compared with other traditional algorithms, the improved deep learning algorithm has a higher recognition rate and significantly improves the recognition rate of safe wearing of electric power workers. Compared with other algorithms, the proposed method has faster running speed and can meet the requirements of real-time computing. The proposed network model has strong feature expression ability. The advantages of good generalization performance and strong robustness.

5 Conclusion

In this paper, through the detection and identification of safety helmets, work clothes, and insulating gloves to carry out normative identification and warning, a deep learning-based safety wear identification method for electric power workers is proposed. The experimental results show that: compared with other traditional algorithms, the improved deep learning algorithm proposed in this paper has a higher recognition rate, significantly improves the recognition rate of safe wearing of electric power workers, and has the advantages of high accuracy and good real-time performance, thus providing the practical work provides guidance.

Data availability statement

The original contributions presented in the study are included in the article/supplementary material, further inquiries can be directed to the corresponding author.

Author contributions

All authors listed have made a substantial, direct, and intellectual contribution to the work and approved it for publication.

Funding

I and my fellow co-authors are fully aware of and agree with the payment of the listed article processing fee should the manuscript be accepted for publication.

Conflict of interest

Authors ZC, CM, JR, FH, and ZW were employed by the company Guangdong Power Co., Ltd.

Publisher's note

References

Aggarwal, L. P. (2019). Data augmentation in dermatology image recognition using machine learning. *Skin Res. Technol.* 25 (6), 815–820. doi:10.1111/srt.12726

Anastasiadou, K., Gavanas, N., Pitsiava-Latinopoulou, M., and Bekiaris, E. (2021). Infrastructure planning for autonomous electric vehicles, integrating safety and

sustainability aspects: A multi-criteria analysis approach. *Energies* 14 (17), 5269–5274. doi:10.3390/en14175269

Bashar, A. (2019). Survey on evolving deep learning neural network architectures[J]. *J. Artif. Intell.* 1 (02), 73–82. doi:10.36548/jaicn.2019.2.003

Chen, Y., and Zhao, Q. (2021). Mineral exploration targeting by combination of recursive indicator elimination with the ℓ2-regularization logistic regression based on geochemical data. *Ore Geol. Rev.* 135 (2), 104213. doi:10.1016/j.oregeorev.2021.104213

Chen, Z., Jin, T., Zheng, X., Liu, Y., Zhuang, Z., and Mohamed, M. A. (2022). An innovative method-based CEEMDAN–IGWO–GRU hybrid algorithm for short-term load forecasting. *Electr. Eng.* 104, 3137–3156. doi:10.1007/s00202-022-01533-4

Chen, Z., Yang, H., Bai, X., Gao, P., and Han, H. (2022). Image recognition method of power equipment based on deep learning [J]. *Electr. Technol.* (09), 34–36.

Dourado, C. M. J. M., da Silva, S. P. P., da Nobrega, R. V. M., Reboucas Filho, P. P., Muhammad, K., and de Albuquerque, V. H. C. (2020). An open IoHT-based deep learning framework for online medical image recognition. *IEEE J. Sel. Areas Commun.* 39 (2), 541–548. doi:10.1109/jsac.2020.3020598

Gangolells, M., Casals, M., Forcada, N., Roca, X., and Fuertes, A. (2010). Mitigating construction safety risks using prevention through design. *J. Saf. Res.* 41 (2), 107–122. doi:10.1016/j.jsr.2009.10.007

Jacob, I. J., and Darney, P. E. (2021). Design of deep learning algorithm for IoT application by image based recognition. *J. ISMAC* 3 (03), 276–290. doi:10.36548/jismac.2021.3.008

Jais, I. K. M., Ismail, A. R., and Nisa, S. Q. (2019). Adam optimization algorithm for wide and deep neural network. *Knowl. Eng. Data Sci.* 2 (1), 41–46. doi:10.17977/um018v2i12019p41-46

Ker, J., Wang, L., Rao, J., and Lim, T. (2017). Deep learning applications in medical image analysis. *IEEE Access* 6 (13), 9375–9389. doi:10.1109/access.2017.2788044

Li, B., Coutiño, M., Giannakis, G. B., and Leus, G. (2021). A momentum-guided frank-wolfe algorithm. *IEEE Trans. Signal Process.* 69 (12), 3597–3611. doi:10.1109/tsp.2021.3087910

Li, Y., Li, J., and Pan, J. S. (2019). Hyperspectral image recognition using SVM combined deep learning[J]. *J. Internet Technol.* 20 (3), 851–859.

Liu, J., Jia, R., Li, W., Ma, F., Abdullah, H. M., Ma, H., et al. (2020). High precision detection algorithm based on improved RetinaNet for defect recognition of transmission lines. *Energy Rep.* 6, 2430–2440. doi:10.1016/j.egyr.2020.09.002

Liu, L., Wang, B., Ma, F., Zheng, Q., Yao, L., Zhang, C., et al. (2022). A concurrent fault diagnosis method of transformer based on graph convolutional network and knowledge graph. *Front. Energy Res.* 10, 127. doi:10.3389/fenrg.2022.837553

Liu, Y., Yuan, D., Gong, Z., Jin, T., and Mohamed, M. A. (2023). Adaptive spectral trend based optimized EWT for monitoring the parameters of multiple power quality disturbances. *Int. J. Electr. Power & Energy Syst.* 146 (2023), 108797. doi:10.1016/j.ijepes.2022.108797

Mezgec, S., Eftimov, T., Bucher, T., and Korousic Seljak, B. (2019). Mixed deep learning and natural language processing method for fake-food image recognition and standardization to help automated dietary assessment. *Public health Nutr.* 22 (7), 1193–1202. doi:10.1017/S1368980018000708

Mroszczyk, J. W. (2015). Improving construction safety: A team effort[J. *J. Prof. Saf.* 60 (06), 55–68.

Postalcıoğlu, S. (2020). Performance analysis of different optimizers for deep learning-based image recognition. *Int. J. Pattern Recognit. Artif. Intell.* 34 (02), 2051003–2051213. doi:10.1142/s0218001420510039

Qin, Z., Ming, L., Song, W., and Zhang, W. (2022). Helmet detection method based on lightweight deep learning model [J]. *Sci. Technol. Eng.* 22 (14), 5659–5665.

Ramcharan, A., Baranowski, K., McCloskey, P., Ahmed, B., Legg, J., and Hughes, D. P. (2017). Deep learning for image-based cassava disease detection. *Front. plant Sci.* 8 (14), 1852–2201. doi:10.3389/fpls.2017.01852

Sharma, A. (2018). Guided stochastic gradient descent algorithm for inconsistent datasets. *Appl. Soft Comput.* 73 (5), 1068–1080. doi:10.1016/j.asoc.2018.09.038

Tang, H., Liu, H., Xiao, W., and Sebe, N. (2020). When dictionary learning meets deep learning: Deep dictionary learning and coding network for image recognition with limited data. *IEEE Trans. neural Netw. Learn. Syst.* 32 (5), 2129–2141. doi:10.1109/tnnls.2020.2997289

Traoré, C., and Pauwels, E. (2021). Sequential convergence of AdaGrad algorithm for smooth convex optimization. *Operations Res. Lett.* 49 (4), 452–458. doi:10.1016/j.orl.2021.04.011

Wang, H., Wang, B., Luo, P., Ma, F., Zhou, Y., Mohamed, M. A., et al. (2021). State evaluation based-feature identification of measurement data for resilient power system. *CSEE J. Power Energy Syst.* 8, 983–992. 10.17775/CSEEJPES.2021.01270.

Xu, D., Zhang, S., Zhang, H., and Mandic, D. P. (2021). Convergence of the RMSProp deep learning method with penalty for nonconvex optimization. *Neural Netw.* 139, 17–23. doi:10.1016/j.neunet.2021.02.011

Yang, J., Zhang, Y., and Mao, X. (2020). Deep learning detection method for safety helmets on construction work surfaces. *[J].Computer Appl.* 40 (S2), 178–182.

Yang, T., Xu, G., and Yan, J. (2022). Design of safety helmet and mask detection system based on deep learning [J]. *Comput. Knowl. Technol.* 18 (10), 15–18.

Yu, Y., Li, J., and Wang, B. (2021). Improved deep learning to optimize image recognition of power equipment defects[J]. *Mech. Des. Manuf.* (07), 176–188.

Yuan, D., Liu, Y., Lan, M., Jin, T., and Mohamed, M. A. (2022). A novel recognition method for complex power quality disturbances based on visualization trajectory circle and machine vision. *IEEE Trans. Instrum. Meas.* 71 (2022), 1–13. doi:10.1109/tim.2022.3204985

frontiers | Frontiers in Energy Research

TYPE Original Research
PUBLISHED 09 February 2023
DOI 10.3389/fenrg.2023.1064067

OPEN ACCESS

EDITED BY
Abdolali K. Sadaghiani,
Sabancı University, Türkiye

REVIEWED BY
Yacine Addad,
Khalifa University, United Arab Emirates
Ali Alshehri,
King Fahd University of Petroleum and Minerals, Saudi Arabia
Monssif Najim,
University of Hassan II Casablanca, Morocco

*CORRESPONDENCE
Min Wei,
weimin@sdu.edu.cn

SPECIALTY SECTION
This article was submitted to Process and Energy Systems Engineering, a section of the journal Frontiers in Energy Research

RECEIVED 07 October 2022
ACCEPTED 18 January 2023
PUBLISHED 09 February 2023

CITATION
Li S, Wei M and Wang X (2023), A numerical study on film condensation of steam with non-condensable gas on a vertical plate. *Front. Energy Res.* 11:1064067. doi: 10.3389/fenrg.2023.1064067

A numerical study on film condensation of steam with non-condensable gas on a vertical plate

Shanwei Li[1], Min Wei[1]* and Xiaojia Wang[2]

[1]School of Energy and Power Engineering, Shandong University, Jinan, China, [2]Tongyuan Design Group Co., Ltd., Jinan, China

The film condensation of steam is very common in several industrial areas, such as condensers in power plants, seawater desalination, and air-conditioning systems. In some studies, the non-condensable gas and liquid film are overlooked for the sake of simplicity. To provide an integral computational scheme, in the present study, the film condensation of steam in the presence of non-condensable gas on a vertical plate has been simulated using a two-dimensional CFD model combining a wall condensation model and volume of fluid (VOF) model. After verification, the proposed computational scheme is used to simulate the steam condensation process, with the mass fractions of non-condensable gas varying from 5% to 45%. The results indicate that the concentration of non-condensable gas in the boundary layer decreases gradually with the condensation process, resulting in a decline in the synergy between temperature and velocity field. It can also be found that the fluctuation of the liquid film can influence the concentration distribution of the non-condensable gas layer. For cases with high concentrations of steam, the thermal resistance of liquid film can reach more than 20% of the total thermal resistance, which should not be ignored.

KEYWORDS

film condensation, heat and mass transfer, non-condensable gas, gas-liquid two phase, computational fluid dynamics

1 Introduction

Film condensation is a common heat transfer phenomenon in many industrial domains, such as condensers in thermal or nuclear power plants, seawater desalination, and air-conditioning systems. In these applications, the steam often contains non-condensable gas, which significantly reduces the heat transfer rate due to the diffusion resistance generated by the gas-vapor boundary layer (Minkowycz and Sparrow, 1966). In addition, the existence of non-condensable gases increases the complexity of heat and mass transfer in the film condensation process, especially near the phase interface (Rao et al., 2008; Zhou et al., 2010; Krishna and Rao, 2017; Wang et al., 2022). Therefore, it is necessary to study the condensation mechanism in the presence of a non-condensable gas further to develop the heat transfer theory and guide its practical applications.

Many researchers have tried to establish a theoretical analysis method to solve film condensation issues with non-condensable gas using the boundary layer theory. For example, Rose (1980) employed an approximate equation based on the uniform-property boundary-layer theory to calculate the transfer rate of steam on the condensate surface in the presence of non-condensable gas. Liao et al. (2009) proposed an analysis method based on a two-phase boundary layer to analyze the condensation of a steam-gas mixture on a vertical

plate, and the effects of superimposed forced convection on natural convection in steam-gas flow were investigated. In addition, they also argued that the bulk flow blowing capability can be defined by a conventional mass transfer driving potential. Other related schemes can also be found in the literature, such as the double film theory (Lewis and Whitman, 1924; Colburn and Hougen, 1934), the diffusion layer theory (Peterson et al., 1993), and the heat and mass transfer analogy theory (Sparrow and Lin, 1964). The theoretical analysis relies on a lumped parameter that usually determines the average heat transfer coefficient at the condensing wall by empirical correlation or by solving the simplified boundary-layer equation without detailed information inside the film. Another popular approach to predicting the condensation process is using empirical or semi-empirical correlations. However, the main obstacle is that most correlations are not universally valid (Kharangate and Mudawar, 2017).

In the experimental aspect, the main research directions focus on the heat transfer characteristics of film condensation under different working conditions and the heat transfer enhancement by variant surface properties (Anderson et al., 1998; Ahn et al., 2022). Al-Diwany and Rose (1973) studied the condensation of an air, argon, nitrogen, and water vapor mixture on a vertical plate under natural convection, and the experimental results are in good agreement with the theoretical solution. Chung et al. (2004) measured the heat transfer rates of steam-air condensation on a vertical plate under forced convection and found that small mixture flows can obviously enhance heat transfers. To further improve the heat transfer efficiency, Wang et al. (2013) proposed a new type of left-right symmetric internally finned tube and confirmed that this design can reduce the thickness of the non-condensable gas layer and enhance the steam condensation. Yi et al. (2016) experimentally investigated the condensation process of an air-steam mixture on an isothermal vertical plate. Four typical condensation modes were observed: drop, drop-streak, film, and streamlet. However, no strict boundaries among these condensation modes were recognized because different modes can coexist under the same experimental condition.

Recently, a numerical calculation has become an important means to solve condensation problems, as it can provide more detailed data compared with experimental methods (e.g., Hammoudi et al., 2018; Feurhuber et al., 2019; Zhang et al., 2019; Kleiner et al., 2020). In the simulation of the condensation process, a key issue is how to implement mass transfer between two phases, which is the phase change method. The Lee model (Lee, 1980), based on the hypothesis of mass transfer at constant pressure in a quasi-thermo-equilibrium state, is the most widely used model for simulating phase problems, especially condensation. Using the finite volume method, Siow et al. (2007) presented a two-phase model to analyze laminar film condensation of vapor with non-condensable gas in declining parallel-plate channels. Tang et al. (2012) solved the heat and mass transfer problem of steam-air mixture condensation outside a smooth horizontal tube with the finite difference method and a double boundary layer model. They observed that the mass concentration and velocity of the non-condensable gas increased from the bulk mixture to the interface. According to the operating conditions, the mass transfer intensity factor is a key empirical coefficient with a wide range in this model (e.g., Alizadehdakhel et al., 2010; Liu et al., 2012; Riva and Col, 2012; Qiu et al., 2014; Lee et al., 2015; Kharangate et al., 2016). More than that, the mass transfer coefficient is usually treated as a constant, which is not physical in the continuous phase change of condensation. In recent years, the wall condensation model (WCM) has been used to study the condensation of steam in the presence of a non-condensable gas. This model calculates the mass flux of steam from Fick's law of diffusion, and the steam concentration near the wall is obtained from its partial pressure at its saturation temperature, which is based on the condensing wall temperature (e.g., Li, 2013; Zschaeck et al., 2014; Punetha and Khandekar, 2017; Kumar et al., 2021). However, in WCM, the liquid boundary layer is neglected during simulations.

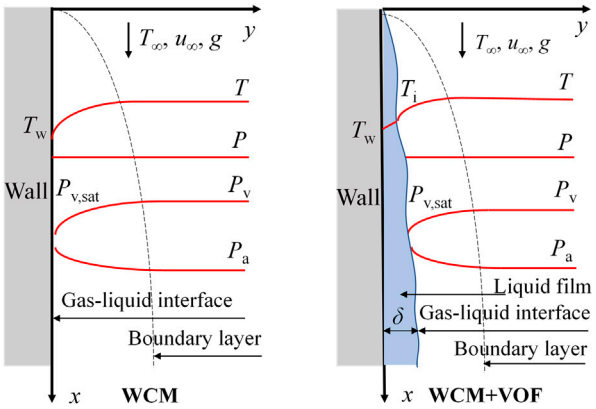

FIGURE 1
Condensation of the steam-air mixture flowing along an isothermal vertical plate: (left) simplified model (adapted from Zschaeck et al., 2014); (right) the model used in this paper.

Actually, the characteristics of both the non-condensable gas layer and the liquid film shape evolved in the condensation process. The wave motion can be observed when the local Reynolds number of the liquid film is greater than 30 (Bejan, 1995), which has a great influence on the heat transfer (Lee et al., 2015; Choi et al., 2020). Wang et al. (2016) confirmed that the wave structure can enhance the condensation rate by up to ten percent and that the wave effects on film condensation should be included in the heat transfer analysis. Therefore, an accurate numerical calculation considering the gas-liquid phase interface in the presence of non-condensable gas is necessary, which is close to the actual physical process. In an attempt to solve the above problem, a new computational scheme combining WCM and the volume of fluid (VOF) method is implemented in the present study to investigate the change laws of the liquid film shapes and the heat transfer characteristics under different air concentrations and surface subcooling. The simulation results are validated by experimental data reported in the literature, implying that the new scheme can aid in the study of physical mechanisms and influence factors of condensation in the presence of non-condensable gases.

2 Methods

In this study, steam and air are chosen as condensation vapor and non-condensable gas, respectively. When the temperature of the wall is lower than the saturation temperature of steam, a liquid film and a non-condensable gas layer are formed during the condensation process.

2.1 Physical model

Figure 1A illustrates the basis of WCM, which usually ignores the existence of condensing liquid film. Considering that the thermal resistance of the liquid film is neglected, this model overpredicts the rate of condensation when the concentration of non-condensable gas is less than 6% (Punetha and Khandekar, 2017). In addition, the interface wave motion and temperature difference between the interface and wall are not discussed, which is inconsistent with the actual condensation process. In order to increase the accuracy of the simulation results, the WCM and VOF models (Figure 1B) are combined in this study to capture the gas-liquid phase interface. A detailed introduction to this model can be found in Sections 2.4 and 2.5. The liquid film thermal resistance and non-condensable gas layer thermal resistance are both considered in this model. Note that the following assumptions are applied in this study: 1) non-condensable gas is insoluble in the liquid film; 2) the steam saturation pressure and temperature are corresponding to the partial pressure of steam in the cells of the gas-liquid interface; 3) momentum transfer caused by condensation at the gas-liquid interface is neglected; and 4) radiation heat transfer is neglected. The condensation wall is assumed to be initially dry, and the liquid film is generated in the condensation process.

2.2 Governing equations

The VOF method is based on the assumption that the two phases do not merge. The volume fraction α is the ratio of one fluid volume to the whole volume in a cell, which is also solved in the calculation to obtain the distribution of different phases in the computational domain. The volume fractions of different phases in each cell satisfy Eq. 1:

$$\sum_{i=1}^{n}\alpha_i = 1 \tag{1}$$

The mass or continuity equation for phase i can be written as:

$$\frac{\partial}{\partial t}\left(\alpha_i\rho_i\right) + \nabla\cdot\left(\alpha_i\rho_i\vec{u}_i\right) = S_m \tag{2}$$

where S_m is the mass source term, which is depicted in Section 2.4.

The conservation of momentum is

$$\frac{\partial}{\partial t}\left(\rho\vec{u}\right) + \nabla\cdot\left(\rho\vec{u}\vec{u}\right) = -\nabla p + \nabla\cdot\left(\mu\left(\nabla\vec{u} + \nabla\vec{u}^{T}\right)\right) + \rho\vec{g} + \vec{F} \tag{3}$$

In this equation, p is the pressure shared by all phases. The addition of surface tension to the VOF calculation results in a source term in the momentum equation, based on the continuum surface force model built-in to ANSYS Fluent, which was proposed by Brackbill et al. (1992). The force generated by surface tension gets balanced by the pressure gradient force across the interface. The pressure drop on the gas-liquid interface can be given by:

$$p_1 - p_2 = \sigma\kappa \tag{4}$$

in which σ is the liquid surface tension coefficient and κ is the interface curvature, which is calculated as follows:

$$\kappa = \nabla\cdot\frac{\nabla\alpha}{|\nabla\alpha|} \tag{5}$$

where α is the volume fraction.

The conservation of energy is given by:

$$\frac{\partial}{\partial t}\left(\rho E\right) + \nabla\cdot\left(\vec{u}\left(\rho E + p\right)\right) = \nabla\left(k_{eff}\nabla T - \sum_{i}^{n}h_i\overrightarrow{J_i}\right) + S_h \tag{6}$$

where the energy E in the VOF model is calculated by Eq. 7 and h_i is the specific enthalpy of phase i

$$E = \frac{\sum_{i=1}^{n}\alpha_i\rho_i E_i}{\sum_{i=1}^{n}\alpha_i\rho_i} \tag{7}$$

2.3 Species transport model

The species conservation equation takes the general form as follows:

$$\frac{\partial}{\partial t}\left(\rho Y_i\right) + \nabla\cdot\left(\rho\vec{u}Y_i\right) = -\nabla\cdot\vec{J}_i + S_i \tag{8}$$

where $\vec{J}_i$ is the diffusion flux of species i, which is related to concentration and temperature gradients and is calculated as follows:

$$\overrightarrow{J_i} = -\rho D_i\nabla Y_i - D_{T,i}\frac{\nabla T}{T} \tag{9}$$

where D_i is the mass diffusion coefficient for species i in the mixture and $D_{T,i}$ denotes the thermal diffusion coefficient. The value of the mass diffusion coefficient is related to pressure, temperature, and the composition of the gas mixture. For binary gas mixtures at low pressure, D_i is inversely proportional to pressure and increases with rising temperature, but has the same value for the two components in the mixture (Fuller et al., 1966).

2.4 Wall condensation model

At the gas-liquid interface, the total mass flow of steam in one cell equals the sum of the mass flow from diffusion and convection, which is defined as follows:

$$\dot{m}_{\mathrm{v}} = \overrightarrow{J_{\mathrm{v}}} + \rho_{\mathrm{v}}\overrightarrow{u_{\mathrm{v}}} = -\rho D_{\mathrm{v}}\nabla Y_{\mathrm{v}} + Y_{\mathrm{v}}\dot{m}_{\mathrm{v}} \tag{10}$$

Therefore, the following equation to calculate the mass condensation rate can be obtained (Dehbi et al., 2013):

$$\dot{m}_{\mathrm{v}} = -\rho D_{\mathrm{v}}\frac{1}{1 - Y_{\mathrm{v}}}\frac{\partial Y_{\mathrm{v}}}{\partial y} \tag{11}$$

The gradient of the steam mass fraction in the y direction is calculated as follows:

$$\frac{\partial Y_{\mathrm{v}}}{\partial y} = \frac{\Delta Y_{\mathrm{v}}}{l} = \frac{Y_{\mathrm{v}} - Y_{\mathrm{v,sat}}}{l} \tag{12}$$

where l represents the distance from the center of the cell to the wall, and $Y_{\mathrm{v},sat}$ is the saturated mass fraction of steam corresponding to the temperature of condensing surface.

The mass of steam condensed per unit volume near the wall is calculated as:

$$S_m = \dot{m}_{\mathrm{v}}\frac{A_w}{V_c} \tag{13}$$

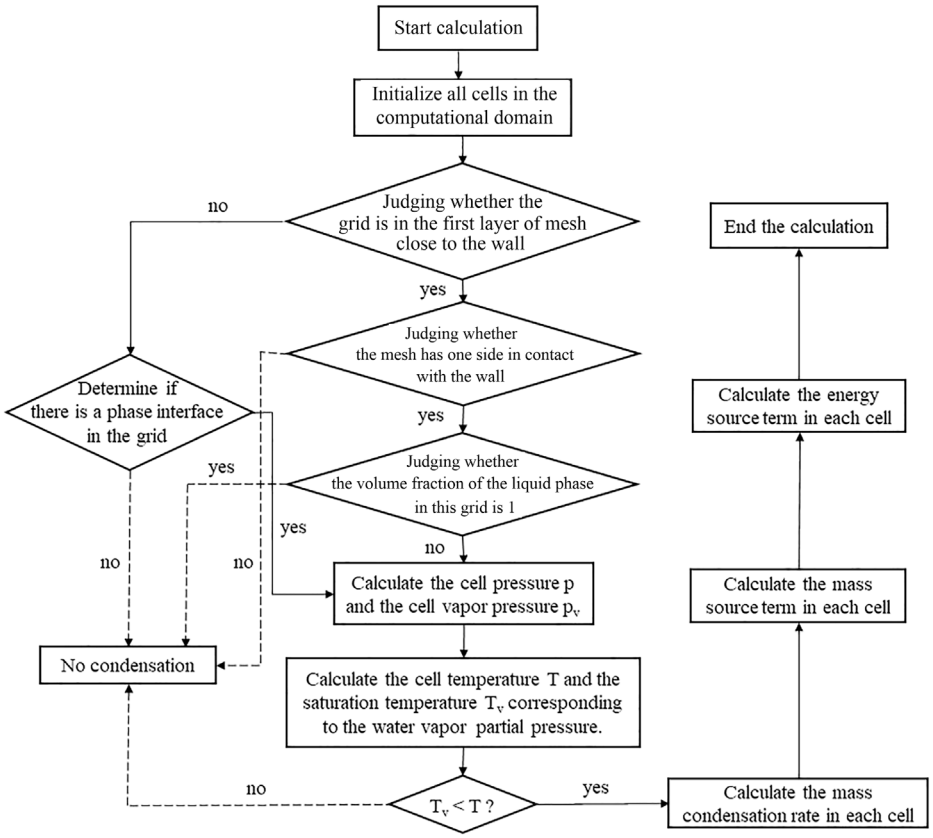

FIGURE 2
Schematic diagram of the computing program in UDF.

in which A_w is the area of the cell adjacent to the wall in the original WCM but to the interface in our study. V_c is the cell volume. The energy source term at the liquid side due to the condensation of vaporized water is given by:

$$S_h = S_m h_{fg} \tag{14}$$

where h_{fg} stands for the latent heat of vaporization.

2.5 Model implementation method

To obtain the shapes of the liquid film, the physical parameters of mixtures and liquid film at the gas-liquid phase interface need to be calculated accurately. The WCM is improved in this study, and the VOF model is used to capture the gas-liquid interface. The concentrations of steam and air near the gas-liquid interface are calculated by a species transport model. User-defined functions (UDF) are used to read variables and add source terms in a fluid solver. The schematic diagram of the computing program is provided in Figure 2, which is realized by ANSYS Fluent, and the numerical procedure is described in detail as follows.

Step 1: The boundary conditions, like the variables of mixture and wall temperature, are initialized. The steam saturation pressure and temperature values adjacent to the film are calculated in the UDF codes.

Step 2: The meshes in the first layer adjacent to the wall are considered to obtain the volume fraction in each mesh and capture the phase interface. If the condensation criterion is met, the source terms in each mesh are added.

Step 3: Other meshes in the computational domain are treated after Step 2 with the same method, and then a complete cycle is completed.

Step 4: In the subsequent calculation phase, Steps 2 and 3 are repeated so that the phase interface is developed step by step. The different shapes of the liquid film and other information at different stages of condensation can also be obtained.

2.6 Computational domain and boundary conditions

The geometric computational domain used in this study is given in Figure 3. The length of the wall is 100 mm, and the width of the inlet and outlet measures 30 mm. The steam-air gas mixture enters from the inlet, and steam condenses on the wall. The entire computational domain is divided by a quadrilateral structural mesh. In this study, the

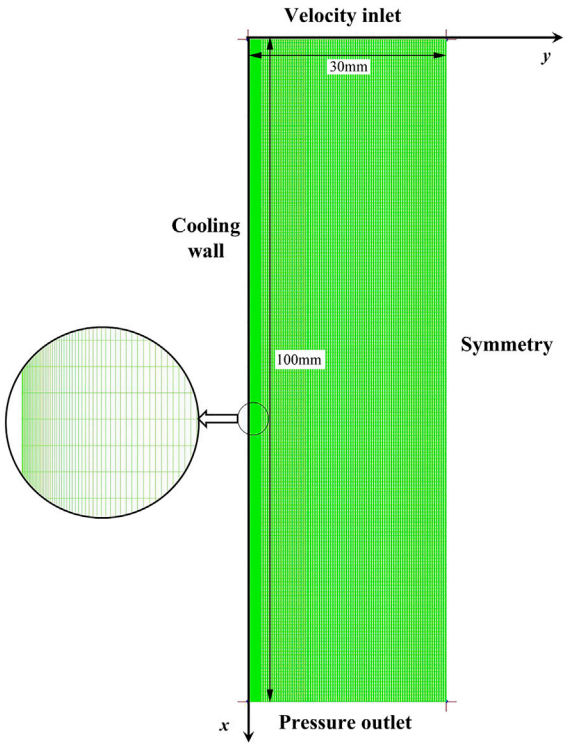

FIGURE 3
Computational domain and mesh.

two-phase flow near the phase interface is complex, so the mesh elements are refined near the wall to achieve high accuracy.

The inlet boundary condition of the steam-air mixture is the velocity at the inlet boundary, which is fixed at 1 m s^{-1}, except in some cases for validation, and the temperature is 373.15 K. The influent mixture contains different mass fractions of air, varying from 0.05 to 0.45. Pressure outlet boundary is set for the outlet with atmospheric pressure. For the condensation wall, a constant temperature is specified according to the operating conditions. The right side of the model is confirmed as the symmetry boundary condition. The properties of the steam and air, such as the viscosities, thermal conductivities, and specific heat capacities, are assumed to be constants during the simulation. Other thermal properties, like latent heat and saturation pressure, are defined as functions of temperature. At the initial time, the computational domain is full of air, and there is no liquid phase on the wall.

3 Model validation

3.1 Simulation techniques

Due to the fact that the thickness of the liquid film, the mass fraction of steam, and the amount of air are always changing with time, a transient solver is chosen in this simulation with the PISO Pressure-Velocity coupling scheme. Through the time step independence check, each time step is set to 0.005 s, and the maximum iteration number in each of them is 80. Convergence is achieved when the volume of liquid on the wall and the mass fraction of air in the outlet reach a constant value. Meanwhile, the residual of the energy equation should be below 10^{-7} and the residuals of other equations should be below 10^{-4}. More details about working conditions can be found in Table 1.

3.2 Grid independence check

To check the independence of the grid, three models with 41101, 60501, and 100651 mesh elements have been tested. The mass fraction of steam in the outlet at 0.75 s in Case 4 and Case 1 is shown in Figure 4. With the increase in grid number, the differences in the results are negligible, so we chose the mesh with 60501 elements in the following cases for a balance between accuracy and computational load.

3.3 Simulation validation

The heat transfer rates in this study were compared with the results obtained in the experimental research of Yi et al. (2016) and the analytical solution of Denny et al. (1971) under the same working conditions. The overall trend of the numerical simulation results is the same as the experimental values, as shown in Figure 5. The average heat transfer coefficients decrease with the increase in air bulk concentration and increase with the decrease in subcooling. In Figure 6, the ratio of heat flux to that from Nusselt's model obtained in our simulation was compared with the results from Denny et al. (1971). Both results show that the influence of non-condensing gas on the heat flux in vertical plates increases with mixture gas flow direction. The average deviation is less than 25% in the data shown in Figures 5, 6, indicating that this simulation model is reliable.

It should be noted that the heat transfer coefficients obtained in this study are lower than the experimental values, especially when the subcooling is 40 K. In our simulation, the computational domain is initialized to be full of air under the same conditions. When the mixture gas flows in the computational domain, some of the existing air in the computational domain is trapped due to the viscous effect, and thus the content of non-condensable gas near the wall slightly increases, which may lead to lower average heat transfer coefficients. On the other hand, the shape of the liquid film obtained through numerical simulation is film condensation. In the experiments, however, the average heat transfer coefficients are obtained under various condensation forms, including drop, drop-streak, streamlet, and film-like condensation, which may lead to the deviation between simulation and experimental results.

4 Results and discussion

4.1 Gas concentration distribution

As the steam-air mixture flows along the vertical wall, the steam begins to condense due to the subcooling, the solid surface is covered by the condensate water, and the liquid film forms on the wall. At the same time, a high-concentration non-condensable gas layer is formed on the surface of the liquid film. The change in air mass fraction and the thickness of the liquid film in the computational region can be seen in Figure 7. With the aggregation of the condensate, the liquid film becomes thicker. Along with the mass and heat transfer near the gas-

TABLE 1 Working conditions during simulation.

Case number	Temperature of the vertical plate (K)	Bulk mass fraction of air	Velocity
Case 1	333.15	0.05	1 m/s
Case 2	333.15	0.1	1 m/s
Case 3	333.15	0.15	1 m/s
Case 4	333.15	0.2	1 m/s
Case 5	333.15	0.3	1 m/s
Case 6	323.15	0.05	1 m/s
Case 7	323.15	0.15	1 m/s
Case 8	323.15	0.45	1 m/s

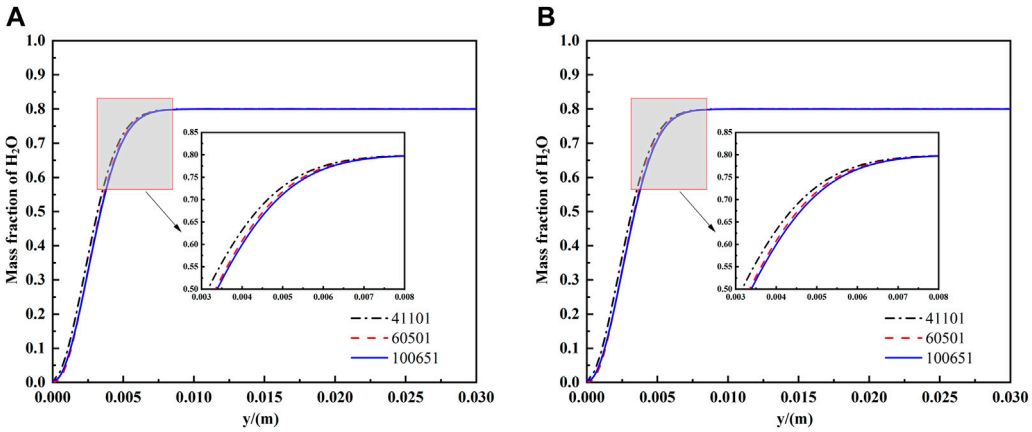

FIGURE 4
Grid independence check with the mass fraction of water vapor in the outlet at 0.75 s: **(A)** Case 4; **(B)** Case 1.

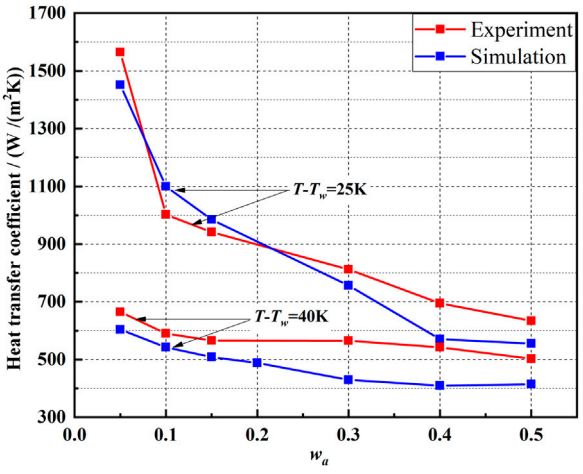

FIGURE 5
Comparison of the average heat transfer coefficients obtained in our simulation and Yi's experiment (u_g = 1 m/s).

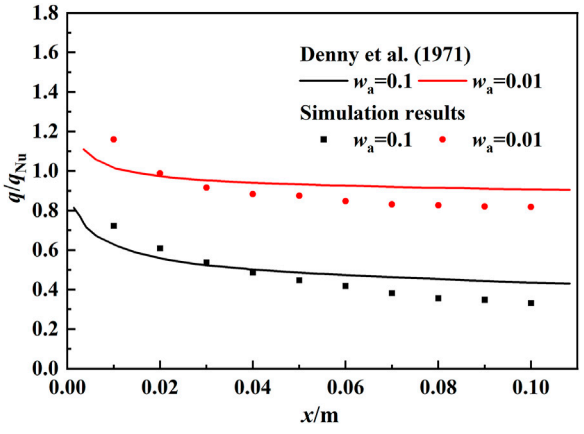

FIGURE 6
Ratio of heat flux to that from Nusselt's model obtained in our simulation and the analytical solution of Denny et al. (1971) (u_g = 3.04 m/s, T-T_w = 22.23 K).

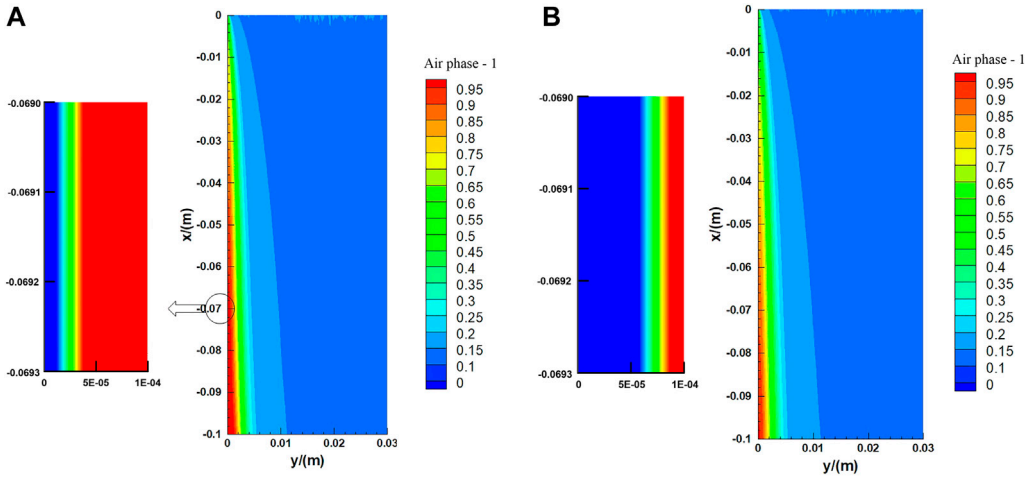

FIGURE 7
Mass fractions of air on the phase interface in Case 2: **(A)** t = 0.5 s; **(B)** t = 4.25 s.

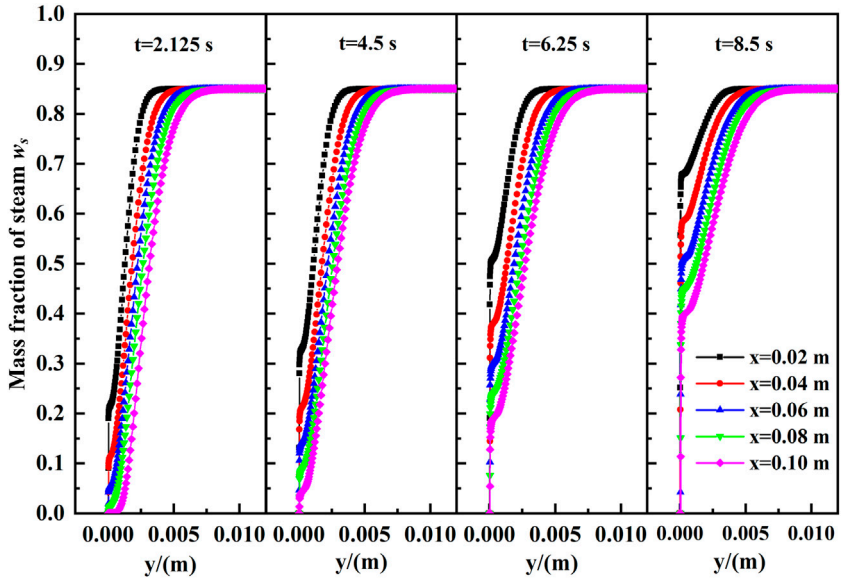

FIGURE 8
Mass fractions of steam in different positions on the wall in Case 7.

liquid interface, the mass fraction of steam and air varies with the phase interface temperature change.

The distributions of steam concentration in the *y* direction along the wall of Case 7 at different moments are shown in Figure 8. At the beginning of condensation, the mass fraction of steam is close to zero near the gas-liquid interface because of steam condensation. At the same position on the wall, the mass fraction of steam in the *y* direction gradually rises to 0.85, which equals the steam concentration in the mainstream. In the non-condensable gas layer region, the mass fraction of steam is increasing along the flow direction at the same distance from the wall. Along with the deepening of the condensation process, under the effect of the diffusion law, the non-condensable gas in the non-condensable gas layer gradually diffuses back to the mainstream due to the higher concentration, which results in a gradually decreased air concentration in the non-condensable gas layer. Finally, both the condensing rate and the concentration of steam and air at the interface, which are determined by the static pressure corresponding to the interface temperature, will be stable.

4.2 Gas velocity distribution

Even though laminar flow is observed on the vertical plate in this study, a small amount of normal velocity may still exist due to the

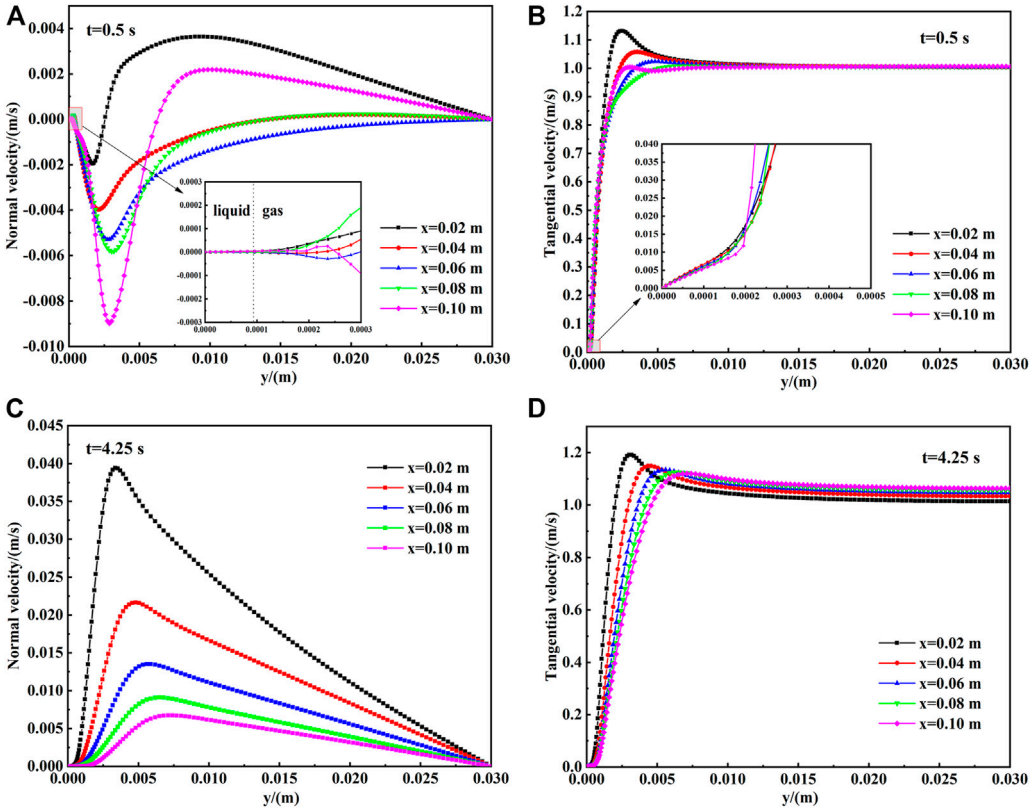

FIGURE 9
Velocity distributions in different positions on the wall in Case 2: **(A)** normal velocity at 0.5 s; **(B)** tangential velocity at 0.5 s; **(C)** normal velocity at 4.25 s; **(D)** tangential velocity at 4.25 s.

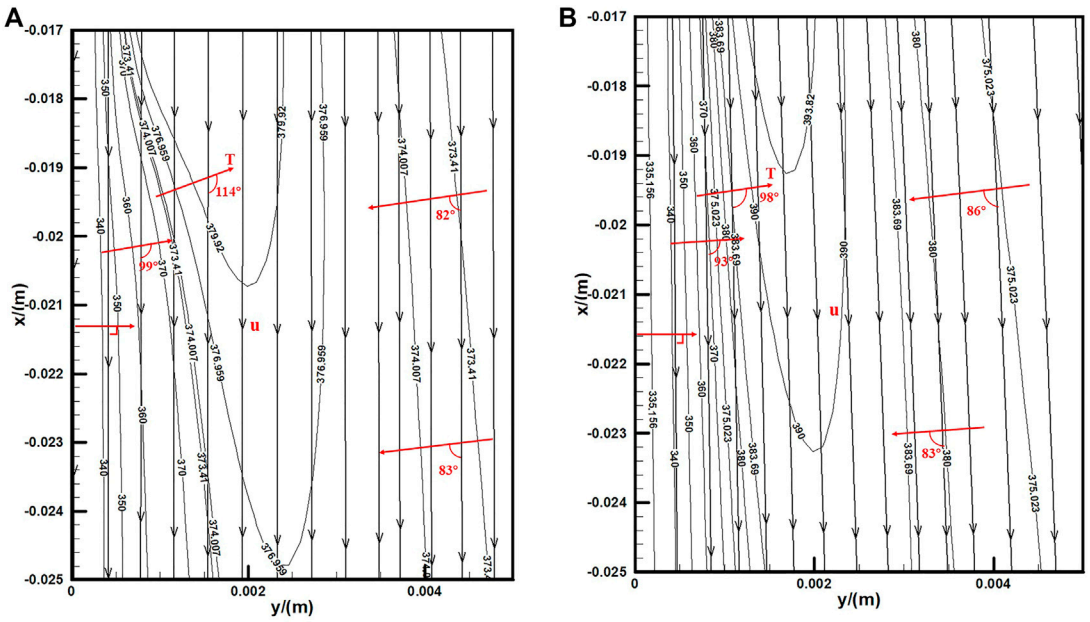

FIGURE 10
Temperature filed and velocity filed near the wall in Case 1: **(A)** t = 0.5 s; **(B)** t = 4.25 s.

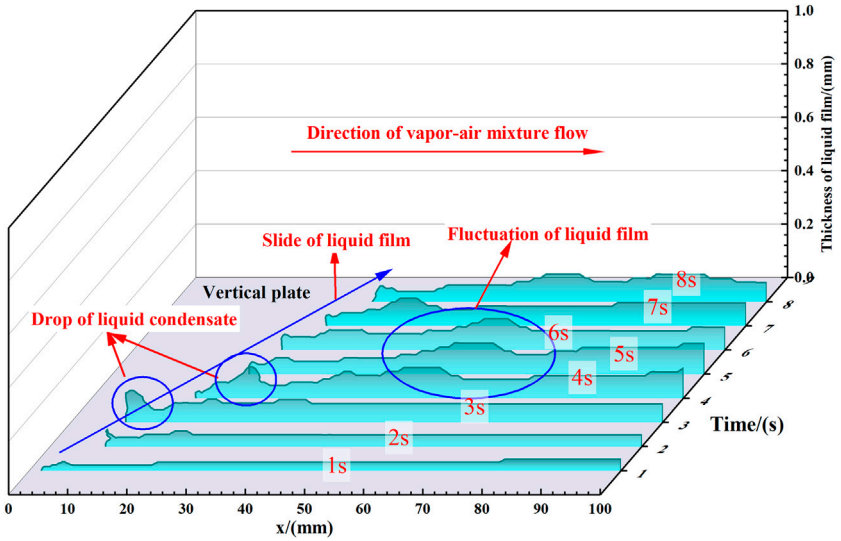

FIGURE 11
Evolution of liquid film shape in Case 5.

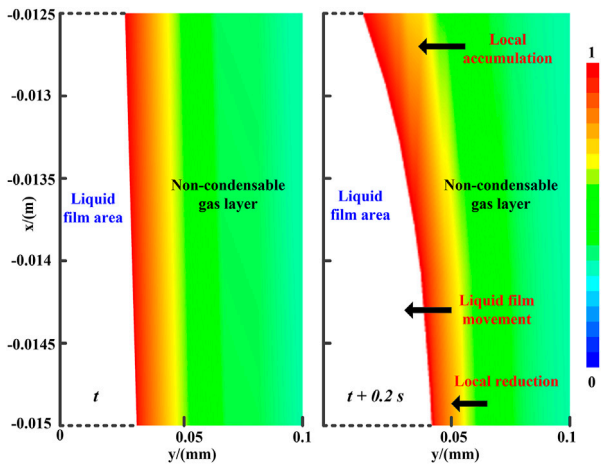

FIGURE 12
Local change of air concentration in the process of the liquid film falling off of Case 5.

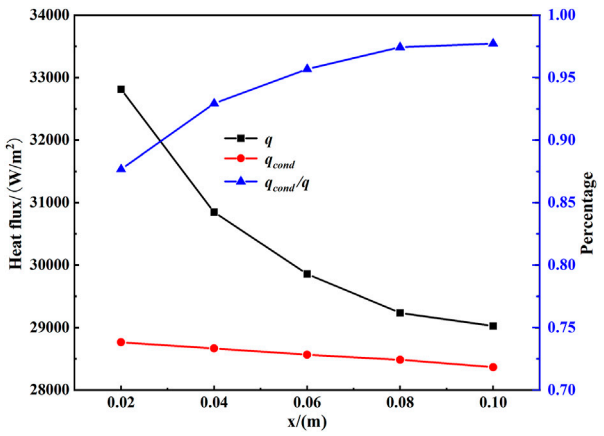

FIGURE 13
Wall heat flux in mixture gas flow direction in Case 3.

condensation of steam and the formation of the liquid film. As shown in Figure 9A, the normal velocity in the liquid film is zero, whereas it is negative in the non-condensable layer near the wall, indicating that the steam moves towards the wall by condensation. When the condensation reaches 4.25 s, the normal velocity distribution in the y direction of the mixture changes from zero near the wall to positive at the gas-liquid interface, as shown in Figure 9C. At this time, the non-condensable gas on the surface of the liquid film diffuses to the mainstream in accordance with the diffusion law, and the peak value of normal velocity decreases gradually in the direction of fluid flow.

Outside the wall, the tangential velocity of the liquid film presents a linear distribution with an obvious velocity gradient. A local acceleration can be observed in the non-condensable gas layer far from the wall, after which the velocity of the fluid returns to the mainstream velocity. Along with the increase in distance in the x direction, the peak value of tangential velocity decreases gradually. The peak value of the tangential velocity at $x = 0.1$ m shifts to the left due to reflux in the outlet, and the return flow of the exit disappears at 4.5 s, as shown in Figure 9D. At this time, the pressure at the outlet is less than that at the inlet, and thus the velocity of the mainstream fluid increases gradually along the flow direction.

The velocity and temperature fields of the mixture on sections of the vertical plate at different times are shown in Figure 10. The value of the synergy angle between the velocity gradient and temperature gradient is close to 120° at the initial stage of condensation. According to the field synergy principle (Tao et al., 2002), the degree of synergy between the velocity field and the temperature field is good at this time, so the average heat transfer rate is high. When condensation proceeds for 4.25 s, the value of the synergy angle decreases to 98°, which is not beneficial to heat transfer, and the average heat transfer rate decreases slightly.

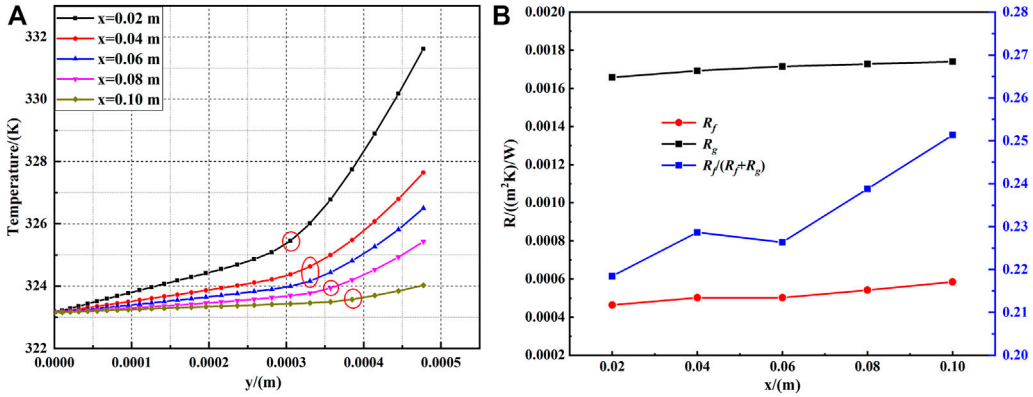

FIGURE 14
Heat transfer analysis in Case 3: **(A)** temperature distribution near the wall; **(B)** thermal resistance profile.

4.3 Characteristics of liquid film

During the condensation process of the steam-air mixture, the condensate adheres to the wall and forms a liquid film or bulge. Due to the interaction of surface tension, gravity, and sheer force at the phase interface, the liquid film cannot exist stably on the vertical wall and falls off, slides, and fluctuates along the wall. The isoline of liquid volume fraction with a value of 0.5 is used as the surface of the liquid film in this numerical simulation so as to obtain the form change of the liquid film, as shown in Figure 11. When the initial mass fraction of air is 0.3, the shape of the liquid film is very smooth at the beginning, the fluctuation is minimal, and the thickness is less than 0.05 mm. With continuous condensation, the liquid film gradually becomes thicker and begins to accumulate at the top of the liquid film, which produces a bulge. The bulge then slides along the wall and spreads downstream, so the liquid film gradually flows down along the wall. After that, with the condensate produced constantly, the liquid film reaches a pseudo-stable state with an alternate pattern of continuous formation and falls off, which can be defined as wavy liquid film.

Since the shapes of the condensate film change with time, the gas-liquid phase interface is similar to the dynamic rough surface, and the liquid film is surrounded by a layer of non-condensable gas. The condensate scours and merges with the liquids beneath during the liquid film fluctuation process. At the same time, this phenomenon also acts on the gas-liquid interface and the non-condensable gas layer, which changes the roughness of the dynamic surface and the partial concentration of the non-condensable gas layer near the phase interface. Figure 12 demonstrates that when the liquid film moves downstream with a slight deformation, the non-condensable gas layer undergoes local accumulation and reduction, which may influence the local thermal resistance. It should be noted that in the data processing, grids with a liquid fraction greater than 0.5 are deleted so that the white area without data represents the liquid film area. The mass transfer in the non-condensable gas layer near the phase interface is related to the shapes of the phase interface, which is consistent with Wang et al. (2016).

4.4 Heat transfer analysis

Case 3 calculation results are used to obtain the total wall heat flux q, which is the sum of condensation and convection heat fluxes, in order to analyze the heat transfer further. The condensation heat flux q_{cond} can be calculated from energy source terms in first-layer grids near the wall, which also determines the convection heat flux q_{conv}. Through this method, the heat transfer due to condensation and convection can be clearly observed, as shown in Figure 13. The condensation and convection heat flux both decrease because of the increased thickness of the non-condensable gas layer, the thermal boundary layer, and the velocity boundary layer in the mixture flow direction. Meanwhile, the percentage of condensation heat transfer to total heat transfer gradually increases, reaching the maximum value of 0.975 at the bottom of the vertical plate.

The liquid film produced under working conditions of low non-condensable gas content is thick. If the liquid film is ignored, the calculation results will deviate significantly. To prove the importance of liquid film thermal resistance under these conditions, a thermal resistance analysis is carried out. In this model, the thermal resistance of the phase interface is neglected, and the liquid film and gas thermal resistances are calculated using Eqs. 15, 16.

$$R_f = \delta / \lambda_f \tag{15}$$

$$R_g = \frac{T - T_i}{q} = \frac{T - T_i}{q_{conv} + q_{cond}} \tag{16}$$

Figure 14A shows the temperature distribution of the mixture near the wall at various positions. Because the thermal conductivities of gas and liquid are different, the points where the slopes of the temperature distribution curves change are taken as the gas-liquid interface, as marked by the circles in the figure. As shown in Figure 14B, the thermal resistances of the liquid film and the non-condensable gas layer increase gradually in the mixture flow direction as the non-condensable gas layer thickens. The thermal resistance of the liquid film accounts for 20%–26% of the total thermal resistance, illustrating that the effect of the liquid film should not be ignored in the condensation process.

5 Conclusion

The combined WCM and VOF model is used to simulate the film condensation process of steam with non-condensable gas on a vertical plate. The purpose of the transient solver is to obtain the variations of

the concentration and velocity fields in the non-condensable gas layer and the evolution of liquid film shapes for different non-condensable gas concentrations. The main conclusions are summarized as follows.

1) The high-concentration non-condensable gas layer is formed at the initial stage of condensation and then gradually diffused back to the mainstream as the condensation continues. The normal velocity of the steam-air gas mixture near the phase interface changes from the negative *y*-axis direction to the positive *y*-axis direction, which causes the degree of synergy between the temperature field and velocity field to decrease.
2) The shapes of the liquid film in different concentrations of non-condensable gases are observed, and the fluctuation, sliding, and falling off of liquid films can be presented in a single condensation process. In addition, heat and mass transfer at the phase interface can be affected by the obvious dynamic behavior of the liquid film, which changes the partial concentration distribution of the non-condensable gas boundary layer near the phase interface.
3) In this model, the thermal resistance of the liquid film is taken into account. For the working conditions of a gas mixture with a high content of steam, the proportion of condensation heat transfer is higher than 90%. The thermal resistance percentage of the liquid film can reach 20%–26% of the total thermal resistance. Therefore, the liquid film cannot be ignored to ensure the model's accuracy.

Data availability statement

The raw data supporting the conclusions of this article will be made available by the authors, without undue reservation.

Author contributions

SL: conceptualization, formal analysis. MW: supervision, writing–reviewing and editing. XW: validation, writing, original draft preparation, methodology.

Funding

The authors are extremely grateful to the Natural Science Foundation of Shandong Province for their financial support (No. ZR2019BEE012).

Conflict of interest

Author XW was employed by Tongyuan Design Group Co., Ltd.

The remaining authors declare that the research was conducted in the absence of any commercial or financial relationships that could be construed as a potential conflict of interest.

Publisher's note

All claims expressed in this article are solely those of the authors and do not necessarily represent those of their affiliated organizations, or those of the publisher, the editors and the reviewers. Any product that may be evaluated in this article, or claim that may be made by its manufacturer, is not guaranteed or endorsed by the publisher.

References

Ahn, T., Moon, J., Kang, J., Jeong, J. J., and Yun, B. (2022). Steam condensation in the presence of non-condensable gas inside a nearly horizontal tube under separated flow. *Int. J. Heat Mass Transf.* 197, 123351. doi:10.1016/j.ijheatmasstransfer.2022.123351

Al-Diwany, H. K., and Rose, J. W. (1973). Free convection film condensation of steam in the presence of non-condensing gases. *Int. J. Heat Mass Transf.* 16, 1359–1369. doi:10.1016/0017-9310(73)90144-0

Alizadehdakhel, A., Rahimi, M., and Alsairafi, A. A. (2010). CFD modeling of flow and heat transfer in a thermosyphon. *Int. Commun. Heat Mass Transf.* 37, 312–318. doi:10.1016/j.icheatmasstransfer.2009.09.002

Anderson, M. H., Herranz, L. E., and Corradini, M. L. (1998). Experimental analysis of heat transfer within the AP600 containment under postulated accident conditions. *Nucl. Eng. Des.* 185, 153–172. doi:10.1016/s0029-5493(98)00232-5

Bejan, A. (1995). *Convection heat transfer*. New Jersey, United States: Wiley-Interscience Publication.

Brackbill, J. U., Kothe, D. B., and Zemach, C. (1992). A continuum method for modeling surface tension. *J. Comput. Phys.* 100, 335–354. doi:10.1016/0021-9991(92)90240-y

Choi, Y., Son, G., and Lee, G. (2020). Numerical simulation of wavy film condensation in a vertical channel with non-condensable gas. *Int. J. Heat Mass Transf.* 149, 119173. doi:10.1016/j.ijheatmasstransfer.2019.119173

Chung, B. J., Kim, S., and Kim, M. C. (2004). An experimental investigation of film condensation of flowing mixtures of steam and air on a vertical flat plate. *Int. Commun. Heat Mass Transf.* 31, 703–710. doi:10.1016/s0735-1933(04)00057-0

Colburn, A. P., and Hougen, O. A. (1934). Design of cooler condensers for mixtures of vapors with noncondensing gases. *Industrial Eng. Chem.* 26, 1178–1182. doi:10.1021/ie50299a011

Dehbi, A., Janasz, F., and Bell, B. (2013). Prediction of steam condensation in the presence of noncondensable gases using a CFD-based approach. *Nucl. Eng. Des.* 258, 199–210. doi:10.1016/j.nucengdes.2013.02.002

Denny, V. E., Mills, A. F., and Jusionis, V. J. (1971). Laminar film condensation from a steam-air mixture undergoing forced flow down a vertical surface. *J. Heat Transf.* 93, 297–304. doi:10.1115/1.3449814

Feurhuber, M., Magno, M., Miranda, M., and Hochenauer, C. (2019). CFD investigations of steam penetration, air-removal and condensation inside hollow loads and cavities. *Appl. Therm. Eng.* 147, 1070–1082. doi:10.1016/j.applthermaleng.2018.10.135

Fuller, E. N., Schettler, P. D., and Giddings, J. C. (1966). A new method for prediction of binary gas-phase diffusion coefficiients. *Industrial Eng. Chem.* 58, 19–27.

Hammoudi, D., Benabdesselam, A., Azzi, A., and Kassim, M. A. (2018). Numerical modeling of steam condensation in vertical channel in presence of noncondensable gas. *Int. J. Therm. Sci.* 126, 263–271. doi:10.1016/j.ijthermalsci.2017.12.032

Kharangate, C. R., Lee, H., Mascarehnas, N., Park, I., and Mudawar, I. (2016). Experimental and computational investigation of vertical upflow condensation in a circular tube. *Int. J. Heat Mass Transf.* 95, 249–263. doi:10.1016/j.ijheatmasstransfer.2015.11.010

Kharangate, C. R., and Mudawar, I. (2017). Review of computational studies on boiling and condensation. *Int. J. Heat Mass Transf.* 108, 1164–1196. doi:10.1016/j.ijheatmasstransfer.2016.12.065

Kleiner, T., Eder, A., Rehfeldt, S., and Klein, H. (2020). Detailed CFD simulations of pure substance condensation on horizontal annular low finned tubes including a parameter study of the fin slope. *Int. J. Heat Mass Transf.* 163, 120363. doi:10.1016/j.ijheatmasstransfer.2020.120363

Krishna, V. M., and Rao, V. D. (2017). Experimental study of condensation of humid air in laminar flow in a vertical channel. *Heat Transf. Res.* 48, 379–390. doi:10.1615/heattransres.2016007475

Kumar, G. V., Cammiade, L. M. F., Kelm, S., Prakash, K. A., Grob, E. M., Allelein, H. J., et al. (2021). Implementation of a CFD model for wall condensation in the presence of non-condensable gas mixtures. *Appl. Therm. Eng.* 187, 116546. doi:10.1016/j.applthermaleng.2021.116546

Lee, H., Kharangate, C. R., Mascarenhas, N., Park, I., and Mudawar, I. (2015). Experimental and computational investigation of vertical downflow condensation. *Int. J. Heat Mass Transf.* 85, 865–879. doi:10.1016/j.ijheatmasstransfer.2015.02.037

Lee, W. H. (1980). Pressure iteration scheme for two-phase flow modeling. *Comput. methods two-phase flow Part. Transp.* 1980, 61–82.

Lewis, W. K., and Whitman, W. G. (1924). Principles of gas absorption. *Industrial Eng. Chem.* 16, 1215–1220. doi:10.1021/ie50180a002

Li, J. (2013). CFD simulation of water vapour condensation in the presence of non-condensable gas in vertical cylindrical condensers. *Int. J. Heat Mass Transf.* 57, 708–721. doi:10.1016/j.ijheatmasstransfer.2012.10.051

Liao, Y., Vierow, K., Dehbi, A., and Guentay, S. (2009). Transition from natural to mixed convection for steam–gas flow condensing along a vertical plate. *Int. J. Heat Mass Transf.* 52, 366–375. doi:10.1016/j.ijheatmasstransfer.2008.06.008

Liu, Z., Sunden, B., and Yuan, J. (2012). VOF modeling and analysis of filmwise condensation between vertical parallel plates. *Heat Transf. Res.* 43, 47–68. doi:10.1615/heattransres.2012004376

Minkowycz, W. J., and Sparrow, E. M. (1966). Condensation heat transfer in the presence of noncondensables, interfacial resistance, superheating, variable properties, and diffusion. *Int. J. Heat Mass Transf.* 9, 1125–1144. doi:10.1016/0017-9310(66)90035-4

Peterson, P., Schrock, V., and Kageyama, T. (1993). Diffusion layer theory for turbulent vapor condensation with noncondensable gases. *J. Heat Transf.* 115, 998–1003. doi:10.1115/1.2911397

Punetha, M., and Khandekar, S. (2017). A CFD based modelling approach for predicting steam condensation in the presence of non-condensable gases. *Nucl. Eng. Des.* 324, 280–296. doi:10.1016/j.nucengdes.2017.09.007

Qiu, G., Cai, W., Li, S., Wu, Z., Jiang, Y., and Yao, Y. (2014). Numerical simulation on forced convective condensation of steam upward flow in a vertical pipe. *Adv. Mech. Eng.* 6, 589250. doi:10.1155/2014/589250

Rao, V. D., Krishna, V. M., Sharma, K. V., and Rao, P. V. J. M. (2008). Convective condensation of vapor in the presence of a non-condensable gas of high concentration in laminar flow in a vertical pipe. *Int. J. Heat Mass Transf.* 51, 6090–6101. doi:10.1016/j.ijheatmasstransfer.2008.03.027

Riva, E. D., and Col, D. D. (2012). Numerical simulation of laminar liquid film condensation in a horizontal circular minichannel. *J. Heat Transf.* 134, 1–8. doi:10.1115/1.4005710

Rose, J. W. (1980). Approximate equations for forced-convection condensation in the presence of a non-condensing gas on a flat plate and horizontal tube. *Int. J. Heat Mass Transf.* 23, 539–546. doi:10.1016/0017-9310(80)90095-2

Siow, E. C., Ormiston, S. J., and Soliman, H. M. (2007). Two-phase modelling of laminar film condensation from vapour-gas mixtures in declining parallel-plate channels. *Int. J. Therm. Sci.* 46, 458–466. doi:10.1016/j.ijthermalsci.2006.07.001

Sparrow, E. M., and Lin, S. (1964). Heat-transfer characteristics of polygonal and plate fins. *Int. J. Heat Mass Transf.* 7, 951–953. doi:10.1016/0017-9310(64)90150-4

Tang, G., Hu, H., Zhuang, Z., and Tao, W. (2012). Film condensation heat transfer on a horizontal tube in presence of a noncondensable gas. *Appl. Therm. Eng.* 36, 414–425. doi:10.1016/j.applthermaleng.2011.10.058

Tao, W., Guo, Z., and Wang, B. (2002). Field synergy principle for enhancing convective heat transfer-its extension and numerical verifications. *Int. J. Heat Mass Transf.* 45, 3849–3856. doi:10.1016/s0017-9310(02)00097-2

Wang, T., Tong, L., and Cao, X. (2022). Improvement of diffusion layer model for steam condensation in the presence of non-condensable gas under turbulent free convection. *Appl. Therm. Eng.* 213, 118631. doi:10.1016/j.applthermaleng.2022.118631

Wang, X., Chang, H., and Corradini, M. (2016). A CFD study of wave influence on film steam condensation in the presence of non-condensable gas. *Nucl. Eng. Des.* 305, 303–313. doi:10.1016/j.nucengdes.2016.06.003

Wang, Y., Zhao, Q., Zhou, Q., Kang, Z., and Tao, W. (2013). Experimental and numerical studies on actual flue gas condensation heat transfer in a left-right symmetric internally finned tube. *Int. J. Heat Mass Transf.* 64, 10–20. doi:10.1016/j.ijheatmasstransfer.2013.03.005

Yi, Q., Tian, M., Yan, W., Qu, X., and Chen, X. (2016). Visualization study of the influence of non-condensable gas on steam condensation heat transfer. *Appl. Therm. Eng.* 106, 13–21. doi:10.1016/j.applthermaleng.2016.05.134

Zhang, L., Zhang, G., Tian, M., Zhang, J., and Zhang, Y. (2019). Modeling of laminar filmwise condensation of methane with nitrogen on an isothermal vertical plate. *Int. Commun. Heat Mass Transf.* 105, 10–18. doi:10.1016/j.icheatmasstransfer.2019.03.018

Zhou, W., Henderson, G., and Revankar, S. T. (2010). Condensation in a vertical tube bundle passive condenser-Part 1: Through flow condensation. *Int. J. Heat Mass Transf.* 53, 1146–1155. doi:10.1016/j.ijheatmasstransfer.2009.10.039

Zschaeck, G., Frank, T., and Burns, A. D. (2014). CFD modelling and validation of wall condensation in the presence of non-condensable gases. *Nucl. Eng. Des.* 279, 137–146. doi:10.1016/j.nucengdes.2014.03.007

Glossary

Nomenclature

A_w area of the cell near the wall (m^2)
D_i mass diffusion coefficient for species i (m^2/s)
$D_{T,i}$ thermal diffusion coefficient (m^2/s)
E internal energy J)
h_{fg} specific enthalpy (J/kg)
J molecular mass flux ($kg/(m^2 \cdot s)$)
k_{eff} effective thermal conductivity ($W/(m \cdot k)$)
m_i mass flux of species i ($kg/(m^2 \cdot s)$)
p pressure (Pa)
q heat flux (W/m^2)
q_{conv} convection heat flux (W/m^2)
q_{cond} condensation heat flux (W/m^2)
R_l thermal resistance of liquid film ($(m^2 \cdot K)/W$)
R_g thermal resistance of gas ($(m^2 \cdot K)/W$)
Re Reynolds number
S_h energy source term (W/m^3)
S_m mass source term ($kg/(m^3 \cdot s)$)
T temperature (K)
T_i phase interface temperature (K)
T_w wall temperature (K)
u velocities (m/s)
V_c cell volume (m^2)
w_a mass fraction of air
w_s mass fraction of steam

Greek symbols

α volume fraction
δ thickness of liquid film (m)
κ interface curvature (1/m)
λ_l thermal conductivity of liquid film ($W/(m \cdot K)$)
ρ density (kg/m^3)
σ surface tension coefficient (N/m)
τ stress-strain tensor

Subscripts

a air
c cell
g gas
l liquid
m mass
sat saturation

frontiers | Frontiers in Energy Research

TYPE Original Research
PUBLISHED 20 February 2023
DOI 10.3389/fenrg.2023.1059503

OPEN ACCESS

EDITED BY
Abdolali K. Sadaghiani,
Sabancı University, Türkiye

REVIEWED BY
Zhongjie Shen,
East China University of Science and Technology, China
Naresh Hanchate,
Institute of Chemical Technology, India

*CORRESPONDENCE
Arijit Ganguli,
ganguliarijit@gmail.com

SPECIALTY SECTION
This article was submitted to Process and Energy Systems Engineering, a section of the journal Frontiers in Energy Research

RECEIVED 01 October 2022
ACCEPTED 23 January 2023
PUBLISHED 20 February 2023

CITATION
Ganguli A and Bhatt V (2023), CFD simulations to study bed characteristics in gas–Solid fluidized beds with binary mixtures of Geldart-B particles: A qualitative analysis.
Front. Energy Res. 11:1059503.
doi: 10.3389/fenrg.2023.1059503

CFD simulations to study bed characteristics in gas–Solid fluidized beds with binary mixtures of Geldart-B particles: A qualitative analysis

Arijit Ganguli* and Viraj Bhatt

School of Engineering and Applied Science, Ahmedabad University, Ahmedabad, India

The bed dynamics of unary and binary fluidized beds play a key role in understanding the pressure drop and hence provides an opportunity for performance improvement of the beds. In the present work, characteristics of fluidized beds with binary mixtures of Geldart-B particles were investigated using CFD simulations. The phenomena of segregation and mixing using simulations were studied, both qualitatively and quantitatively, at a range of superficial gas velocities (0.3–0.6 m/s) and two different bed heights. The study was divided into two parts. In Part I, the current study, a qualitative analysis of flow patterns for seven different binary mixtures, is presented. The quantitative analysis, including particle and gas velocity profiles, particle volume fraction profiles, and correlations for minimum fluidization velocity and pressure drop, will be presented in Part II of this work. A mathematical model consisting of an Eulerian-Eulerian model with RNG k-ε model and KTGF model to capture the bubble dynamics was used. The standardized values of coefficients and plastic stresses have been used for all simulations. The CFD model was validated using experimental data from the literature. Qualitative predictions of volume fraction profiles of small-sized particles showed that, for mixtures within a range of 40%–60% Geldart-B type large particles, the bubble and solid particle dynamics were different from those of single particles of the superficial gas velocities considered. In contrast to the single particles in the given superficial gas velocity range that were in bubbling regime, the binary particles showed a transition from bubbling to slugging to turbulent regime, as demonstrated by qualitative analysis. A homogeneous regime was observed for lower superficial gas velocities for mixtures consisting of 0%–20% large particles.

KEYWORDS

fluidized bed, binary mixtures, pressure drop, minimum fluidization velocity, flow patterns, particle velocity, CFD

Abbreviations: 2D two-dimensional **3D** three-dimensional **BFB** bubbling fluidized bed **CFD** computational fluid dynamics **GS** gas–solid **LLDPE** linear low-density polyethylene **KTGF** kinetic theory of granular flow **PSD** particle size distribution **RNG** renormalization group **RPT** radioactive particle tracking **SIMPLE** semi-implicit method for pressure-linked equations **TFB** turbulent fluidized bed.

1 Introduction

Gas–solid (GS) fluidized beds have been important in various applications, such as drying (Yohana et al., 2020), granulation (Behzadi et al., 2009), blending, combustion, gasification (Roy et al., 2021), and conversion of methanol to olefins (Chang et al., 2019), for more than seven decades. One of the several advantages of fluidized beds over fixed beds is their ability to be operated isothermally, with minimal axial temperature gradients (Menéndez et al., 2019). Analytical models of fluidized beds are complex, involving dynamics and transport phenomena of two or more phases; for example, gas and solids/particles and bed phases such as bubble, cloud, and emulsion. The first pioneering work in analytical modeling of fluidized beds was carried out by Harris et al. (2002) and Yoshida et al. (1969), and involved taking mass balances. However, modeling the dynamics of fluidized beds poses a challenge due to particle size distribution (PSD), influence of geometric parameters, such as column diameter, height of bed to column diameter ratio, properties of gas and particles or mixture of particles, operating parameters such as superficial gas velocity on bed pressure drop, and minimum fluidization velocity. Due to the influence of the aforementioned parameters, the GS flow in a fluidized bed changes and encounters different regimes, namely homogeneous, bubbling, turbulent, fast fluidization, and pneumatic regimes (Bi and Grace, 1995; Lim et al., 1995; Bi, 2011). Geldart (1973) defined four particle size groups for bed expansion, known as Geldart-A, -B, -C, and -D. Based on these particle sizes, it can be determined whether the bed can be fluidized, how much the bed can be fluidized, and the type of fluidization. With the advent of the 21st century, researchers emphasized the need for studies on the hydrodynamics of Geldart-B-type particles and binary mixtures (Zhang et al., 2006). In fluidized beds with binary systems, the primary fraction that forms the top layer of the bed, or the one that floats, is called the flotsam and the one at the bottom layer, or the one that sinks, is called the jetsam. A major challenge in binary systems is that the beds reach equilibrium with either mixing or segregation of particles as two extremes. These dynamics are studied using advanced experimental techniques that include non-intrusive methods like tomography, radioactive particle tracking (RPT) (Roy et al., 2021), and intrusive techniques that include pressure probes for measuring pressure drops and quality of fluidization, and optical probes for measuring particle diameter, particle velocity, etc. Dynamics and transport phenomena in fluidized beds have also been studied both qualitatively and quantitatively using computational fluid dynamics (CFD) (mostly Eulerian–Eulerian approaches)/mathematical modeling (Cooper and Coronella, 2005; Du et al., 2006; Gao et al., 2009; Pei et al., 2010; Zaabout et al., 2010; Chang et al., 2012; Mostafazadeh et al., 2013; Benzarti et al., 2014; Sahoo and Sahoo, 2016; Bakshi et al., 2017; Agrawal et al., 2018; Chang et al., 2019; Daryus et al., 2019; Khezri et al., 2019; Shrestha et al., 2019; Kotoky et al., 2020).

In the current study, the experimental lab scale fluidized bed was operated in transition regime for a binary mixture. Hence, relevant literature works on bubbling, slugging, turbulent, and fast fluidizing regimes are summarized in Table 1. In this part of the work, numerical studies on qualitative analysis of the low patterns were elaborated, showing prominent experimental and numerical works highlighting the operating regimes, operating parameters, major findings, limitations/opportunities, geometrical details of equipment (diameter and height), and particle characteristics (size, shape, etc.).

1.1 Numerical and experimental studies on fluidized beds involving binary systems

The major challenges in CFD modeling of fluidized beds involve the modeling of solid–solid and solid–fluid interactions with the help of the kinetic theory of granular flow (KTGF) for Eulerian–Eulerian models. Furthermore, recent studies suggest that 3D models capture the dynamics better than 2D models. The numerical studies explained in this section focus on bubbling fluidized beds (BFBs) and turbulent fluidized beds (TFBs) operating with binary mixtures, along with a few studies on unary beds. The following is a discussion of numerical studies carried out over the last few decades, along with combined experimental and numerical studies.

Huilin et al. (2003) performed simulations with binary mixtures using a KTGF model and the Euler–Euler approach (a multifluid model). The authors investigated the segregation of GS fluidized beds for binary mixtures for a bed height of 0.4 m and column diameter of 0.3 m. Finer particles tended to go up in the bed, while larger particles settled at the bottom, at lower superficial gas velocities (U_{gs} = 1.6 m/s). The authors found that at 10 s, complete segregation occurred at a superficial gas velocity of U_{gs} = 1.6 m/s. Furthermore, the authors observed that, with further increase in superficial gas velocity, solid volume fraction was more uniform in the axial direction. The authors concluded that the correct dynamics depended on distribution of particle size and energy dissipation due to solid–solid interactions.

Additionally, Philippsen et al. (2015) investigated the effect of various drag models to be used in fluidization and found that the Syamlal–O'Brien model (Syamlal and O'Brien, 1987) was the best drag model through which to assess the dynamics of fluidized beds.

Daryus et al. (2019) compared two turbulence models, namely the standard k–ε and the RNG k–ε models to understand the effects of turbulence on CFD simulations of fluidized beds. The authors concluded that, while neither model could accurately predict the pressure drop for superficial gas velocities of less than minimum fluidization velocity (U_{mf}), pressure drops were predicted accurately when the superficial gas velocities were higher than U_{mf}. Furthermore, the RNG k–ε model was found to predict the regimes and the static pressure distribution more accurately than the standard k–ε models.

Cooper and Coronella, (2005) carried out numerical simulations for a bubbling fluidized bed reactor in the titanium refining industry with rutile (small size and high-density) and coke (large size and low density) particles. Outcomes signifying the importance of numerical simulations and bed characteristics included: 1. prediction of accurate dynamic similarity in flow patterns using mixing and segregation during scaleup; 2. prediction of bubble wake formations directly below the gas bubble and dynamics of the wake below the bubbles as depicted in their solid volume fraction contours; 3. eruption of the bubbles causing deposition of solids at the bed surface; and 4. downward movement of those bubbles that did not travel in the bubble wake; 5. flotsam and jetsam had similar but distinct velocity trajectories; 6. a minor difference in apparent slip velocity of bubbles and its influence on bed dynamics over

TABLE 1 Literature review.

Author	Fluidized bed details				Operating parameter	Type of study			Key objective and findings	Remark
	Length, diameter, and shape of bed	Bed height	Particle size, single or mixture	Distributor details if provided	Superficial gas velocity	Analytical/ experimental/CFD simulation	Range of dimensionless numbers operated in, like Reynolds number, etc.	Flow regime		
Noda et al. (1986)	Diameter: 160 mm; height: 1700 mm; cylindrical	-	Sand (μm): 454, 1310, 1910, 2,800; glass beads (μm): 454, 843, 1000, 1680; wood (μm): 6540,8840,12500; Marten shot (μm): 647,772; soyabean (μm): 7800; small bean (μm): 5760; rubber (μm): 2,830; mixture	Brass distributor with diameter 2 mm and 10% holes	0–2 m/s (based on U_{mf})	Analytical/experimental	Reynolds number and Archimedes number	-	29	1, 2, 3, 5, 6
Chyang et al. (1989)	Diameter: 7.11 cm; cylindrical	-	Glass beads: 610–2,810 μm; iron shot: 1000–1560 μm; molecular sieve particles: 1510 μm, 1810 μm; mixture	Porous plate distributor	-	Analytical/experimental	Reynolds number and Archimedes number	-	30	1, 2, 3, 6
Čársky et al. (1987)	Diameter: 0.085 m; cylindrical	-	Glass (mm): 0.475, 0.2, 0.95; iron (mm): 0.17, 0.325; sand (mm): 0.145; mixture	Grid distributor	0–0.963 m/s	Experimental	-	-	1	1, 2, 4, 5, 6
Wirth (1988)	Diameter: 0.19 m; height: 11.5 m; cylindrical	-	Glass beads: 90 μm; single	-	0.9, 1.8, 3.3 m/s	Experimental	-	-	2	1, 2, 4, 6
Zhou et al. (1995)	Height = 9.14 m; Shape = circular	9.14 m	Ottawa sand of mean diameter = 213 μm; particle density = 2,640 kgm^{-3}	Multi-orifice distributor	5.5 m/s	Experimental	-	-	39.40	1, 3, 4, 5, 6
Cho et al. (2000)	Height = 0.80 m; shape = circular	0.80 m	Diameter = 772 μm; single LLDPE particle	-	0.30 m/s to 0.90 m/s	Experimental	Reynolds number and Peclet number	Turbulent regime	38	1, 2, 3, 6
Huilin et al. (2003)	Width: 0.3 m; Height: 1 m; rectangular slab	0.4 m	1 mm, 2.5 mm; mixture	-	1.3–2.1 m/s	CFD simulation	-	Bubbling regime	6	2, 3, 4, 6
Cooper and Coronella (2005)	Width: 0.15 m; height: 0.8 m; rectangular slab	0.2 m	Coke: 355 μm; rutile: 69.5 μm;	-	3.825 m/s	CFD simulation	-	Bubbling regime	9	2, 4, 9, 10
Ellis et al. (2004)	Small: diameter: 0.29 m, height: 4.5 m, cylindrical; large: diameter: 0.61 m, height: 9.8 m, cylindrical	-	FCC (μm): 78, 58, 81, 98; single particles	Small: aluminum perforated plate with the area ratio of 3.7%; large: perforated-plate with open area ratio 5.9%	0–1.6 m/s	Analytical/experimental	Reynolds number and Archimedes number	Turbulent regime	17	1, 2, 6, 11

(Continued on following page)

10.3389/fenrg.2023.1059503

TABLE 1 (*Continued*) Literature review.

Author	Fluidized bed details				Operating parameter	Type of study			Key objective and findings	Remark
	Length, diameter, and shape of bed	Bed height	Particle size, single or mixture	Distributor details if provided	Superficial gas velocity	Analytical/ experimental/CFD simulation	Range of dimensionless numbers operated in, like Reynolds number, etc.	Flow regime		
Coltters and Rivas (2004)	-	-	-	-	0.01–1000 cm/s (based on U_{mf})	Analytical	-	-	31	1, 2, 3, 6
Leion et al. (2018)	Diameter: 22 mm; height: 820 mm; Cylindrical	-	Metal oxide particles: 125–180 μm; binary mixture	Porous quartz plate	-	Experimental	-	-	57	1, 2, 3, 4, 5, 6, 7, 9, 10, 11
Chew et al. (2010)	Diameter: 18.5 cm; cylindrical	-	Sand particles: 80–670 μm	Stainless steel sintered porous plate, with an average porosity of 40% and 1.6 mm thickness	0–1.4 m/s	Experimental	-	Bubbling regime	8	1, 4, 10
Zaabout et al. (2010)	Circular	50 mm, 100 mm, 150 mm	Particle size = 109 μm and 175 μm; two particles of different sizes	-	For particle size = 109 μm, V = 0.35–0.91 m/s; For particle size = 175 μm, V = 0.66–1.14 m/s	Analytical/experimental	Dimensionless velocity, U = 1 for H = 100 mm and U = 0.32 for H = 150 mm	Turbulent regime	35.36.37	1, 3, 4, 9
Chang et al. (2012)	Height = 0.6 m; Width = 0.35 m; Shape = rectangular	0.6 m	300 μm–400 μm solid particles	-	0.25 m/s	CFD simulation	Reynolds number	-	58, 59	3, 4, 5, 6, 8, 10, 11
Di Maio et al. (2012)	-	-	-	-	-	Analytical	Reynolds number	-	3	1, 2, 3, 4, 5, 6, 9
Obuseh et al. (2012)	Length: 7 cm; width: 30 cm; height: 91 cm; rectangular column	-	Single particles of aluminum, glass, and nylon with diameter 6 mm	Multi-orifice distributor with 0.4 cm diameter and 23% open area ratio	0.0197–1.4033 m/s	Experimental	Reynolds number	Particulate flow regime	7	1, 2, 3, 9, 11
Mostafazadeh et al. (2013)	Height = 80 cm; diameter = 8 cm; Shape = cylindrical	80 cm	A binary mixture of particles with diameter of 1 and 2 mm and density of 2,400, and 2,500 kgm^{-3} were fluidized	The distributor consisted of a perforated plate with an open-area ratio of 0.8%	0.5–2.5 m/s	Numerical	Reynolds number	Flow regime; transport regime	46.47.48	1, 2, 3, 4, 7, 10
Benzarti et al. (2014)	Height = 2 m; width = 0.2 m; Shape = rectangular	2 m	Glass spheres with a density of 2,400 kgm^{-3} and a mean diameter of 120 μm	-	1 m/s	Experimental	Reynolds number	Turbulent regime	55.56	4, 6, 9, 10

(Continued on following page)

10.3389/fenrg.2023.1059503

TABLE 1 (*Continued*) Literature review.

Author	Fluidized bed details				Operating parameter	Type of study			Key objective and findings	Remark
	Length, diameter, and shape of bed	Bed height	Particle size, single or mixture	Distributor details if provided	Superficial gas velocity	Analytical/ experimental/CFD simulation	Range of dimensionless numbers operated in, like Reynolds number, etc.	Flow regime		
Lan et al. (2014)	Upper section is ϕ 500 mm × 12 mm × 4000 mm and the lower section is ϕ 500 mm × 12 mm × 3,000 mm	1.335 m	FCC catalyst: 60 μm; new particle: 930 μm; single	-	0.2–0.6 m/s	CFD simulation	-	Turbulent regime	15.16	4, 5, 9
Sande and Ray (2014)	Height = 12 cm	12 cm	Geldart-A particle of 70 μm and density = 2000 kgm^{-3}	-	0.008 m/s	CFD simulation	-	Homogeneous expansion regime	49.50	1, 2, 3, 4, 6, 9, 10
Sahoo and Sahoo (2016)	Height = 100 cm; cylindrical	100 cm	Diameter = 63 μm; alumina powder	Filter cloth with pores of approx. 40 microns was used as distributor	0.016–0.067 m/s	CFD simulation	Reynolds number	Compressible regime	32.33.34	1, 2, 4, 11
Bakshi et al. (2017)	Diameter = 50 cm; Height = 50 cm	50 cm	Alumina = 0.29 mm; glass = 0.50 mm; LLDPE = 1.15 mm	-	2–4 m/s	CFD simulation	-	Bubbling regime	51.52.53.54	4, 7
Formisani et al. (2008)	Diameter: 10 cm; cylindrical	-	Molecular sieves (μm): 624, 800; glass ballotini (μm): 354, 271, 428, 499, 593, 612; Steel shots (μm): 439; mixture	4-mm-thick plastic porous distributor	0–0.6 m/s	Experimental	-	-	26	1, 2, 3, 4, 6
Fu et al. (2019)	Diameter (mm): 101.6, 152.4, 203.2; cylindrical	-	Magnetite: 221 μm; sand: 351 μm; gangue: 386 μm; coal: 366 μm; mixture	Two plastic perforated plates with filter cloth in between; the orifice diameter is 1.5 mm with the total open area of 11%	0–1.5 m/s (based on U_{mf})	Analytical/experimental	Reynolds number, and Archimedes number	-	27.28	1, 2, 3, 4, 7, 8, 9
Kotoky et al. (2020)	Height = 0.4 m; shape = spherical	0.4 m	Spherical glass beads; particle diameter = 350, 400, 450, 500 μm; Particle density = 2000 kgm^{-3}	-	0.54 m/s	CFD simulation	-	-	41.42.43	4, 5, 6, 7, 9, 10
Chang et al. (2019)	Height = 3.00 m, width = 0.4 m; Shape = rectangular	3 m	Geldart-B particles of 440 μm; particle density = 2,480 kgm^{-3}	-	3.5 m/s, 4 m/s	CFD simulation	Reynolds number	Bubbling regime; turbulent regime	44.45	1, 2, 3, 4, 5, 6, 9

(Continued on following page)

10.3389/fenrg.2023.1059503

TABLE 1 (*Continued*) Literature review.

Author	Fluidized bed details				Operating parameter	Type of study			Key objective and findings	Remark
	Length, diameter, and shape of bed	Bed height	Particle size, single or mixture	Distributor details if provided	Superficial gas velocity	Analytical/ experimental/CFD simulation	Range of dimensionless numbers operated in, like Reynolds number, etc.	Flow regime		
Daryus et al. (2019)	Width 10 cm, height 40 cm, thickness 1 cm, rectangular	80 mm	Fuse alumina grit with diameter 320 μm, single	Perforated plate with uniform holes in the whole plate	0.20–1 m/s	Experimental/CFD simulation	-	-	21	1, 2, 3, 4, 5, 6, 9, 10
Shrestha et al. (2019)	Width 0.02 m, height 0.08 m, thickness 0.0004 m, cuboidal	-	Oblate: 126 × 126 × 63 μm, 110 × 110 × 83 μm, spherical: 100 × 100 × 100 μm, prolate: 87 × 87 × 131 μm, 79 × 79 × 159 μm, single	-	0.006–0.03 m/s (based on U_{mf})	CFD simulation	-	Bubbling regime	4	4, 11
Shao et al. (2020)	Length 1200 mm, diameter 41 mm, cylindrical	10 cm	Silica particles with an average diameter of 0.4 mm, mixture	Mesh with a pore size of 100 μm	0–0.12 m/s (based on U_{mf})	Analytical/experimental	Reynolds number and Archimedes number	_	5	1, 2, 3, 5, 8, 9
Chew and Cocco (2021)	Fast fluidization regime: diameter 0.3 m, height 18.3 m, cylindrical	-	Fast fluidization regime: large glass 650 μm, small glass 170 μm, large HDPE 650 μm, turbulent regime: glass 165 μm, polystyrene 327.5 μm, sand 196 μm	Fast fluidization regime: mixing pot	Fast fluidization regime: 10–17 m/s	Analytical	-	Fast fluidization regime, turbulent regime	12.13	1, 2, 3, 4, 7, 8, 10
	Turbulent regime: diameter 0.184 m, height 4 m, cylindrical			turbulent regime: sintered stainless steel porous plate	turbulent regime: 1.5 and 1.7 m/s					
Gupta and De (2021)	Square cross-section	-	Coal: 820 μm; sand: 325 μm; mixture	-	0–0.4 m/s	Analytical/experimental	-	-	10.11	1, 4, 7, 8, 10, 11
	200 mm × 200 mm: Height: 1400 mm; rectangular									
Korkerd et al. (2021)	Height 50 cm, diameter 12.5 cm, cylindrical	-	Average particle diameters of sand: 0.19 mm, 0.46 mm, 0.92 mm, mixture	Stainless-steel plate with a 10.1% open area and hole size of 0.4 cm	0–0.8 m/s (based on U_{mf})	Analytical/experimental	Archimedes number	-	25	1, 2, 3, 5, 6, 7, 8, 9, 10, 11
Roy et al. (2021)	Height 100 cm, diameter 10 cm, cylindrical	-	Glass beads of diameter as 2 mm, mixture	Steel wire mesh with an opening of 350 μm	0–2 m/s	Experimental	-	-	22., 23., 24	4, 7, 8, 10, 11

(Continued on following page)

10.3389/fenrg.2023.1059503

TABLE 1 (*Continued*) Literature review.

Author	Fluidized bed details				Operating parameter	Type of study			Key objective and findings	Remark
	Length, diameter, and shape of bed	Bed height	Particle size, single or mixture	Distributor details if provided	Superficial gas velocity	Analytical/ experimental/CFD simulation	Range of dimensionless numbers operated in, like Reynolds number, etc.	Flow regime		
Emiola-Sadiq et al. (2021)	Diameter 14.5 cm, Height 78 cm, cylindrical	22 cm	Soyhull pellet D = 5 mm, L = 10 mm (cylindrical); oat hull pellet D = 5.5 mm, L = 7 mm (cylindrical); sawdust 1120 μm (needle-like); silica sand 329 μm (spherical); mixture	Porous plate mesh with a pore size of 0.06 mm	0–0.5 m/s	Experimental	-	-	18.19.20	4, 7, 8, 10, 11

Objectives and findings: 1. Criterion for a mixed and segregated bed for binary systems was derived. 2. Comprehensive plots of pressure drop v/s superficial gas velocities for operating circulating fluidized beds were presented. 3. Analytical model to predict segregation in a FB, having binary mixture of different materials. 4. CFD simulations to study the effect of particle shape on bubble dynamics in bubbling FB. The bubble dynamics are significantly different for different shapes. 5. Correlation development for minimum fluidization velocity. Effect of unary and binary particle size distributions for different temperature and pressure. 6. CFD simulations for BFB of binary mixtures considering effect of particle size distributions and energy dissipation due to non-ideal particle–particle interactions. Importance of the KTGF model was highlighted. 7. Experimental study of binary mixtures of three different types of same sized and different density particles. Correlations were developed for minimum fluidization velocities. 8. Experimental investigations on segregation and mixing characteristics of BFBs containing Geldart-B particles. 9. CFD studies for mixing and segregation of binary mixtures in BFBs. The model developed was able to predict the characteristics for different operating conditions of binary mixtures. 10. Experimental investigation of segregation characteristics for binary mixtures in dual fluidized beds for change in operating parameters like fluidization velocity, particle mixture properties, and solid holdup. 11. Hydrodynamic characteristics of binary beds are significantly different than unary beds. 12. Comparative study of cluster formations, mass flux variation, and segregations in turbulent fluidization and fast fluidization regimes. 13. Cluster formation probability was higher in turbulent fluidized beds, while segregation extents were the same. 14. Mass fluxes were more dependent on particle properties in turbulent regime than fast fluidized regimes. 15. Hydrodynamics in a turbulent FB with binary mixture of polydisperse particles were studied using CFD with population balance. 16. The model gave important insights into the dynamics of particles with small and large differences in particle size distributions. 17. Study of dynamics of turbulent FB for different column diameters and development of a correlation for minimum fluidization velocity. 18. Experimental study of mixing and segregation of binary mixtures consisting of different percentage of biomass (5%–20%). 19. Amount of mixing increased with increased superficial gas velocity up to biomass concentration of 20%, after which it decreased. 20. Most of the materials used were non-spherical in shape and size and greater than 1 mm. 21. Two-dimensional CFD simulations using Geldart-B particles comparing standard k-ε and RNG k–ε models were carried out. The RNG k–ε model was found to be better than the standard k–ε model. 22. Experimental study of the effect of higher proportion of large particle sizes on bubble rise velocities. 23. An important finding was that increased higher fraction decreased bubble rise velocities, and hence particle velocities. 24. Data for velocity distribution were not available for binary and polydisperse beds. 25. Correlation development for minimum fluidization velocity and pressure drop using the artificial neural network. 26. Experimental investigations of pressure drop with the superficial gas velocity profile for binary mixture and compositions of particles at different places. 27. Experimental measurements and correlation development for minimum fluidization velocity for binary mixtures. 28. Predictions showed good match with experimental and published data. 29. Experimental investigations and correlation development for minimum fluidization velocity and pressure drop for binary mixtures. Predictions showed good match with experimental and published data. 30. Experimental investigations and correlation development for minimum fluidization velocity and pressure drop. Predictions showed good match with experimental data. 31. Experimental investigations and correlation development for minimum fluidization velocity and pressure drop. 32. CFD investigations were carried out for Geldart-A and -C type particles. 33. Sensitivity analyses of various geometric, operating, particle shape, size, and density were performed, and gas and solid fractions were analyzed. 34. The results will aid in design of fluidized bed reactors. 35. Experimental investigations were carried out in the dilute region of the riser in a CFB. 36. The shape of the axial and transverse profiles were dependent on the bed height and superficial gas velocities. 37. For lower bed heights, the movement is toward the center; with increased bed height, the movement is toward the wall. 38. Experimental investigation of gas mixing and axial dispersion in a bubbling fluidized bed using the RTD approach for linear low-density polyethylene was carried out, and a correlation for the dimensionless dispersion coefficient relating Re and aspect ratio was developed. 39. Experimental investigations to measure axial velocities of rising and falling particles were carried out for circulating fluidized bed riser. 40. The axial and transverse particle velocities were affected by superficial gas velocities and solids circulation rate. 41. Numerical investigations were carried out to understand the effect of particle diameter on bubbling GS fluidized beds. 42. Particle velocities decreased with increased particle diameter, which increased particle volume fractions. 43. The increase in particle velocity in the fluidization zone was higher for smaller particles and decreased with particle diameter. 44. CFD investigations of a turbulent fluidized bed with 2D and 3D simulations. Three-dimensional simulations were found to be more sensitive to specularity and restitution coefficients. 45. Two-dimensional simulations over-estimated particle volume fractions in the middle and top of the bed. 46. Two-dimensional CFD simulations for FBs were carried out. 47. Increased bed height led to increased bed height but decreased average diameter of particles in the bed. 48. Significance of restitution coefficient in understanding the false segregation in beds in numerical simulations. 49. CFD simulations to study the effect of mesh size on transition from homogeneous to bubbling regime using Eulerian–Eulerian models. 50. The presence of a dilute region was dependent on selection of drag law, with Gidaspow and Syamlal–O'Brien models showing good predictions that omitted frictional stress and improper wall boundary conditions and showed appropriate minimum bubbling velocities. 51. Investigation of mixing dynamics and their dependence on operating conditions using CFD simulations for fluidized bed biomass gasification. 52. Bubble-induced solid micro-mixing induced solids up flow in nose and wake regions, and down flow along bubble walls. 53. Development of an analytical model for the fluidized bed. 54. Solid mixing was adversely affected in the presence of gas bypass, particularly in cases of heavier particles. 55. Three-dimensional CFD investigations to analyze the capabilities of different drag models to predict the dynamics of turbulent fluidized beds filled with Geldart-B particles. 56. The Gidaspow model was found to be the best to predict drag coefficients per this investigation. 57. Development of a new experimental method to test the reactivity of particles in a GS fluidized bed. 58. CFD modeling to study heat transfer between particles in a fluidized bed. 59. Heat transfer coefficient increased with large particle size and superficial gas velocity.
Limitations: 1. Investigations of flow patterns depicting volume fractions of solid particles, bubble dynamics, and mixing were not performed. 2. Axial velocity profiles for gas and particles across radial distance for different axial positions were not performed. 3. Particle volume fraction profiles across vertical centerline were not shown. 4. Correlations for minimum fluidization velocity and pressure drop were not developed. 5. The work was limited to binary mixture of particles of same size. 6. Densities of the particles were the same. 7. The particle sizes were larger than the Geldart classification of sizes. 8. Experimental investigations/CFD simulations were carried out at the same bed height. 9. Sensitivity analyses in terms of superficial gas velocities and different combinations of particle diameters were not performed. 10. Two-dimensional simulations were carried out, which did not show good predictions in the middle and top parts of the beds. 11. The work was limited to single particles of different sizes.

10.3389/fenrg.2023.1059503

passage of both time and additional bubbles. The authors have substantiated the aforementioned outcomes for a wide range of particle sizes and superficial gas velocities.

Mazzei et al. (2010) carried out numerical simulations for a binary mixture of particles to understand two cases. Case 1: Investigation of minimum fluidization velocities at which the mixture no longer remains fixed, but starts segregating, and transient fluidization takes place; and Case 2: The mixture becomes steadily fluidized and fully mixed. The authors assessed the following: 1. numerical stability of models in fast segregating beds; 2. mutual effects of plastic viscosity and granular temperature; 3. the role played by plastic solid stress; and 4. selection of an appropriate time-step to ensure invariance of numerical results. The authors emphasized the role of plastic stress in the modeling of collapsing monodisperse fluidized beds. The authors found that, in the case of collapsing monodisperse fluidized beds, plastic stress and plastic solid viscosity are important, whereas plastic solid pressure can be ignored. The authors further used the standardized parameter to find the bed characteristics; for instance, the minimum fluidization velocity (U_{mf}), superficial gas velocity (U_{gs}), necessary for complete mixing, and velocity for oscillating pressure drop. The authors used the multifluid model or KTGF model as specified via Ansys Fluent software.

Jayarathna and Halvorsen, 2011 carried out both experimental and numerical investigations with different binary mixtures of glass particles and studied the pressure drop and volume fraction changes for lab scale fluidized beds. The authors conducted experiments for two different bed heights, each for a range of superficial gas velocities (U_{gs} = 0.3–1 m/s). The authors validated their numerical model through experimental measurements of pressure drop with CFD predictions and found moderate agreement due to lack of distributor availability. Furthermore, the authors observed that, at slugging conditions, bubbles were moving upward using a zigzag path.

Mostafazadeh et al. (2013), with the help of their in-house code, carried out numerical investigations for mixtures of 1 mm and 2 mm particles with densities of 2,400 kgm^{-3} and 2,500 kgm^{-3}, respectively, for a superficial gas velocity range of U_{gs} = 0.5–2.5 m/s. The authors observed that increased mass fraction of small particles from 49% to 59% led to increased bed height and decreased average diameter of particles in the bed. The authors also observed that differences in restitution coefficient can cause segregation, even among particles of the same size and density. Hence, an appropriate restitution coefficient value is needed for suitable bed characteristics.

Benzarti et al. (2014) examined the ability of the mathematical/CFD models to predict dynamics of TFBs filled with Geldart-B particles. The authors investigated the significance of drag coefficient models and restitution coefficient values on the prediction of dynamics of fluidized beds in CFD. The authors concluded that the restitution coefficient, which accounts for the inelasticity of the particle-particle collisions, needs to be considered, especially when the superficial gas velocity is less than the minimum fluidization velocity. The authors concluded that, for Geldart-B particles, the Gidaspow model (Huilin et al., 2003) gave the most reasonable results, both in terms of qualitative and quantitative predictions. Furthermore, with a specularity coefficient value of 1 and a restitution coefficient of 0.9, the model gave near accurate predictions. While analyzing the effect of superficial gas velocity (U_{gs}), the authors also found that increased superficial gas velocity caused particles to be entrained into the dilute region of a turbulent fluidized bed.

Sande and Ray (2014) carried out numerical studies of transition from a homogeneous to bubbling regime for Geldart-A particles and concluded that the drag laws played an important role in the identification of the dilute region of fluidization. The authors, in their qualitative analysis using CFD, also found that inappropriate selection of wall boundary conditions and inclusion of frictional stress led to inappropriate predictions of minimum fluidization velocity. Such studies have not been carried out for Geldart-A, -B, -C, and -D particles. Both the Gidaspow (Huilin et al., 2003) and Syamlal–O'Brien models (Syamlal and O'Brien, 1987) gave good results for moderate superficial gas velocities (of approximately U_{gs} = 0.008 m/s), whereas for other velocities (of approximately U_{gs} = 0.01 m/s), the Wen Yu drag law model gave good results.

Sahoo and Sahoo (2016) carried out CFD simulations for Geldart-C and -A fine particles (monodisperse particles) in a cylindrical fluidized column. The effect of parameters, such as static bed height, particle density, size of particle, and superficial velocity of fluidizing medium were studied and compared with experimental results. The bed expansion and pressure drop variation with increased superficial velocity of the gas was found to be similar to that of conventional fluidized beds. The authors were able to simulate and confirm that fluidization under normal conditions is a challenge for Geldart particles due to action of strong cohesive forces.

Bakshi et al. (2017) carried out CFD simulations to study the effects of solids mixing on thermal and concentration gradients, and on the performance of fluidized bed reactors. The authors found that the bubble-induced solids were responsible for the micro-mixing during the up flow of the solids. This included the wake region during the up flow of solids. Furthermore, the mixing of solids was affected by gas bypass or through flow, particularly during fluidization of heavier particles. The authors also investigated the dynamics of the motion of gas and solids, and their interaction, under specific operating conditions.

Chang et al. (2019) studied dynamics in fluidized beds with Geldart-B particles (binary systems) with 2D and 3D simulation approaches. An important aspect in Eulerian-Eulerian modeling is the restitution coefficient. Hence, analysis of sensitivity of the restitution coefficient was carried out and it was determined that a value of 0.9–1 for the restitution coefficient predicted realistic results for Geldart-B particles. Furthermore, the authors found that 2D simulations predicted the dynamics of the dense phase (bottom layer) well, whereas they over-estimated aspects of the dynamics of the middle and upper regions. The 2D simulations also over-estimated the bubble sizes and bed expansion, solid concentration, and solid velocities compared to experimental results. Hence, the authors suggested that 3D simulations should be carried out to obtain realistic results in studies of the dynamics of fluidized beds with Geldart-B particles.

Kotoky et al. (2020) carried out CFD simulations using an in-house code for Geldart-B particles to analyze the bed dynamics of unary fluidized bed reactors. The authors concluded that, with increased particle diameter, the particle velocity at any section in a fluidized zone decreased while the particle volume fraction increased, i.e., particle velocities were higher for smaller sized particles, especially in the dilute region of the bed, whereas velocities were lower for larger particle sizes. Hence, maximum value of time-averaged volume fractions was found for larger particles at the bottom of the reactor.

1.2 Discussion

From Section 1.1:

1. Turbulence models like the RNG k–ε model are better than the standard k–ε model for both unary and binary mixtures.
2. KTGF can capture bubble dynamics for bubbling beds, including bubble movement in the bed, bubble wake, and bubble eruption.
3. Roles of plastic solid stress, plastic viscosity, granular temperature, plastic solid pressure in unary/monodispersed beds using commercial software Ansys Fluent have been standardized and found to predict bed characteristics well via comparison with experimental measurements.
4. The standardized values of the restitution coefficient and specularity coefficient should be used in predicting correct bed characteristics using CFD models. The values reported in the literature are in the range of 0.9–1.
5. For predicting the suitable drag coefficient, the Gidaspow (Huilin et al., 2003) and Syamlal–O'Brien (Syamlal and O'Brien, 1987) models were found to be most appropriate when focusing on bed dynamics. However, if thermal and concentration gradients are coupled with bed dynamics, the Wen and Yu drag law provides better results.

1.3 Objective of the present work

In the present work, the flow patterns (both steady and transient) of binary mixture particles with the same densities were investigated using CFD simulations. Geldart-B particles were used at different operating conditions. For this purpose, geometry available in the current literature (Jayarathna and Halvorsen, 2011) was considered. The CFD model considers the standard values for different parameters, such as friction pressure, plastic viscosity, plastic pressure, specularity coefficient, and restitution coefficient, as reported in the literature, and the drag and other laws used in KTGF modeling. In future work, a sensitivity analysis will be carried out for different combinations wherever suitable. The model will then be validated with experimental data from the literature. In the case of good agreement, seven different binary mixtures will be taken, and simulations for three different superficial velocities, each for two different bed heights, will be carried out. The quantitative analysis will be carried out in Part II of the study and reported in a subsequent article.

The originality of this manuscript lies in: 1. the comprehensive combination of the particle size of binary mixtures and the operating parameters considered; 2. the CFD model that considered all the current best practices; and 3. investigation of whether unusual bed characteristics were present in any of the cases considered.

2 Mathematical modeling

2.1 Assumptions

1. No mass transfer between the phases is taking place in the system. 2. Two different solid phases of the same density, but containing particles of different sizes, are simultaneously interacting with each other and with the gas phase. 3. All the solid particles are spherical. 4. The gas fluid phase is a Newtonian fluid. 5. No other force or energy, other than gravity, is affecting the fluidized bed system in any manner.

2.2 Models

Different models were used for modeling the interaction between the solid phase and the gas phase. Table 2 shows the models used for quantities.

2.3 Mathematical modeling with equations

The Eulerian model, or two-fluid model, considers each phase as a continuum, where the phases are interacting and interpenetrating in nature. The solid phase may be assumed to be a pseudo-fluid. For the given study, the Eulerian model is used for the modeling of the fluidized bed system.

2.3.1 Continuity equations

The continuity equation of a phase i is given by:

$$\frac{\partial}{\partial t}\left(\varepsilon_i \rho_i\right) + \nabla \cdot \left(\varepsilon_i \rho_i U_i\right) = 0 \tag{1}$$

where ε represents the volume fraction of the phase i, ρ represents the density of the phase i, and U represents the velocity of the phase i.

In the system, there are three phases interacting with each other. They are given by: 1. g representing the fluid gas phase; 2. s_1 representing solid phase with smaller particle size; and 3. s_2 representing solid phase with larger particle size.

2.3.2 Momentum equations

The momentum equation for the gas fluid phase is given as:

$$\frac{\partial}{\partial t}\left(\varepsilon_g \rho_g U_g\right) + \nabla \cdot \left(\varepsilon_g \rho_g U_g U_g\right) = \left(-\nabla \cdot P_g\right) + \nabla \cdot \Pi_g + \left(\varepsilon_g \rho_g g\right) + \sum_{i=1}^{2} \phi_{g,si}\left(U_{si} - U_g\right) \tag{2}$$

where P_g represents the total fluid pressure, Π_g represents the stress tensor of the gas phase, g represents gravitational acceleration, and $\phi_{g,si}$ represents the drag interaction coefficient between the gas phase and the solid phase s_i.

The stress tensor of the gas phase is given by:

$$\Pi_g = \varepsilon_g \mu_g \left[\nabla \cdot U_g + \nabla \cdot U_g^T\right] - \frac{2}{3}\varepsilon_g \mu_g \nabla \cdot U_g \tag{3}$$

where μ_g represents the dynamic viscosity of the gas phase, $\nabla \cdot U_g$ represents the divergence of U_g, and $\nabla \cdot U_g^T$ represents the divergence of the transpose of U_g.

The solid phase momentum equation is given by:

$$\frac{\partial}{\partial t}\left(\varepsilon_{si} \rho_{si} U_{si}\right) + \nabla \cdot \left(\varepsilon_{si} \rho_{si} U_{si} U_{si}\right) = \nabla \cdot \Pi_{si} + \left(\varepsilon_{si} \rho_{si} g\right) + \phi_{g,si}\left(U_g - U_{si}\right) + \sum_{j=1, j \neq i}^{2} \phi_{si,sj}\left(U_{sj} - U_{si}\right) \tag{4}$$

where Π_{si} represents the total stress tensor for the phase s_i and $\phi_{si,sj}$ represents the drag interaction coefficient interacting between the solid phase s_i and the solid phase s_j.

The total solid phase tensor is given by:

TABLE 2 Models used for different quantities.

Quantity	Model
Multiphase	Eulerian–Eulerian
Viscous	RNG k–ϵ
Granular viscosity	Syamlal et al. (1993)
Granular bulk viscosity Frictional viscosity	Lun et al. (1984) Schaeffer (1987)
Frictional pressure	Schaeffer model
	Syamlal et al. (1993)
Solids pressure	Ahmadi and Ma (1990)
Radial distribution	Ahmadi and Ma (1990)
Drag	Syamlal and O'Brien (1987)

$$\Pi_{si} = (-P_{si} I_{si}) + \varepsilon_{si}\left[\xi_{si}(\nabla \cdot U_{si}) + \mu_{si}\left(\nabla \cdot U_{si} + \nabla \cdot U_{si}^{T}\right)\right] \quad (5)$$

where P_{si} represents the total solid phase pressure of the phase s_i, I_{si} represents the moment of inertia of particles of the phase s_i, ξ_{si} represents the granular bulk phase viscosity of the phase s_i, and μ_{si} represents the solid phase granular viscosity for the phase s_i.

The solid phase granular viscosity given by Syamlal and O'Brien (1987) is:

$$\mu_{si} = \mu_{si(col)} + \mu_{si(kin)} + \mu_{si(fr)} \quad (6)$$

where $\mu_{si(col)}$ represents the collisional viscosity, $\mu_{si(kin)}$ represents the kinetic viscosity, and $\mu_{si(fr)}$ represents the frictional viscosity.

The collisional viscosity is given as:

$$\mu_{si(col)} = \frac{4}{5}\varepsilon_{si}\rho_{si}d_{p,si}G_{si,sj}(1+e_{si})\left(\frac{\Theta_{si}}{\pi}\right)^{\frac{1}{2}}\varepsilon_{si} \quad (7)$$

where $d_{p,si}$ represents the particle size diameter of the phase s_i, which is the same for all, $G_{si,sj}$ represents the radial distribution of the solid–solid particle interaction between the solid phases s_i and s_j, Θ_{si} represents the granular temperature of the phase s_i, and e_{si} represents the total coefficient of restitution for the phase s_i.

The kinetic viscosity is given by:

$$\mu_{si(kin)} = \frac{\varepsilon_{si}d_{p,si}\rho_{si}\sqrt{\Theta_{si}\pi}}{6(3-e_{si})}\left[1 + \frac{2}{5}(1+e_{si})(3e_{si}-1)\varepsilon_{si}G_{si,sj}\right] \quad (8)$$

The total solid phase pressure is given by the Ma-Ahmadi model (Ahmadi and Ma, 1990) as:

$$P_{si} = \varepsilon_{si}\rho_{si}\Theta_{si}\left[\left(1 + 4\varepsilon_{si}G_{si,sj}\right) + \frac{1}{2}\left[(1+e_{si})\left(1 - e_{si} + 2\mu_{si(fr)}\right)\right]\right] \quad (9)$$

The granular bulk phase viscosity is given by the mathematical model of Lun et al. (1984), as shown:

$$\xi_{si} = \frac{4}{3}\varepsilon_{si}d_{p,si}G_{si}(1+e_{si})\sqrt{\frac{\Theta_{si}}{\pi}}. \quad (10)$$

The total coefficient of restitution is given as:

$$e_{si} = \frac{e_{si,si} + e_{si,sj}}{2} \quad (11)$$

where $e_{si,si}$ represents the coefficient of restitution between the similar particles of the phase s_i and $e_{si,sj}$ represents the coefficient of restitution between the dissimilar particles of the phases s_i and s_j.

The radial distribution function is given by the Ma-Ahmadi model (Ahmadi and Ma, 1990):

$$G_{si} = \frac{1 + 2.5\varepsilon_{si} + 4.59\varepsilon_{si}^2 + 4.52\varepsilon_{si}^3}{\left\{1 - \left(\frac{\varepsilon_{si}}{\varepsilon_{si(max)}}\right)^3\right\}^{0.68}} \quad (12)$$

$$G_{si,sj} = \frac{1 + 2.5\varepsilon_{si} + 4.59\varepsilon_{si}^2 + 4.52\varepsilon_{si}^3}{\left(1 - \left(\frac{\varepsilon_{si}}{\varepsilon_{si(max)}}\right)^3\right)^{0.678}} + \frac{1}{2}d_{p,sj}\sum_{i=1}^{2}\frac{\varepsilon_{si}}{d_{p,si}} \quad (13)$$

where $\varepsilon_{si(max)}$ represents the maximum possible volume fraction for the solid phase s_i.

The granular temperature is calculated using the algebraic model:

$$\Theta_{si} = \left[-k_1\varepsilon_{si}tr(\Pi_{si}) + \frac{\sqrt{k_1^2\varepsilon_{si}^2tr^2(\Pi_{si}) + 4k_2\varepsilon_{si}\left(k_2tr^2(\Pi_{si}) + 2k_3tr(\Pi_{si}^2)\right)}}{2\varepsilon_{si}k_4}\right]^2 \quad (14)$$

where k_1, k_2, k_3, and k_4 are equation constants given by:

$$k_1 = 2(1+e_{si})\varepsilon_{si}G_{si} \quad (15)$$

$$k_2 = \frac{4}{3\sqrt{\pi}}d_{p,si}\rho_{si}(1+e_{si})\varepsilon_{si}G_{si} - \frac{2}{3}k_3 \quad (16)$$

$$k_3 = \frac{d_{p,si}\varepsilon_{si}\sqrt{\pi}}{6(3-e_{si})}\left(1 + \frac{2}{3}(1+e_{si})(3e_{si}-1)\varepsilon_{si}G_{si}\right) + \frac{8d_{p,si}\varepsilon_{si}G_{si}(1+e_{si})}{10\sqrt{\pi}} \quad (17)$$

$$k_4 = \frac{12(1-e_{si}^2)\varepsilon_{si}G_{si}}{d_{p,si}\sqrt{\pi}} \quad (18)$$

2.3.3 Turbulence governing equations

The turbulence-based modeling of the system was carried out using the Renormalization Group RNG k–ϵ model for turbulent viscosity, since the previous sensitivity analysis provided good results. The model equations are similar to the standard k–ϵ model, with the constant C_μ in turbulent viscosity modeled by a differential equation. A constant value of 0.0845 can also be derived from the differential equations. In the current study, the constant value was provided. The model uses the following equations:

$$\mu_{tur} = \rho_g C_\mu \frac{k^2}{\epsilon} \quad (19)$$

$$\frac{\partial}{\partial t}\left(\rho_g k\right) + \frac{\partial}{\partial x_r}\left(\rho_g k U_r\right) = \frac{\partial}{\partial x_z}\left[\left(\mu_g + \frac{\mu_{tur}}{\sigma_k}\right)\frac{\partial k}{\partial x_z}\right] + Y_k + Y_b - \rho_g\epsilon - Y_c + S_k \quad (20)$$

$$\frac{\partial}{\partial t}\left(\rho_g \epsilon\right) + \frac{\partial}{\partial x_r}\left(\rho_g \epsilon U_r\right) = \frac{\partial}{\partial x_z}\left[\left(\mu_g + \frac{\mu_{tur}}{\sigma_\epsilon}\right)\frac{\partial \epsilon}{\partial x_z}\right] + C_{1\epsilon}\frac{\epsilon}{k}(Y_k + C_{3\epsilon}Y_b) - C_{2\epsilon}\rho_g\frac{\epsilon^2}{k} + S_\epsilon \quad (21)$$

where r and z represent the directions, μ_{tur} represents the turbulent viscosity, k represents the turbulence kinetic energy, ϵ represents the dissipation rate of turbulence kinetic energy, U_r represents the component of U_g in the direction of r, Y_k represents the turbulence kinetic generation due to mean velocity gradients, Y_b represents the buoyancy turbulence kinetic energy generation, Y_c

represents the compressible turbulence by fluctuating dilation, S_k and S_ϵ are the user-defined source terms (if any), and C_μ, σ_k, σ_ϵ, $C_{1\epsilon}$, $C_{2\epsilon}$, and $C_{3\epsilon}$ are the model equation constants.

$$Y_k = \mu_{tur}\bar{S}^2 \tag{22}$$

$$\bar{S} = \sqrt{2\bar{S}_{ij}\bar{S}_{ij}} \tag{23}$$

$$Y_b = \beta g_r \frac{\mu_{tur}}{\rho_g Pr_{tur}} \frac{\partial T}{\partial x_r} \tag{24}$$

$$\beta = -\frac{1}{\rho_g}\left(\frac{\partial \rho_g}{\partial T}\right)_P \tag{25}$$

$$Y_c = 2\rho_g \epsilon M_{tur}^2 \tag{26}$$

$$M_{tur} = \sqrt{\frac{k}{ZRT}} \tag{27}$$

In calculation of the aforementioned quantities, $\bar{S}$ represents the modulus of mean rate of strain tensor, β represents the coefficient of thermal expansion, g_r represents the component of gravity in the direction of r, Pr_{tur} represents the turbulent Prandtl number given as 0.85, M_{tur} represents the turbulent Mach number, and Z represents the compressibility of the fluid gas.

The values of the constants are as follows: $C_\mu = 0.0845$; $C_{1\epsilon} = 1.44$; $C_{2\epsilon} = 1.92$; $\sigma_k = 1.0$; and $\sigma_\epsilon = 1.3$.

2.3.4 Kinetic energy equations

KTGF is used for kinetic based modeling of the fluidized bed system and is the extended version of the kinetic theory of gases. The model assumes unequal granular temperature for different phases and uses collisions as a potential source of energy transfer and a variable affecting the granular temperature. The model equation for granular temperature of a solid phase is as follows:

$$\frac{3}{2}\left[\frac{\partial}{\partial t}\left(\varepsilon_{si}\rho_{si}\Theta_{si}\right) + \nabla\cdot\left(\varepsilon_{si}\rho_{si}\Theta_{si}U_{si}\right)\right] = \left(\Pi_s\colon \nabla\cdot U_{si}\right) + \nabla\cdot q_{si} - \gamma_{si} - 3\phi_{g,si}\Theta_{si} \tag{28}$$

where q_{si} represents the collisional heat flux for solid phase s_i and γ_{si} represents the dissipation of the turbulent kinetic energy due to particle collisions.

The collisional heat flux is given by:

$$q_{si} = \sum_{j=1}^{2} P_{si(col)}\left(1+e_{si}\right)\left\{\frac{9m_{sj}}{5m_s}\left(U_{sj}-U_{si}\right) + d_{si,sj}\left[\left(\frac{2m_{sj}^2\Theta_{sj}}{\pi\left(m_{si}^2\Theta_{si}+m_{sj}^2\Theta_{sj}\right)}\right)^{\frac{1}{2}\star}\left(\nabla ln\left(\frac{\varepsilon_{si}}{\varepsilon_{sj}}\right) + 3\nabla\left(\frac{ln\left(m_{sj}\Theta_{sj}\right)}{ln\left(m_{si}\Theta_{si}\right)}\right)\right) + 3\left(\frac{2m_{si}^3m_{sj}^3\Theta_{si}\Theta_{sj}}{\pi\left(m_{si}^2\Theta_{si}+m_{sj}^2\Theta_{sj}\right)}\right)^{\frac{1}{2}}\left(\frac{m_{sj}\Theta_{si}\Theta_{sj}}{\Theta_{si}+\Theta_{sj}}\right)^{\star}\left(\frac{\nabla\Theta_{si}}{\Theta_{si}^2}-\frac{\nabla\Theta_{sj}}{\Theta_{sj}^2}\right) + 6m_{sj}\left(\frac{2m_{si}^3m_{sj}^3\Theta_{si}\Theta_{sj}}{m_{si}^2\Theta_{sj}+m_{sj}^2\Theta_{sj}}\right)^{\frac{3}{2}\star}\left(\frac{\nabla\Theta_{si}}{m_{si}\Theta_{si}^2}-\frac{\nabla\Theta_{sj}}{m_{sj}\Theta_{sj}^2}\right)\right]\right\} \tag{29}$$

where $P_{si(col)}$ represents the collisional pressure generated by particle collisions, m_s represents the combined mass of the solid phases s_i and s_j, and $d_{si,sj}$ represents the average particle size of the solid phases s_i and s_j.

The collisional pressure given by Gidaspow and Huilin (1996) is:

$$P_{si(col)} = \frac{\pi\left(1+e_{si}\right)d_{si,sj}^3G_{si}n_{si}n_{sj}m_{si}m_{sj}m_s\Theta_{si}\Theta_{sj}}{3\left(m_{si}^2\Theta_{si}+m_{sj}^2\Theta_{sj}\right)}\star \left[\frac{m_s^2\Theta_{si}\Theta_{sj}}{\left(m_{si}^2\Theta_{si}+m_{sj}^2\Theta_{sj}\right)\left(\Theta_{si}+\Theta_{sj}\right)}\right]^{\frac{3}{2}}\star \left(1-3\Delta+6\Delta^2-10\Delta^3\ldots\right) \tag{30}$$

where Δ is an equation constant, n_{si} and n_{sj} represent the total number of particles of the solid phases s_i and s_j, respectively, and m_{si} and m_{sj} represent the single particle masses of the solid phases s_i and s_j, respectively.

The equation constant Δ is given as:

$$\Delta = \frac{m_{si}\Theta_{si}-m_{sj}\Theta_{sj}}{\left[\left(m_{si}^2\Theta_{si}^2+m_{sj}^2\Theta_{sj}^2\right)+\Theta_{si}\Theta_{sj}\left(m_{si}^2+m_{sj}^2\right)\right]} \tag{31}$$

The average particle size of two solid phases is given by:

$$d_{si,sj} = \frac{d_{si}+d_{sj}}{2} \tag{32}$$

where d_{si} represents the particle size of the solid phase s_i and d_{sj} represents the particle size of the solid phase s_j.

The combined mass for two solid phases is defined as:

$$m_s = \left(m_{si}+m_{sj}\right) \tag{33}$$

The single particle mass is calculated as:

$$m_{si} = \frac{\pi}{6}d_{si}^3\rho_{si} \tag{34}$$

The total number of particles is defined as:

$$n_{si} = \frac{6\varepsilon_{si}}{\pi d_{si}^3} \tag{35}$$

The turbulent kinetic energy dissipation by particle collisions is given by the Gidaspow and Huilin model (Gidaspow and Huilin, 1996) as:

$$\gamma_{si} = \sum_{j=1}^{2}\left\{\frac{3}{d_{si,sj}}\left(\frac{2m_s^2\Theta_{si}\Theta_{sj}}{\pi\left(m_{si}^2\Theta_{si}+m_{sj}^2\Theta_{sj}\right)}\right)^{\frac{1}{2}} - \frac{3m_s\left(m_{si}\Theta_{si}+m_{sj}\Theta_{sj}\right)}{4\left(m_{si}^2\Theta_{si}+m_{sj}^2\Theta_{sj}\right)}\nabla\cdot U_{si}\right\} \left(1-e_{si}\right)P_{si(col)} \tag{36}$$

2.3.5 Drag equations

The Syamlal–O'Brien model (Syamlal and O'Brien, 1987) was used for the drag modeling of the fluidized bed system. The model equation for the gas-solid particle drag interaction is as follows:

$$\phi_{g.si} = \frac{\frac{3}{4}\varepsilon_{si}\varepsilon_g\rho_g}{\vartheta_r^2 d_{p,si}}C_{dr}\left(U_g-U_{si}\right) \tag{37}$$

where C_{dr} represents the drag coefficient of the gas–solid system represented by Eq. 38, ϑ_r is the equation constant, and

$$C_{dr} = \left(0.63+\frac{4.8}{\sqrt{\frac{Re_{si}}{\vartheta_r}}}\right)^2 \tag{38}$$

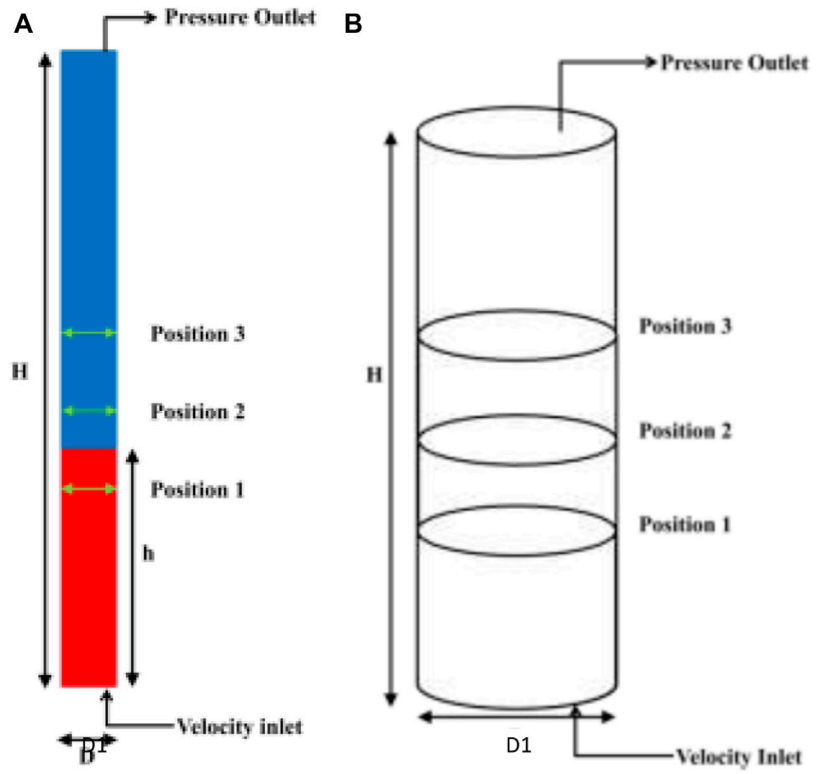

FIGURE 1
Schematic representation of fluidized bed. **(A)** Schematic of 2D plane (from Ansys Fluent 18.1) showing bed height and axial positions. **(B)** 3D Schematic with representation (current schematic assumes 0.335 m initial bed height).

where Re_{si} is the Reynolds number of the solid phase s_i.

The Reynolds number for the solid phase is given as:

$$Re_{si} = \frac{\varepsilon_g \rho_g \left(U_g - U_{si}\right) d_{p,si}}{\mu_g} \tag{39}$$

The equation constant ϑ_r is represented by the following equation:

$$\vartheta_r = 0.5\left(A - 0.06Re_{si} + \sqrt{(0.06Re_{si})^2 + 0.12Re_{si}(2B - A) + A^2}\right) \tag{40}$$

where A and B are given as:

$$A = \varepsilon_g^{4.14} \tag{41}$$

$$B = \begin{cases} 0.8\varepsilon_g^{1.28} & (\varepsilon_g \le 0.85), \\ \varepsilon_g^{2.65} & (\varepsilon_g > 0.85). \end{cases} \tag{42}$$

The particle–particle drag interaction coefficient is governed by the Syamlal and O'Brien model (Syamlal and O'Brien, 1987) as:

$$\phi_{si,sj} = \frac{3\left(1 + e_{si,sj}\right)\left(\frac{\pi}{2} + \frac{\pi^2 f}{8}\right)\varepsilon_{si}\varepsilon_{sj}\rho_{si}\rho_{sj}\left(d_{si} + d_{sj}\right)^2 G_{si,sj}\left(U_{si} - U_{sj}\right)}{2\pi\left(\rho_{si}d_{si}^3 + \rho_{sj}d_{sj}^3\right)} \tag{43}$$

where f represents the coefficient of friction from interaction between the solid phases s_i and s_j.

2.3.6 Frictional equations

The frictional pressure is derived from KTGF and is given by Syamlal et al. (1993) as:

$$P_{fr} = \rho_{si}\varepsilon_{si}\Theta_{si}[1 + 2(1 + e_{si})G_{si}\varepsilon_{si}] \tag{44}$$

The frictional viscosity given by Schaffer is as follows:

$$\mu_{fr} = \frac{P_{fr}\sin\alpha}{2\sqrt{II_{si(2D)}}} \tag{45}$$

where P_{fr} represents the frictional pressure, α is the angle of internal friction taken as 30°, and $\Pi_{si(2D)}$ represents the second invariant of the deviatoric stress tensor.

2.4 Geometry and mesh details

A 3D cylindrical geometry of radius 0.036 m with a height of 1.4 m was created in Ansys Workbench 18.1. The bottom was designated as the air inlet, while the upper circular geometry was used as the outlet. Figure 1A shows the 2D plane from 3D geometry with bed height and axial positions at t = 0 s, and Figure 1B shows the 3D geometry representation at t = 0s. The diameter of the cylinder is given by D_1, and H represents the total height of the cylinder. At t = 0 s, h represents the initial bed height of the glass particles. Figure 2 shows different views of the mesh used for simulations, including the axial and radial zoomed views of the 3D geometry.

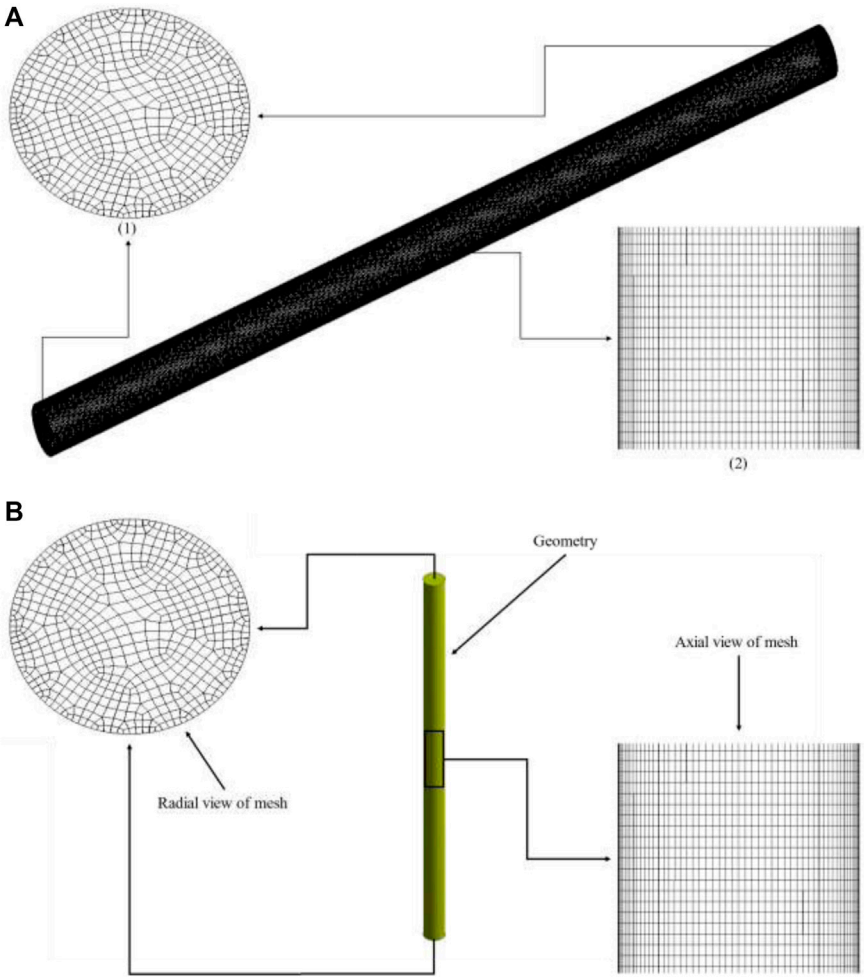

FIGURE 2
Mesh details used for simulations. **(A)** 3D mesh slanting direction: (1) axial view and (2) radial view. **(B)** 3D mesh vertical direction showing axial and radial views.

2.5 Boundary conditions

"Velocity-inlet" is used as a boundary for the gas inlet condition. "Pressure-outlet" is used as a boundary condition for outlet. The packing limit for glass particles was taken as 0.63. No-slip condition was applied on the walls. The time-step used in simulation was 0.001 s. The total simulation was run for 7 s.

2.6 Material properties

Glass particles were used as the solid phase and air was used as the fluid phase. Glass particles of two different sizes, 154 μm and 488 μm, were used, and average particle sizes varied between groups. The densities that were used are as follows: 2485 kgm^{-3} for glass and 1.22 kgm^{-3} for air. The viscosities used were 0.00082 $kgm^{-1}s^{-1}$ for glass and 0.000017 $kgm^{-1}s^{-1}$ for air. The material properties used for simulations were as indicated by Jayarathna and Halvorsen (2011).

2.7 Grid sensitivity

Three different meshes were used for simulations: Mesh 1 with 173,040 elements, Mesh 2 with 267,786 elements, and Mesh 3 with 497,568 elements. The mesh elements are hexahedral and more refined near the wall, with a near-wall yplus of around 30. The initial volume fractions in the 2D plane are shown for both bed heights (h_{s1} = 0.335 m and h_{s1} = 0.635 m) in Figure 3. The axial velocity magnitudes in the radial direction for a bed height of 0.335 m were plotted. Figure 4 shows the radial velocity profile at Position 2 of Figure 1 for different meshes. The deviation between Mesh 2 and Mesh 3 was 2%, while maximum deviation for Mesh 1 and Mesh 2 was 10%. Hence, Mesh 2 was used. Figure 4 shows axial and radial views of Mesh 2.

2.8 Method of solution

The simulations were carried out using commercial fluid software Ansys Fluent 18.1. A first order upwind scheme was

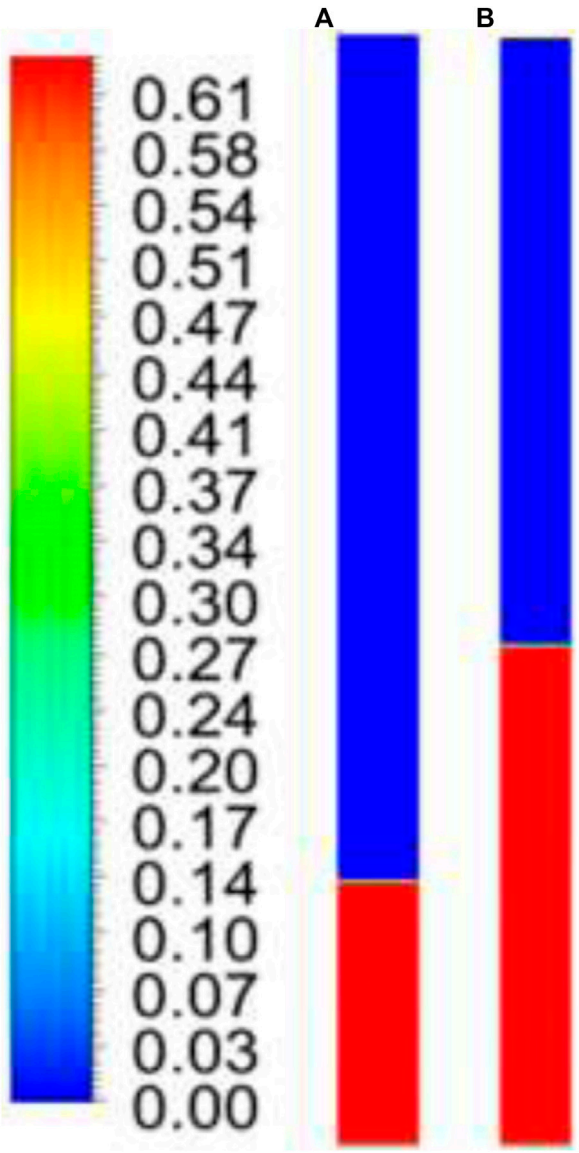

FIGURE 3
Initial volume fraction contours at t = 0 s for **(A)** 0.335 m initial bed height and **(B)** 0.635 m initial bed height.

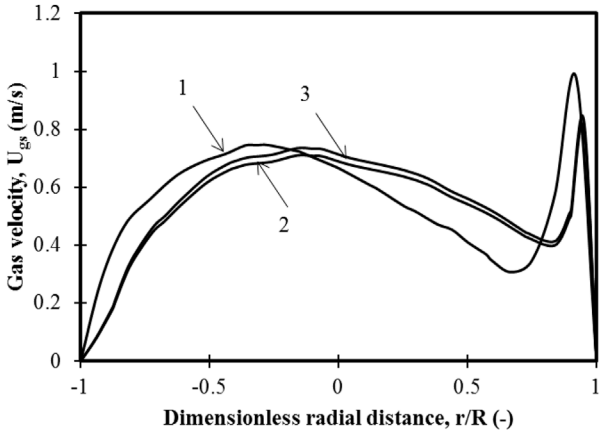

FIGURE 4
Variation of gas velocity for three different grids for position 2 of Figure 1 at steady state for superficial velocity of 0.3 m/s and 100% small particles of the binary mixture: 1.173040 mesh elements; 2.267786 mesh elements; 3.497568 mesh elements.

used to solve momentum, volume fraction, turbulent kinetic energy, and turbulent dissipation rate equations. A phase-coupled SIMPLE scheme was used to solve pressure–velocity coupling. For transient formulation, a first order implicit scheme was used. Convergence criterion for continuity was 0.001; it was 10^{-4} for other equations. The parametric data (for initial bed heights, as shown in Figure 3, including superficial velocity, binary mixtures, and both individual and average particle sizes) used for the simulations are shown in Table 3.

3 Results and discussion

First, the standard values and models for the parameters, as discussed in Section 1.2, were chosen from those available in the literature. Similarly, the drag and turbulence model was chosen per the literature. The model was validated with experimental data available from published studies that used these standard settings. The transient solid particle dynamics in the bed was then presented in the form of qualitative solid volume fraction contours to understand the segregation and mixing characteristics for different particle size mixtures considered in the study. In this section, $100 \times x$% mixture represents the percentage of large particles and $100 \times (1 - x)$% represents the percentage of the small particles. All the contours presented in the figures are steady-state time-averaged volume fraction contours of particles. Herein, x represents the weight fraction of large particles.

3.1 Regime analysis

Lim et al. (1995) have emphasized the importance of particle size, particle composition, and baffles, which lead to transition from bubbling or slugging regime to turbulent regime. The criteria for the dimensionless velocity that characterizes the regimes are given by Eq. 3. An effort has been made to identify the regime in which the present work was carried out, per analysis demonstrated by Lim et al. (1995). Eqs 46–49 represent the dimensionless numbers and velocities, as well as the average particle diameter for a binary mixture.

Figure 5 shows the plot of the regime analysis (Lim et al., 1995) for the superficial velocities considered in the present work. The analysis shows that the entire zone is in bubbling regime. However, it must be noted that the analysis derived by Lim et al. (1995) was based on experimental data from unary beds.

$$Re_g = \frac{\rho_g U_g d_{p(si,sj)}}{\mu_g} \tag{46}$$

TABLE 3 Parametric data used for simulations.

Mixture (%)	Particle size (m)	Initial bed height (m)	Superficial gas velocity (m/s)
0	0.000154, 0	0.335, 0.635	0.3, 0.45, 0.6
20	0.000154, 0.0000976	0.335, 0.635	0.3, 0.45, 0.6
25	0.000154, 0.000122	0.48	0.15, 0.3, 0.45, 0.6, 0.75, 0.9
40	0.000154, 0.0001952	0.335, 0.635	0.3, 0.45, 0.6
60	0.000154, 0.0002928	0.335, 0.635	0.3, 0.45, 0.6
80	0.000154, 0.0003904	0.335, 0.635	0.3, 0.45, 0.6
100	0, 0.000488	0.335, 0.635	0.3, 0.45, 0.6

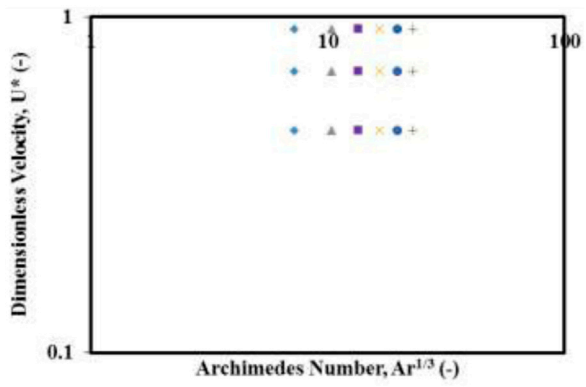

FIGURE 5
Regime analysis, based on the criteria of Bi and Grace (1995), showing the scope of the present analysis of bubbling and slugging regimes. Large particle percentages and corresponding notations: ◆—0% large particles; ▲—20% large particles; ■—40% large particles; ×—60% large particles; ●—80% large particles; and +—100% large particles.

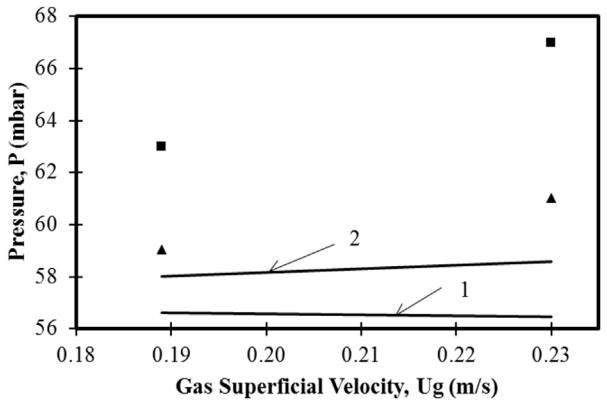

FIGURE 6
Variation of pressure drop as function of gas superficial velocity (U_{gs}) for bed height = 0.235 m. Numbers 1 and 2 denote CFD simulations for increasing order of particle sizes, respectively, while symbols denote experimental measurements. ■—0% large particles; ▲—40% large particles.

$$Ar_g = \frac{\rho_g\left(\rho_{si} - \rho_g\right)d^3_{p\,(si,sj)}}{\mu_g} \tag{47}$$

$$U^* = \frac{Re_g}{Ar_g^{\left(\frac{1}{3}\right)}} \tag{48}$$

$$d_{p\,(si,sj)} = \sum_{i=1}^{2} x_{si} d_{p,si} \tag{49}$$

where x_{si} is the initial weight fraction of the solid phase s_i.

3.2 Model validation

For model validation, two mixtures of 0% and 40% were simulated at 0.235 m of initial bed height and superficial gas velocities varying from U_{gs} = 0.184 m/s to 0.225 m/s each. Figure 6 shows a deviation of around 5%–7% between experimental data and numerical predictions for a binary mixture with 0% large sized particles (or 100% small particles), whereas there was less than 3% deviation for a binary mixture with 40% large particles. The deviation is attributed to the absence of distributor details from the published literature.

3.3 Flow patterns

Figure 7i shows the steady-state time-averaged solid volume fraction contours for different superficial gas velocities and 0% mixture (100% fine particles) for a bed height of 0.635 m. For superficial gas velocity of U_{gs} = 0.3 m/s, a well-mixed pattern can be observed. However, slugs of particles seemed to deposit at different axial locations at the walls. A large bubble with solid particles was observed at an axial location of z/H = 0.5 when the maximum height of fluidization was 1.25 m at steady state. A similar flow pattern was observed for a higher superficial gas velocity of U_{gs} = 0.45 m/s. However, the solids were deposited on the right-hand wall of the bed between the dimensionless heights of z/H = 0.35 and z/H = 0.8. A bubble formed on the left-hand wall with particles moving in the space between the bubble and wall. For a superficial gas velocity of U_{gs} = 0.6 m/s, a large bubble was seen at the outlet with a wake below and followed by another bubble. A prominent zigzag pattern was observed from bottom to top, with slugs of solid particles alternating on the right and left wall. These results confirm the bubble wake and bubble formation, as has been reported in published literature (Cooper and Coronella, 2005).

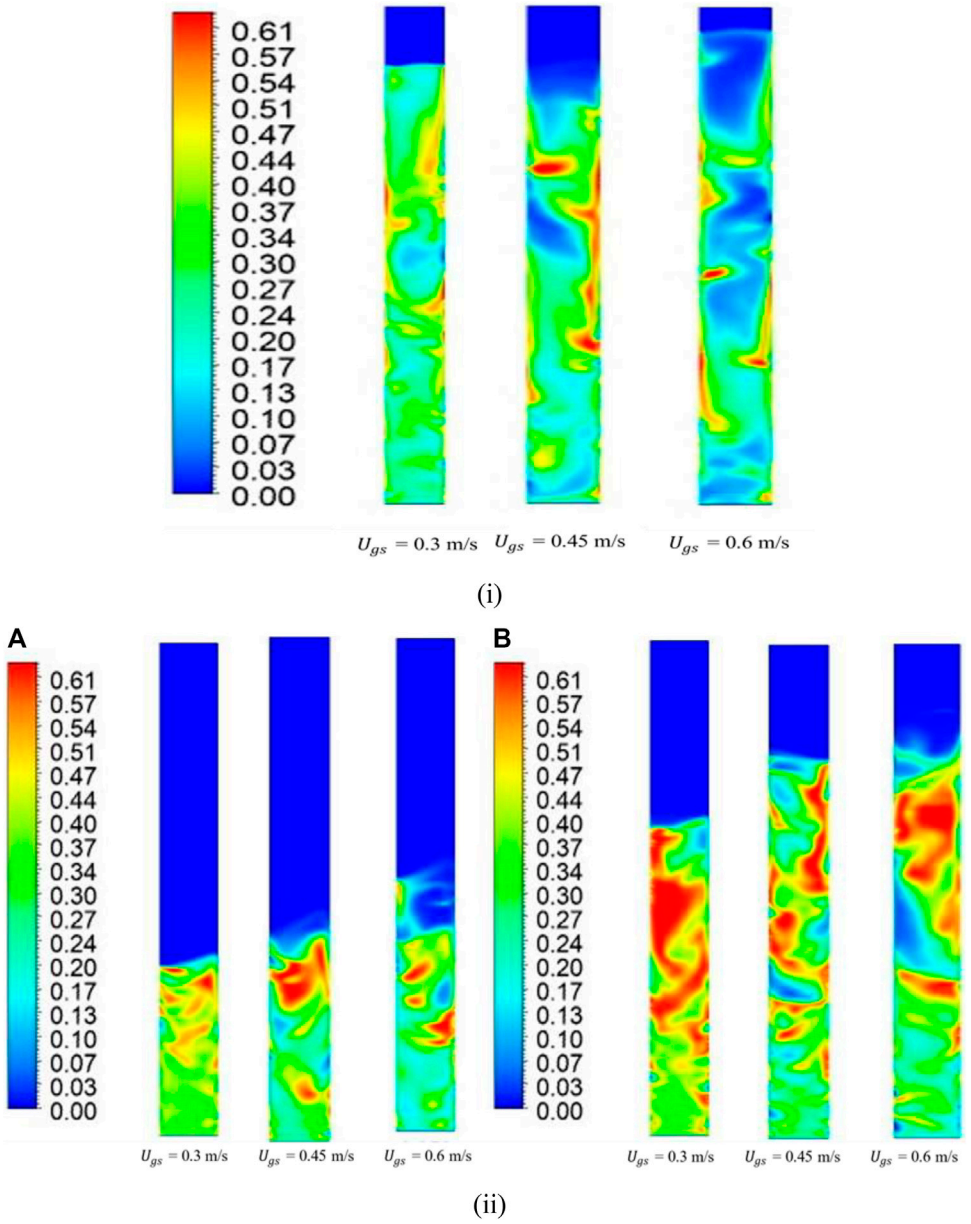

FIGURE 7
Time-averaged steady-state solid-phase volume fraction contours for **(i)** 0% mixture at 0.635 m bed height and **(ii)** 20% mixture at **(A)** 0.335 m bed height and **(B)** 0.635 m bed height.

Furthermore, bubble formation and dynamics were also captured by the model.

Figure 7ii shows steady-state, time-averaged volume fraction contours for two different bed heights of 0.335 m and 0.635 m for the three superficial gas velocities. The binary mixture contained 20% large particles and 80% small particles. Figure 7iiA shows that, for initial bed height of 0.335 m, the fluidized bed steady-state heights were 0.45 m, 0.5 m, and 0.65 m for superficial gas velocities of U_{gs} = 0.3 m/s, U_{gs} = 0.45 m/s, and U_{gs} = 0.6 m/s, respectively. A well-mixed pattern was observed for the three superficial gas velocities considered at this initial bed height. With a superficial gas velocity of U_{gs} = 0.45 m/s, a small layer of dense solid particles accumulated at the top, indicating that most of the finer particles go to the top, resulting in segregation. On the other hand, at a superficial gas velocity of U_{gs} = 0.6 m/s, slugs of particles were formed, as in the previous case shown in Figure 7i. Furthermore, a large bubble was formed at the top of the fluidized bed at this superficial gas velocity. These patterns are similar to those observed by Lan et al. (2014), where partial segregation was predicted.

Figure 7iiB shows the solid phase volume fractions for a higher initial bed height (z = 0.635 m) for the same set of conditions as in Figure 7iiA. When the superficial gas velocity was lower (U_{gs} = 0.3 m/s), the finer particles formed larger slugs in the upper half of the bed, while the lower half had mostly coarser particles. The fluidized bed height was approximately 0.85 m. As the superficial

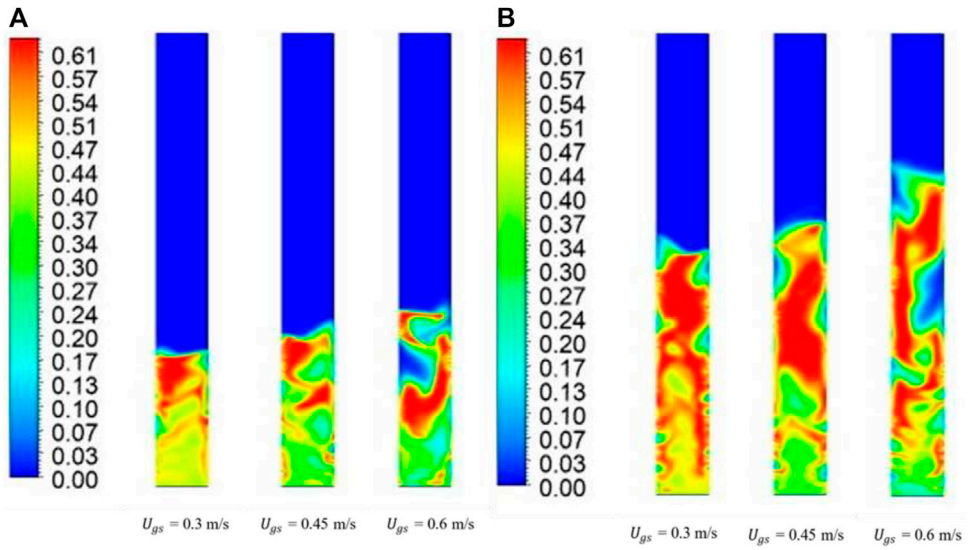

FIGURE 8
Time-averaged steady-state solid-phase volume fraction contours for 40% mixture at **(A)** 0.335 m bed height and **(B)** 0.635 m bed height.

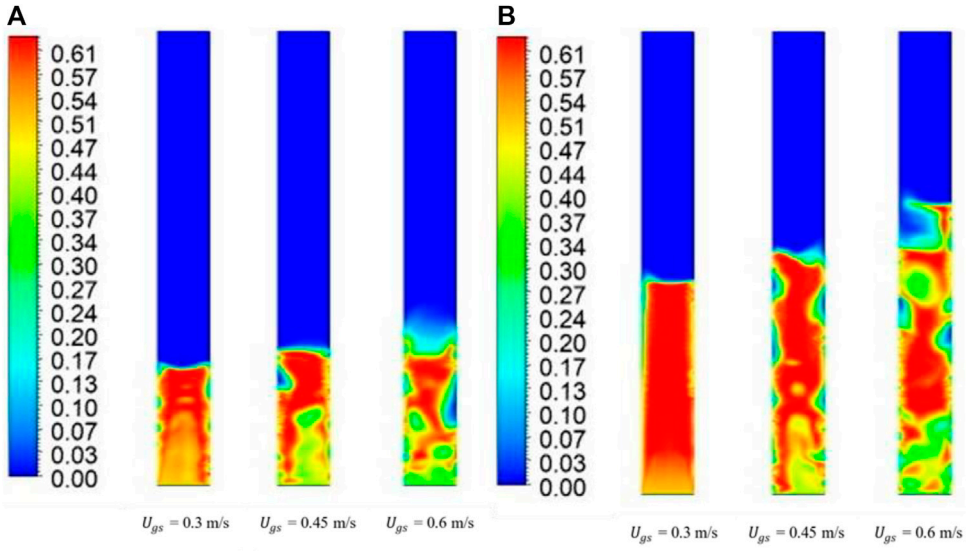

FIGURE 9
Time-averaged steady-state solid-phase volume fraction contours for 60% mixture at **(A)** 0.335 m bed height and **(B)** 0.635 m bed height.

gas velocity increased (U_{gs} = 0.45 m/s), bubbles formed in the bed, while the slug sizes of finer particles decreased and became thinner and covered greater length at the top of the bed. A bubble formed at the midpoint of the bed (z = 0.55 m). A further increase in superficial gas velocity caused the top portion to be occupied by finer particles and the bottom portion to consist of coarser particles, with some area in the middle covered by a large bubble. Thus, complete segregation was observed at the highest velocity. This also corresponded with results reported by Lan et al. (2014), who found similar patterns where the top bed was well-mixed, while the bottom part was stagnant with coarser particles.

Figure 8 shows the time-averaged steady state solid phase volume fraction contours for a binary mixture of 40% large particles and 60% small particles. Figure 8A shows that, for a lower bed height, there was complete segregation of flotsam and jetsam. However, mixing was observed when the superficial gas velocity was increased (U_{gs} = 0.45 m/s), and complete segregation did not take place. With further increase in superficial gas velocity (U_{gs} = 0.6 m/s), the following characteristics were observed: bubbles occupied the top area, while finer particles were restrained to the middle of the bed, and the top of the bed consisted of mixed particle sizes. The bottom of the bed consisted mostly of jetsam, which denotes intermediate

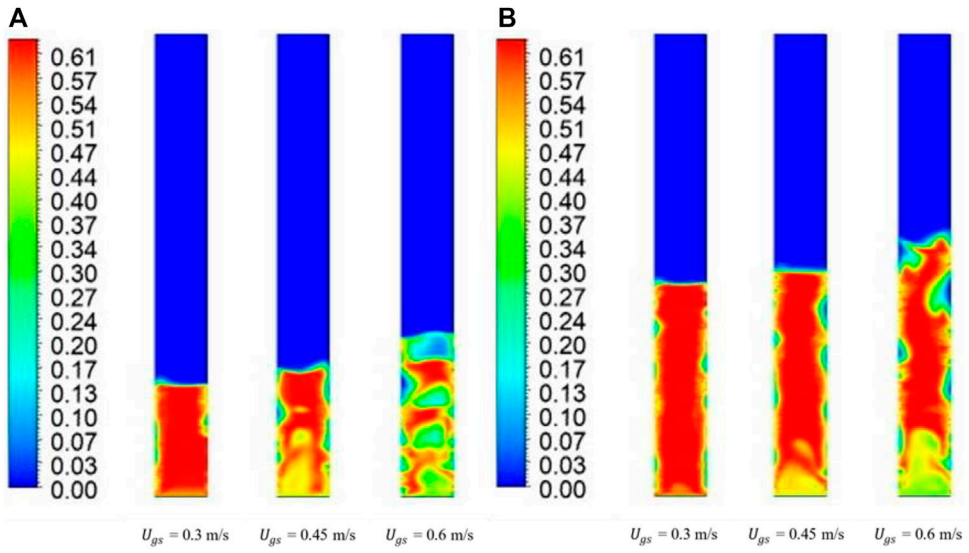

FIGURE 10
Time-averaged steady-state solid-phase volume fraction contours for 80% mixture at **(A)** 0.335 m bed height and **(B)** 0.635 m bed height.

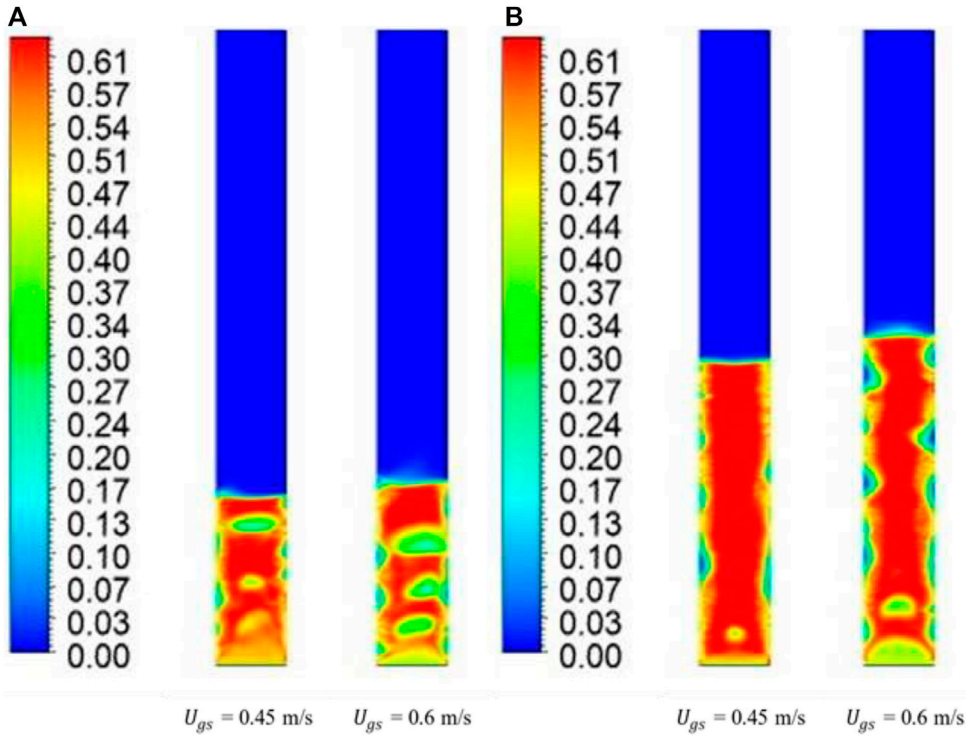

FIGURE 11
Time-averaged steady-state solid-phase volume fraction contours for 100% mixture at **(A)** 0.335 m bed height and **(B)** 0.635 m bed height.

mixing. Figure 8B shows that, for a bed with an initial height of 0.635 m, volume fractions in jetsam were higher for lower superficial gas velocities (U_{gs} = 0.3 m/s), and the fluidized bed height was 0.75 m, indicating that, due to the presence of large particles, there was less mixing and greater segregation. The scenario changed with an increase in superficial gas velocity. For U_{gs} = 0.45 m/s, the bed was still segregated, but some mixing occurred. For 0.6 m/s, the bed was well mixed.

Figure 9 shows the time-averaged steady-state solid-phase volume fraction for a binary mixture of 60% large particles and 40% small particles. An interesting observation can be made from Figure 9A for a superficial gas velocity of U_{gs} = 0.3 m/s, where a jet of fluid rose and

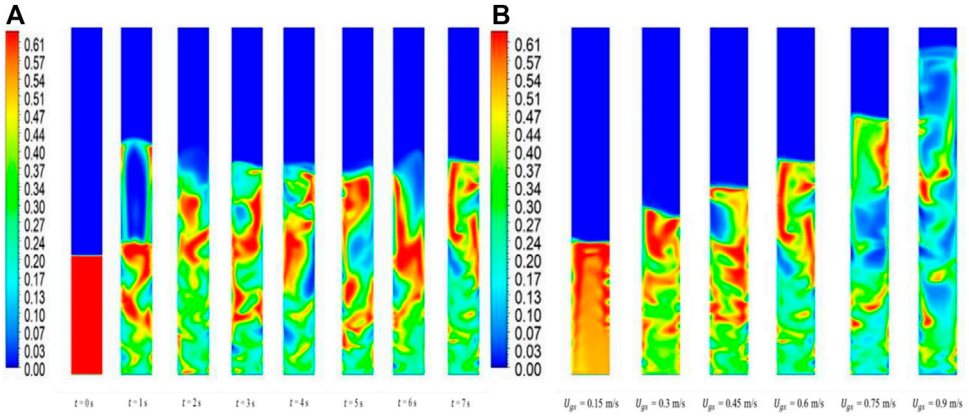

FIGURE 12
Time-averaged solid-phase volume fraction contour for 25% mixture and 0.48 m. **(A)** Transient flow patterns and **(B)** steady state flow patterns at different superficial gas velocities.

caused smaller bubbles to rise at the bed surface. With increased superficial gas velocity (U_{gs} = 0.45 m/s), however, the bed tended to be segregated, while with further increased superficial gas velocity (U_{gs} = 0.6 m/s), bubbles and slugs of solids started forming, indicating transition to a turbulent regime. Figure 9B shows a similar analysis for a higher bed height. Here, for a lower superficial gas velocity, the bed remained stagnant, while with increased superficial gas velocity there was transition from bubbling (U_{gs} = 0.45 m/s) to a turbulent regime (U_{gs} = 0.6 m/s).

Figure 10 shows interesting results for a binary mixture with 80% large solids and 20% fine solids. Figure 10A shows that, for U_{gs} = 0.3 m/s, the bed reached minimum fluidization, while for U_{gs} = 0.45 m/s it had a fluid jet that entered the bed and a bubble that adhered to the wall. An extremely interesting flow pattern was observed for a velocity of a superficial gas velocity of U_{gs} = 0.6 m/s. Alternate slugs of fine and dense mixtures were observed rising up the bed. Figure 10B shows similar patterns for a case of higher initial bed height. An interesting pattern was observed at a superficial gas velocity of U_{gs} = 0.6 m/s, which showed bubble formation and its rise at the bottom of the bed similar to the one observed, both experimentally and numerically, by Cooper and Coronella (2005).

Figure 11 shows time-averaged steady-state flow patterns for a binary mixture with 100% large solids and 0% fine solids. It was observed that for both bed heights of 0.335 m and 0.635 m and a low superficial gas velocity of U_{gs} = 0.3 m/s, the bed remained as a fixed bed and no fluidization was possible, as shown in Figure 11A. For higher superficial gas velocities of U_{gs} = 0.45 m/s and U_{gs} = 0.6 m/s, a bubbling fluidized regime was observed. For a higher initial bed height of 0.635 m (Figure 11B), bubbles formed at the bottom and adhered near the wall. No mixing was observed for the superficial gas velocities, but slug formation was observed for U_{gs} = 0.6 m/s.

Interestingly, until 40% large particle diameter, for most of the superficial gas velocities and bed heights, we observed small structures of bubbles and solid slugs which were representative of the slugging/turbulent regime. However, the flow patterns of a binary mixture with 20%–80% large particles showed more mixing than the cases with 40% and 60% large particles.

Although both cases seemed to represent a turbulent fluidization regime, two distinct questions were posed: 1) Would mixtures of between 20% and 40% large particles be in turbulent range or transition range? and 2) what are the transient dynamics of this process?

Since all the cases from Figures 7–11 were steady-state time-averaged, it was worth observing the transient flow patterns for an intermediate mixture composition and high superficial gas velocity for a different bed height (in between the bed heights already considered). A binary mixture of 25% small particles and 75% large particles was considered for analysis with an initial bed height of 0.48 m. Figure 12 shows the volume fraction contours for the same. Transient volume fraction contours show that, at the end of one second, a large bubble is formed at the top. After each subsequent second, the intermixing throughout the column was evident as turbulent fluidization (although the criterion for fluidization requires confirmation). A similar exercise with increasing superficial gas velocity showed that height of the bed increased as the superficial gas velocity increased, with bubbles forming at U_{gs} = 0.3 m/s and U_{gs} = 0.75 m/s. A detailed study on this can be carried out to determine whether the bed undergoes turbulent fluidization that indicates a turbulent regime, in contradiction to the bubbling regime predicted in Figure 5. This is, however, outside the scope of the present work.

4 Conclusion

The conclusions drawn from this study are:

1. Qualitative flow patterns and quantitative gas and particle velocity profiles indicate transition from bubbling and slugging regime to turbulent regime for some of the binary mixtures considered. These observations at dimensionless velocity, per the criteria of Lim et al. (1995), are different and may be attributed to the presence of particle size distribution, resulting in breakage of bubbles/slugs during bed expansion.

2. Low volume fractions of 0%–20% of large particles and low superficial gas velocity of U_{gs} = 0.3 m/s with no large particles result in homogeneous regimes for both bed heights, while higher superficial gas velocities of U_{gs} = 0.45 m/s and U_{gs} = 0.6 m/s show intermixing at higher axial locations of the bed, and completely mixed steady-state profiles are observed. For mixtures with 20%–40% volume fraction range of large particles for both bed heights, gas bubbles were seen on the near-wall zone, and about 30% of the bed remained segregated at superficial velocities of 0.3 m/s and 0.45 m/s, with mixing restricted to the top part of the bed; the bed was well mixed under the 0.6 m/s condition.
3. For a 40% volume fraction of large particles, the bed remained 70% segregated at both bed heights and superficial velocity of 0.3 m/s. For a higher superficial velocity, the bed was well mixed.
4. For a 60% volume fraction of large particles, the bed was largely segregated for both bed heights and at lower superficial velocity of 0.3 m/s, while for a higher superficial velocity (0.45 m/s), the bed at lower height was well mixed. At the higher bed height, 80% of the bed was well mixed. Furthermore, for a higher superficial velocity of 0.6 m/s, the bed was well mixed at both bed heights.
5. For mixtures with 80% and 100% large particles at lower superficial velocity of 0.3 m/s, the bed did not fluidize, while fluidization of approximately 30%–35% was observed for a superficial velocity of 0.45 m/s at a bed height of 0.635 m. For a lower bed height, the amount of fluidization was around 65%. For the highest velocity considered, the bed was well mixed for lower bed height (0.335 m) and 70% mixed for a higher bed height (0.635 m).

5 Future work

1. In Part II of this two-part series, the present conclusions will be substantiated with comprehensive study of the gas and particle velocity profiles, as well as particle volume fraction profiles, for all the particle mixtures, bed heights, and superficial velocities considered in the present study.
2. Furthermore, the generated data will be used to develop correlations for minimum fluidization velocity and pressure drop for binary mixtures in Part II of the study.
3. Similar comprehensive studies will be taken up, focusing on simulations using the discrete element method (DEM) for lab-scale fluidized beds of Geldart-B and other Geldart group particles, which have practical applications depending on experimental data.
4. Simulation studies focusing on particles larger than 1 mm should be conducted, as has been reported in the experimental literature.

Data availability statement

The simulation data supporting the conclusion of this article will be made available by the authors, without undue reservation.

Author contributions

Conceptualization, AG and VB; methodology, AG; software, AG; validation, VB; formal analysis, VB; investigation, AG and VB; resources, AG; data curation, VB; writing—original draft preparation, AG and VB; writing—review and editing, AG; visualization, AG; supervision, AG; project administration, AG; funding acquisition, AG.

Acknowledgments

The authors thank the School of Engineering and Applied Sciences, Ahmedabad University, for the resources and their continuous support during the project.

Conflict of interest

The authors declare that the research was conducted in the absence of any commercial or financial relationships that could be construed as a potential conflict of interest.

Publisher's note

References

Agrawal, V., Shinde, Y., Shah, M. T., Utikar, R. P., Pareek, V. K., and Joshi, J. B. (2018). Effect of drag models on CFD–DEM predictions of bubbling fluidized beds with Geldart D particles. *Adv. Powder Technol.* 29, 2658–2669. doi:10.1016/j.apt.2018.07.014

Ahmadi, G., and Ma, D. (1990). A thermodynamical formulation for dispersed multiphase turbulent flows—1: Basic theory. *Int. J. Multiph. Flow* 16, 323–340. doi:10.1016/0301-9322(90)90062-n

Bakshi, A., Ghoniem, A., and Altantzis, C. (2017). Mixing dynamics in bubbling fluidized beds. *AIChE J.* 63, 4316–4328. doi:10.1002/aic.15801

Behzadi, S. S., Prakasvudhisarn, C., Klocker, J., Wolschann, P., and Viernstein, H. (2009). Comparison between two types of artificial neural networks used for validation of pharmaceutical processes. *Powder Technol.* 195, 150–157. doi:10.1016/j.powtec.2009.05.025

Benzarti, S., Mhiri, H., Bournot, H., and Occelli, R. (2014). Numerical simulation of turbulent fluidized bed with Geldart B particles. *Adv. Powder Technol.* 25, 1737–1747. doi:10.1016/j.apt.2014.06.024

Bi, H., and Grace, J. (1995). Flow regime diagrams for gas-solid fluidization and upward transport. *Int. J. Multiph. Flow* 21, 1229–1236. doi:10.1016/0301-9322(95)00037-x

Bi, X. T. (2011). *A generalized flow regime diagram for fluid-solid vertical transport.*

Čársky, M., Pata, J., Veselý, V., and Hartman, M. (1987). Binary system fluidized bed equilibrium. *Powder Technol.* 51, 237–242. doi:10.1016/0032-5910(87)80024-4

Chang, J., Wang, G., Gao, J., Zhang, K., Chen, H., and Yang, Y. (2012). CFD modeling of particle–particle heat transfer in dense gas-solid fluidized beds of binary mixture. *Powder Technol.* 217, 50–60. doi:10.1016/j.powtec.2011.10.008

Chang, J., Wu, Z., Wang, X., and Liu, W. (2019). Two-and three-dimensional hydrodynamic modeling of a pseudo-2D turbulent fluidized bed with Geldart B particle. *Powder Technol.* 351, 159–168. doi:10.1016/j.powtec.2019.04.028

Chew, J. W., and Cocco, R. A. (2021). Fast versus turbulent fluidization of Geldart Group B particles. *AIChE J.* 67, e17216. doi:10.1002/aic.17216

Chew, J. W., Wolz, J. R., and Hrenya, C. M. (2010). Axial segregation in bubbling gas-fluidized beds with Gaussian and lognormal distributions of Geldart Group B particles. *AIChE J.* 56, 3049–3061. doi:10.1002/aic.12219

Cho, H. I., Chung, C.-H., Han, G. Y., Ahn, G. R., and Kong, J. S. (2000). Axial gas dispersion in a fluidized bed of polyethylene particles. *Korean J. Chem. Eng.* 17, 292–298. doi:10.1007/bf02699043

Chyang, C. S., Kuo, C. C., and Chen, M. Y. (1989). Minimum fluidization velocity of binary mixtures. *Can. J. Chem. Eng.* 67, 344–347. doi:10.1002/cjce.5450670222

Coltters, R., and Rivas, A. (2004). Minimum fluidation velocity correlations in particulate systems. *Powder Technol.* 147, 34–48. doi:10.1016/j.powtec.2004.06.013

Cooper, S., and Coronella, C. J. (2005). CFD simulations of particle mixing in a binary fluidized bed. *Powder Technol.* 151, 27–36. doi:10.1016/j.powtec.2004.11.041

Daryus, A., Siswantara, A. I., BudiarsoGunadi, G. G. R., and Pujowidodo, H. (2019). "CFD simulation of multiphase fluid flow in a two-dimensional gas-solid fluidized bed using two different turbulence models," in *AIP conference proceedings* (New York, United States: AIP Publishing LLC), 020016.

Di Maio, F. P., Di Renzo, A., and Vivacqua, V. (2012). A particle segregation model for gas-fluidization of binary mixtures. *Powder Technol.* 226, 180–188. doi:10.1016/j.powtec.2012.04.040

Du, W., Bao, X., Xu, J., and Wei, W. (2006). Computational fluid dynamics (CFD) modeling of spouted bed: Influence of frictional stress, maximum packing limit and coefficient of restitution of particles. *Chem. Eng. Sci.* 61, 4558–4570. doi:10.1016/j.ces.2006.02.028

Ellis, N., Bi, H., Lim, C., and Grace, J. (2004). Hydrodynamics of turbulent fluidized beds of different diameters. *Powder Technol.* 141, 124–136. doi:10.1016/j.powtec.2004.03.001

Emiola-Sadiq, T., Wang, J., Zhang, L., and Dalai, A. (2021). Mixing and segregation of binary mixtures of biomass and silica sand in a fluidized bed. *Particuology* 58, 58–73. doi:10.1016/j.partic.2021.01.010

Formisani, B., Girimonte, R., and Longo, T. (2008). The fluidization process of binary mixtures of solids: Development of the approach based on the fluidization velocity interval. *Powder Technol.* 185, 97–108. doi:10.1016/j.powtec.2007.10.003

Fu, Z., Zhu, J., Barghi, S., Zhao, Y., Luo, Z., and Duan, C. (2019). Minimum fluidization velocity growth due to bed inventory increase in an Air Dense Medium Fluidized Bed. *Chem. Eng. J.* 359, 1372–1378. doi:10.1016/j.cej.2018.11.041

Gao, J., Lan, X., Fan, Y., Chang, J., Wang, G., Lu, C., et al. (2009). Hydrodynamics of gas–solid fluidized bed of disparately sized binary particles. *Chem. Eng. Sci.* 64, 4302–4316. doi:10.1016/j.ces.2009.07.003

Geldart, D. (1973). Types of gas fluidization. *Powder Technol.* 7, 285–292. doi:10.1016/0032-5910(73)80037-3

Gidaspow, D., and Huilin, L. (1996). Collisional viscosity of FCC particles in a CFB. *AIChE J.* 42, 2503–2510. doi:10.1002/aic.690420910

Gupta, S., and De, S. (2021). Investigation of hydrodynamics and segregation characteristics in a dual fluidized bed using the binary mixture of sand and high-ash coal. *Adv. Powder Technol.* 32 (8), 2690–2702.

Harris, A., Davidson, J., and Thorpe, R. (2002). The prediction of particle cluster properties in the near wall region of a vertical riser (200157). *Powder Technol.* 127, 128–143. doi:10.1016/s0032-5910(02)00114-6

Huilin, L., Yurong, H., and Gidaspow, D. (2003). Hydrodynamic modelling of binary mixture in a gas bubbling fluidized bed using the kinetic theory of granular flow. *Chem. Eng. Sci.* 58, 1197–1205. doi:10.1016/s0009-2509(02)00635-8

Jayarathna, C., and Halvorsen, B. (2011). Experimental and computational study of pressure drop and void fraction in a bubbling fluidized bed. *WIT Trans. Eng. Sci.* 70, 177–188.

Khezri, R., Wan Ab Karim Ghani, W. A., Masoudi Soltani, S., Awang Biak, D. R., Yunus, R., Silas, K., et al. (2019). Computational fluid dynamics simulation of gas–solid hydrodynamics in a bubbling fluidized-bed reactor: Effects of air distributor, viscous and drag models. *Processes* 7, 524. doi:10.3390/pr7080524

Korkerd, K., Soanuch, C., Gidaspow, D., Piumsomboon, P., and Chalermsinsuwan, B. (2021). Artificial neural network model for predicting minimum fluidization velocity and maximum pressure drop of gas fluidized bed with different particle size distributions. *South Afr. J. Chem. Eng.* 37, 61–73. doi:10.1016/j.sajce.2021.04.003

Kotoky, S., Dalal, A., and Natarajan, G. (2020). A computational analysis of the role of particle diameter on the fluidization behavior in a bubbling gas–solid fluidized bed. *Comput. Part. Mech.* 7, 555–565. doi:10.1007/s40571-019-00279-4

Lan, X., Yan, W., Xu, C., Gao, J., and Luo, Z.-H. (2014). Hydrodynamics of gas–solid turbulent fluidized bed of polydisperse binary particles. *Powder Technol.* 262, 106–123. doi:10.1016/j.powtec.2014.04.056

Leion, H., Frick, V., and Hildor, F. (2018). Experimental method and setup for laboratory fluidized bed reactor testing. *Energies* 11, 2505. doi:10.3390/en11102505

Lim, K., Zhu, J., and Grace, J. (1995). Hydrodynamics of gas-solid fluidization. *Int. J. Multiph. flow* 21, 141–193. doi:10.1016/0301-9322(95)00038-y

Lun, C., Savage, S. B., Jeffrey, D., and Chepurniy, N. (1984). Kinetic theories for granular flow: Inelastic particles in Couette flow and slightly inelastic particles in a general flowfield. *J. fluid Mech.* 140, 223–256. doi:10.1017/s0022112084000586

Mazzei, L., Casillo, A., Lettieri, P., and Salatino, P. (2010). CFD simulations of segregating fluidized bidisperse mixtures of particles differing in size. *Chem. Eng. J.* 156, 432–445. doi:10.1016/j.cej.2009.11.003

Menéndez, M., Herguido, J., Bérard, A., and Patience, G. S. (2019). Experimental methods in chemical engineering: Reactors—Fluidized beds. *Can. J. Chem. Eng.* 97, 2383–2394. doi:10.1002/cjce.23517

Mostafazadeh, M., Rahimzadeh, H., and Hamzei, M. (2013). Numerical analysis of the mixing process in a gas–solid fluidized bed reactor. *Powder Technol.* 239, 422–433. doi:10.1016/j.powtec.2013.02.008

Noda, K., Uchida, S., Makino, T., and Kamo, H. (1986). Minimum fluidization velocity of binary mixture of particles with large size ratio. *Powder Technol.* 46, 149–154. doi:10.1016/0032-5910(86)80021-3

Obuseh, C. C., Feng, Z.-G., and Paudel, B. D. (2012). An experimental study on fluidization of binary mixture in particulate flows. *J. dispersion Sci. Technol.* 33, 1379–1384. doi:10.1080/01932691003800163

Pei, P., Wu, G., Zhang, K., Yu, B., Jiang, J., and Wen, D. (2010). CFD simulation of jet behaviors in a binary gas-solid fluidized bed: Comparisons with experiments. *Front. Chem. Eng. China* 4, 242–249. doi:10.1007/s11705-009-0277-3

Philippsen, C. G., Vilela, A. C. F., and Dalla Zen, L. (2015). Fluidized bed modeling applied to the analysis of processes: Review and state of the art. *J. Mater. Res. Technol.* 4, 208–216. doi:10.1016/j.jmrt.2014.10.018

Roy, S., Pant, H. J., and Roy, S. (2021). Velocity characterization of solids in binary fluidized beds. *Chem. Eng. Sci.* 246, 116883. doi:10.1016/j.ces.2021.116883

Sahoo, P., and Sahoo, A. (2016). CFD simulation for hydrodynamic behaviour of fine particles in a fluidized bed. *Indian J. Chem. Technol. (IJCT)* 23, 253–261.

Sande, P., and Ray, S. (2014). Mesh size effect on CFD simulation of gas-fluidized Geldart A particles. *Powder Technol.* 264, 43–53. doi:10.1016/j.powtec.2014.05.019

Schaeffer, D. G. (1987). Instability in the evolution equations describing incompressible granular flow. *J. Differ. Equations* 66, 19–50. doi:10.1016/0022-0396(87)90038-6

Shao, Y., Li, Z., Zhong, W., Bian, Z., and Yu, A. (2020). Minimum fluidization velocity of particles with different size distributions at elevated pressures and temperatures. *Chem. Eng. Sci.* 216, 115555. doi:10.1016/j.ces.2020.115555

Shrestha, S., Kuang, S., Yu, A., and Zhou, Z. (2019). Bubble dynamics in bubbling fluidized beds of ellipsoidal particles. *AIChE J.* 65, e16736. doi:10.1002/aic.16736

Syamlal, M., and O'brien, T. (1987). *The derivation of a drag coefficient formula from velocity-voidage correlations*. NETL, Morgantown, WV: Technical Note, US Department of energy, Office of Fossil Energy.

Syamlal, M., Rogers, W., and Obrien, T. J. (1993). *MFIX documentation theory guide*. WV (United States)): USDOE Morgantown Energy Technology Center.

Wirth, K. E. (1988). Axial pressure profile in circulating fluidized beds. *Chem. Eng. Technol.* 11, 11–17. doi:10.1002/ceat.270110103

Yohana, E., MuchammadTauviqirrahman, M., Sayekti, A. A., Choi, K.-H., and Paramita, V. (2020). Effect of particle size and bed height on the characteristic of a fluidized bed dryer. *Cogent Eng.* 7, 1738185. doi:10.1080/23311916.2020.1738185

Yoshida, K., Kunii, D., and Levenspiel, O. (1969). Axial dispersion of gas in bubbling fluidized beds. *Industrial Eng. Chem. Fundam.* 8, 402–406. doi:10.1021/i160031a006

Zaabout, A., Bournot, H., Occelli, R., and Kharbouch, B. (2010). *Characterization of turbulent regime behavior in the dilute zone of a circulating fluidized bed riser*.

Zhang, D., Deen, N., and Kuipers, J. (2006). Numerical simulation of the dynamic flow behavior in a bubble column: A study of closures for turbulence and interface forces. *Chem. Eng. Sci.* 61, 7593–7608. doi:10.1016/j.ces.2006.08.053

Zhou, J., Grace, J., Lim, C., and Brereton, C. (1995). Particle velocity profiles in a circulating fluidized bed riser of square cross-section. *Chem. Eng. Sci.* 50, 237–244. doi:10.1016/0009-2509(94)00241-i

Nomenclature

Alphabetical Symbols

Ar Archimedes number
Bo Bond number
C coefficient
D, D_1 diameter, m
G radial distribution function
H height, m
I moment of inertia, kg·m^2
M Mach number
P pressure, Pa
Pr Prandtl number
R radius of the cylinder, m
Re Reynolds number
S source term
$\bar{S}$ modulus of the mean rate of the strain tensor
T temperature, K
U velocity, m·s^{-1}
Y generation term
Z compressibility factor
d particle diameter size, m
e coefficient of restitution
f coefficient of friction
g gravitational acceleration = 9.81 m·s^{-2}
h height of the initial bed, m
k turbulence kinetic energy, m^2·s^{-2}
m mass, kg
n number of particles
q collisional heat flux, W·m^{-2}
r radial distance of observation, m
t time, s
tr trace
x weight fraction
z height of observation, m

Greek Symbols

∇ gradient operator
Θ granular temperature, m^2·s^{-2}
Π stress tensor, Pa
ϕ drag interaction coefficient, kg·m^{-3}·s^{-1}
α angle of internal friction = 30°
β coefficient of thermal expansion
γ dissipation of the turbulent kinetic energy due to particle collisions, kg·m^{-1}·s^{-3}
δ tapered angle °
ε volume fraction
ϵ dissipation rate of turbulence kinetic energy
μ viscosity, Pa·s
ξ granular bulk phase viscosity Pa·s
π constant pi = 3.14
ρ density, kg·m^{-3}
ø sphericity

Subscripts

b interaction with buoyancy
c interaction with compressibility
co column
col collisional
cr critical
dr drag
fr frictional
g gas phase
gs superficial gas
i i phase
k interaction with turbulence kinetic energy
kin kinetic
max maximum
mf minimum fluidization
min minimum
r radial direction
*s*1 solid phase with smaller particle size
*s*2 solid phase with larger particle size
si solid phase si
sj solid phase sj
st stagnant
tur turbulent
z axial direction
g, *si* interaction between the gas phase g and solid phase si
p, *si* for the particles of the solid phase si
si, *si* interaction between the solid phase si and the solid phase si
si, *sj* interaction between the solid phase si and the solid phase sj
ϵ interaction with dissipation rate of turbulence kinetic energy

Superscripts

B bottom
T transpose
Top top
* dimensionless parameter

frontiers | Frontiers in Thermal Engineering

TYPE Review
PUBLISHED 14 April 2023
DOI 10.3389/fther.2023.1143987

OPEN ACCESS

EDITED BY
Gaweł Żyła,
Rzeszów University of Technology,
Poland

REVIEWED BY
Po-Chih Kuo,
Delft University of Technology,
Netherlands
Angela Malara,
Mediterranea University of Reggio
Calabria, Italy

*CORRESPONDENCE
Arijit Ganguli,
ganguliarijit@gmail.com

SPECIALTY SECTION
This article was submitted to Thermal
Science and Energy Systems,
a section of the journal
Frontiers in Thermal Engineering

RECEIVED 13 January 2023
ACCEPTED 28 March 2023
PUBLISHED 14 April 2023

CITATION
Ganguli A and Bhatt V (2023), Hydrogen
production using advanced reactors by
steam methane reforming: A review.
Front. Front. Therm. Eng. 3:1143987.
doi: 10.3389/fther.2023.1143987

Hydrogen production using advanced reactors by steam methane reforming: A review

Arijit Ganguli* and Viraj Bhatt

School of Engineering and Applied Sciences, Ahmedabad University, Ahmedabad, India

The present review focuses on the current progress on harnessing the potential of hydrogen production by Methane Steam Reforming (MSR). First, based on the prominent literature in last few years, the overall research efforts of hydrogen production using different feed stocks like ethanol, ammonia, glycerol, methanol and methane is presented. The presented data is based on reactor type, reactor operating conditions, catalyst used and yield of hydrogen to provide a general overview. Then, the most widely used process [steam methane reforming (SMR)/ methane steam reforming (MSR)] are discussed. Major advanced reactors, the membrane reactors, Sorption Enhanced methane steam reforming reactors and micro-reactors are evaluated. The evaluation has been done based on parameters like residence time, surface area, scale-up, coke formation, conversion, space velocity and yield of hydrogen. The kinetic models available in recently published literature for each of these reactors have been presented with the rate constants and other parameters. The mechanism of coke formation and the rate expressions for the same have also been presented. While membrane reactors and sorption enhanced reactors have lot of advantages in terms of process intensification scale-up to industrial scale is still a challenge due to factors like membrane stability and fouling (in membrane reactors), decrease in yield with increasing WHSV (in case of Sorption Enhanced Reactors). Micro-reactors pose a higher potential in terms of higher yield and very low residence time in seconds though the volumes might be substantially lower than present industrial scale conventional reactors.

KEYWORDS

steam methane reforming, process intensification, residence time, space velocity, microreactors, microreactor, membrane reactor, sorption enhanced reactor

1 Introduction

Hydrogen as a chemical is highly useful for various purposes. A few examples are: It acts as the robust backbone for the ammonia-based fertilizer industry and is highly useful for hydro-treating and hydro-cracking in petroleum industries. Moreover, over the last few years, hydrogen has developed as a fuel due to two major reasons (for example, in fuel cells) 1) zero emissions creating no environmental hazards and 2) as a byproduct gives cleaning drinking water. The demand for pure hydrogen has increased over a decade. Hydrogen can be classified into four major types based on their production source and methodology. Figure 1 shows the classification of hydrogen on the basis of their production methodology and source. Green hydrogen is based on the production of hydrogen from electrolysis of water. Grey Hydrogen and Blue Hydrogen are produced from same raw material as natural gas which majorly consists of methane and from same process of steam reforming. The only difference between them is that the latter has the carbon capturing technologies while the

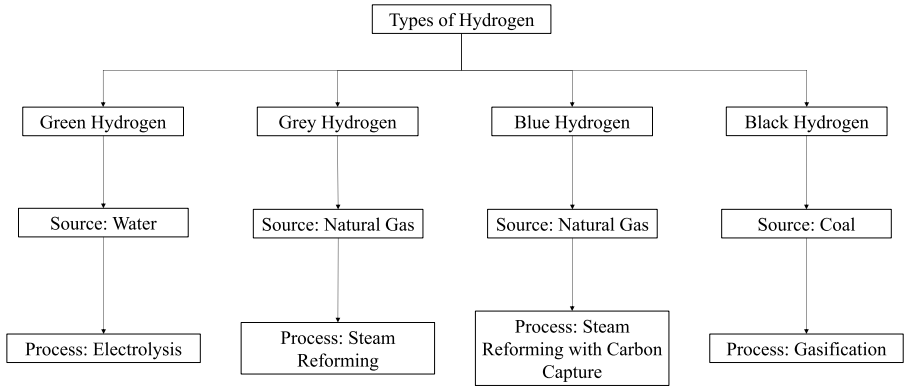

FIGURE 1
Hydrogen classification on the basis of their production source and methodology.

TABLE 1 Recent Studies for Hydrogen Production using various Chemical Species as feed.

References	Reactor type	Feed	Reactor temperature (°C)	Reactant conversion	H_2 production	Catalyst
Itoh et al. (2021)	MR	Ammonia	325–425	20%–100%	—	Ru
Huang et al. (2020)	MR	Ammonia	300–600	0%–100%	Rate = 0.304–0.6 mmol/min·gcat	Co/CeO_2
Huang et al. (2019)	QR	Ammonia	300–550	90.7%	Rate = 800–1,150 mmol/min·gcat	Ru/La_2O_3
Chen et al. (2021)	FBR	Ethanol	700	75%–95%	Yield = 50%–60%	La, Mg or Ca-Ni/sepiolite
Greluk et al. (2020)	QR	Ethanol	420	40%–100%	Selectivity = 70%–90%	Co or Ni/CeO_2 + La_2O_3
Lytkina et al. (2019a)	TFR, MR	Ethanol	380–630	—	Yield = 0.1–4 mol/h·g	Pt, Pd, Rh-Ru
Wang et al. (2019)	FBR	Ethanol	377–777	50%–100%	Mole Fraction = 0.1–0.65	Ni/CeO_2
					Rate = 70–160 mL/min·gcat	
Qingli et al. (2021)	FBR	Glycerol	400–800	77.5%–97.5%	Yield = 10%–90%	Ni/Attapulgite + MgO
					Selectivity = 30%–90%	
Charisiou et al. (2020)	FBR	Glycerol	400–750	70%–90%	Selectivity = 5%–80%	Ni/Y_2O_3-ZrO_2
					Yield = 0.5–8 mol/mol glycerol	
Saidi and Moradi (2020)	MR	Glycerol	350–500	75%–99%	Recovery = 50%–100%	$NiO/A1_2O_3$
					Yield = 30%–75%	
Charisiou et al. (2019)	FBR	Glycerol	400–750	5%–90%	Selectivity = 50%–90%	Ni/ZrO_2 + SiO_2
					Yield = 0.5–9 mol/mol glycerol	

FBR, Fixed Bed Reactor; MR, Membrane Reactor; TFR, Tubular Flow Reactor; QR, Quartz Reactor.

former does not. Black hydrogen is obtained from coal gasification. The present article deals with the production of hydrogen from methane, i.e., Grey Hydrogen and Blue Hydrogen.

Hydrogen can be produced from various routes using chemicals like methane, ethanol, ammonia, methanol, and glycerol. Current trends on the production of hydrogen include processes involving decomposition of ammonia, and steam reforming of ethanol and glycerol (Lytkina et al., 2019a; Saidi and Moradi, 2020; Itoh et al., 2021). In recent years, methanol steam reforming using innovative reactor configurations has also become an emerging field of research (Shtyka et al., 2018; Lytkina et al., 2019a; Lytkina et al., 2019b; Cai et al., 2019; Cao et al., 2019; Fasanya et al., 2019; Kamyar et al., 2019;

TABLE 2 Recent Studies for Hydrogen Production using Methanol.

References	Reactor type	Reactor temperature (°C)	Reactant conversion	H_2 production	Catalyst
Mohtashami and Taghizadeh (2019)	TPBR	150	71.3%–99.8%	Selectivity = 65.5%–99.5%	Cu-ZnO-ZrO_2
Shtyka et al. (2018)	FTQR	250–300	>75%	—	Pt, Ru/CNT-$KMnO_4$
Cao et al. (2019)	FBR	240–310	20.86%–100%	Selectivity = 95.78%–99.54%	Cu-Fe/ATP
Fasanya et al. (2019)	FBR	180–350	<70%	—	CuO-ZnO
Kim et al. (2019)	FBR	167–287	35%–100%	Selectivity = 75%–100%	Cu-Zn
Kamyar et al. (2019)	MoMMR	150–300	30%–95%	Selectivity = 62.5%–92.5%	Pt-SnO
Cai et al. (2019)	FBR	150–400	10%–100%	Production = 50–90 mmmol/h/g	Nb-Pd-Zr-Zn
Zeng et al. (2019)	FBR	250–380	5%–98%	—	Pd/ZnO
Lytkina et al. (2019a)	TFR, MR	200–360	—	Yield = 0.1–4 mol/h/g	Pt, Pd, Rh-Ru
Lian et al. (2019)	PCCR	355–727	40%–92%	Selectivity = 60%–92%	Ni, Fe-Cu/γ-Al_2O_3
Sarafraz et al. (2019)	MMR	250–500	70%–97%	—	Cu-SiO_2
Lytkina et al. (2019b)	TFR, MR	200–400	5%–85%	Yield = 0.1–4.5 mol/h/g	Pd, Ru-Rh
Khani et al. (2019)	MoMMR	150–300	20%–95%	Selectivity = 45%–95%	Cu-ZnO/La_2O_3-Al_2O_3

FBR, Fixed Bed Reactor; FTQR, Flow-Type Quartz Reactor; MMR, Micro Reactor; MR, Membrane Reactor; MoMMR, Monolith Micro Reactor; PCCR, Plasma Chain Catalytic Reactor; TPBR, Tubular Packed Bed Reactor; TFR, Tubular Flow Reactor.

TABLE 3 Recent Studies for Hydrogen Production using Methane.

References	Reactor type	Reactor temperature (°C)	Reactant conversion	H_2 production	Catalyst
Kim et al. (2018)	MR	500	56.5%–79.5%	Recovery = 97.9%–98.7%	Pd-Ru/$A1_2O_3$
Fukuda et al. (2021)	CPR	500–800	8%–90%	—	—
Huang et al. (2021b)	FBR	352–402	30–90	Yield = 30%–90%	Ni/Al_2O_3
Anzelmo et al. (2017)	MR	400	32.1%–84%	Recovery = 82%	Pd/PSS
				Production = 22.4–58.1 mL/min	
Bernardo et al. (2010)	MR	500	50%–100%	—	Pd
Chompupun et al. (2018)	MoMMR	500–600	5%–90%	Mole Fraction = 0.1–0.4	Ni/$A1_2O_3$
				Recovery = 20%–95%	
Ashraf et al. (2020)	CPR	>120	84.9%	—	Pt/$A1_2O_3$
Irankhah et al. (2014)	CRICC	400–750	55%–99%	—	Ni/$CaAl_2O_4$
					Pt-Sn/$A1_2O_3$
Pashchenko et al. (2021)	CPR	527–727	<60%	Mole Fraction = 0.1–0.2	Ni/$A1_2O_3$
Antzaras et al. (2020)	FBR	650	—	Yield: 72%–90%	NiO/ZrO_2
Yuan et al. (2017)	TPBR	600–1,000	18.4%–92.3%	Mole Fraction < 0.5	Ni/Al_2O_3
Abanades et al. (2014)	PBSR	1,000–1,200	100%	Selectivity = 100%	Carbon Black
				Yield = 100%	

CPR, Catalytic Plate Reactor; CRICC, Compact Reformer Integrated with Catalytic Combustion; MR, Membrane Reactor; MoMMR, Monolith Micro Reactor; PBSR, Packed Bed Solar Reactor; TPBR, Tubular Packed Bed Reactor; TFR, Tubular Flow Reactor; TWMR, Tube-Wall Membrane Reactor.

Khani et al., 2019; Kim et al., 2019; Lian et al., 2019; Mohtashami and Taghizadeh, 2019; Sarafraz et al., 2019; Zeng et al., 2019).

Traditionally, methane had remained an effective source of hydrogen production. Various strategies for hydrogen production using methane include Partial Oxidation of Methane (POM) and Methane Steam Reforming (MSR). The most efficient and pure hydrogen production of all the methods have been developed using steam reforming of methane. Challenges in current technologies and increasing demands for lower capital and operating expenses in chemical production have fueled interest in developing novel approaches such as process intensification (Benson and Ponton, 1993; Moulijn and Stankiewicz, 2004). MSR produces nearly 48% of hydrogen globally (Gaudernack, 1998) using natural gas, with a maximum efficiency of 75% (Veziroglu and Barbir, 1998). To understand the feasibility of other raw materials than methane, three different tables are presented below. Table 1 summarizes the prominent works of hydrogen production using various feeds other than methane while Table 2 summarizes the recent advancements in hydrogen production using methanol and Table 3 for hydrogen production using methane. Most importantly, it can be observed that different types of reactors and catalysts are used by different authors to achieve high yields of hydrogen from different feed stocks other than methane. However, while the works of some authors are interesting the catalysts used by them are made of elements which are expensive and might be difficult for commercialization at industrial scale. Similarly, Table 2 focuses only on methanol where the recent studies have reported a varied range of conversion and selectivities from as low as 10% to as high as 100% providing very high yields. The different reactors in which these studies have been carried out, different operating conditions and catalyst types are also listed. Similarly, a listing of the most recent studies for methane as a feed stock in Table 3 shows that the advent of newer reactor types and different catalyst types (dominated predominantly by Nickel, Palladium and Platinum) have reduced reactor operating temperatures from conventional range of 800°C–1,000°C to 350°C–500°C maintaining yields above 90% which is a major advantage for MSR technology and process intensification. One of the major limitations of MSR as the most widely used process for hydrogen production is its high energy consumption. Due to this a major thrust has been pursued on process intensification. Hence, process intensification is of primary importance to further reduce the cost. Various strategies of process intensification can be acquired either by integrating unit processes involving chemical reactions and unit operations such as separation and heat exchanger or, more recently, by the miniaturization of the characteristic flow paths into unambiguous, structured geometries (Simsek et al., 2011; Önsan and Avci, 2011). One of the strategies of process intensification is coupling of innovative methods in catalyst design and reactor design. Process intensification (PI) is a technique for increasing energy efficiency using the strategies like 1 overcoming thermodynamic limitations 2 reduction in mass transfer resistances (De Deken et al., 1982; Soliman et al., 1988), 3 reduction in heat transfer resistance. PI can be very effective in conventional MSR, due to a) mass transfer limitations (Elnashaie, 1994), b) limitations due to thermodynamics and c) coke formation leading to the deactivation of the catalyst (Trimm, 1997). Adsorptive or membrane catalytic reactors may help overcome thermodynamic limitations (Adris et al., 1991; Hufton et al., 1999), while mass transfer limitations can be reduced through multifunctional catalysts (catalyst particles capable of doing multiple tasks, e.g., a catalyst particle having dual functionality, i.e., acting as a catalyst and also having membrane properties) (Dietrich et al., 2005). Innovative catalyst design, on the other hand, can aid in achieving desired kinetics. Thus, intensification of MSR can be achieved either by replacing conventional catalysts with multifunctional catalysts (Rusu and Cormier, 2003) or by intensifying processes like adsorptive or membrane catalytic reactors. Micro-reactors provide an integration of exothermic combustion channel and endothermic reforming channel. In addition, the metal walls that are responsible for the indirect heat exchange are made of advanced materials with higher heat transfer coefficients. This aids in improving the thermal efficiency of the process. On the other hand, advances in novel catalysts (e.g., Ni based catalysts) aids in a) decrease in residence times b) decrease in reactor volumes and c) increase in throughput (Tonkovich et al., 2004; Tonkovich et al., 2007).

Following are the objectives of the present study: a) to present a comparison of the most recent studies on hydrogen production using different feed stocks based on reactor types, operating conditions, catalysts and yield of hydrogen, b) classify and select major types of process intensification based advanced reactors most suited for industrial production c) perform a critical analysis of the key strengths in those reactors, their challenges and current status with respect to industrial implementation d) perform a detailed analysis of the kinetic models (essentially their rate expressions, kinetic rate constants and other parameters) and mechanism of coke formation (along with their rate expressions) for the chosen reactors and f) comparison of the MSR's based on their advantages and limitations.

The Figures 2A–D show the schematics of the different types of reactors and their functioning. Figure 3 shows the various advantages and limitations of each of the reactors chosen for comparison and the applications for which they are used other than MSR.

2 Novel reactor configurations

2.1 Membrane reactors (MR)

MR consists of a reactor volume filled with catalyst with one of its sides consisting of membrane (as shown in Figures 2A, C) that selectively removed hydrogen during MSR process due to pressure difference. The schematic of the MR in Figure 2A, shows that reactant (methane + steam) enters the catalyst section which is separated from the central section using the membrane. Hydrogen produced by MSR permeates into the central section and collected at the end with sweep steam while the unpermeated gas is collected at outlet of catalytic section. Depending on the geometric and operating parameters like reactor length, pressure, and temperature, the methane conversion upto 100% can be achieved, and pure hydrogen can be produced. These results in optimization in terms of number of equipments required in process material cost and temperature control is possible aiding the economics and design of the process.

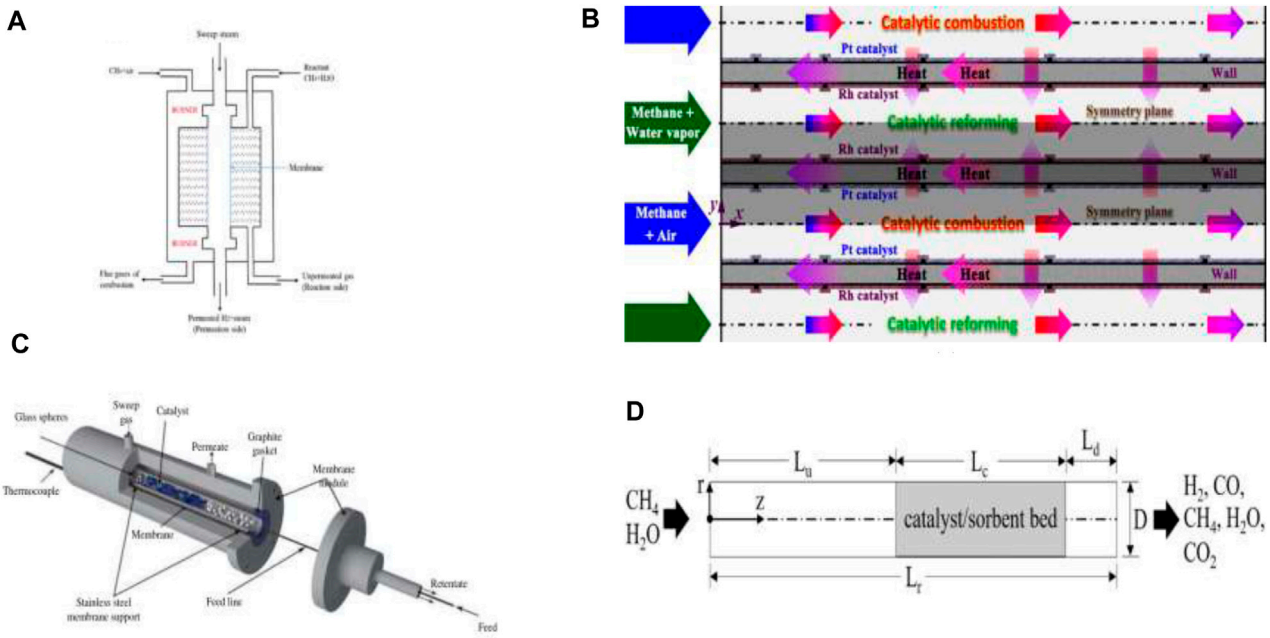

FIGURE 2
Various Types of Reactor Configurations **(A)** Membrane Reactor. Reproduced under CC-BY 4.0 from Hafeez et al. (2020). **(B)** Micro-channel Reactor. Reproduced from Chen et al. (2019), with permission from ACS Publications. **(C)** Tubular Packed Bed Reactor. Reproduced from Iulianelli et al. (2016), with permission from Taylor and Francis. **(D)** Sorption Enhanced Methane steam Reformer. Reproduced from Huang W.-J. et al. (2021), with permission from Elsevier.

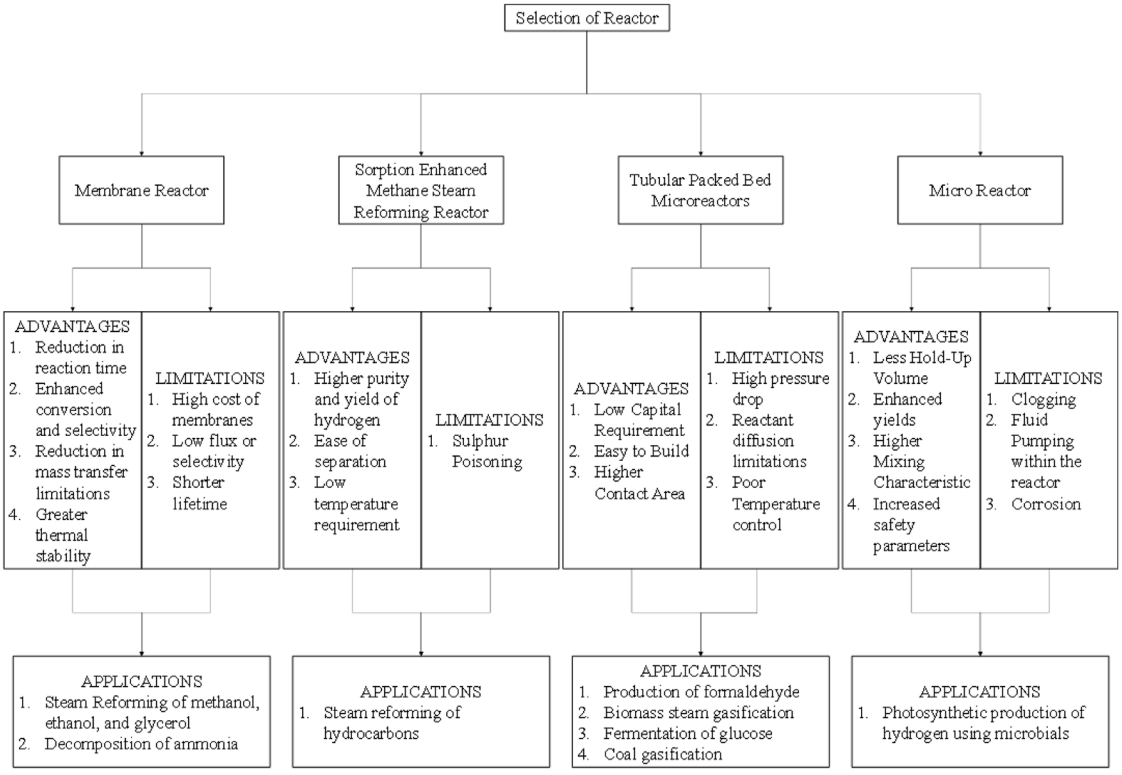

FIGURE 3
Comparison of reactors on the basis of applications, advantages and limitations.

Further, such reactors consist of three major steps, namely, reforming, water-gas shift and purification all taking place in the same reactor. Membrane reactors combine the capabilities of fixed or fluidized beds with perm-selective membranes embedded in the reactors. The membranes are especially useful in shifting conventional thermodynamic equilibrium and *in-situ* separation while also reducing the undesired by-products. To summarize, as the membrane reactor combines the reactor and separator units into one, it helps in reducing overall capital cost whilst increasing the yield and selectivity of hydrogen production.

2.1.1 Membrane selection

Membrane reactors face problems like membrane fouling. Another important parameter is the strength of the membrane is important since the pressure at which the hydrogen is obtained is higher than atmospheric pressure. Other criteria like the purity of hydrogen obtained as the product and the mass transfer from the membrane is vital to decide good membrane performance. Hence, the type of membrane used is a crucial parameter in performance of MR's. Palladium based membranes are mostly used but they are expensive. Hence, palladium with combination of cesium oxide (Tong et al., 2005), or dense ceramic membranes or modified pervoskite membranes (Bouwmeester, 2003; Thursfield and Metcalfe, 2004) or mixed ceramic metal membranes (Dong et al., 2001) have been used. Recent studies have shown that Carbon Molecular Sieve Membranes (CMSM) have been found useful for the production of hydrogen at low temperatures and are also resistant to CO and Sulphur poisoning (Bernardo et al., 2020). Palladium-based membranes provide a combination of both as a catalyst for hydrogen production whilst helping in the purification of hydrogen with excellent hydrogen selectivity (Bernardo et al., 2020). Electrochemical Hydrogen Pumping Membranes (EHPM) have high hydrogen permeation and selectivity at low energy consumption (Bernardo et al., 2020). In addition to this, the quality of feed and operating conditions harms membrane stability.

2.1.2 Implementation of membrane reactors

Membrane reactors are being tested on a small scale. For example, a small MR built and tested for production of hydrogen (capacity of 15 Nm^3/hr) by Tokyo gas company (Seki et al., 2000). Other projects like hydrogen production initiatives by European Commission-funded project using Ag/Pd membranes faced challenges in commercialization due to several design issues (Dams et al., 2000). Research and development on hydrogen separation catalysts are ongoing in several companies (John Matthey catalysts, Aspen systems). Several government and private organizations like (Northwest power systems, Natural resources Canada, Institute of Gas Technology, and Dais-Analytic) (Huang et al., 2003) have granted patents for this technology. Micro-Membrane reactors have been extensively used for the hydrogen production due to enhanced heat and mass transfer characteristics, removal of mass transfer limitations and intense process intensification due to integration of different process units into single unit (Hafeez et al., 2020).

2.2 Sorption Enhanced methane steam reforming (SEMSR)

Figure 2D shows a typical SEMSR in a tubular fixed bed reactor. The length of the tube (L_r) is divided into three parts where L_c is the catalyst bed while some distance is kept before and after the bed to maintain fully developed flow/hydrodynamics (denoted by L_u and L_d). SEMSR involves addition of sorbents to have a twofold advantage a) increases in reaction rate b) *in situ* carbon-dioxide separation. The temperatures to achieve these reaction rates are in the range of 450°C–650°C. It also has advantages like high ability to adsorb and lower operating temperatures for calcination and carbonation. Pressure Swing Adsorption (PSA) is generally used for adsorption.

2.2.1 Multi-functional catalyst design

A multifunctional catalyst involves the characterization of the catalyst particle for different adsorbent fractions in the particle and diffusivities inside the particle (Zanfir and Gavriilidis, 2003; Yuan et al., 2007). These are also called combined sorbent catalyst particles (CSCM) (Di Giuliano et al., 2020) in which the solid particles consist of both the catalyst for MSR and the sorbent for CO_2 capture. It possesses unique advantages like negligible inter and intra particle resistances, thermal integration between endothermic and exothermic reactions and reduced solid hold up in the case of heterogeneous reactors. Recently, the multifunctional catalyst configurations have been in the form of Nickel for MSR and CaO as the sorbent for CO_2 capture. These enable the MSR process to be carried out at atmospheric pressures and 650°C than the high pressures and temperatures required in the conventional industrial processes.

2.2.2 Implementation of SEMSR

Air Products and Chemical Inc. have shown the implementation of SEMSR *via* a pilot plant that essentially saves capital expenditure compared to conventional SMR's (McLeod et al., 1997). The feasibility to use multifunctional catalysts like CaO15Ni(N)10 for industrial scale have been successfully demonstrated by researchers for 200 cycles (Di Giuliano et al., 2020). However, it has also been found that Ni sintering causes deactivation of the catalyst which would need further investigation in terms of Ni stability. Other characteristics like wet impregnation, wet mixing and attrition resistance were found to be good in these types of catalysts when tested on industrial scale.

Implementation of SEMSR's are however challenging also due to the non-uniform temperature distribution due to the endothermic reaction of MSR and the exothermic reaction of CO_2 sorption. Due to this it has been observed that the hydrogen production decreases with increase in weight hourly space velocity (WHSV) for the same geometric conditions (Huang W.-J. et al., 2021). This suggests more amount of research to be performed on industrial scale conditions for higher tube diameters for coming up with strategies to obtain higher hydrogen yields.

2.3 Micro-reactors

Micro-reactors used for hydrogen production are of different types in terms of whether the reactor has catalyst particles packed in the reactor or they are wall coated. This will in explained in the forthcoming subsections.

2.3.1 Tubular packed bed micro-reactors (TPBM)

TPBM contains a concentric tubular system in which the inner tube is a membrane containing a catalyst. The feed enters inside the annular space between the concentric tube or the smaller concentric tube. The reaction happens on the surface of the catalyst. If the feed enters into the annular space between the concentric tube, then the reactants will permeate through the membrane and the product will be received through the outlet of the membrane itself. But if the feed enters into the smaller catalyst membraned concentric tube, the product permeates out of the membrane and received from the annular space. For Tubular membrane reactors (TMR's), a two-step methane reforming process will be more efficient than the single-step conventional methane reforming. The authors also discussed that the optimum conditions for MSR by the two-step strategy are 720°C, Steam carbon ratio of 4, and pressure ranging between 3 and 10 bar. The two-step process also gives an energy efficiency of 35%–40%. Abanades et al. (2014) studied MSR in a solar-powered tubular packed bed reactor. The reactor directly used the solar indirect-irradiation concept to gain higher temperatures and also for complete driving of the endothermic MSR reaction. Carbon black was used as a catalyst for the reactor. The product received was 100% pure hydrogen without any by-products. The product contained no CO_2. The authors discussed that the residence time and the temperature of the gas flowing through the catalyst bed act as important parameters influencing the chemical conversion and hydrogen yield.

2.3.2 Wall coated micro-reactors (MIR)

Micro-channel process technology consists of reactors with channels in the range of 50–5,000 μm working in a laminar flow regime. A typical micro-channel reactor is shown in Figure 2B. It consists of alternating channels of catalytic combustion and reforming with inlets of methane-air mixture and methane-water mixture respectively. The walls on the reforming side are coated with Ruthenium catalyst while those on combustion side are coated with platinum catalyst. The heat transfer takes place through the walls as shown in the figure. Two types of catalytic systems: Palladium MMRs and Zeolite MMRs are used for hydrogen production (Kiani et al., 2021). Typical characteristics of micro-reactors include a high surface-to-volume ratio (for SMR also) improved heat and mass transfer rates (typically the rates are inversely proportional to channel diameters), low-pressure drops, and ease in thermal integration (Tonkovich et al., 2004; Delsman et al., 2005; Lou et al., 2008; Zhai et al., 2011). Further, micro-channel reactors can be scaled up by numbering up of several micro-channels in parallel that helps in production due to increase in throughput. Micro-reactors are characterized by micro-channels (which may have different shapes) in the range ~10^{-5} and 10^{-3} m. Flow in these cases is essentially laminar. The construction material consists of plates (substrates) in which the channels are constructed. The surface areas are in the 1×10^4–5×10^4 m^2m^{-3}, which are ca. 50–100 times higher than those of their conventional packed bed counterparts (Simsek et al., 2011). The presence of the higher surface areas, smaller dimensions of sub-millimeters in combination with the use of metal-based catalysts help in uniform temperature distribution. The catalyst can either be packed into the channels or coated as a layer on the internal channel walls. MSR is favored at higher steam to carbon ratios of the feed at high temperatures. MSR being an endothermic reaction, a packed bed reactor would encounter axial and radial temperature gradients which in turn require cautious heat input and removal. On the other hand, coating catalysts on the walls, causes are helpful in minimization of transport resistances and provides a uniform temperature distribution over the catalyst layer. It is evident however that the above advantages of the micro-reactors can be harnessed depending on catalyst characteristics, stability, coating ability and activity.

2.3.2.1 Effect of geometric and operating parameters

In SMR process, two parameters that play a vital role are temperature and flow arrangement, the former being the most important. In micro-channels, the length scale for complete combustion is very small. At temperatures in the range 930°C–1,000°C overall conversion of 96% is achieved. Cross flow arrangement is mostly used while wall coated Fe-Cr-Al-Y catalysts are used in micro-reactors for MSR as per published literature (Stutz et al., 2006). Investigations have suggested that the complete combustion of methane takes place at a very short reactor distance at channel entry. One of the many advantages of micro-reactors is the ability to house multiple operations in a single unit (Tonkovich et al., 2007). This includes multiple inlets (like inlets for feed components like methane and steam and for preheating materials like fuel and air which make the process energy efficient).

Micro-channel reactors have been found to perform well at high space velocities higher than 10^5 h^{-1}. In a study by (Zhai et al., 2011), the authors found conversions up to 100% for high space velocities upto 1.2×10^5 h^{-1}. A three time increase in space velocity caused 50% decrease in conversion while an increase of five times decreased conversion by 30%.

2.3.2.2 Energy optimization in micro-reactors

Micro-reactors provide a reduction in plant complexity by incorporating multiple unit operations in a single modular reactor (Tonkovich et al., 2007). This can essentially help in small scale processing (Tonkovich et al., 2007) including specialty chemicals, fuel processing, and combinatorial or analytical applications.

Further, micro-reactors have the potential to reduce the cost of energy-consuming pieces of equipment like blowers and compressors. For example, as per study of the literature, a pilot scale micro-reactor in 40 h of continuous operation can give 90% MSR methane conversion at around 150 kPa pressure, and 850°C with about 25% of excess air and reaction times as low as 6 ms (Tonkovich et al., 2007). Further, the heat flux required to maintain the reaction temperature due to the reaction being endothermic does not destroy the mechanical integrity (Tonkovich et al., 2007). As per the published literature, around 55% of the total energy produced by combustion (fuel + air) was consumed to overcome endothermicity higher than conventional reactors. Further, of the 700 W produced by combustion in the micro-reactor, 311 W were consumed by the

endothermic MSR reaction (6 ms contact time) and about 314 W (45%) were associated with thermal losses. The losses may be very low for pilot-scale systems due to the large surface-area to volume ratio. However, in a commercial-scale system, the thermal losses are calculated to drop below 5% while combustion contact times were 4 ms.

2.3.2.3 Implementation and scale-up of micro-reactors

Micro-reactors have successfully been scaled up to produce 10 m^3/s of hydrogen (Tonkovich et al., 2004). Numbering of reactors plays a major role in increasing the plant capacity during scaleup (Tonkovich et al., 2004). Conventional large-scale reformers suffer from the inefficient use of heat recovered from combustion gases in the form of steam and reduced thermal efficiencies of radiant reformer.

In a micro-structured steam–methane reformer, the heat transfer area required for recovering heat does not depend on the reactor volume which provides ample opportunity for process intensification and high energy savings as compared to conventional tubular reformers (Endou et al., 2004). In some cases, the energy required for reforming process is obtained from energy recovered from hot exhaust streams. In others, the catalytic fixed beds are embedded with heat exchangers providing high thermal efficiency (due to additional heat transfer area requirement), no extra steam generation (avoiding the necessity of steam utilization) least requirement of process control and high scalability.

2.3.2.4 Role of catalysts in micro-reactors

In terms of dispersion, sintering and coking characteristics, the authors observed that good supports ensured lower tendency of sintering and coking. The lesser carbon formation in Ni catalyst was attributed to high saturation concentration of carbon in the smaller nickel crystals. The authors also observed distinct possibilities of catalysts being coated on the walls of the micro-channel to achieve high performance in terms of low sintering and coking and shorter residence times. Further, the authors also found that catalysts prepared by mixing Nickel, Magnesium and Alumina (e.g., $Ni_{0.5}Mg_{2.5}AlO_9$) were cost effective, stable, and active for long residence times comparable or better than Rhodium catalysts. The authors have also found that existence of $NiAl_2O_4$ helped to restrain sintering and keep small crystal size.

3 Kinetic modeling of MSR

Development of kinetic models for couple processes has always posed a challenge to the research fraternity. Kinetic models depend heavily on the basic data like the rate constants and order of reaction obtained from experimental data. However, depending only on experimental data is not advisable and advanced techniques like molecular modeling needs to be used to determine the above parameters. This is also possible due to the increase in computational power over more than a decade now. A few researchers have been able to predict kinetic parameters with different reaction mechanisms (Yang et al., 2000; Chen et al., 2004). However, the information, obtained from molecular dynamic simulations cannot be used directly during the scale-up of reactors. Scale-up methodology involves model development for different length and time scales, due to which the rate-limiting parameters need to be identified at the molecular level. Further, a correlation of these parameters (at micro-scale) with parameters at the macro level needs to be established and controlled by manipulating the micro-scale parameters. This approach has been referred to as multi-scale modeling approach by various authors (Bhat and Sadhukhan, 2009). The major advantage of such multi-scale modeling is in catalyst design only. Other aspects like predictions in conversion, yield, etc. can be achieved even by tuning the existing empirical models if coupled with changes in online experimental and multi-scale modeling does not provide any specific advantage.

With reference to the above discussion, an effort has been made to find the current status of the kinetic models in the published literature (Chen et al., 2020; Katheria et al., 2020; Niu et al., 2020; Parvasi et al., 2020; Huang W.-J. et al., 2021). The kinetic models [of the most recent and prominent research works (Parvasi et al., 2020; Huang W.-J. et al., 2021)] along with their rate constant expressions developed for the membrane and sorption enhanced reactors have been presented in Table 4. Below are the reactions occurring in a reactor during MSR:

$$CH_4 + H_2O \leftrightarrow CO + 3H_2 \quad (1)$$

$$CO + H_2O \leftrightarrow CO_2 + H_2 \quad (2)$$

$$CH_4 + 2H_2O \leftrightarrow CO_2 + 4H_2 \quad (3)$$

$$CH_4 + CO_2 \leftrightarrow 2CO + 2H_2 \quad (4)$$

$$CaO + CO_2 \rightarrow CaCO_3 \quad (5)$$

The reaction kinetics and the rate constants for the reaction systems depends on several parameters. The major parameters affecting the reaction system are temperature, pressure, and activation energy. The activation energy for the reaction system depends upon the reactor system and the catalyst used for the reactor. Table 4 summarizes the reactions kinetics for the same.

4 Coke formation

Coke Formation results as an undesirable side reaction during MSR. Coke formation causes the formation of a layer of carbon over the layer of the catalyst. Because of the collection of coke over the catalyst, the active sites of the catalyst which should be used by reactants for product formation, gets consumed. This leads to catalyst deactivation and efforts are needed to minimize them. Figure 4 shows coke formation on a metal catalyst with support.

Though it is clear that there is coke formation during the MSR reactions, the complete mechanism of the coke formation should be understood to avoid it. Sheintuch and German (2021) studied the reaction mechanism of coke formation during MSR in a Pd membrane. They also modelled the coke formation using a micro-kinetic model. According to the authors, the following reaction steps occur during MSR when coke formation takes place:

$$* + CH_4(g) \leftrightarrow CH_4{}^* \quad (6)$$

$$* + CH_4{}^* \leftrightarrow CH_3{}^* + H^* \quad (7)$$

$$* + CH_3{}^* \leftrightarrow CH_2{}^* + H^* \quad (8)$$

TABLE 4 Reaction kinetics for various reactor systems.

References	Reactor	Catalyst	Reaction kinetics and rate constants
Parvasi et al. (2020)	Membrane Reactor	Ni/CeO_2	*Reaction Kinetics* $R_1 = \frac{\frac{k_1}{P_{H_2}^{2.5}}(P_{CH_4}P_{H_2O} - \frac{P_{H_2}^4 P_{CO_2}}{K_1})}{(1+K_{CH_4}P_{CH_4}+K_{H_2}P_{H_2}+K_{CO}P_{CO}+K_{H_2O}P_{H_2O}/P_{H_2})^2}$
			$R_2 = \frac{\frac{k_2}{P_{H_2}^{3.5}}(P_{CH_4}P_{H_2O}^2 - \frac{P_{H_2}^4 P_{CO_2}}{K_2})}{(1+K_{CH_4}P_{CH_4}+K_{H_2}P_{H_2}+K_{CO}P_{CO}+K_{H_2O}P_{H_2O}/P_{H_2})^2}$
			$R_3 = \frac{\frac{k_3}{P_{H_2}}(P_{CO}P_{H_2O} - \frac{P_{H_2}P_{CO_2}}{K_3})}{(1+K_{CH_4}P_{CH_4}+K_{H_2}P_{H_2}+K_{CO}P_{CO}+K_{H_2O}P_{H_2O}/P_{H_2})^2}$
			$R_4 = \frac{k_4 k_5 K_4 P_{CH_4} P_{CO_2}}{k_4 K_4 P_{CH_4} P_{CO_2} + k_4 P_{CH_4} + k_5 K_4 P_{CO_2}}$
			Rate Constants $k_1 = 7.24166 \times 10^{-7} \exp[\frac{240.100}{R}(\frac{1}{648} - \frac{1}{T})]$
			$k_2 = 1.6882 \times 10^{-9} \exp[\frac{243.900}{R}(\frac{1}{648} - \frac{1}{T})]$
			$k_3 = 2.5440 \exp[\frac{67.100}{R}(\frac{1}{648} - \frac{1}{T})]$
			$k_4 = 2.633550 \times 10^{-3} \exp[\frac{-4300.0}{T}]$
			$k_5 = 8.474329 \times 10^{2} \exp[\frac{-7500.0}{T}]$
			$K_i = \exp(-\frac{\Delta G^{\circ}_{rxn_i}}{RT})$ i = 1, 2, 3 and 4
			$K_{CH_4} = 1.8 \times 10^{-1} \exp[\frac{-38300}{R}(\frac{1}{823} - \frac{1}{T})]$
			$K_{H_2} = 2.9 \times 10^{-2} \exp[\frac{-82900}{R}(\frac{1}{648} - \frac{1}{T})]$
			$K_{CO} = 40.9 \exp[\frac{-70700}{R}(\frac{1}{648} - \frac{1}{T})]$
			$K_{H_2O} = 0.4 \exp[\frac{88700}{R}(\frac{1}{823} - \frac{1}{T})]$
Huang et al. (2021a)	SEMSR	Ni/Al_2O_3	*Reaction Kinetics*
			$R_1 = \frac{\rho_{cat}\frac{k_1'}{P_{H_2}^{2.5}}(P_{CH_4}P_{H_2O} - \frac{P_{H_2}^3 P_{CO}}{K_1'})}{(DEN)^2}$
			$R_2 = \frac{\rho_{cat}\frac{k_2'}{P_{H_2}}(P_{CO}P_{H_2O} - \frac{P_{H_2}P_{CO_2}}{K_2'})}{(DEN)^2}$
			$R_3 = \frac{\rho_{cat}\frac{k_3'}{P_{H_2}^{3.5}}(P_{CH_4}P_{H_2O}^2 - \frac{P_{H_2}^4 P_{CO_2}}{K_3'})}{(DEN)^2}$
			$R_5 = \rho_{sorb}\frac{6(\frac{V_{CaO}}{\delta_{CaO}})(1-X)^{\frac{2}{3}}k''(C_{As} - C_{Aeq})}{1+\frac{\delta_{CaO}}{2D_{PL}}k''\sqrt{1-X}(1-\sqrt[3]{\frac{1-X}{1+(Z-1)X}})}$
			$R_{CH_4} = (-R_1 - R_3)M_{CH_4}$
			$R_{H_2O} = (-R_1 - R_2 - 2R_3)M_{H_2O}$
			$R_{CO} = (-R_1 - R_2)M_{CO}$
			$R_{CO_2} = (R_2 + R_3 - \frac{R_5}{M_{CaO}})M_{CO_2}$
			$R_{H_2} = (3R_1 + R_2 + 4R_3)M_{H_2}$
			$R_{CaO} = -R_5$
			$R_{CaCO_3} = \frac{R_5 M_{CaCO_3}}{M_{CaO}}$
			Rate Constants and Other Parameters
			$\rho_{cat} = \frac{\text{Loading of } Ni/Al_2O_3}{\text{Volume of catalyst/sorbent bed}}$ (gm^{-3})
			$\rho_{sorb} = \frac{\text{Loading of CaO}}{\text{Volume of catalyst/sorbent bed}}$ (gm^{-3}) $k_1' = 1.243 \times 10^{14} \exp(\frac{-240.1}{RT})$
			$k_2' = 1.955 \times 10^{6} \exp(\frac{-67.13}{RT})$
			$k_3' = 3 \times 10^{13} \exp(\frac{-243.9}{RT})$
			$K_1' = 1.198 \times 10^{17} \exp(\frac{-26830}{T})$

(Continued on following page)

TABLE 4 (*Continued*) Reaction kinetics for various reactor systems.

References	Reactor	Catalyst	Reaction kinetics and rate constants
			$K_2^{'} = 1.767 \times 10^{-2} \exp\left(\frac{4400}{T}\right)$
			$K_3^{'} = 2.117 \times 10^{15} \exp\left(\frac{-22430}{T}\right)$
			$DEN = \frac{1+K_{CO}^{'}P_{CO}+K_{H_2}^{'}P_{H_2}+K_{CH_4}^{'}P_{CH_4}+K_{H_2O}^{'}P_{H_2O}}{P_{H_2}}$
			$K_{CO}^{'} = 8.23 \times 10^{-5} \exp\left(\frac{70.65}{RT}\right)$
			$K_{H_2}^{'} = 6.12 \times 10^{-9} \exp\left(\frac{82.9}{RT}\right)$
			$K_{CH_4}^{'} = 6.65 \times 10^{-4} \exp\left(\frac{38.28}{RT}\right)$
			$K_{H_2O}^{'} = 1.77 \times 10^{5} \exp\left(\frac{-88.68}{RT}\right)$
			$C_{Aeq} = \frac{P_{Aeq}}{RT}$
			$D_{PL} = D_{PL0} \exp\left(-aX^{b}\right)$
			$P_{Aeq} = 4.137 \times 10^{-7} \exp\left(\frac{-20474}{T}\right)$
			$Z = \frac{V_{CaCO_3}}{V_{CaO}}$

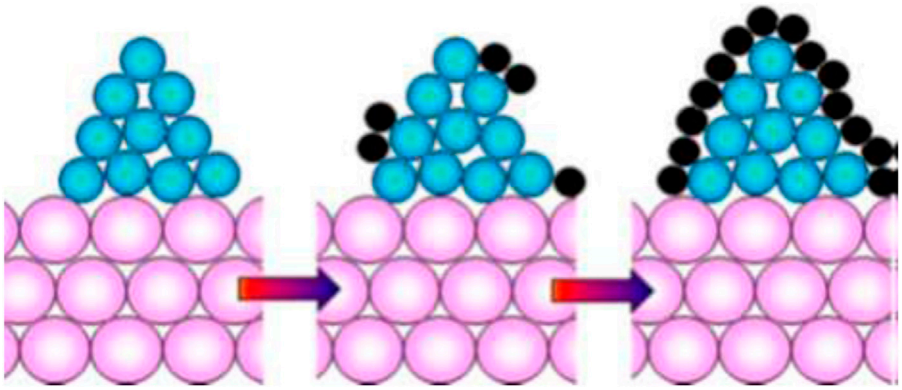

FIGURE 4
Coking mechanism on catalyst [Reproduced under CC-BY 4.0 from Stenina and Yaroslavtsev (2022)], Pink-Catalyst Support; Blue-Metal Catalyst; Black-Carbon.

$$* + CH_2^* \leftrightarrow CH^* + H^* \quad (9)$$
$$* + CH^* \leftrightarrow C^* + H^* \quad (10)$$
$$H^* + H^* \leftrightarrow H_2^* + * \quad (11)$$
$$H_2^* \leftrightarrow H_2(g) + * \quad (12)$$
$$* + H_2O(g) \leftrightarrow H_2O^* \quad (13)$$
$$* + H_2O^* \leftrightarrow OH^* + H^* \quad (14)$$
$$* + OH^* \leftrightarrow O^* + H^* \quad (15)$$
$$C^* + O^* \leftrightarrow CO^* + * \quad (16)$$
$$CO^* \leftrightarrow CO(g) + * \quad (17)$$
$$CH^* + O^* \leftrightarrow CHO^* + * \quad (18)$$
$$* + CHO^* \leftrightarrow CO^* + H^* \quad (19)$$

The reaction kinetics are given as follows:

$$R_6 = k_{6f}P_{CH_4}\theta^* - k_{6b}\theta_{CH_4}$$
$$R_7 = k_{7f}\theta_{CH_4}\theta^* - k_{7b}\theta_{CH_3}\theta_H$$
$$R_8 = k_{8f}\theta_{CH_3}\theta^* - k_{8b}\theta_{CH_2}\theta_H$$
$$R_9 = k_{9f}\theta_{CH_2}\theta^* - k_{9b}\theta_{CH}\theta_H$$
$$R_{10} = k_{10f}\theta_{CH}\theta^* - k_{10b}\theta_C\theta_H$$
$$R_{11} = k_{11f}\theta_H^2 - k_{11b}\theta_{H_2}\theta^*$$
$$R_{12} = k_{12f}\theta_{H_2} - k_{12b}P_{H_2}\theta^*$$
$$R_{13} = k_{13f}P_{H_2O}\theta^* - k_{13b}\theta_{H_2O}$$
$$R_{14} = k_{14f}\theta_{H_2O}\theta^* - k_{14b}\theta_{OH}\theta_H$$
$$R_{15} = k_{15f}\theta_{OH}\theta^* - k_{15b}\theta_O\theta_H$$
$$R_{16} = k_{16f}\theta_C\theta_O - k_{16b}\theta_{CO}\theta^*$$
$$R_{17} = k_{17f}\theta_{CO} - k_{17b}P_{CO}\theta^*$$
$$R_{18} = k_{18f}\theta_{CH}\theta_O - k_{18b}\theta_{CHO}\theta^*$$
$$R_{19} = k_{19f}\theta_{CHO}\theta^* - k_{19b}\theta_{CO}\theta_H$$

The authors observed that the at high temperatures of 873 K and low hydrogen pressure of less than 1 millibar, there is formation of

TABLE 5 Advanced reactors: Performance, advantages and limitations.

Type of reactor	Temperature (°C)	Methane conversion	H_2 recovery	H_2 mole fraction	Advantages	Limitations
Membrane Reactor (MR)	400–500	32%–84%	82%–99%	—	1, 2, 3, 4, 5, 6	7, 8, 9, 10
Tubular Packed Bed Micro Reactor (TPBMR)	600–1,000	18%–92%	—	<0.5	4, 11, 12, 13, 14, 15	16, 17, 18, 19
Micro-Reactor (MMR)	500–600	5%–90%	20%–95%	0.1–0.4	20, 21, 22, 23, 24	25, 26, 27, 28, 29
Plate Reformer (PR)	527–727	85%	—	0.1–0.2	4, 30, 31, 32	33, 34, 35
Catalytic Wall Reactor (CWR)	500–800	8%–90%	—	—	36, 37	—
Sorbtion-Enhanced methane steam reformers	350–500	10%–90%	25%–99%	0.10.35	38, 39	40, 41, 42

1 Low Energy Requirements 2 Low Space Requirements 3 Enhanced Yields and Selectivity 4 Low Capital Requirements 5 Low Temperature Requirements 6 High H_2 Recovery 7 Ineffectiveness in Scale-Up 8 Limited Life of Membrane 9 Performance Decrease because of fouling 10 High costs of Membrane 11 High Conversion Rate Per Weight of Catalyst 12 Easy to Build 13 Higher Contact Area 14 Higher efficiencies at high temperatures and pressures 15 Minimal side reactions 16 Difficult Temperature Control 17 Dead zones within the Reactor 18 Heat Transfer challenges within the Reactor 19 Difficulty in catalyst separation 20 Better Reaction Control 21 Less Hold-Up Volume 22 Enhanced yields 23 Higher Mixing Characteristics 24 Increased safety parameters 25 Difficult to scale-up 25 High Fabrication Cost 26 Clogging of the Reactor 27 Limited Reaction Time Range 28 Low Conversion 29 Low H_2 Recovery 30 Decrease in Performance because of precipitating products 31 Faster Start-Up 32 Compact Design 33 High heat transfer within the reactor 34 Extremely Sensitive to Carbon Deposition 35 High side reactions 36 Lower-Pressure Drop 37 Better Thermal Energy Management 38 No catalyst attrition 39 Process intensification with both carbon capture and hydrogen production in the same unit 40 Non-uniform temperature distribution in the catalyst bed 41 Decrease in hydrogen production with increase in WHSV for same geometric conditions 42 Difficulty to scale-up in a TPBMR. The recovery of H_2 is highest in an MR with the lowest being in an MMR. The side reactions are minimalist in a TPBMR. PR has the highest amounts of side reactions.

CH and O intermediates in very large amounts. This leads to coke formation. At the same time, at high hydrogen pressure and low temperature of 773 K, there is negligible amount of coke formation.

Studies have been done to diminish the coke formation effects (Ali et al., 2023).

5 Comparison between different novel reactors for hydrogen production using MSR

Table 5 summarizes the performance, advantages and limitations of the usage of several reactors. The salient features of each of the reactors have been described below:

Membrane Reactors have wide advantages like continuous production, and low energy and space requirements while giving enhanced yields and selectivity with reduced capital costs. Because of these reasons, the use of MR has increased for hydrogen production using MSR. MR has been found effective for H_2 production in a working temperature range of 400°C–500°C. Moreover, a higher conversion of 84% can be achieved using MSR. The recovery of the produced H_2 is also appreciable (≈98.7%). However, the use of MR has also certain limitations. The major limitation of an MR is the ineffectiveness of MR in scale-up. The performance of an MR decreases rapidly because of membrane fouling. Moreover, there is a requirement for high working capital investment because of the limited life of a membrane and the excessive costs of a membrane. However, integration of membranes with conventional fluidized and packed beds have shown positive results by some researchers and breakthroughs can be expected in the near future.

Tubular Packed Bed Micro Reactors are an easy-to-build reactor system with low capital investment. Moreover, on using TPBMR, there is a high conversion rate per weight of catalyst used. TPBMR also provides a high contact area. TPBMR has higher efficiencies at higher temperatures and pressures. TPBMRs are operative in a temperature range of 600°C–1,000°C. It also provides a conversion of 92%. MSR can also achieve a stream of high H_2 (mole fraction = 0.5) with very low side reactions. While it provides a high conversion, temperature control and heat transfer within the reactor are difficult. The catalyst is also difficult to separate.

Wall coated Micro Reactors (MIR) are an excellent reactor choice when the reaction requires higher mixing characteristics. MIR also has better reaction control and fewer hold-up volume requirements. The reactor has increased safety parameters with the best reagent usage. The scale-up of the reactor system is also achievable. A temperature range of 500°C–600°C is optimum for use of MIR. MIR can achieve a high conversion rate of 90% with an appreciable H_2 recovery of 95%. The stream can also possess a high amount of mole fraction of 0.4, limiting the side reactions. However, the fabrication cost of a reactor is high. The performance of an MIR is also highly affected by clogging and precipitating products. Also, the reaction time is low and hence the reaction should be falling within that particular range.

Plate Reformers have a compact design with a faster start-up. There is also higher heat transfer within the reactor simultaneously with low capital investment. PR has been effectively tested within a temperature range of 527°C–727°C. PR can achieve a high conversion of 85%. However, the side reactions can lead to a stream with low H_2 content (mole fraction = 0.1–0.2). PR is also highly sensitive to carbon deposition. Catalytic Wall Reactors have a small area requirement as the reactor system is smaller in size. CWR is the best reactor system for gaseous reactions because of the low-pressure drops. Thermal energy management is also excellent in a CWR. CWR can achieve a high conversion of up to 90% of methane.

Sorption Enhanced Methane steam Reformers have unique process intensification capabilities with an ability to produce hydrogen and capture carbon simultaneously due to the catalyst and sorbent particles present in the same catalyst bed. They also have a good operating temperature range and potential for high hydrogen recovery. The inherent difficulties of non-uniform temperature distribution due to simultaneous exothermic and endothermic reactions in the catalyst bed promote decrease in

hydrogen production at higher WHSV's. This is primarily one of the major hurdles for scale-up of these reactors.

6 Conclusion

Hydrogen production using both methane and methanol have been carried out for four major novel reactor systems. The following conclusions can be drawn based on their characteristics:

- Membrane Reactors gives higher conversions at lower temperatures with a combination of separation unit in themselves. They can also be integrated with conventional fixed or fluidized bed reactors. Hence, Membrane Reactors have the potential to be the most suitable reactors for hydrogen production using MSR except for the high capital and maintenance expenditure.
- Sorption Enhanced Methane Steam Reformers poses a very good process intensification method since the carbon separation happens in the catalyst bed which consists of catalyst and sorbent particles thus enhancing the reaction rate.
- Micro Reactors are found to be having optimized hydrogen production with an efficient hydrogen recovery. These have the advantages of low residence time, better thermal efficiencies, reaction control, high yields, and higher conversions.
- Nickel catalysts having different compositions of magnesium and alumina are found to have the potential for uniform dispersion on certain supports which can result in higher stability and lower sintering and coking. This has been seen as a cost-effective alternative to Rh catalysts. This is also preferred due to its ability to be coated on walls of micro-channels.
- Energy utilization in micro-reactors has been seen to be much better than conventional reactors due to non-necessity of steam export, less heat transfer, area requirement due to a decoupled requirement of reaction volume and heat transfer area.
- Micro-reactors (packed bed or wall coated) have an edge over other reactors due to their high yields and short residence times and have a high potential to be commercialized for lower volumes of hydrogen production
- Kinetic models for membrane reactors and Sorption enhanced type of reactors reported in literature are mostly chemisorption with surface reaction based LHHW kinetics. These largely depend on the catalyst used. The kinetics of MSR's in micro-reactors are not that widely available and have not been presented
- Coke formation mechanisms and their models available in the literature are able to explain the coke formation. Further, ways and means to suppress the formation is also available and reported
- Membrane reactors are difficult to scale-up due to the high cost and maintenance charges of membranes due to membrane fouling while Sorption enhanced reactors suffer from the non-uniform temperature distribution in the catalyst beds as the WHSV increases posing difficulties in scale-up. Micro-reactors have shown good potential for scale-up in cases of hydrogen production

7 Future work

A comprehensive review of hydrogen production with the variants like green hydrogen and gray hydrogen along with blue and black hydrogen would be taken up in future work. This would include details of research work carried on with different technologies like electrolysis of water.

Author contributions

Conceptualization, AG and VB; methodology, AG; formal analysis, VB; investigation, AG and VB; resources, AG; writing—original draft preparation, AG and VB; writing—review and editing, AG and VB; supervision, AG; project administration, AG; funding acquisition, AG. Both authors contributed to the article and approved the submitted version.

Conflict of interest

The authors declare that the research was conducted in the absence of any commercial or financial relationships that could be construed as a potential conflict of interest.

Publisher's note

References

Abanades, S., Kimura, H., and Otsuka, H. (2014). Hydrogen production from thermo-catalytic decomposition of methane using carbon black catalysts in an indirectly-irradiated tubular packed-bed solar reactor. *Int. J. hydrogen energy* 39, 18770–18783. doi:10.1016/j.ijhydene.2014.09.058

Adris, A., Elnashaie, S., and Hughes, R. (1991). A fluidized bed membrane reactor for the steam reforming of methane. *Can. J. Chem. Eng.* 69, 1061–1070. doi:10.1002/cjce.5450690504

Ali, S., Gamal, A., and Khader, M. M. (2023). Development of highly active and coke-resilient Ni-based catalysts for low-temperature steam reformation of methane. *Catal. Commun.*, 106605.

Antzaras, A. N., Heracleous, E., and Lemonidou, A. A. (2020). Sorption enhanced–chemical looping steam methane reforming: Optimizing the thermal coupling of regeneration in a fixed bed reactor. *Fuel Process. Technol.* 208, 106513. doi:10.1016/j.fuproc.2020.106513

Anzelmo, B., Wilcox, J., and Liguori, S. (2017). Natural gas steam reforming reaction at low temperature and pressure conditions for hydrogen production via Pd/PSS membrane reactor. *J. Membr. Sci.* 522, 343–350. doi:10.1016/j.memsci.2016.09.029

Ashraf, M. A., Tacchino, S., Peela, N. R., Ercolino, G., Gill, K. K., Vlachos, D. G., et al. (2020). Experimental insights into the coupling of methane combustion and steam reforming in a catalytic plate reactor in

transient mode. *Industrial Eng. Chem. Res.* 60, 196–209. doi:10.1021/acs.iecr.0c04837

Benson, R., and Ponton, J. (1993). Process miniaturisation: A route to total environmental acceptability? *Chem. Eng. Res. Des.* 71, 160–168.

Bernardo, G., Araújo, T., Da Silva Lopes, T., Sousa, J., and Mendes, A. (2020). Recent advances in membrane technologies for hydrogen purification. *Int. J. Hydrogen Energy* 45, 7313–7338. doi:10.1016/j.ijhydene.2019.06.162

Bernardo, P., Barbieri, G., and Drioli, E. (2010). Evaluation of membrane reactor with hydrogen-selective membrane in methane steam reforming. *Chem. Eng. Sci.* 65, 1159–1166. doi:10.1016/j.ces.2009.09.071

Bhat, S. A., and Sadhukhan, J. (2009). Process intensification aspects for steam methane reforming: An overview. *AIChE J.* 55, 408–422. doi:10.1002/aic.11687

Bouwmeester, H. J. (2003). Dense ceramic membranes for methane conversion. *Catal. today* 82, 141–150. doi:10.1016/s0920-5861(03)00222-0

Cai, F., Lu, P., Ibrahim, J. J., Fu, Y., Zhang, J., and Sun, Y. (2019). Investigation of the role of Nb on Pd– Zr– Zn catalyst in methanol steam reforming for hydrogen production. *Int. J. Hydrogen Energy* 44, 11717–11733. doi:10.1016/j.ijhydene.2019.03.125

Cao, L., Lu, M., Li, G., and Zhang, S. (2019). Hydrogen production from methanol steam reforming catalyzed by Fe modified Cu supported on attapulgite clay. *React. Kinet. Mech. Catal.* 126, 137–152. doi:10.1007/s11144-018-1493-y

Charisiou, N. D., Siakavelas, G., Tzounis, L., Dou, B., Sebastian, V., Hinder, S. J., et al. (2020). Ni/Y2O3–ZrO2 catalyst for hydrogen production through the glycerol steam reforming reaction. *Int. J. Hydrogen Energy* 45, 10442–10460. doi:10.1016/j.ijhydene.2019.04.237

Charisiou, N., Papageridis, K., Siakavelas, G., Sebastian, V., Hinder, S., Baker, M., et al. (2019). The influence of SiO2 doping on the Ni/ZrO2 supported catalyst for hydrogen production through the glycerol steam reforming reaction. *Catal. Today* 319, 206–219. doi:10.1016/j.cattod.2018.04.052

Chen, D., Bjørgum, E., Lødeng, R., Christensen, K. O., and Holmen, A. (2004). "Microkinetic model assisted catalyst design for steam methane reforming," in *Studies in surface science and catalysis* (Elsevier), 139–144.

Chen, J., Song, W., and Xu, D. (2019). Compact steam-methane reforming for the production of hydrogen in continuous flow microreactor systems. *ACS omega* 4, 15600–15614. doi:10.1021/acsomega.9b02063

Chen, K., Zhao, Y., Zhang, W., Feng, D., and Sun, S. (2020). The intrinsic kinetics of methane steam reforming over a nickel-based catalyst in a micro fluidized bed reaction system. *Int. J. Hydrogen Energy* 45, 1615–1628. doi:10.1016/j.ijhydene.2019.11.080

Chen, M., Liang, D., Wang, Y., Wang, C., Tang, Z., Li, C., et al. (2021). Hydrogen production by ethanol steam reforming over M-Ni/sepiolite (M= La, Mg or Ca) catalysts. *Int. J. Hydrogen Energy* 46, 21796–21811. doi:10.1016/j.ijhydene.2021.04.012

Chompupun, T., Limtrakul, S., Vatanatham, T., Kanhari, C., and Ramachandran, P. A. (2018). Experiments, modeling and scaling-up of membrane reactors for hydrogen production via steam methane reforming. *Chem. Eng. Processing-Process Intensif.* 134, 124–140. doi:10.1016/j.cep.2018.10.007

Dams, R., Moore, S., and Hayter, P. (2000). "Compact, fast response methanol fuel processing systems for PEMFC electric vehicles," in Fuel cell seminar), 526–529.

De Deken, J., Devos, E., and Froment, G. (1982). "Steam reforming of natural gas: intrinsic kinetics, diffusional influences, and reactor design," in *Chemical Reaction Engineering–Boston* (Boston: ACS Publications).

Delsman, E., Laarhoven, B., De Croon, M., Kramer, G., and Schouten, J. (2005). Comparison between conventional fixed-bed and microreactor technology for a portable hydrogen production case. *Chem. Eng. Res. Des.* 83, 1063–1075. doi:10.1205/cherd.04260

Di Giuliano, A., Gallucci, K., Di Carlo, A., Stendardo, S., Courson, C., and Foscolo, P. U. (2020). Sorption enhanced steam methane reforming by Ni/CaO/mayenite combined systems: Overview of experimental results from E uropean research project ASCENT. *Can. J. Chem. Eng.* 98, 1907–1923. doi:10.1002/cjce.23779

Dietrich, W., Lawrence, P. S., Grünewald, M., and Agar, D. W. (2005). Theoretical studies on multifunctional catalysts with integrated adsorption sites. *Chem. Eng. J.* 107, 103–111. doi:10.1016/j.cej.2004.12.016

Dong, H., Shao, Z., Xiong, G., Tong, J., Sheng, S., and Yang, W. (2001). Investigation on POM reaction in a new perovskite membrane reactor. *Catal. Today* 67, 3–13. doi:10.1016/s0920-5861(01)00277-2

Elnashaie, S. S. (1994). *Modelling, Simulation and Optimization of Industrial Fixed Bed Catalytic Reactors*. London: CRC Press.

Endou, A., Jung, C., Kusagaya, T., Kubo, M., Selvam, P., and Miyamoto, A. (2004). Combinatorial computational chemistry approach to the design of metal catalysts for deNOx. *Appl. Surf. Sci.* 223, 159–167. doi:10.1016/s0169-4332(03)00913-9

Fasanya, O. O., Al-Hajri, R., Ahmed, O. U., Myint, M. T., Atta, A. Y., Jibril, B. Y., et al. (2019). Copper zinc oxide nanocatalysts grown on cordierite substrate for hydrogen production using methanol steam reforming. *Int. J. Hydrogen Energy* 44, 22936–22946. doi:10.1016/j.ijhydene.2019.06.185

Fukuda, T., Harada, M. R., Ookawara, S., Hamzah, A. B., Yoshikawa, S., and Matsumoto, H. (2021). Double-layered catalytic wall-plate microreactor for process intensification of dry reforming of methane: Reaction activity improvement and coking suppression. *Chem. Eng. Processing-Process Intensif.* 164, 108406. doi:10.1016/j.cep.2021.108406

Gaudernack, B. (1998). Hydrogen production from fossil fuels. *Hydrogen power Theor. Eng. solutions*, 75–89. doi:10.1007/978-94-015-9054-9_10

Greluk, M., Rotko, M., and Turczyniak-Surdacka, S. (2020). Enhanced catalytic performance of La2O3 promoted Co/CeO2 and Ni/CeO2 catalysts for effective hydrogen production by ethanol steam reforming. *Renew. Energy* 155, 378–395. doi:10.1016/j.renene.2020.03.117

Hafeez, S., Al-Salem, S., Manos, G., and Constantinou, A. (2020). Fuel production using membrane reactors: A review. *Environ. Chem. Lett.* 18, 1477–1490. doi:10.1007/s10311-020-01024-7

Huang, C., Yu, Y., Tang, X., Liu, Z., Zhang, J., Ye, C., et al. (2020). Hydrogen generation by ammonia decomposition over Co/CeO2 catalyst: Influence of support morphologies. *Appl. Surf. Sci.* 532, 147335. doi:10.1016/j.apsusc.2020.147335

Huang, C., Yu, Y., Yang, J., Yan, Y., Wang, D., Hu, F., et al. (2019). Ru/La2O3 catalyst for ammonia decomposition to hydrogen. *Appl. Surf. Sci.* 476, 928–936. doi:10.1016/j.apsusc.2019.01.112

Huang, K., Zhan, X.-L., Chen, F.-Q., and Lü, D.-W. (2003). Catalyst design for methane oxidative coupling by using artificial neural network and hybrid genetic algorithm. *Chem. Eng. Sci.* 58, 81–87. doi:10.1016/s0009-2509(02)00432-3

Huang, W.-J., Yu, C.-T., Sheu, W.-J., and Chen, Y.-C. (2021a). The effect of non-uniform temperature on the sorption-enhanced steam methane reforming in a tubular fixed-bed reactor. *Int. J. Hydrogen Energy* 46, 16522–16533. doi:10.1016/j.ijhydene.2020.07.182

Huang, Y., Zhang, Z., Wei, W., Long, Y., and Li, G. (2021b). Experimental study on characteristics of hydrogen production from exhaust gas-fuel reforming in a catalytic fixed-bed reactor. *Fuel* 290, 120068. doi:10.1016/j.fuel.2020.120068

Hufton, J., Mayorga, S., and Sircar, S. (1999). Sorption-enhanced reaction process for hydrogen production. *AIChE J.* 45, 248–256. doi:10.1002/aic.690450205

Irankhah, A., Rahimi, M., and Rezaei, M. (2014). Performance research on a methane compact reformer integrated with catalytic combustion. *Chem. Eng. Technol.* 37, 1220–1226. doi:10.1002/ceat.201300469

Itoh, N., Kikuchi, Y., Furusawa, T., and Sato, T. (2021). Tube-wall catalytic membrane reactor for hydrogen production by low-temperature ammonia decomposition. *Int. J. Hydrogen Energy* 46, 20257–20265. doi:10.1016/j.ijhydene.2020.03.162

Iulianelli, A., Liguori, S., Wilcox, J., and Basile, A. (2016). Advances on methane steam reforming to produce hydrogen through membrane reactors technology: A review. *Catal. Rev.* 58, 1–35. doi:10.1080/01614940.2015.1099882

Kamyar, N., Khani, Y., Amini, M. M., Bahadoran, F., and Safari, N. (2019). Embedding Pt-SnO nanoparticles into MIL-101 (Cr) pores: Hydrogen production with low carbon Monoxide content from a new methanol steam reforming catalyst. *ChemistrySelect* 4, 6113–6122. doi:10.1002/slct.201901071

Katheria, S., Kunzru, D., and Deo, G. (2020). Kinetics of steam reforming of methane on Rh–Ni/MgAl2O4 catalyst. *React. Kinet. Mech. Catal.* 130, 91–101. doi:10.1007/s11144-020-01767-y

Khani, Y., Bahadoran, F., Safari, N., Soltanali, S., and Taheri, S. A. (2019). Hydrogen production from steam reforming of methanol over Cu-based catalysts: The behavior of ZnxLaxAl1-xO4 and ZnO/La2O3/Al2O3 lined on cordierite monolith reactors. *Int. J. hydrogen energy* 44, 11824–11837. doi:10.1016/j.ijhydene.2019.03.031

Kiani, M. R., Meshksar, M., Makarem, M. A., and Rahimpour, E. (2021). Catalytic membrane micro-reactors for fuel and biofuel processing: A mini review. *Top. Catal.*, 1–20. doi:10.1007/s11244-021-01505-1

Kim, C.-H., Han, J.-Y., Lim, H., Lee, K.-Y., and Ryi, S.-K. (2018). Methane steam reforming using a membrane reactor equipped with a Pd-based composite membrane for effective hydrogen production. *Int. J. Hydrogen Energy* 43, 5863–5872. doi:10.1016/j.ijhydene.2017.10.054

Kim, J. H., Jang, Y. S., Kim, J. C., and Kim, D. H. (2019). Anodic aluminum oxide supported Cu-Zn catalyst for oxidative steam reforming of methanol. *Korean J. Chem. Eng.* 36, 368–376. doi:10.1007/s11814-018-0211-9

Lian, H.-Y., Liu, J.-L., Li, X.-S., Zhu, X., Weber, A. Z., and Zhu, A.-M. (2019). Plasma chain catalytic reforming of methanol for on-board hydrogen production. *Chem. Eng. J.* 369, 245–252. doi:10.1016/j.cej.2019.03.069

Lou, Y., Smith, R., and Sadhukhan, J. (2008). "Decarbonisation in process sites", in: *2008 AIChE spring national meeting, conference proceedings*).

Lytkina, A., Mironova, E. Y., Orekhova, N., Ermilova, M., and Yaroslavtsev, A. (2019a). Ru-containing catalysts for methanol and ethanol steam reforming in conventional and membrane reactors. *Inorg. Mater.* 55, 547–555. doi:10.1134/s0020168519060104

Lytkina, A., Orekhova, N., Ermilova, M., Petriev, I., Baryshev, M., and Yaroslavtsev, A. (2019b). RuRh based catalysts for hydrogen production via methanol steam reforming

in conventional and membrane reactors. *Int. J. hydrogen energy* 44, 13310–13322. doi:10.1016/j.ijhydene.2019.03.205

Mcleod, A., Johnston, M., and Gladden, L. (1997). Development of a genetic algorithm for molecular scale catalyst design. *J. Catal.* 167, 279–285. doi:10.1006/jcat.1997.1565

Mohtashami, Y., and Taghizadeh, M. (2019). Performance of the ZrO2 promoted CuZnO catalyst supported on acetic acid-treated MCM-41 in methanol steam reforming. *Int. J. Hydrogen Energy* 44, 5725–5738. doi:10.1016/j.ijhydene.2019.01.029

Niu, J., Wang, Y., Qi, Y., Dam, A. H., Wang, H., Zhu, Y.-A., et al. (2020). New mechanism insights into methane steam reforming on Pt/Ni from DFT and experimental kinetic study. *Fuel* 266, 117143. doi:10.1016/j.fuel.2020.117143

Önsan, Z. I., and Avci, A. K. (2011). "Reactor design for fuel processing," in *Fuel cells: Technologies for fuel processing* (Elsevier), 451–516.

Parvasi, P., Jokar, S., Shamseddini, A., Babapoor, A., Mirzaie, F., Abbasfard, H., et al. (2020). A novel recovery loop for reducing greenhouse gas emission: Simultaneous production of syngas and pure hydrogen in a membrane reformer. *Renew. Energy* 153, 130–142. doi:10.1016/j.renene.2020.01.147

Pashchenko, D., Mustafin, R., and Mustafina, A. (2021). Steam methane reforming in a microchannel reformer: Experiment, CFD-modelling and numerical study. *Energy* 237, 121624. doi:10.1016/j.energy.2021.121624

Qingli, X., Zhengdong, Z., Kai, H., Shanzhi, X., Chuang, M., Chenge, C., et al. (2021). Ni supported on MgO modified attapulgite as catalysts for hydrogen production from glycerol steam reforming. *Int. J. Hydrogen Energy* 46, 27380–27393. doi:10.1016/j.ijhydene.2021.06.028

Rusu, I., and Cormier, J.-M. (2003). On a possible mechanism of the methane steam reforming in a gliding arc reactor. *Chem. Eng. J.* 91, 23–31. doi:10.1016/s1385-8947(02)00043-8

Saidi, M., and Moradi, P. (2020). Conversion of biodiesel synthesis waste to hydrogen in membrane reactor: Theoretical study of glycerol steam reforming. *Int. J. Hydrogen Energy* 45, 8715–8726. doi:10.1016/j.ijhydene.2020.01.064

Sarafraz, M., Safaei, M. R., Goodarzi, M., and Arjomandi, M. (2019). Reforming of methanol with steam in a micro-reactor with Cu–SiO2 porous catalyst. *Int. J. Hydrogen Energy* 44, 19628–19639. doi:10.1016/j.ijhydene.2019.05.215

Seki, T., Komiya, J., Fujiki, H., Shirasaki, Y., Inoue, K., Miura, T., et al. (2000). "(Year) development of fuel processing systems for PEFC residential stationary application," in Fuel cell seminar abstract), 376–379.

Sheintuch, M., and German, E. D. (2021). Permeance inhibition due to reaction, coking and leakage of Pd membranes during methane steam reforming estimated from a micro-kinetic model. *Chem. Eng. J.* 411, 128272. doi:10.1016/j.cej.2020.128272

Shtyka, O., Higashino, Y., Kedziora, A., Dubkov, S., Gromov, D., and Maniecki, T. (2018). Monometallic Ru, Au, and Pt catalysts deposited on carbon nanotubes for oxidative steam reforming of methanol. *Fibre Chem.* 50, 301–305. doi:10.1007/s10692-019-09980-9

Simsek, E., Avci, A. K., and Önsan, Z. I. (2011). Investigation of catalyst performance and microstructured reactor configuration for syngas production by methane steam reforming. *Catal. today* 178, 157–163. doi:10.1016/j.cattod.2011.08.021

Soliman, M., El-Nashaie, S., Al-Ubaid, A., and Adris, A. (1988). "Simulation of steam reformers for methane," in *Tenth international symposium on chemical reaction engineering* (Elsevier), 1801–1806.

Stankiewicz, A. I., and Moulijn, J. A. (2004). *Re-engineering the Chemical Processing Plant: Process Intensification*. Boca Raton: M. Dekker.

Stenina, I., and Yaroslavtsev, A. (2022). Modern technologies of hydrogen production. *Processes* 11, 56.

Stutz, M. J., Hotz, N., and Poulikakos, D. (2006). Optimization of methane reforming in a microreactor—Effects of catalyst loading and geometry. *Chem. Eng. Sci.* 61, 4027–4040. doi:10.1016/j.ces.2006.01.035

Thursfield, A., and Metcalfe, I. S. (2004). The use of dense mixed ionic and electronic conducting membranes for chemical production. *J. Mater. Chem.* 14, 2475–2485. doi:10.1039/b405676k

Tong, J., Matsumura, Y., Suda, H., and Haraya, K. (2005). Thin and dense Pd/CeO2/MPSS composite membrane for hydrogen separation and steam reforming of methane. *Sep. Purif. Technol.* 46, 1–10. doi:10.1016/j.seppur.2005.03.011

Tonkovich, A. L. Y., Yang, B., Perry, S. T., Fitzgerald, S. P., and Wang, Y. (2007). From seconds to milliseconds to microseconds through tailored microchannel reactor design of a steam methane reformer. *Catal. Today* 120, 21–29. doi:10.1016/j.cattod.2006.07.022

Tonkovich, A., Perry, S., Wang, Y., Qiu, D., Laplante, T., and Rogers, W. A. (2004). Microchannel process technology for compact methane steam reforming. *Chem. Eng. Sci.* 59, 4819–4824. doi:10.1016/j.ces.2004.07.098

Trimm, D. L. (1997). Coke formation and minimisation during steam reforming reactions. *Catal. Today* 37, 233–238. doi:10.1016/s0920-5861(97)00014-x

Veziroglu, T., and Barbir, F. (1998). "Emerging technology series, hydrogen energy technologies," in *Tech. rep.* (Vienna): United Nations Industrial Development Organization).

Wang, F., Zhang, L., Deng, J., Zhang, J., Han, B., Wang, Y., et al. (2019). Embedded Ni catalysts in Ni-O-Ce solid solution for stable hydrogen production from ethanol steam reforming reaction. *Fuel Process. Technol.* 193, 94–101. doi:10.1016/j.fuproc.2019.05.004

Yang, W.-S., Xiang, H.-W., Li, Y.-W., and Sun, Y.-H. (2000). Micro-kinetic analysis and Monte Carlo simulation in methane partial oxidation into synthesis gas. *Catal. today* 61, 237–242. doi:10.1016/s0920-5861(00)00368-0

Yuan, J., Ren, F., and Sundén, B. (2007). Analysis of chemical-reaction-coupled mass and heat transport phenomena in a methane reformer duct for PEMFCs. *Int. J. Heat Mass Transf.* 50, 687–701. doi:10.1016/j.ijheatmasstransfer.2006.07.005

Yuan, Q., Gu, R., Ding, J., and Lu, J. (2017). Heat transfer and energy storage performance of steam methane reforming in a tubular reactor. *Appl. Therm. Eng.* 125, 633–643. doi:10.1016/j.applthermaleng.2017.06.044

Zanfir, M., and Gavriilidis, A. (2003). Catalytic combustion assisted methane steam reforming in a catalytic plate reactor. *Chem. Eng. Sci.* 58, 3947–3960. doi:10.1016/s0009-2509(03)00279-3

Zeng, Z., Liu, G., Geng, J., Jing, D., Hong, X., and Guo, L. (2019). A high-performance PdZn alloy catalyst obtained from metal-organic framework for methanol steam reforming hydrogen production. *Int. J. Hydrogen Energy* 44, 24387–24397. doi:10.1016/j.ijhydene.2019.07.195

Zhai, X., Ding, S., Liu, Z., Jin, Y., and Cheng, Y. (2011). Catalytic performance of Ni catalysts for steam reforming of methane at high space velocity. *Int. J. hydrogen energy* 36, 482–489. doi:10.1016/j.ijhydene.2010.10.053

Nomenclature

Alphabetical letters

C_i Concentration of Species i $molm^{-3}$

ΔG_i° Standard Gibbs Free Energy for Reaction i $Jmol^{-1}$

K_i Equilibrium Constant for Reaction i -

K_j, $K_j^{'}$ Rate Constant for Species j -

M_i Molecular Weight of Species i $gmol^{-1}$

P_i Partial Pressure of Species i Pa

R Gas Constant $Jmol^{-1}K^{-1}$

R_i Rate of Reaction for Reaction i $molm^{-3}s^{-1}$

T Temperature K

V_i Volume of Species i m^3

X Sorbent Conversion -

Z Volume Comparison Parameter -

a, b Fitting Parameters -

k_i, $k_i^{'}$, $k_i^{''}$ Rate Constant for Reaction i -

k_{if} Forward Reaction Rate Constant for Reaction i -

k_{ib} Backward Reaction Rate Constant for Reaction i -

Greek alphabets

θ_i Correction Due to Competitive Adsorption for Species i -

δ_i Average Diameter of Species i m

ρ_i Density of Species i kgm^{-3}

Subscripts

C Specific to Carbon

CH_4 Specific to Methane

CH_3 Specific to CH_3 activated complex

CH_2 Specific to CH_2 activated complex

CH Specific to CH activated complex

CHO Specific to CHO activated complex

CO Specific to Carbon Monoxide

CO_2 Specific to Carbon Dioxide

$CaCO_3$ Specific to Calcium Carbonate

CaO Specific to Calcium Oxide

H Specific to H activated complex

H_2 Specific to Hydrogen

H_2O Specific to Water

O Specific to O activated complex

OH Specific to OH activated complex

Aeq Specific to Species A at Equilibrium

As Specific to Species A at the Surface

PL Product Layer

Superscripts

* Permeate Conditions

frontiers | Frontiers in Energy Research

TYPE Original Research
PUBLISHED 07 July 2023
DOI 10.3389/fenrg.2023.1150943

OPEN ACCESS

EDITED BY
Abdolali K. Sadaghiani,
Sabancı University, Türkiye

REVIEWED BY
Miryan Celeste Cassanello,
University of Buenos Aires, Argentina
Chenlong Duan,
China University of Mining and Technology, China

*CORRESPONDENCE
Arijit Ganguli,
ganguliarijit@gmail.com

RECEIVED 25 January 2023
ACCEPTED 22 May 2023
PUBLISHED 07 July 2023

CITATION
Ganguli A and Bhatt V (2023), CFD simulations to study bed characteristics in gas–solid fluidized beds with binary mixtures of Geldart B particles: II quantitative analysis.
Front. Energy Res. 11:1150943.
doi: 10.3389/fenrg.2023.1150943

CFD simulations to study bed characteristics in gas–solid fluidized beds with binary mixtures of Geldart B particles: II quantitative analysis

Arijit Ganguli* and Viraj Bhatt

School of Engineering and Applied Science, Ahmedabad University, Ahmedabad, India

Hydrodynamics of fluidized beds with binary mixtures of particles is important in many industrial applications. The binary particles are generally in the Geldart particle range. In our earlier work, (Part I) of this work simulations were carried out and qualitative analysis was presented. Quantitative predictions of gas velocity and particle velocity profiles have been presented in the present work, which is Part II of the two-part work on computational fluid dynamics (CFD) simulations of binary fluidized beds. It was observed that the dynamics of the bed vary for different binary mixtures and are a strong function of superficial velocity and bed height. Mixing and segregation in beds for two different initial bed heights and six different binary mixtures and superficial velocities have been identified. Segregation is prominent for binary mixtures with 20 wt.% and 80 wt.% of large particles, whereas mixing is observed in 40 wt.% and 60 wt.% large particle mixtures. Bypassing of gas near the walls is prominently seen for 60 wt.% large particles with gas velocities as high as 5 m/s. Time-averaged axial particle volume fractions have been observed to be lower in the dilute phase with large undulations in the middle whenever the bed is well mixed for central axial profiles. The axial volume fraction profiles also confirm the mixing and segregation for the 40 wt.% and 20 wt.% composition of large particles for the operating conditions considered for the study. Bed height expansion is linear until a certain superficial velocity with the increase or decrease depending on the superficial velocity or bed height of operation. Furthermore, correlations for minimum fluidization velocity and pressure drops from the literature have been compared with experimental results. The simulated data have been considered for the development of a correlation for minimum fluidization velocity. The predicted results match experimental data with a 10%–15% deviation.

KEYWORDS

fluidized bed, binary mixtures, computational fluid dynamics modeling, minimum fluidization gas velocity, KTGF model, pressure drop, hydrodynamics

1 Introduction

Fluidized beds are one of the most important multiphase reactors having gas–solid, liquid–solid, or gas–liquid–solid flows. Some of the most common applications of fluidization include catalytic cracking and coal gasification. Hydrodynamics is critical for the good performance of fluidized beds because it involves spatial and temporal variation of

the phases that affect the transport phenomena (heat and mass transfer characteristics). While unary fluidized beds have been extensively studied for many decades, binary fluidized beds continue to interest researchers. With the advent of computational fluid dynamics (CFD) and advanced experimental techniques to measure velocity and volume fraction distributions of both phases, researchers have conducted interesting studies on binary fluidized beds. Furthermore, an important aspect in binary particle-based fluidized beds is that the minimum fluidization velocity varies non-linearly with bottom or top particles in contrast to a uniformly sized bed, and the particle velocity increases with an increase in the superficial velocity. A comprehensive literature review on the work carried out by the various authors using experimental techniques (Čársky et al., 1987; Hoffmann et al., 1993; Chehbouni et al., 1994; Gauthier et al., 1999; Leu and Wu, 2000; Harris et al., 2002; Ellis et al., 2004; Chew et al., 2010; Mazzei et al., 2010; Rao et al., 2010; Jayarathna and Halvorsen, 2011; Sau and Biswal, 2011; Di Maio et al., 2012; Obuseh et al., 2012; Lan et al., 2014; Philippsen et al., 2015; Leion et al., 2018; Menéndez et al., 2019; Penn et al., 2019; Chew and Cocco, 2021; Emiola-Sadiq et al., 2021; Gupta and De, 2021) and mathematical modeling/CFD (Cooper and Coronella, 2005; Du et al., 2006; Gao et al., 2009; Pei et al., 2010; Zaabout et al., 2010; Chang et al., 2012; Mostafazadeh et al., 2013; Benzarti et al., 2014; Sahoo and Sahoo, 2016; Bakshi et al., 2017; Agrawal et al., 2018; Chang et al., 2019; Daryus et al., 2019; Khezri et al., 2019; Shrestha et al., 2019; Kotoky et al., 2020) has been presented in Part I of our work (Ganguli and Bhatt, 2023). In Part II (the present work), the major focus is to understand the prominent experimental works dealing with the gas and particle velocity distribution across the bed, along with prominent correlations on minimum fluidization velocity and pressure drop for binary fluidized beds in the published literature.

With the advent of the 21st century, researchers (Zhang et al., 2006) emphasized the need for studies on the bed dynamics of the Geldart B type of particles and binary mixtures. Furthermore, experimental studies on binary mixtures gained importance at the end of the 20th century (Noda et al., 1986; Chyang et al., 1989) because the bed dynamics differed from the single-particle beds. In fluidized beds with binary systems, the fraction that mostly forms the top layer of the bed or the one that floats is called the flotsam, and the one at the bottom layer or the one that sinks is called the jetsam. A major challenge in binary systems is that the beds reach equilibrium with either mixing or segregation of particles as two extremes. In applications like coal gasification, where synthetic gas (syngas) is the desired output, the segregation of particles may lead to the coal particles remaining unreacted, reducing the syngas yield (Roy et al., 2021). Furthermore, segregation is observed when binary mixtures of particles with varying densities are present in the bed, whereas mixing is observed when mixtures of varying sizes are present. In such beds, the bubbles rise through the center of the bed, and the rise velocity of the bubbles increases with the superficial velocity of the gas. Recently, interesting and significant progress in studies on bed dynamics of binary fluidized beds using experimental techniques for bubbling fluidized beds related to velocity distribution of bubble and solid particles (both flotsam and jetsam) have been carried out (Zhang et al., 2017; Kalo et al., 2019; Singh et al., 2019; Roy et al., 2021). The bed dynamics of fluidized beds with binary mixtures have been studied by advanced experimental techniques that include non-intrusive techniques like 1. electrical capacitance tomography (ECT) (Singh et al., 2019), 2. radioactive particle tracking (RPT) (Roy et al., 2021), 3. digital image analysis, 4. magnetic resonance imaging (MRI), and 5. positron emission particle tracking and intrusive techniques like 1. pressure probes for measuring pressure drops and quality of fluidization and 2. optical probes for measuring particle diameter, particle velocity, etc.

1.1 Experimental studies on fluidized beds involving unary and binary systems

Hoffmann et al. (1993) carried out experimental investigations in binary mixtures to study mixing and segregation behavior. A new empirical correlation was developed for bubble wake angles for Geldart B particles. The rate of material interchange between the wake of a rising bubble and the surrounding bubbles is independent of minimum fluidization velocity. The authors modeled mixing/segregation behavior in binary systems.

Singh et al. (2019) carried out mixing and segregation studies for unary and binary beds using ECT measurements to understand the temporal particle velocity and bubble size distribution in binary beds. The authors investigated the effect of different parameters like the same and different size ratios, namely, 96 μm, 430 μm, 922 μm, and 3,500 μm, on the hydrodynamics of beds with binary mixtures and unary beds of particle sizes 96 μm and 922 μm. The gas superficial velocity was varied in the range of 0.006–0.684 m/s. The authors found extremely novel and interesting facts on the dynamics of beds with binary mixtures in transient situations and segregating beds. Some salient features revealed were the characterization of segregated regions in the bed large diameter ratios (96 μm and 922 μm), the effect of bubbling behavior on segregation, and the effects of gas velocity and mixture composition on transient segregation of binary beds. The authors also found the importance of a higher amount of smaller particles in the reduction of segregation in beds. According to the authors, the data provided by their study would be helpful in building robust Eulerian–Eulerian CFD models for predicting dynamics of segregation and mixing in unary and binary fluidized beds.

Kalo et al. (2019) studied the dynamics of unary and binary fluidized conical beds using RPT composed of particle sizes of 0.6 and 1 mm, respectively. The authors found interesting results in terms of gas–solid and particle–particle interactions in conical beds using time-averaged quantities (mean and rms velocities). One of the major findings was the ability of conical beds to provide better mixing even at lower superficial velocities compared to cylindrical beds. Furthermore, the authors observed that gas–solid interactions played a vital role at the bottom while particle–particle interactions played an important role at the top in the dynamics of binary conical beds with 50–50 wt.% composition.

Gupta and De (2021) performed experimental measurements for a dual fluidized bed under a fast fluidization regime. The authors found that poly-disperse binary mixtures have different pressure profiles than unary (uniformly sized) sand particles with narrow particle size distribution. Segregation is high in the bubbling fluidized bed riser and decreases with increases in superficial velocities. Furthermore, the authors highlighted the influence of

pressure drop on poly-disperse mixtures and presented an analytical model to justify their results. The authors also found that the trends of pressure drop with an increase in superficial velocities were similar to those of bubbling fluidized beds.

Roy et al. (2021) carried out experimental investigations to study bed dynamics in a binary fluidized bed with different particle sizes (0.5 and 2 mm sized particles). The authors found that with an increase in the 2 mm fraction from 10 wt.% to 40 wt.%, the computed bubble-rise velocity decreased, which in turn caused a decrease in the velocity of particles. This is in contrast to the results for a bed of uniformly sized particles (also termed a unary bed), where the influence of superficial velocity on bubble diameter and rise velocity has an increasing trend (Penn et al., 2019). In unary beds, as the ratio of superficial velocity (U_{gs}) to minimum superficial velocity (U_{mf}) increased from 1 to 3, a corresponding increase in bubble-rise velocity was observed. For a particle diameter of 0.5 mm, the difference in particle velocity at the center increased, while when a coarser fraction was added to 0.5 mm particles, the bubble-rise velocities decreased. The authors also investigated the axial velocity profiles for both particles and gas. For lower superficial velocities, the axial velocities of the particles were fully developed while having an inversion near the walls. With the increase in the coarse fraction of particles, the authors observed an increase in particle velocities. The authors emphasize that the data for velocity distribution are not available for binary/polydisperse beds.

1.2 Objective of the present work

The following points have been deduced from the literature review: 1. few numerical investigations on velocity and volume fraction distributions of both phases in binary fluidized beds exist, while experimental data for binary systems for bubbling fluidized beds are available using RPT and ECT. 2. Researchers have found that more than a 50 wt.% presence of small particles in a binary mixture caused changes in the axial profiles of particle holdup and abrupt changes in the bed height at the final steady state. 3. Few correlations predict minimum fluidization velocity and pressure drop for binary mixtures and Geldart B particles.

This study envisages the following numerical simulations using six different binary mixtures: 1. Characterization of the bubbling fluidized bed in terms of time-averaged mean gas and particle velocities (of both small and large particle sizes) in the bottom, middle, and dilute zones. 2. Characterization of bed dynamics in terms of time-averaged solid holdup in the axial direction. 3. Investigation of the effect of operating parameters like superficial velocity and initial bed height on bed dynamics (minimum fluidization velocity and pressure drop). 4. Development of correlations for minimum fluidization velocity and pressure drop for binary systems.

2 Numerical modeling

2.1 Models

Two-phase modeling has been performed using the Eulerian–Eulerian multiphase model coupled with an RNG k–ε model. The Syamlal et al. (1993) model was used for the modeling of granular viscosity, while the Syamlal and O'Brien (1987) model was used for modeling the drag of the system. The Schaeffer (1987) model (Schaeffer model) was used for simultaneous calculations of frictional pressure and viscosity. Granular bulk viscosity was modeled by the Lun et al. (1984) model; the Ahmadi and Ma (1990) model was used for simultaneous modeling of solids pressure and radial distribution. All the models and governing equations and various other parameters were kept the same in Ansys Fluent 18.1. A detailed description can be found in Ganguli and Bhatt (2023).

2.2 Geometry details

A 3D cylindrical geometry of height 1.4 m and diameter of 0.072 m was chosen for simulations. Figure 1A shows the 2D schematic of the geometry created in Ansys Fluent 18.1. Three different radial positions were used for collection of data, as shown in Figure 1A.

2.3 Material properties

Air as a fluid phase with a combination of glass particles as a solid phase is used in the system. The density of air is 1.22 kgm^{-3}, and the dynamic viscosity is 0.000017 $kgm^{-1}s^{-1}$. The glass particles have a varying diameter between 154 μm (fine particles) and 488 μm (large particles) (with a size ratio of 3.2) based on the percentage of large particles in the mixture. The density of glass particles is 2,485 kgm^{-3}, and the dynamic viscosity is 0.00082 $kgm^{-1}s^{-1}$. The phase properties have also been used for simulation purposes by Jayarathna and Halvorsen (2011).

2.4 Grid sensitivity

Figure 2 shows the radial gas velocity profile at Position 2 of Figure 1A for three different meshes. The mesh elements are as follows: Mesh 1 has 173,040 elements, Mesh 2 has 267,786 elements, and Mesh 3 has 497,568 elements. As the mesh number increases, the mesh refinement near the wall also increases. The error between Mesh 1 and Mesh 2 is 10%, while that between Mesh 2 and Mesh 3 is 2%. Therefore, Mesh 2 was used for further simulations. Figure 1A shows axial and radial views of Mesh 2. The mesh used is the same as the one used by Ganguli and Bhatt (2023).

2.5 Simulation details

The solution method for all the simulations is the same as our previous work (Ganguli and Bhatt, 2023). Only a brief description is provided. The convergence criterion was kept as 10^{-3} for the continuity equation and 10^{-4} for the other equations. A first-order implicit scheme was used for the transient formations. Pressure–velocity coupling was achieved using the phase-coupled SIMPLE scheme. For the calculations of volume fraction, momentum, turbulent

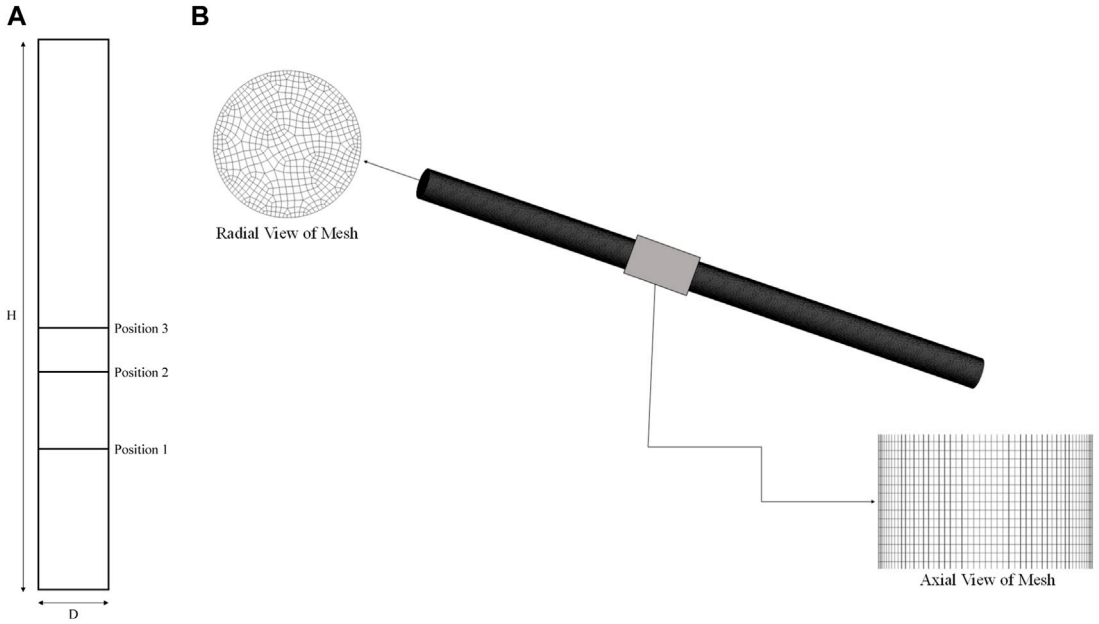

FIGURE 1
(A) Schematic of 2D plane (from Ansys Fluent 18.1) showing radial positions for data collection. **(B)** Different views of Mesh 2.

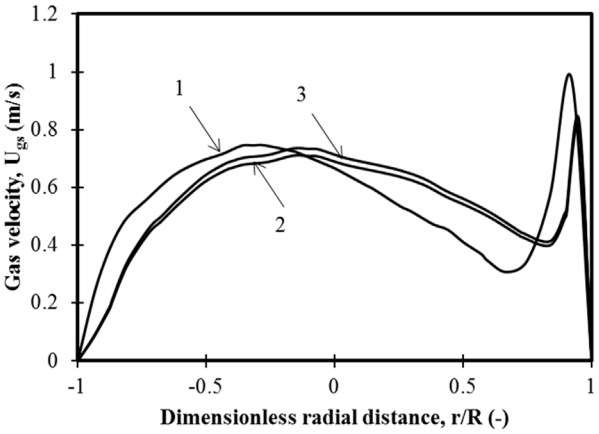

FIGURE 2
Variation in gas velocity for three different grids for Position 2 of Figure 1 at a steady state for superficial velocity of 0.3 m/s and 100 wt.% small particles of the binary mixture 1. 173,040 mesh elements, 2. 267,786 mesh elements, and 3. 497,568 mesh elements.

dissipation rate, and turbulent kinetic energy, the first-order upwinding scheme was used. Table 1 gives the details of the simulations about the mixture types, particle size, initial bed heights, and superficial gas velocities.

3 Results and discussion

In this section, the gas and particle velocity profiles for both unary and binary beds have been presented for two bed heights and three superficial velocities for each bed height and all compositions. The velocity profiles (radial profiles) are presented at three different axial positions from the time-averaged data of 7 s. Furthermore, axial particle volume fraction profiles of the centerline are presented for two compositions for the superficial velocities and bed heights considered. An empirical correlation between pressure drop and minimum fluidization velocity has been obtained by regression of the data generated from the validated CFD model. All compositions referred to in the work are in weight percentage (wt.%).

3.1 Model validation

The validated model used in our previous work has been used (Ganguli and Bhatt, 2023). Further validation of the model for pressure drop has been performed with additional data available for the mixtures of 40 wt.% large particles and 60 wt.% large particles, while for work to determine the mean velocity distribution of small and large particles has been performed with the experimental data of Roy et al. (2021). For pressure drop predictions, simulations were performed for a bed with an initial bed height of 0.235 m, and the superficial gas velocity was varied in a range of U_{gs} = 0.08–0.225 m/s. Figure 3 shows the variations of pressure drop with variations in superficial gas velocity for 40 wt.% and 60 wt.% large particles mixtures. The average error between the model and the experimental value was 6%. Figures 4A–C shows the comparison of predicted results of mean velocity profiles with the results of published literature (Roy et al., 2021) for the case of a 10 wt.% binary mixture composition and superficial velocities in the range of 1.1–2.1 m/s. Deviations in the range of 10% have been observed

TABLE 1 Parametric data for the simulations.

Mixture data		Particle size (μm)	Initial bed height (m)	Superficial gas velocity U_{gs} (m/s)
Fine particle (wt.%)	Large particle (wt.%)			
100	0	154	0.335, 0.635	0.3, 0.45, 0.6
80	20	220.8	0.335, 0.635	0.3, 0.45, 0.6
60	40	287.6	0.335, 0.635	0.3, 0.45, 0.6
40	60	354.4	0.335, 0.635	0.3, 0.45, 0.6
20	80	421.2	0.335, 0.635	0.3, 0.45, 0.6
0	100	488	0.335, 0.635	0.3, 0.45, 0.6

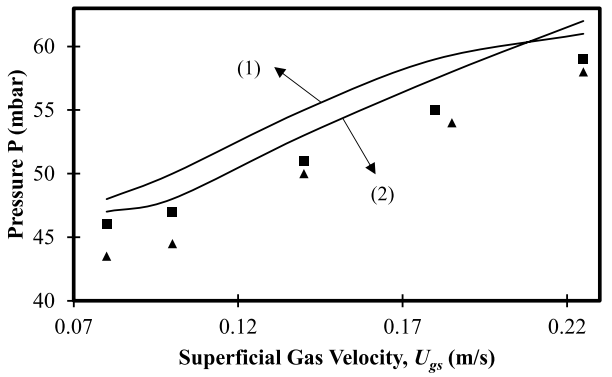

FIGURE 3
Variation in pressure drop as a function of gas superficial velocity (U_{gs}) for bed height = 0.235 m. (1) 40 wt.% large particles experimental data. (2) 60 wt.% large particles experimental data. ■ 40 wt.% large particles CFD predicted data; ▲ 60 wt.% large particles CFD predicted data.

for the compositions considered in the literature. This clarifies two aspects: the first being that validation with pressure drop measurements is not a sufficient criterion for model validation, and second, Eulerian–Eulerian models need to be tested with more experimental data. A further argument can also be made that the investigations of published literature have been made with a size ratio of 4 with larger sized particles in the size range (0.5–2 mm), while the present work has used the size range of (0.154–0.488 mm) and a size ratio of 3.2. The comparison for the other two compositions (30 wt.% and 40 wt.%) has been provided in the Supplementary Material. The deviations in these cases were less than 10%, suggesting that the Eulerian–Eulerian models with KTGF model predict well for binary mixtures.

3.2 Effect of mixture composition, superficial velocity, and bed height on gas and particle velocity profiles

The gas and particle dynamics for both small and large particles are quantified in the validated model by plotting each of the mean velocity profiles for all particle mixtures at three different superficial velocities for three different bed heights. For understanding, the dynamics of solid particle quantification have been further determined in the form of particle axial volume fraction profiles for the centerline. The axial locations at which the radial velocity profiles have been calculated are shown in Table 2.

The gas and particle velocity profiles at different axial locations for different superficial velocities and bed heights for the 20 wt.%, 40 wt.%, 60 wt.%, and 80 wt.% mixtures of large-sized particles are plotted in Figures 5–8, while those for the 0 wt.%, 80 wt.%, and 100 wt.% mixtures of large-sized particles are provided in the Supplementary Material because the main focus of the present work is understanding segregation and mixing in binary beds. Numbers have been used to denote the axial locations for the collection of axial velocity data in radial positions. The axial positions are chosen in the bottom, middle, and dilute zone based on the experimental data collection positions as per Jayarathna and Halvorsen (2011). Furthermore, the axial positions depend on the bed height considered. The axial positions and radial variations have been represented in dimensionless form for all figures. This is because the steady state bed height is different for different initial bed heights, and the axial positions are non-dimensionalized using the final steady state bed height. The mean gas and particle velocities have been time-averaged over 7 s before the results are presented. Similarly, the particle volume fractions for the vertical centerline of the bed have been presented after time-averaging. The size ratio has been considered constant as 3.2 for all simulations, and only compositions have been varied [binary mixtures having 0 wt.%, 20 wt.%, 40 wt.%, 60 wt.%, 80 wt.%, and 100 wt.% of large particles (488 μm), respectively].

The dimensionless distance range is taken as $-1 < r/R < 1$. During the profile analysis, the start position is the leftmost radial position (or left-hand wall), and the end position is the rightmost radial position (right-hand wall). The terminology for axial positions and superficial velocities describing velocity profiles for an initial bed height of 0.335 m (z/H = 0.24) and 0.635 m (z/H = 0.45) has been tabulated in Table 2.

3.2.1 Binary mixture with 0 wt.% large particles and 100 wt.% small particles: initial bed height of 0.635 m (z/H = 0.45)

The information for the unary bed of the present case is shown in Supplementary Figure S2. The gas velocity and particle velocity

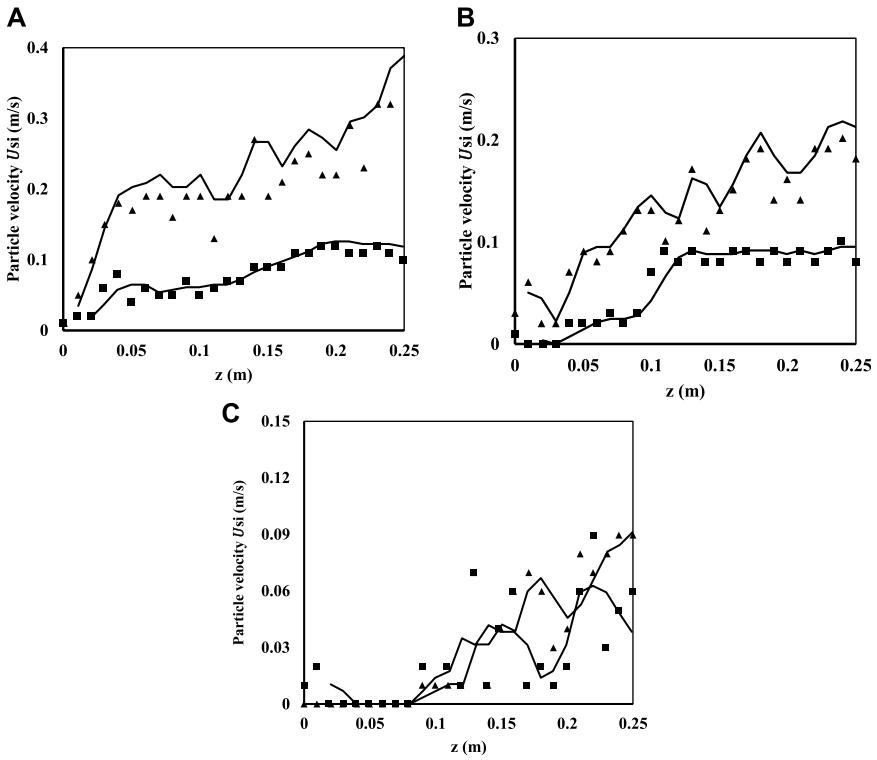

FIGURE 4
Comparison of model predictions with experimental data of Roy et al. (2021) for 10 wt.% large particles (2 mm size) and 90 wt.% small particles (0.5 mm size). **(A)** U_{gs} = 1.1 m/s. **(B)** U_{gs} = 1.6 m/s. **(C)** U_{gs} = 2.1 m/s. Bold triangle symbols (▲) denote smaller particles, while square symbols (■) denote larger particles. Solid lines denote CFD predictions.

TABLE 2 Dimensionless axial locations for various superficial velocities for all binary mixtures.

Case no.	Superficial velocity (m/s)	0 wt.% large and 100 wt.% small particles (Positions 1, 2, 3)	20 wt.% large and 80 wt.% small particles (Positions 1, 2, 3)	40 wt.% large and 60 wt.% small particles (Positions 1, 2, 3)	60 wt.% large and 40 wt.% small particles (Positions 1, 2, 3)	80 wt.% large and 20 wt.% small particles (Positions 1, 2, 3)	100 wt.% large and 0 wt.% small particles (Positions 1, 2, 3)
1	0.3	0.28, 0.61, 0.85	0.20, 0.40, 0.59	0.16, 0.33, 0.43	0.15, 0.29, 0.37	0.13, 0.27, 0.33	None
2	0.45	0.28, 0.61, 0.85	0.20, 0.40, 0.59	0.16, 0.33, 0.43	0.15, 0.29, 0.37	0.13, 0.27, 0.33	0.14, 0.28, 0.34
3	0.6	0.28, 0.61, 0.85	0.20, 0.40, 0.59	0.16, 0.33, 0.43	0.15, 0.29, 0.37	0.13, 0.27, 0.33	0.14, 0.28, 0.34

profiles for the binary mixture with 0 wt.% large particles and an initial bed height of 0.635 m (z/H = 0.45) are first presented. For a superficial velocity of U_{gs} = 0.3 m/s (Case 1) and the dimensionless axial position of 0.3 (Position 1), clear upward parabolic profiles near the walls (with a maximum axial velocity of U_g = 0.9 m/s) and downward near the walls are observed. However, for the dimensionless axial position of 0.6 (Position 2), a flow reversal near the wall is observed with an increase in velocities until r/R = 0.5 and a decrease in velocities from there to the wall. For the dimensionless axial position of 0.85 (Position 3), the velocities reach 1 m/s for r/R = 0.9, follow a straight line until r/R = 0.75, and then decrease and experience flow reversal very near to the wall. Thus, the velocity profiles show that flow is distinctly upward in the central region of the bed with a downward counter flow near the wall.

For a superficial velocity of U_{gs} = 0.45 m/s (Case 2) and Position 1, an off-center maximum is seen at r/R = 0.5, after which the velocities decrease non-linearly with a flow reversal near the left wall. Similarly, for Position 2, an upward velocity near the wall (with maximum velocity up to U_g = 4 m/s) decreases to U_g = 0 m/s at the center and then goes in the downward direction with a maximum velocity of U_g = −0.5 m/s near the left wall and finally ending at U_g = 0 m/s at the right wall. This indicates mixing in the region of Position 2. For Position 3, a flat profile in the central region with a flow reversal at both ends of the walls is observed (with a maximum velocity of U_g = 1 m/s from r/R = 0.5 to r/R = −0.5, after which it decreases until near the wall).

For superficial velocity of U_{gs} = 0.6 m/s (Case 3) and Position 1, the gas velocities increase until a certain dimensionless radial

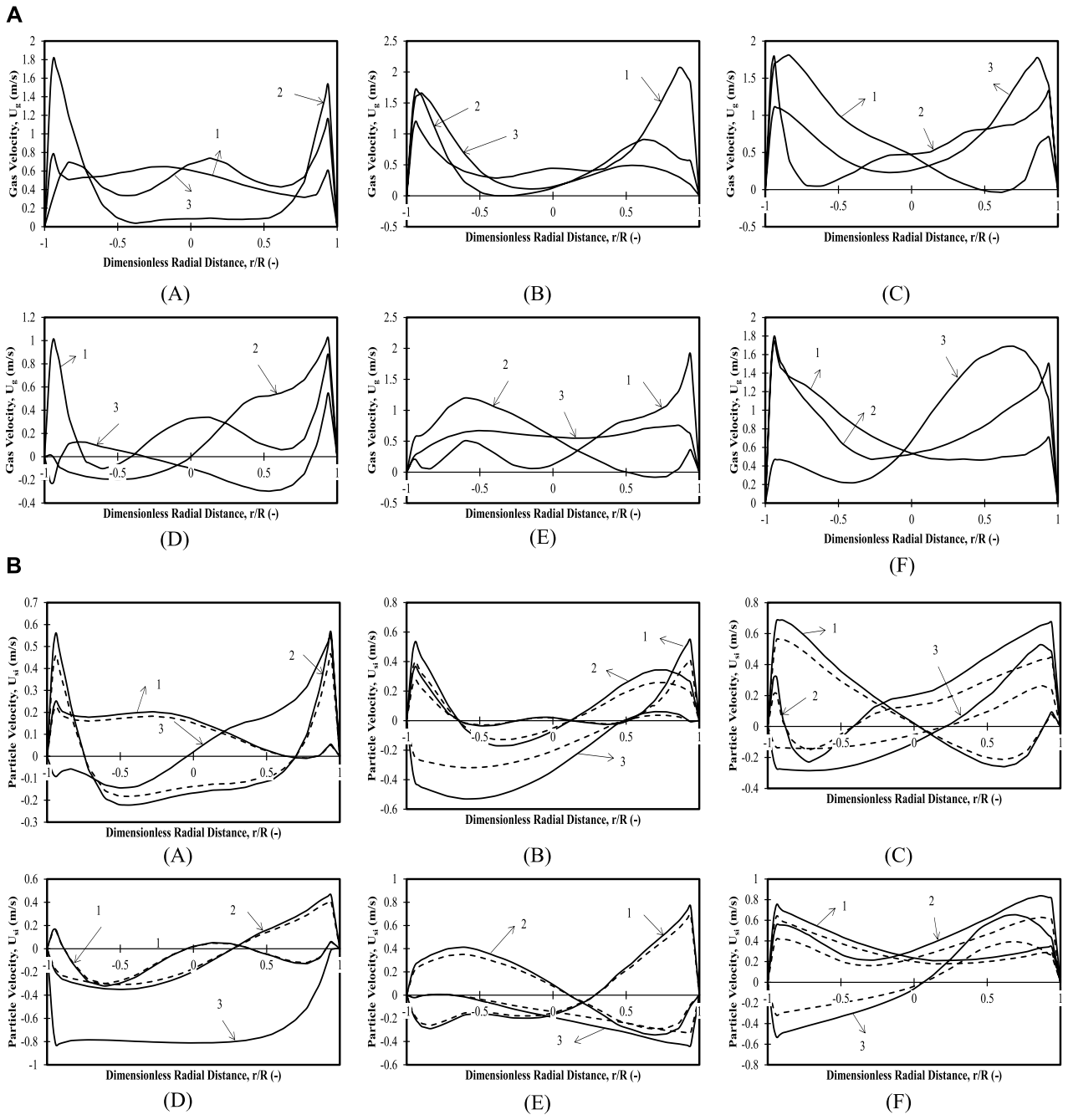

FIGURE 5
(A) Time-averaged mean axial gas velocity profiles for 20 wt.% large particles in mixture: 0.335 m (z/H = 0.24) initial bed height with (A) U_{gs} = 0.3 m/s, (B) U_{gs} = 0.45 m/s, and (C) U_{gs} = 0.6 m/s. 1. z/H = 0.33, 2. z/H = 0.66, and 3. z/H = 0.87, and 0.635 m (z/H = 0.45) initial bed height with (D) U_{gs} = 0.I/s, (E) U_{gs} = 0.45 m/s, and (F) U_{gs} = 0.6 m/s. 1. z/H = 0.20, 2. z/H = 0.40, and 3. z/H = 0.59. The solid line denotes smaller particles, while the dotted line denotes larger particles. **(B)** Time-averaged mean axial particle velocity profiles for 20 wt.% large particles in mixture and 0.335 m (z/H = 0.24) initial bed height with (A) U_{gs} = 0.3 m/s, (B) U_{gs} = 0.45 m/s, and (C) U_{gs} = 0.6 m/s. 1. z/H = 0.33, 2. z/H = 0.66, and 3. z/H = 0.87, and 0.635 m (z/H = 0.45) initial bed height with (D) *I* 0.3 m/s, (E) U_{gs} = 0.45 m/s, and (F) U_{gs} = 0.6 m/s. 1. z/H = 0.20, 2. z/H = 0.40, and 3. z/H = 0.59. The solid line denotes smaller particles, while the dotted line denotes larger particles.

distance of r/R = −0.6, then decrease for a short distance and become flat. Then, the gas velocities decrease up to r/R = 0.5, after which there is a downward flow and an upward flow near the wall. For Position 2, a downward flow is observed (with velocities up to U_g = −0.5 m/s) near the walls with upward velocities from r/R = −0.5 to 1, with an off-center maximum at r/R = 0.45, and then decrease to zero at the wall. For Position 3, a similar trend as that of Position 2 is observed. The only difference is that the maximum occurs at r/R = 0.15, and a flow reversal occurs near the left wall. Thus, for Case 3 at lower positions, gas recirculation is observed with upward velocities on the left side of the column and downward velocities on the right side of the column, signifying

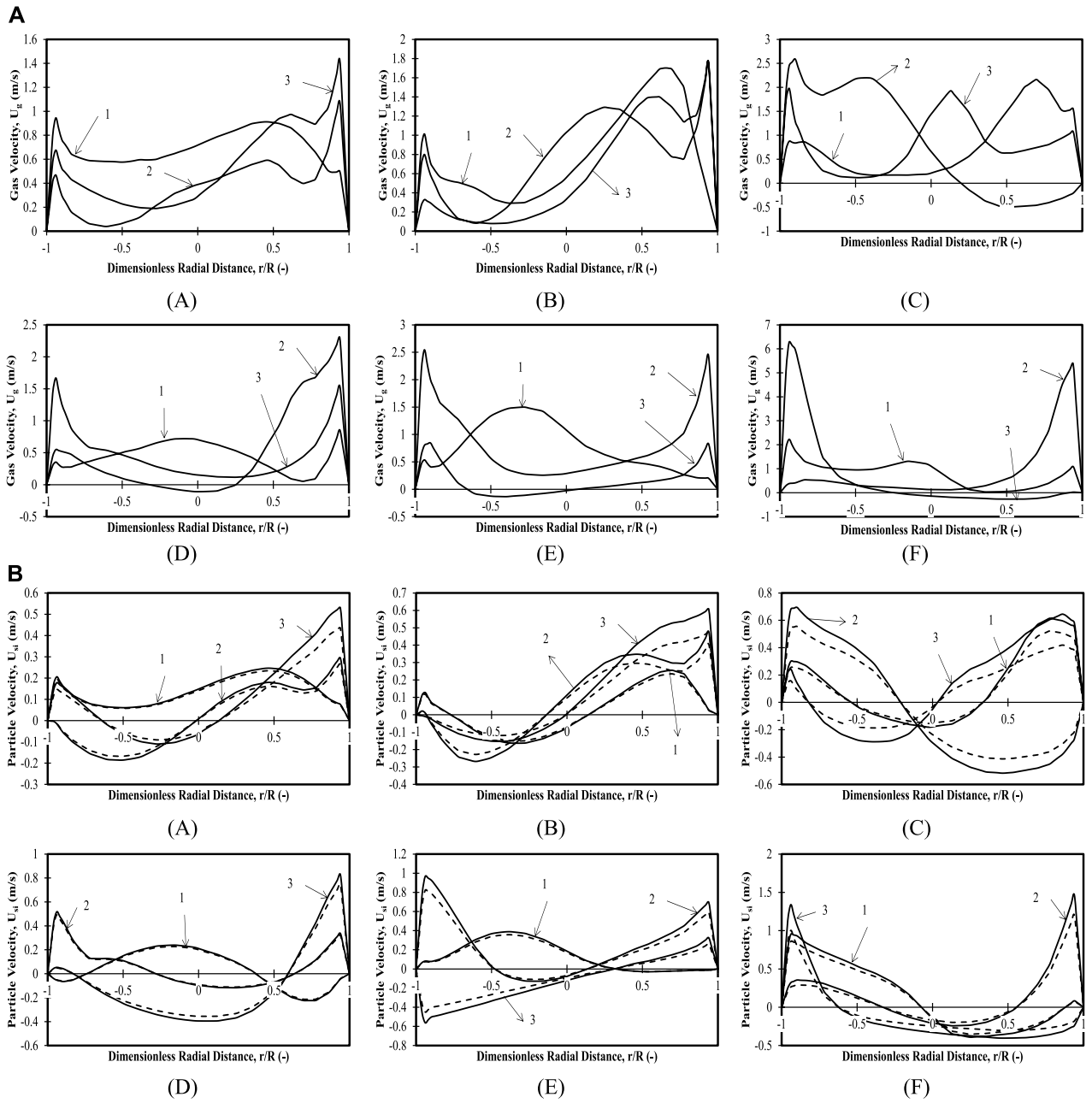

FIGURE 6
(A) Time-averaged mean axial gas velocity profiles for 40 wt.% large particles in the mixture and 0.335 m (z/H = 0.24) initial bed height with (A) U_{gs} = 0.3 m/s, (B) U_{gs} = 0.45 m/s, and (C) U_{gs} = 0.6 m/s. 1. z/H = 0.33, 2. z/H = 0.66, and 3. z/H = 0.87, and 0.635 m (z/H = 0.45) initial bed height with (D) U_{gs} = 0.3 m/s, (E) U_{gs} = 0.45 m/s, and (F) U_{gs} = 0.6 m/s. 1. z/H = 0.21, 2. z/H = 0.43, and 3. z/H = 0.64. The solid line denotes smaller particles, while the dotted line denotes larger particles. **(B)** Time-averaged mean axial particle velocity profiles for 40 wt.% large particles in the mixture. (i) 0.335 m (z/H = 0.24) initial bed height with (A) U_{gs} = 0.3 m/s, (B) U_{gs} = 0.45 m/s, and (C) U_{gs} = 0.6 m/s. 1. z/H = 0.33, 2. z/H = 0.66, and 3. z/H = 0.87, and 0.635 m (z/H=0.45) initial bed height with (D) U_{gs} = 0.3 m/s, (E) U_{gs} = 0.45 m/s, and (F) U_{gs} = 0.6 m/s 1. z/H = 0.33, 2. z/H = 0.66, and 3. z/H = 0.87. The solid line denotes smaller particles, while the dotted line denotes larger particles.

mixing. For the middle and top of the bed, the gas velocities are skewed toward the right with 90% of the upward flow with magnitudes up to 3 m/s and minor downward velocities at the left wall with magnitudes of U_g = −0.5 m/s.

Particle velocities for Cases 1, 2, and 3 have been demonstrated in Supplementary Figure S2. At Position 1 Case 1, a parabolic profile is observed at the central portion with downward particle velocities near the walls (asymmetric in nature), which indicates fully developed flow in the central portion. For Position 2, an asymmetric parabolic profile with peak velocities at the right and downward velocities only at the left wall is observed, which indicates a drift of upward particle flow toward the right and downward particle flow toward the left. For position 3, a tectonic shift is observed in the particle velocity profile with upward velocities on the left and downward velocities on the right. The profile is

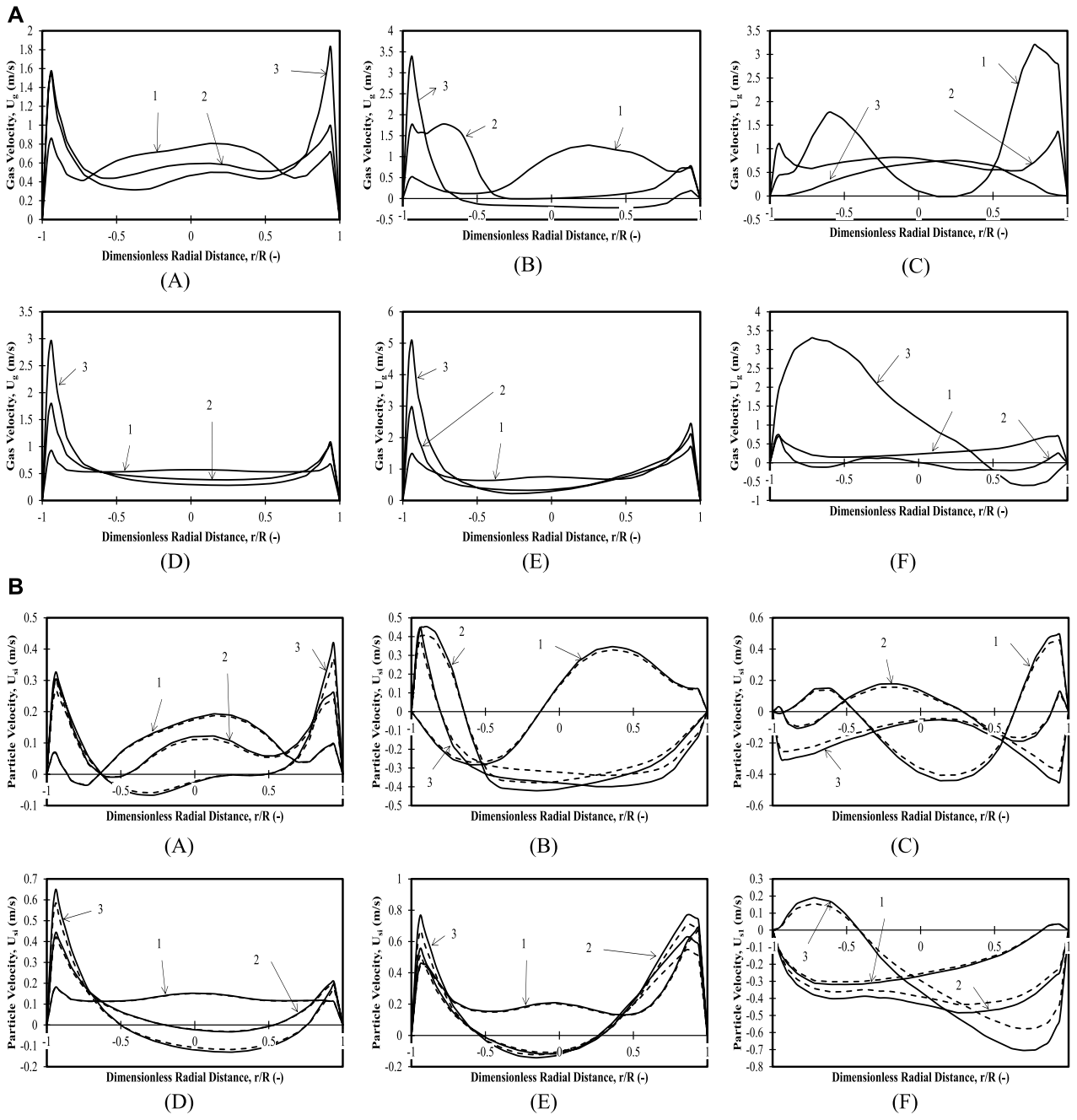

FIGURE 7
(A) Time-averaged mean axial gas velocity profiles for 60 wt.% mixture and 0.335 m (z/H = 0.24) initial bed height with (A) U_{gs} = 0.3 m/s, (B) U_{gs} = 0.45 m/s, and (C) U_{gs} = 0.6 m/s. 1. z/H = 0.33, 2. z/H = 0.66, and 3. z/H = 0.87, and 0.635 m (z/H = 0.45) initial bed height with (D) U_{gs} = 0.3 m/s, (E) U_{gs} = 0.45 m/s, and (F) U_{gs} = 0.6 m/s. 1. z/H = 0.33, 2. z/H = 0.66, and 3. z/H = 0.87. **(B)** Time-averaged mean axial particle velocity profiles for 60 wt.% mixture and 0.335 m (z/H = 0.24) initial bed height with (A) U_{gs} = 0.3 m/s, (B) U_{gs} = 0.45 m/s, and (C) U_{gs} = 0.6 m/s. 1. z/H = 0.33, 2. z/H = 0.66, and 3. z/H = 0.84, and 0.635 m (z/H = 0.45) initial bed height with (D) U_{gs} = 0.3 m/s, (E) U_{gs} = 0.45 m/s, and (F) U_{gs} = 0.6 m/s. 1. z/H = 0.33, 2. z/H = 0.66, and 3. z/H = 0.84.

a mirror image of the one for Position 2 with higher velocities for both upward and downward flows. The velocity magnitudes increase as we go from position 1 to 3 in the axial direction.

For Case 2 and Position 1, upward velocities with maxima approximately U_{s1} = 0.9 m/s are observed near the left wall, while downward velocities are seen from r/R = 0.35 to the end at the left wall. For Position 3, the velocity profile is slightly different, with a near-wall peak at the left wall while remaining constant over a certain radial distance, decreasing linearly until r/R = 0.5, till velocity becomes zero and then decreasing velocities with negative magnitude from r/R = 0.5 to the left wall.

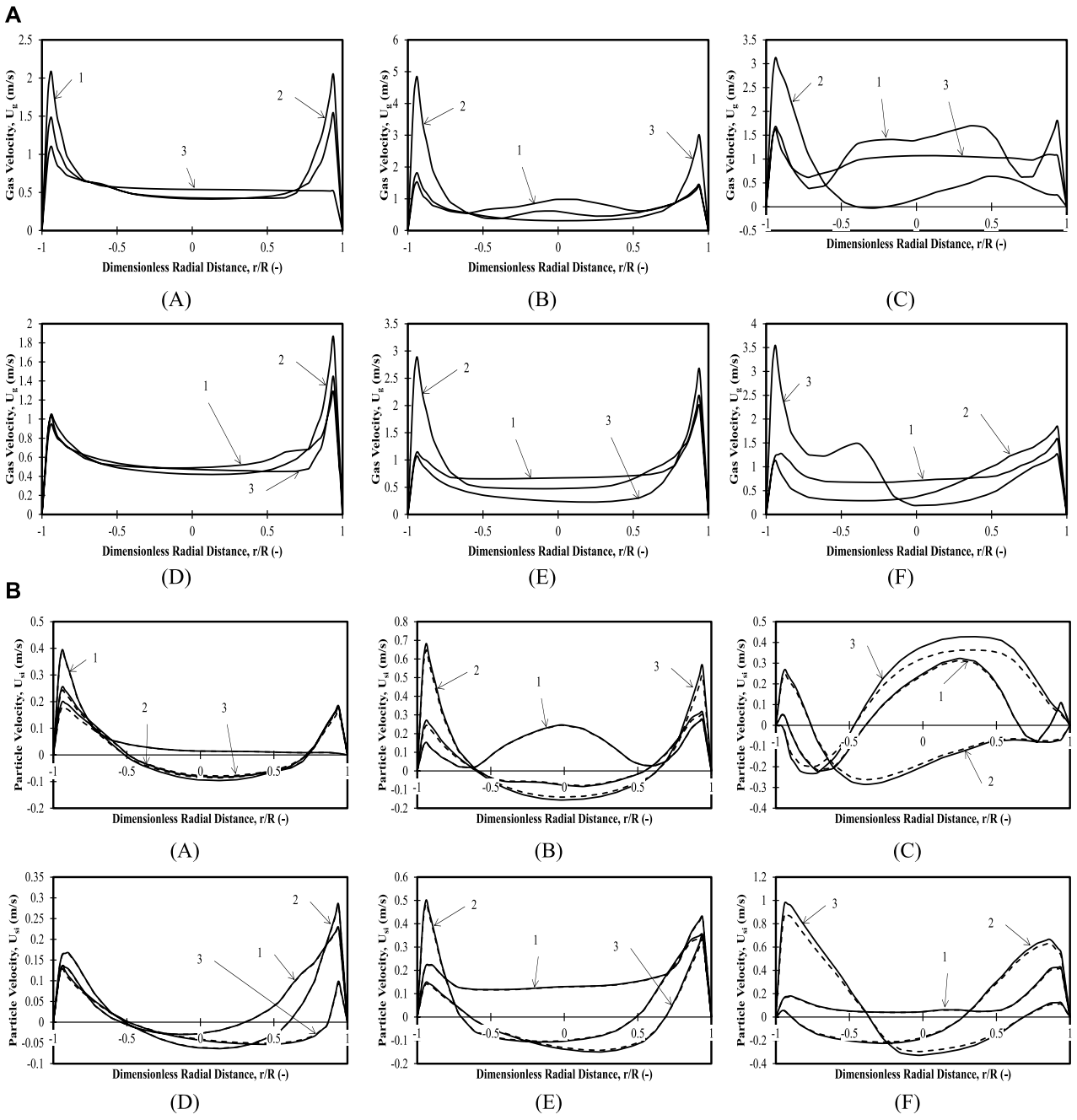

FIGURE 8
(A) Time-averaged mean axial gas velocity profiles for 80 wt.% mixture and 0.335 m (z/H = 0.24) initial bed height with (A) U_{gs} = 0.3 m/s, (B) U_{gs} = 0.45 m/s, and (C) U_{gs} = 0.6 m/s. 1. z/H = 0.33, 2. z/H = 0.66, and 3. z/H = 0.87, and 0.635 m (z/H = 0.45) initial bed height with (D) U_{gs} = 0.3 m/s, (E) U_{gs} = 0.45 m/s, and (F) U_{gs} = 0.6 m/s. 1. z/H = 0.33, 2. z/H = 0.66, and 3. z/H = 0.87. **(B)** Time-averaged mean axial particle velocity profiles for 80 wt.% mixture and 0.335 m (z/H = 0.24) initial bed height with (A) U_{gs} = 0.3 m/s, (B) U_{gs} = 0.45 m/s, and (C) U_{gs} = 0.6 m/s. 1. z/H = 0.11, 2. z/H = 0.21, and 3. z/H = 0.32, and 0.635 m (z/H = 0.45) initial bed height with (D) U_{gs} = 0.3 m/s, (E) U_{gs} = 0.45 m/s, and (F) U_{gs} = 0.6 m/s 1. z/H = 0.21, 2. z/H = 0.43, and 3. z/H = 0.64.

For Case 3 and Position 1, a profile similar to Case 2 is observed with higher maximum velocities. Position 2 is characterized by downward velocities near the left wall and upward velocities from r/R = −0.4, with a maximum of U_{s1} = 0.85 m/s near the left wall.

Thus, fully developed profiles for all velocities in the bottom, middle, and top portions are observed for lower superficial velocities. As the superficial velocity is increased, asymmetric sinusoidal profiles are observed. Magnitudes of maximum particle velocities are higher as the superficial velocities increase, ranging from U_{s1} = −1 to U_{s1} = 1.25 m/s on the right and left sides, respectively. Thus, although gas velocities have fully developed profiles, particle velocities have sinusoidal profiles denoting good mixing.

3.2.2 Binary mixture with 20 wt.% large particles and 80 wt.% small particles: initial bed height of 0.335 m (z/H = 0.24)

Figures 5A–C shows the gas velocity profiles for the binary mixture with 20 wt.% large particles and an initial bed height of 0.335 m (z/H = 0.24). It can be observed that gas velocity profiles for all three superficial velocities and all axial positions considered are less than U_g = 0.75 m/s in the bulk (center of the bed) in magnitude and have flat profiles except for the case of U_{gs} = 0.6 m/s. The gas velocities near the walls represent maxima for all the axial positions, increasing with superficial velocities. The profile for Position 1 and Case 3 shows a higher maximum (U_g ~ 1.75 m/s) near the left wall decreasing to zero at r/R = 0.5 and a maximum at the right wall. Both these patterns represent bypassing of the gas for all velocities. Similarly, for Position 1 Case 2, a maximum at the right wall occurs at U_g = 1.25 m/s, while that at the left wall occurs at U_g = 2 m/s. Position 2 for Case 3 also has an increasing trend from r/R = −0.2 to r/R = 0.8. The profiles show an upward trend. An important observation is that when gas velocities (referred also as bubble-rise velocity) of Cases 2 and 3 are compared at the highest position, an inverted parabolic profile is observed in both cases with nearly same magnitudes. This is attributed to the fact that the larger particles tend to decrease the effect of superficial velocity on the bubble-rise velocity. This contradicts the fact that an increase in superficial velocity would cause a corresponding increase in rise velocity.

Figures 5A–C shows the variation in particle velocities for the binary mixture for both large and small particles at an initial bed height of 0.335 m (z/H = 0.24). For Case 1, Position 1 shows upward velocities for all radial locations. Furthermore, lower particle velocities are observed for all axial positions with downward velocities for Position 2 in bulk and upward velocities near the wall. Both small and large particles demonstrate the same trends with a slight difference in their magnitudes (the smaller particles have higher velocities than the larger particles). An asymmetric profile with downward particle velocities of smaller diameter particles in the left portion of the bed and upward velocities in the right portion of the bed has been observed for Position 3. The particle velocities for larger particles are not observed for this axial position (Position 3) superficial velocity bed height. This might be attributed to the difference in dispersion height of the bed as also observed by Singh et al. (2019). For Case 2 Position 1, the particle velocities are found to be nearly zero with upward velocities near both walls (in region 0 < r/R < −0.4; 0.5 < r/R < 1) for smaller particles, while the larger particle velocity magnitudes are lower for the entire bed, indicating that the kinetic energy of larger particles depends on the particle–particle collisions, gas–particle collisions, and collisions with the walls. Position 2 shows a very different profile with upward velocities in the region 0 < r/R < −0.4, downward velocities in the region 0 < r/R < 0.1, and upward velocities in the region (0.1 < r/R < 1) for both diameters of particles (with a difference in velocity magnitudes). For Position 3, downward velocities with maximum velocity magnitudes of −0.34 m/s (for smaller particles) on the left-hand side and upward velocities on the right-hand side are observed. On the right-hand side, a maximum is seen at position r/R = 0.8. For Case 3, an asymmetric profile with upward velocities in the left portion of the wall (in region 0 < r/R < 0.2) and downward velocities on the right half is observed for Position 1. Positions 2 and 3 have downward velocities with maximum velocity magnitudes of −0.56 m/s (for smaller particles), respectively, on the left-hand walls (in region 0 < r/R < 0.5).

To summarize, the particle velocities for larger particles are always lower than those of the smaller particles for this composition. This is evident for all superficial velocities and all positions. At lower superficial velocities, the larger particles do not reach the topmost position due to difference in dispersion height. Bypassing of the gas for lower superficial velocities takes place through the near-wall region with clear segregation of the bed as observed from the particle velocity profiles. This is explained as follows: because the particle velocities of both particle sizes are higher than minimum fluidization velocities, they move at different velocities. The larger particles reach a particular height and either move axially or radially in the case of mixing or remain at a constant position. The smaller particles, however, move to a higher height and keep moving both radially and axially. Hence, for the highest position and the highest superficial velocity, there is no presence of larger particles for the composition under consideration. In other words, the larger particles are segregated in the bottom, while smaller particles are segregated at the top.

3.2.3 Binary mixture with 20 wt.% large particles and 80 wt.% small particles: initial bed height of 0.635 m (z/H = 0.45)

Figure 5D–F shows the gas velocity profiles for the binary mixture with 20 wt.% large particles and an initial bed height of 0.635 m (z/H = 0.45). Gas velocity profiles for all three superficial velocities and all axial positions considered are less than U_g = 0.75 m/s in the bulk (center of the bed) and have flat profiles except in the case of U_{gs} = 0.6 m/s. The gas velocities near the walls represent maxima for all the axial positions, increasing with superficial velocities. The profile for Position 1 and Case 2 shows a maximum (U_g ~ 0.5 m/s) near the left wall near r/R = −0.5, which decreases to zero at r/R = 0 and then increases to a maximum at the right wall. Similarly, for Position 1 Case 1, a maximum at the left wall occurs at 1 m/s, while that at the right wall occurs at U_g = 0.5 m/s. Position 3 for Case 2 attains a stagnant trend (U_g ~ 0.5 m/s) from r/R = −0.2 to r/R = 0.8. The higher gas velocities (maxima) near the walls for certain axial positions denote the presence of bubbles or core annular structures, while lower velocities denote the absence of the gas and presence of particles.

Figure 5D–F shows the variation in particle velocities for the binary mixture with 20 wt.% large particles for both particle sizes and an initial bed height of 0.635 m (z/H = 0.45). For Case 1, Position 1 starts with high upward velocities and shows a minimum at r/R = −0.5 and r/R = 0.7 and a maximum at r/R = 0.1. Position 2 shows an upward velocity moving from the left wall to the right wall. Position 3 shows small particles moving in the downward direction with velocities up to 0.8 m/s and a flat velocity profile. The larger particles, however, are not observed at this position. This might be due to the difference in dispersion height indicating segregation for the case considered. For Case 2, the trends of particle velocities for both particle sizes are similar, with magnitudes of particle velocities depending on the particle sizes. Position 1 shows decreasing velocities from the left wall to r/R < 0.3 and upward velocities near the right wall. Position 2 shows a

maximum at r/R = −0.5 and a decreasing trend from there to the right wall. Position 3 shows a decreasing upward velocity profile from −1<r/R < −0.4 and an increasing upward velocity profile in the remaining portion. Position 1 Case 3 shows a stagnant downward velocity of 0.8 m/s (for smaller particles) from the left wall to r/R = 0.5 and an increasing behavior to the right wall. Position 2 shows a continuous decreasing downward velocity trend starting with 0 m/s at the left wall. Position 3 shows an increasing downward velocity from the left wall to the right wall with a maximum at r/R = 0.6. The maxima in particle velocities near walls denote the core annular structure with a concave region in the center. These observations have also been observed in circulating fluidized bed risers by Zaabout et al. (2010). It is also noticed that the superficial velocities where core-annular structures form are in the range suggested by Van den Moortel et al. (1998).

For the present case, it has been observed that as the superficial velocity increases, the gas–solid (GS) interactions increase, and there is a reduction in the particle–particle frictional forces. The maximum GS interaction happens at the highest superficial velocities, and the minimum interactions happen at the lowest superficial velocity. This promotes mixing as observed in the top position (Position 3) of the last case for both large and small particle velocities. For the lowest superficial velocity, the particle–particle interactions are higher, causing the segregation of the bed. It should also be noted that bed height plays an important role along with superficial velocity in determining the segregation and mixing phenomena for a particular composition.

3.2.4 Binary mixture with 40 wt.% large particles and 60 wt.% small particles: initial bed height of 0.335 m (z/H = 0.24)

Figures 6A–C shows that the gas velocities for all the cases and positions show a similar trend of low velocities in the entire bed except on the right-hand side. The only exceptions are Case 2 Positions 2 and 3, which show maxima at different r/R locations, and Case 3 Position 2, where upward velocities are seen on the left-hand side, and downward velocities are seen on the right-hand side. The maxima indicate the presence of either a bigger bubble or smaller bubbles that can be observed from the comparison of the particle velocity because the trends are the same, but the particle velocities are not present at some spatial locations, indicating only the presence of gas that indirectly indicates gas bubbles.

Figures 6A–C shows that particle velocities for both particle sizes for all cases and positions have symmetric or asymmetric profiles with upward and downward velocities on the left- and right-hand sides, respectively. The asymmetric profiles might be attributed to the presence of gas bubbles, which is also evident when one compares the particle velocity trends with the gas velocity trends for the operating conditions and the spatial locations. This shows that an increase in superficial velocity causes a corresponding increase in intermixing. It should also be noted that mixing is evident in all the cases for the composition considered in terms of both the operating condition and the bed height.

3.2.5 Binary mixture with 40 wt.% large particles and 60 wt.% small particles: initial bed height of 0.635 m (z/H = 0.45)

Figures 6D–F shows that gas velocity magnitudes are higher for lower axial positions with maxima on the left-hand side for Positions 2 and 3, Cases 2 and 3. Similarly, for higher superficial velocities (Cases 2 and 3) and the axial position (Position 3), there is a maximum on the right-hand side of the bed. This shows that a fully developed flow for the gas phase occurs for higher superficial velocities at higher axial positions, and a steady state is reached.

Figures 6D–F shows particle velocities for both sized particles. A swirling action can be seen from lower to higher axial positions because, at higher axial positions (Positions 2 and 3) and higher superficial velocity (Case 3), the particles attain an off-center parabolic profile on the right-hand side, while for Position 3, the maximum and parabolic profile is on the right. Such trends have been reported by Zaabout et al. (2010). However, an important conclusion that can be made is that with an increase in bed height, the amount of mixing is lowered at lower superficial velocities of 0.3 and 0.45 m/s, and good mixing is only observed at 0.6 m/s.

For the present case, both gas and particle velocities for Cases 2 and 3 show mixing patterns corresponding to a bubbling regime. Furthermore, a comparison of particle and gas velocities indicates the presence of bubbles near the walls instead of in the center as in the previous case of lower bed height. Furthermore, it can be concluded that bypassing occurs at lower superficial velocities, reducing the mixing in the bed, although segregation is not observed. This also reiterates the fact that bed height plays an important role in the dynamics of fluidized beds.

3.2.6 Binary mixture with 60 wt.% large particles and 40 wt.% small particles: initial bed height of 0.335 m (z/H = 0.24)

Figures 7A–C shows the gas velocities for the aforementioned composition of binary mixture. For the different positions, the analysis shows that for Case 1, as the position increases, the gas velocities decrease, and a flat velocity is observed at the topmost position. The existence of gas bubbles may be interpreted at the lowermost position away from the centers with high velocity magnitudes. An increase in superficial velocity causes bypassing of the gas with an increase in the spatial position, with the gas passing nearly uniformly across the bed in the lowermost position for Case 2 and slowly decreasing across the bed and bypassing near the left wall.

Particle velocities (for both particle sizes) in Figures 7A–C however, show rapid mixing patterns in the form of sinusoidal waveforms for Cases 2 and 3 for Positions 2 and 1, respectively. Downward velocities are observed for Positions 2 and 3 and Case 2, while in Position 3 and Case 3, a flat profile in the bulk in the downward direction can be observed. Overall rapid mixing for both Case 2 and Case 3 are observed. It is important to note that for this composition, there is no difference in dispersion height for the entire range of superficial velocities considered across all positions for the present bed height.

For the present combination, both gas and particles are present in the bed causing good mixing with the characteristics of a bubbling regime for Cases 2 and 3.

3.2.7 Binary mixture with 60 wt.% large particles and 40 wt.% small particles: initial bed height of 0.635 m (z/H = 0.45)

Figures 7D–F shows gas velocity profiles for a higher bed height. For mostly all cases and all positions, high velocities near the left walls are seen with flat velocity profiles in the bulk. For the highest superficial velocity, the gas velocities undergo a maximum at the highest position. This may be attributed to the existence of the bubble that occurs at the dispersed height of the bed. The existence of the bubbles has been already described in detail in Part I of our analysis (Ganguli and Bhatt, 2023). These bubbles also play a role in carrying the larger particles and increasing the kinetic energy of the larger particles by transferring part of their own kinetic energy to the larger particles.

Figures 7D–F shows particle velocities for both particle sizes for the aforementioned case. Particle velocity profiles are similar to gas velocity profiles for Cases 1 and 2 with a velocity magnitude that is five times smaller. Similarly, for Case 3 and all axial locations, downward velocities are observed for all the positions. The higher velocities near the walls and lower velocities at the center form a concave structure (core annular profile) similar to the ones observed by Zaabout et al. (2010). It can also be observed that mixing occurs at the highest superficial velocity (0.6 m/s) for this case with GS interactions dominating over particle–particle interactions. For lower velocities, however, the bed acts more or less as a distributor, with higher particle velocities restricted only near the walls due to the gas bypassing that occurs. This also denotes segregation at the superficial velocities of 0.3 and 0.45 m/s at a bed height of 0.635 m (z/H = 0.45) with particle–particle interactions causing frictional forces to dominate over GS interactions. These represent patterns similar to the ones predicted by Lan et al. (2014).

3.2.8 Binary mixture with 80 wt.% large particles and 20 wt.% small particles: initial bed height of 0.335 m (z/H = 0.24)

Figures 8A–C shows a flat profile in the bulk and higher gas velocities near the wall, indicating that most of the gas exits from the near-wall regions. The magnitudes of gas velocities are highest in Position 1 of Case 3. Figures 8D–F show the particle velocities for the mixture composition considered. The bed is seen to be well mixed for all positions for Case 3 or the highest superficial velocity. Upward velocities in bulk are observed for Positions 1 and 3 for Case 2 and only for Position 1 for Case 3. Downward velocities in bulk are observed for all other positions. Near-wall maxima with different velocity magnitudes are seen in most of other positions and cases except Case 1. The profiles represent a concave structure (core annular profile) similar to the ones observed by Zaabout et al. (2010).

3.2.9 Binary mixture with 80 wt.% large particles and 20 wt.% small particles: initial bed height of 0.635 m (z/H = 0.45)

Figures 8A–C show that when the bed height is increased, the trends of the gas velocity profiles remain the same, with nearly half the magnitudes the same as for a lower bed height case. The particle velocities for both particle sizes in Figures 8D–F also show mixing in the case of the highest superficial velocity. This clearly suggests that the trends for this particular composition are similar and differ only in magnitudes for both bed heights. It can be concluded that the dynamics of the bed are independent of the bed height for the present case of operating conditions considered for this particular composition.

3.2.10 Binary mixture with 100 wt.% large particles and 0 wt.% small particles: initial bed height of 0.335 m (z/H = 0.24)

This analysis has been included in the Supplementary Material. In this case (refer to Supplementary Figure S3), during simulations, no gas or particle dynamics was observed for Case 1, and the bed acts as a fixed bed. Hence, only Cases 2 and 3 were analyzed, and Case 1 is not reported. Figures (A) and (B) show that gas velocities show similar dynamics as seen for higher amounts of large particles. The particle velocities (for 488 micron), however, show undulations in the entire bed for Positions 2 and 3 and Cases 2 and 3 except for Position 2 of Case 3.

3.2.11 Binary mixture with 100 wt.% large particles and 0 wt.% small particles: initial bed height of 0.635 m (z/H = 0.45)

The gas and particle velocity profiles are demonstrated in Supplementary Figure S3. Both gas and particle velocities are stagnant in the bulk of the bed, while very high values are present near the walls. Furthermore, the particle velocities for all cases and positions considered are downward showing that for the superficial velocities considered for this composition, the bed acts as a distributor irrespective of bed height. Some cases have not been considered for the study because they act as a fixed bed at the superficial velocities.

3.3 Effect of superficial velocity and initial bed height on axial solid phase volume fraction profiles

In this section, solid phase volume fractions across the axial centerline of the final bed height have been presented for the three superficial velocities and two mixture compositions considered, namely, 20 wt.% and 40 wt.%. Both bed heights have been chosen for each of the compositions. The discussion has been restricted to only two compositions to demonstrate the segregation and mixing that can be analyzed using the solid volume fractions. The other compositions also have similar trends with slight differences due to the presence of higher amounts of large particles but have not been included.

Figure 9A, B shows solid fraction profiles for both large and small volume fractions for the 20 wt.% mixture case for both bed heights. Similar profiles have been reported by Lan et al. (2014). For all three superficial velocities and the lower bed height of 0.335 m (z/H = 0.24), segregation is observed in the bottom layer with a larger amount of large particles and a relatively lower volume fraction of smaller particles, and vice versa in the top layer. The middle layer showed some mixing between the large and small particles. Furthermore, the dispersion height was found to be higher for smaller particles for all three superficial velocities. For the lowest superficial velocity of 0.3 m/s, the dispersion height for large

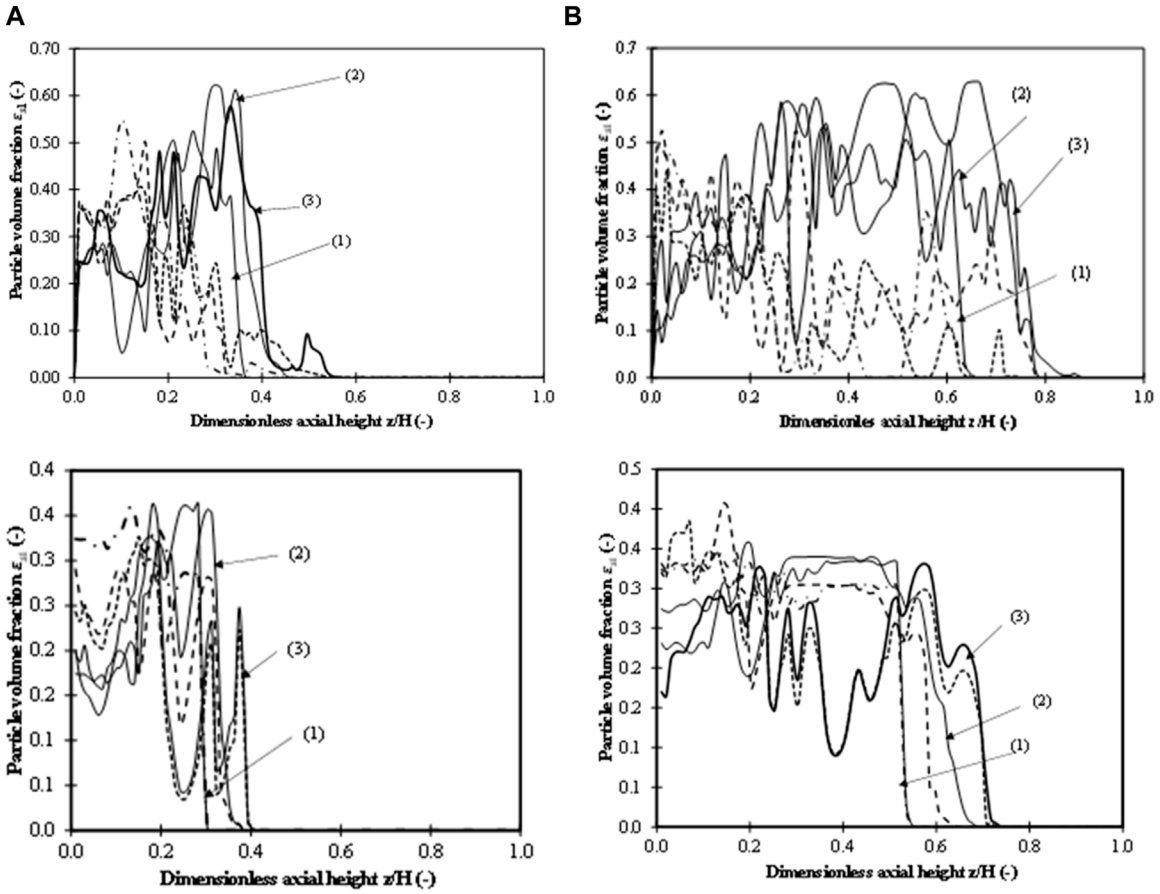

FIGURE 9
Time-averaged axial particle volume fraction profiles for (i) 20 wt.% mixture; (ii) 40 wt.% mixture. **(A)** Initial bed height of 0.335 m (z/H = 0.24). **(B)** Initial bed height of 0.635 m (z/H = 0.45). (1) U_{gs} = 0.3 m/s, (2) U_{gs} = 0.45 m/s, and (3) U_{gs} = 0.6 m/s. Dotted lines denote large particle composition, and solid lines denote smaller particles. ---------- U_{gs} = 0.3 m/s, – – – – U_{gs} = 0.45 m/s, and ••••••• U_{gs} = 0.6 m/s.

particles is 0.31 m (z/H = 0.22), while the dispersion height for small particles is 0.36 m. This also compliments the findings observed in the velocity distributions where the particle velocities are not observed for Position 3. However, volume fractions lower than 0.0005 are observed for the superficial velocity of 0.6 m/s, while corresponding volume fraction for 0.45 m/s is 0.007. This is due to the higher kinetic energy of the gas and the smaller particles, and only a very few large particles are carried over. Because very few particles reach the top or the dilute zone, the velocity distributions depict the larger particles in the profiles. Dispersion heights, however, are 0.5–0.7 m. Furthermore, the undulations or decrease in volume fractions indicate bubble-containing solids and can also be seen in volume fraction contours as depicted in our earlier work (Ganguli and Bhatt, 2023). These patterns confirm a bubbling regime and well mixed patterns. For an initial height of 0.635 m (z/H = 0.45), complete segregation is observed in all the layers with all small particles in the top layer and large particles in the bottom layer. Interestingly, here, two layers are formed, while three layers are formed in the previous case with a lower bed height. Some large particles, however, reach the top layer in all three cases, although the dispersion heights for all three heights are different.

Figure 9A, B shows solid fraction profiles for the 40 wt% mixture case for both bed heights. For the lower initial bed height (z/H = 0.24), segregation at the bottom layer is evident for all superficial velocities, and the highest segregation occurs at 0.3 m/s. However, from z/H = 0.15, some amount of mixing is observed until the dispersed bed height is reached. The volume fractions of both large and small particles are similar in the middle of the bed (starting at z/H = 0.12 and evident until z/H = 0.3 for all superficial velocities), with small particles becoming higher at the top of the bed (or the dilute zone), especially for superficial velocities of 0.3 and 0.45 m/s. The mixing is most evident for z/H = 0.13 to 0.4 for a superficial velocity of 0.6 m/s, where substantial volume fractions of large particles are observed compared to small particles, indicating good mixing. This may be attributed to three major factors: the influence of gas velocity and bubbles that increase the kinetic energy of large particles, higher GS interactions dominating the particle–particle interactions, and lower hindrance of small particles. For a bed height of 0.635 m (z/H = 0.45), the particle volume fraction profiles also depict segregation at the bottom (volume fractions of larger particles are higher by 10%–35%) and mixing at both the middle and top layers with small particles having higher volume fractions (15%–20% higher) compared to larger

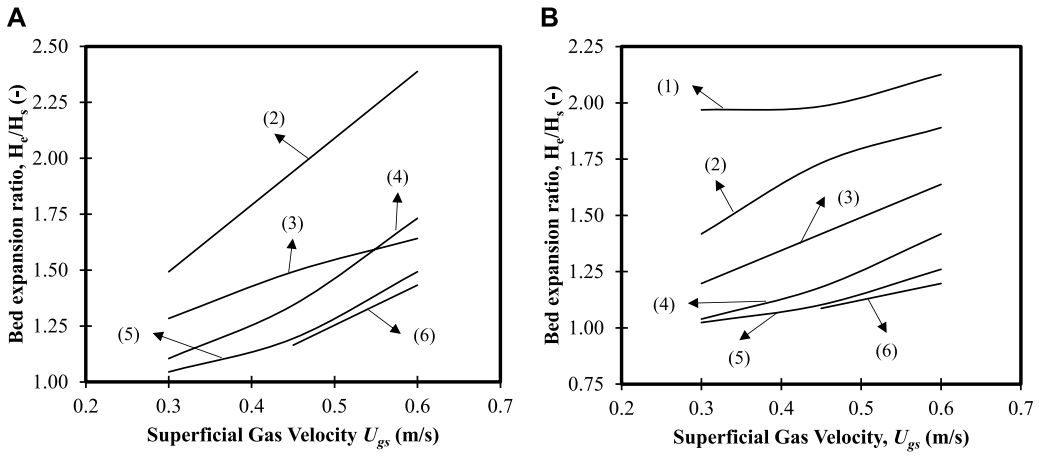

FIGURE 10
Bed expansion ratio profiles for different superficial velocities for **(A)** initial bed height of 0.335 m (z/H = 0.24); **(B)** initial bed height of 0.635 m (z/H = 0.45). (1) 0 wt.% mixture, (2) 20 wt.% mixture, (3) 40 wt.% mixture, (4) 60 wt.% mixture, (5) 80 wt.% mixture, and (6) 100 wt.% mixture.

particles. The undulations at the middle and top portions depict the presence of bubbles. For U_{gs} = 0.6 m/s, a dip in the volume fraction both of small and large particles is observed that denotes the formation of larger bubbles.

3.4 Effect of superficial velocity on final bed height

Figures 10A, B represent the final bed height for the fluidized bed after reaching a steady state for two initial bed heights, 0.335 m (z/H = 0.24) and 0.635 m (z/H = 0.45). The bed height considered does not indicate the bed height for two different particle sizes, but the highest bed height that can be observed at a steady state is taken, which mostly consists of small particles. In Figure 10A, it can be observed that for a mixture with 20 wt.% large particles, there is a linear increase in the bed expansion ratio for all superficial velocities. Furthermore, the bed expands 1.5 times the initial bed height for a superficial velocity of U_{gs} = 0.3 m/s and goes up to 2.4 m for a superficial velocity of U_{gs} = 0.6 m/s. This reiterates the significant role of bubble volume in occupying the expanded bed volume, clearly indicating a bubbling fluidized bed regime. For a 40 wt.% mixture, however, the bed expansion increases for superficial velocities up to U_{gs} = 0.45 m/s (1.28 times for U_{gs} = 0.3 m/s and 1.49 times for U_{gs} = 0.45 m/s), and there is a decrease in bed expansion for higher superficial velocities. This indicates that for this binary mixture, a bubbly regime exists for initial superficial velocities, but a transition to a turbulent regime that breaks the bubbles, reduces the bubble volume, and promotes mixing takes place. This causes a lower increase in bed height than expected, as seen in the 20 wt.% mixture. For the 60 wt.% mixture, however, the increase in bed volume is lower (1.1 times the initial height) for a superficial velocity of U_{gs} = 0.3 m/s, indicating a homogeneous regime. This is followed by 1.3 times initial height for U_{gs} = 0.45 m/s, which indicates a transition to a bubbling regime, and then an increase of 1.73 times the initial bed height for U_{gs} = 0.6 m/s, which indicates a bubbling regime with a considerable number of bubbles occupying the expanded bed volume. A similar trend of increase in expanded bed height is shown for an 80 wt.% mixture of large particles for the superficial velocities considered. For a 100 wt.% large particle mixture, a linear increase of height for the two superficial velocities is observed with a bubbling/slugging regime for a superficial velocity of U_{gs} = 0.6 m/s.

Figure 10B shows the effect of superficial velocity on bed expansion for all the binary mixtures considered with an initial bed height of 0.635 m (z/H = 0.45). It can be observed that for the 0 wt.% large particles, the bed expands to approximately two times the initial bed height. However, there is no significant effect on the bed expansion for the superficial velocities considered. For 20 wt.% large particles in the binary mixture, the bed expansion is 1.4 times for the lowest superficial velocity and then tapers for a velocity of U_{gs} = 0.6 m/s, indicating a transition from a bubbling to a turbulent regime. For 40 wt.% large particles in the binary mixture, there is a linear increase in the bed expansion ratio, indicating that for all superficial velocities, the bed follows a bubbling regime. For 60 wt.% and 80 wt.% large particles in the binary mixtures, a minor relative increase in bed expansion ratios is observed at lower superficial velocities, while a steep increase is observed for superficial velocities approximately U_{gs} = 0.6 m/s. A linear increase in bed expansion ratio is also observed for 100 wt.% large particles.

3.5 Correlation development

Table 3 summarizes the correlations for minimum fluidization velocities and pressure drops available in the literature. Because a comprehensive analysis in terms of quantification of pressure drop and velocity distribution of both gas and particle velocities has been made in the present work, it was thought worthwhile to find a correlation between minimum fluidization velocity and pressure drop. To determine the pressure drop, simulations for different superficial velocities (0.02–0.75 m/s) starting from fixed bed to fluidized bed were carried out for all the binary mixtures and bed pressure drop versus superficial velocity were plotted. The

TABLE 3 Correlations for minimum fluidization velocity and pressure drop available in the literature.

Reference	Minimum fluidization velocity correlation	Pressure drop correlation
Wen and Yu (1966)	$Re_{mf} = (33.7^2 + 0.0408 Ar_{si})^{(\frac{1}{2})} - 33.7$ (3)	—
	$Ar_{si,sj} = \frac{\rho_{mf(max)}(\rho_{mf(max)} - \rho_g) g d^3_{p(si,sj)}}{\mu^2_g}$	
	$U_{mf} = \frac{Re_{mf}\mu_g}{d_{p(si,sj)}\rho_g}$	
Khani (2011)	$Re_{mf} = 7.16 (Ar_{si})^{0.393} (\frac{d_{si,sj}}{D^B_{co}})^{0.987} (\frac{\varepsilon_g}{\varnothing_{si}})^{-0.833} (cos\,\delta)^{-275.486}$	$\frac{\Delta P_{max.}}{\rho_{si} g H_{st}} = 106.729 (\frac{\rho_{si}}{\rho_g})^{-0.522} (\frac{d_{si,sj}}{D^B_{co}})^{0.309} (\frac{h}{D^B_{co}})^{-0.976} (cos\,\delta)^{-10.858}$
	$0° \le \delta \le 4.5°$	$0° \le \delta \le 4.5°$
Rasteh et al. (2015)	$Re_{mf} = 0.203 (Ar_{si})^{0.588} (\frac{\varepsilon_g}{\varnothing_{si}})^{2.69} (\frac{h}{D^B_{co}})^{0.276} (\cos\delta)^{-6.42}$	$Eu_{mf} = 3.69 \times 10^6 (Ar_{si})^{-0.547} (\frac{\varepsilon_g}{\varnothing_{si}})^{-0.848} (\frac{h}{D^B_{co}})^{-0.299} (\cos\delta)^{6.33}$
	$Bo < 0.05$	$Bo < 0.05$
Fu et al. (2019)	$Re_{mf} = \frac{(33.7^2 + 0.0408 Ar_{si})^{(\frac{1}{2})} - 33.7}{1 - \exp(-14.45 \Delta P^{-0.3})}$	—
Sau et al. (2008)	—	$\Delta P_{max} = 7.457 (\frac{D^{Top}_{co}}{D^B_{co}})^{0.038} (\frac{d_{si,sj}}{D^B_{co}})^{0.222} (\frac{H_{st}}{D^B_{co}})^{0.642} (\frac{\rho_{si}}{\rho_g})^{0.723}$

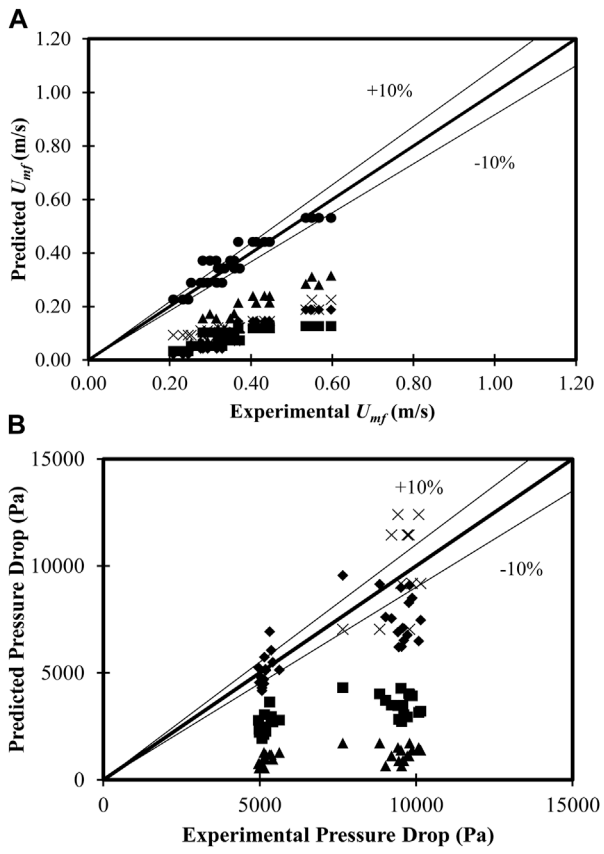

FIGURE 11
Parity plot for the newly developed correlations. **(A)** Minimum fluidization velocity: ◆ Wen and Yu (1966), ■ Khani (2011), ▲ Fu et al. (2019), × Rasteh et al. (2015), and ● Present work. **(B)** Pressure drop: ◆ Sau et al. (2008), ■ Khani (2011), ▲ Rasteh et al. (2015), and × present work.

minimum fluid velocity was determined from the intersection of the linear graph where the bed changes from fixed to fluidized bed. The corresponding gas volume fraction in the bed was found by taking the time-averaged volume fraction of the bed after 7 s for all the cases while the particles were considered to be spherical [as per experimental data of Jayarathna and Halvorsen (2011)] with sphericity equal to 1. Because the pressure drop was found to be a function of the initial bed height to column diameter ratio, it was also considered for the correlation of pressure drop, although only two bed heights have been considered.

A new correlation for minimum fluidization velocity is given by the following equation:

$$Re_{mf} = 0.143 Ar_{si}^{0.58} \left(\frac{\varepsilon_g}{\varnothing_{si}}\right)^{0.63}. \quad (1)$$

The correlation for maximum pressure drop is given by

$$Eu_{mf} = 261.45 * 10^3 Ar_{si}^{-0.33} \left(\frac{\varepsilon_g}{\varnothing_{si}}\right)^{-3.57} \left(\frac{h}{D^B_{co}}\right)^{-0.99}. \quad (2)$$

Figure 11A shows the parity plot of minimum fluidization velocity predicted by previous works with respect to the experimental data used from the literature. It can be observed that the predictions from the correlation developed fall within a ±15% deviation from experimental data. The correlations available in the literature predict with deviations of more than 80%. This is due to the fact that the superficial velocities considered by the authors are much lower than the ones considered in the present analysis. Figure 11B shows the parity plot of pressure drop with experimental data. The developed correlation predicts well within ±15% deviation. The predictions of Sau et al. (2008) also fall within a ±15% deviation from experimental data, while other correlations show very high deviations (>80%).

4 Conclusion

Radial gas and particle velocity profiles for different axial locations and vertical centerline particle volume fraction profiles have been presented for each of seven binary mixtures using three different superficial velocities and two different bed heights.

Correlations for minimum fluidization velocity and pressure drop are also presented. The following conclusions can be drawn:

1. For unary beds of small and large particles, the gas and particle velocities depicts characteristics of fluidized bubbling similar to the velocities observed in the literature. This is the case for all superficial velocities and all bed heights.
2. For the 20 wt.% mixture of larger particles, segregation is observed for a lower bed height both at the bottom and top of the beds. Particle velocities are higher for smaller particles with higher superficial velocities, and a mixed pattern is observed. Although larger particles are also observed in the velocity distribution profiles, solid volume fraction profiles show that only a few large particles might reach the top of the bed.
3. For the 40 wt.% mixture, the bed is segregated at the bottom and well mixed at the middle and top, with the volume fraction of smaller particles larger than that of larger particles. The gas velocities for lower fractions of large particles up to 40 wt.% show a convex structured profile and bypassing near the walls for all superficial velocities and bed heights considered. Particle velocities are also higher near the walls and lower in the middle. Positive and negative velocities of particles are observed, representative of good mixing. This is also confirmed by observing the solid volume fraction profiles.
4. For the 60 wt.% mixture, the bed is slightly segregated at the bottom while well mixed at the middle and top, similar to the 40 wt.% mixture. The only difference is the percentage of large particles is higher in all three layers of the final bed height. Furthermore, with an increase in particle size, that is, 60 wt.% large particles, the bypassing of gas velocities increases as high as U_g = 5 m/s for an initial bed height of 0.635 m (z/H = 0.45) and a superficial velocity of U_{gs} = 0.45 m/s and is observed more toward the left wall.
5. For the 80 wt.% large particle mixture, the bed acts as a distributor with little increase in its final height. Higher gas velocities near the walls are observed.
6. The axial particle volume fraction profiles show undulations in the middle zone of the fluidized bed with low volume fractions in the top/dilute zone for binary mixtures up to 60 wt.% large particles. For higher percentages of large particles, profiles confirm that the bed remains stagnant for all superficial velocities considered.
7. Bed height expansion is seen to be a linear function for superficial velocities up to U_{gs} = 0.45 m/s for all binary mixtures considered, with increases or decreases depending on the percentage of large particles present for both initial bed heights. For a lower initial bed height of 0.335 m (z/H = 0.24), the slopes of the lines are different but have similar trends.
8. Correlations for minimum fluidization velocity and the pressure drop for binary mixtures have been made. Predictions are compared with correlations available in the literature as well as the experimental data from the literature (Jayarathna and Halvorsen, 2011). A good agreement between predictions and experiments is found.

The conclusions drawn from the flow patterns and profiles could help design a better fluidized bed by choosing the operating window based on the binary mixture at hand.

Data availability statement

The original contributions presented in the study are included in the article/Supplementary Material, further inquiries can be directed to the corresponding author.

Author contributions

Conceptualization: AG; CFD modeling: VB; model validation: AG and VB; writing the manuscript: AG and VB; reviewing: AG; supervision: AG; formal analysis: AG and VB; data curation: VB and AG. All authors contributed to the article and approved the submitted version.

Acknowledgments

The authors would like to thank School of Engineering and Applied Sciences, Ahmedabad University, for their continuous support during the entire project.

Conflict of interest

The authors declare that the research was conducted in the absence of any commercial or financial relationships that could be construed as a potential conflict of interest.

Publisher's note

Supplementary material

The Supplementary Material for this article can be found online at: https://www.frontiersin.org/articles/10.3389/fenrg.2023.1150943/full#supplementary-material

References

Agrawal, V., Shinde, Y., Shah, M. T., Utikar, R. P., Pareek, V. K., and Joshi, J. B. (2018). Effect of drag models on CFD–DEM predictions of bubbling fluidized beds with Geldart D particles. *Adv. Powder Technol.* 29, 2658–2669.

Ahmadi, G., and Ma, D. (1990). A thermodynamical formulation for dispersed multiphase turbulent flows—1: Basic theory. *Int. J. Multiph. Flow* 16, 323–340.

Bakshi, A., Ghoniem, A., and Altantzis, C. (2017). Mixing dynamics in bubbling fluidized beds. *AIChE J.* 63, 4316–4328.

Benzarti, S., Mhiri, H., Bournot, H., and Occelli, R. (2014). Numerical simulation of turbulent fluidized bed with Geldart B particles. *Adv. Powder Technol.* 25, 1737–1747.

Čársky, M., Pata, J., Veselý, V., and Hartman, M. (1987). Binary system fluidized bed equilibrium. *Powder Technol.* 51, 237–242.

Chang, J., Wang, G., Gao, J., Zhang, K., Chen, H., and Yang, Y. (2012). CFD modeling of particle–particle heat transfer in dense gas-solid fluidized beds of binary mixture. *Powder Technol.* 217, 50–60.

Chang, J., Wu, Z., Wang, X., and Liu, W. (2019). Two-and three-dimensional hydrodynamic modeling of a pseudo-2D turbulent fluidized bed with Geldart B particle. *Powder Technol.* 351, 159–168.

Chehbouni, A., Chaouki, J., Guy, C., and Klvana, D. (1994). Characterization of the flow transition between bubbling and turbulent fluidization. *Industrial Eng. Chem. Res.* 33, 1889–1896.

Chew, J. W., and Cocco, R. A. (2021). Fast versus turbulent fluidization of Geldart Group B particles. *AIChE J.* 67, e17216.

Chew, J. W., Wolz, J. R., and Hrenya, C. M. (2010). Axial segregation in bubbling gas-fluidized beds with Gaussian and lognormal distributions of Geldart Group B particles. *AIChE J.* 56, 3049–3061.

Chyang, C. S., Kuo, C. C., and Chen, M. Y. (1989). Minimum fluidization velocity of binary mixtures. *Can. J. Chem. Eng.* 67, 344–347.

Cooper, S., and Coronella, C. J. (2005). CFD simulations of particle mixing in a binary fluidized bed. *Powder Technol.* 151, 27–36.

Daryus, A., Siswantara, A. I., BudiarsoGunadi, G. G. R., and Pujowidodo, H. "CFD simulation of multiphase fluid flow in a two-dimensional gas-solid fluidized bed using two different turbulence models," in Proceedings of the AIP Conference Proceedings, Bali, Indonesia, November 2019, 020016.

Schaeffer, D. G. (1987). Instability in the evoluations describing incompressible granular flow. *J. Differ. Equations* 66, 19–50.

Di Maio, F. P., Di Renzo, A., and Vivacqua, V. (2012). A particle segregation model for gas-fluidization of binary mixtures. *Powder Technol.* 226, 180–188.

Du, W., Bao, X., Xu, J., and Wei, W. (2006). Computational fluid dynamics (CFD) modeling of spouted bed: Influence of frictional stress, maximum packing limit and coefficient of restitution of particles. *Chem. Eng. Sci.* 61, 4558–4570.

Ellis, N., Bi, H., Lim, C., and Grace, J. (2004). Hydrodynamics of turbulent fluidized beds of different diameters. *Powder Technol.* 141, 124–136.

Emiola-Sadiq, T., Wang, J., Zhang, L., and Dalai, A. (2021). Mixing and segregation of binary mixtures of biomass and silica sand in a fluidized bed. *Particuology* 58, 58–73.

Fu, Z., Zhu, J., Barghi, S., Zhao, Y., Luo, Z., and Duan, C. (2019). Minimum fluidization velocity growth due to bed inventory increase in an Air Dense Medium Fluidized Bed. *Chem. Eng. J.* 359, 1372–1378.

Ganguli, A., and Bhatt, V. (2023). CFD simulations to study bed characteristics in gas-solid fluidized beds with binary mixtures of geldart-B particles: I qualitative analysis. *Front. Energy Res.* 11, 72.

Gao, J., Lan, X., Fan, Y., Chang, J., Wang, G., Lu, C., et al. (2009). Hydrodynamics of gas–solid fluidized bed of disparately sized binary particles. *Chem. Eng. Sci.* 64, 4302–4316.

Gauthier, D., Zerguerras, S., and Flamant, G. (1999). Influence of the particle size distribution of powders on the velocities of minimum and complete fluidization. *Chem. Eng. J.* 74, 181–196.

Gupta, S., and De, S. (2021). Investigation of hydrodynamics and segregation characteristics in a dual fluidized bed using the binary mixture of sand and high-ash coal. *Adv. Powder Technol.* 32. doi:10.1016/j.apt.2021.04.023

Harris, A., Davidson, J., and Thorpe, R. (2002). The prediction of particle cluster properties in the near wall region of a vertical riser (200157). *Powder Technol.* 127, 128–143.

Hoffmann, A., Janssen, L., and Prins, J. (1993). Particle segregation in fluidised binary mixtures. *Chem. Eng. Sci.* 48, 1583–1592.

Jayarathna, C., and Halvorsen, B. (2011). Experimental and computational study of pressure drop and void fraction in a bubbling fluidized bed. *WIT Trans. Eng. Sci.* 70, 177–188.

Kalo, L., Pant, H. J., Cassanello, M. C., and Upadhyay, R. K. (2019). Time series analysis of a binary gas-solid conical fluidized bed using radioactive particle tracking (RPT) technique data. *Chem. Eng. J.* 377, 119807.

Khani, M. (2011). Models for prediction of hydrodynamic characteristics of gas–solid tapered and mini-tapered fluidized beds. *Powder Technol.* 205, 224–230.

Khezri, R., Karim Ghani, W. A., Masoudi Soltani, S., Awang Biak, D. R., Yunus, R., Silas, K., et al. (2019). Computational fluid dynamics simulation of gas–solid hydrodynamics in a bubbling fluidized-bed reactor: Effects of air distributor, viscous and drag models. *Processes* 7, 524.

Kotoky, S., Dalal, A., and Natarajan, G. (2020). A computational analysis of the role of particle diameter on the fluidization behavior in a bubbling gas–solid fluidized bed. *Comput. Part. Mech.* 7, 555–565.

Lan, X., Yan, W., Xu, C., Gao, J., and Luo, Z.-H. (2014). Hydrodynamics of gas–solid turbulent fluidized bed of polydisperse binary particles. *Powder Technol.* 262, 106–123.

Leion, H., Frick, V., and Hildor, F. (2018). Experimental method and setup for laboratory fluidized bed reactor testing. *Energies* 11, 2505.

Leu, L. P., and Wu, C. N. (2000). Prediction of pressure fluctuations and minimum fluidization velocity of binary mixtures of geldart group B particles in bubbling fluidized beds. *Can. J. Chem. Eng.* 78, 578–585.

Lun, C., Savage, S. B., Jeffrey, D., and Chepurniy, N. (1984). Kinetic theories for granular flow: Inelastic particles in Couette flow and slightly inelastic particles in a general flowfield. *J. fluid Mech.* 140, 223–256.

Mazzei, L., Casillo, A., Lettieri, P., and Salatino, P. (2010). CFD simulations of segregating fluidized bidisperse mixtures of particles differing in size. *Chem. Eng. J.* 156, 432–445.

Menéndez, M., Herguido, J., Bérard, A., and Patience, G. S. (2019). Experimental methods in chemical engineering: Reactors—Fluidized beds. *Can. J. Chem. Eng.* 97, 2383–2394.

Mostafazadeh, M., Rahimzadeh, H., and Hamzei, M. (2013). Numerical analysis of the mixing process in a gas–solid fluidized bed reactor. *Powder Technol.* 239, 422–433.

Noda, K., Uchida, S., Makino, T., and Kamo, H. (1986). Minimum fluidization velocity of binary mixture of particles with large size ratio. *Powder Technol.* 46, 149–154.

Obuseh, C. C., Feng, Z.-G., and Paudel, B. D. (2012). An experimental study on fluidization of binary mixture in particulate flows. *J. dispersion Sci. Technol.* 33, 1379–1384.

Pei, P., Wu, G., Zhang, K., Yu, B., Jiang, J., and Wen, D. (2010). CFD simulation of jet behaviors in a binary gas-solid fluidized bed: Comparisons with experiments. *Front. Chem. Eng. China* 4, 242–249.

Penn, A., Boyce, C. M., Conzelmann, N., Bezinge, G., Pruessmann, K. P., and Müller, C. R. (2019). Real-time magnetic resonance imaging of fluidized beds with internals. *Chem. Eng. Sci.* 198, 117–123.

Philippsen, C. G., Vilela, A. C. F., and Dalla Zen, L. (2015). Fluidized bed modeling applied to the analysis of processes: Review and state of the art. *J. Mater. Res. Technol.* 4, 208–216.

Rao, A., Curtis, J. S., Hancock, B. C., and Wassgren, C. (2010). The effect of column diameter and bed height on minimum fluidization velocity. *AIChE J.* 56, 2304–2311.

Rasteh, M., Farhadi, F., and Bahramian, A. (2015). Hydrodynamic characteristics of gas–solid tapered fluidized beds: Experimental studies and empirical models. *Powder Technol.* 283, 355–367.

Roy, S., Pant, H. J., and Roy, S. (2021). Velocity characterization of solids in binary fluidized beds. *Chem. Eng. Sci.* 246, 116883.

Sahoo, P., and Sahoo, A. (2016). CFD simulation for hydrodynamic behaviour of fine particles in a fluidized bed. *Indian J. Chem. Technol. (IJCT)* 23, 253–261.

Sau, D., and Biswal, K. (2011). Computational fluid dynamics and experimental study of the hydrodynamics of a gas–solid tapered fluidized bed. *Appl. Math. Model.* 35, 2265–2278.

Sau, D., Mohanty, S., and Biswal, K. (2008). Correlations for critical fluidization velocity and maximum bed pressure drop for heterogeneous binary mixture of irregular particles in gas–solid tapered fluidized beds. *Chem. Eng. Process. Process Intensif.* 47, 2386–2390.

Shrestha, S., Kuang, S., Yu, A., and Zhou, Z. (2019). Bubble dynamics in bubbling fluidized beds of ellipsoidal particles. *AIChE J.* 65, e16736.

Singh, B. K., Roy, S., and Buwa, V. V. (2019). Dynamics of segregation and fluidization of binary mixtures in a cylindrical fluidized bed. *AIChE J.* 65, e16682.

Syamlal, M., and O'brien, T. (1987). *The derivation of a drag coefficient formula from velocity-voidage correlations*. Morgantown, WV, United States: US Department of energy, Office of Fossil Energy NETL.

Syamlal, M., Rogers, W., and Obrien, T. J. (1993). *MFIX documentation theory guide*. Morgantown, WV, United States: USDOE Morgantown Energy Technology Center.

Van Den Moortel, T., Azario, E., Santini, R., and Tadrist, L. (1998). Experimental analysis of the gas–particle flow in a circulating fluidized bed using a phase Doppler particle analyzer. *Chem. Eng. Sci.* 53, 1883–1899.

Wen, C., and Yu, Y. (1966). A generalized method for predicting the minimum fluidization velocity. *AIChE J.* 12, 610–612.

Zaabout, A., Bournot, H., Occelli, R., and Kharbouch, B. "Characterization of turbulent regime behavior in the dilute zone of a circulating fluidized bed riser," in Proceedings of the 13th International Conference on Fluidization - New Paradigm in Fluidization Engineering, Korea, May 2010.

Zhang, D., Deen, N., and Kuipers, J. (2006). Numerical simulation of the dynamic flow behavior in a bubble column: A study of closures for turbulence and interface forces. *Chem. Eng. Sci.* 61, 7593–7608.

Zhang, Y., Zhao, Y., Lu, L., Ge, W., Wang, J., and Duan, C. (2017). Assessment of polydisperse drag models for the size segregation in a bubbling fluidized bed using discrete particle method. *Chem. Eng. Sci.* 160, 106–112.

Nomenclature

Alphabetical Symbols

Ar	Archimedes' number	-
Bo	Bond number	-
***D*, D_1**	Diameter	m
Eu	Euler number	-
H	Height	m
P	Pressure	Pa
R	Radius of the cylinder	m
Re	Reynolds' number	-
U	Velocity	$m{\cdot}s^{-1}$
d	Particle diameter size	m
g	Gravitational acceleration = 9.81	$m{\cdot}s^{-2}$
h	Height of the initial bed	m
r	Radial distance of observation	m
z	Height of observation	m

Greek Symbols

Δ	Difference operator	-
δ	Tapered angle	°
ε	Volume fraction	-
μ	Viscosity	Pa·s
ρ	Density	$kg{\cdot}m^{-3}$
∅	Sphericity	-

Subscripts

co	Column
e	Expanded
g	Gas phase
gs	Superficial gas
mf	Minimum fluidization
p	Particle
s	Initial
s1	Solid phase with smaller particle size
si	Solid phase si
st	Stagnant
si, sj	Interaction between the solid phase si and the solid phase sj

Superscripts

b	Bottom
Top	Top

Abbreviations

3D	Three dimensional
CFD	Computational fluid dynamics
DEM	Discrete element method
RPT	Radioactive particle tracking

Frontiers in
Energy Research

Advances and innovation in sustainable, reliable and affordable energy

Explores sustainable and environmental developments in energy. It focuses on technological advances supporting Sustainable Development Goal 7: access to affordable, reliable, sustainable and modern energy for all.

Discover the latest Research Topics

See more →

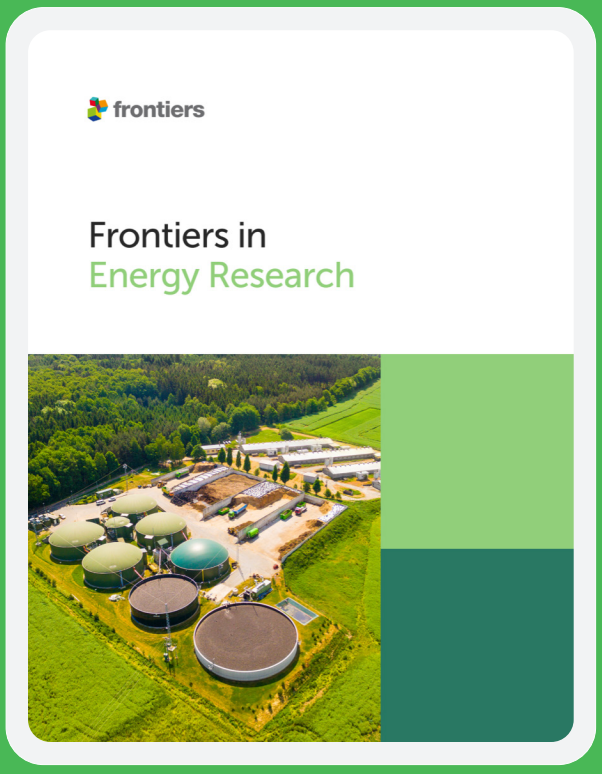

Frontiers

Avenue du Tribunal-Fédéral 34
1005 Lausanne, Switzerland
frontiersin.org

Contact us

+41 (0)21 510 17 00
frontiersin.org/about/contact